Development of the PUMA Antiproton and Ion Trap

Entwicklung der PUMA Antiprotonen- und Ionen-Falle
Zur Erlangung des Grades eines Doktors der Naturwissenschaften (Dr. rer. nat.)
Genehmigte Dissertation von Alexander Schmidt aus Weilburg
Tag der Einreichung: November 13, 2023, Tag der Prüfung: Dezember 20, 2023

1. Gutachten: Prof. Dr. Alexandre Obertelli
2. Gutachten: Prof. Dr. Wilfried Nörtershäuser
Darmstadt, Technische Universität Darmstadt

TECHNISCHE
UNIVERSITÄT
DARMSTADT

Physics Department
Institut für Kernphysik
AG Prof. Dr. Obertelli

Development of the PUMA Antiproton and Ion Trap
Entwicklung der PUMA Antiprotonen- und Ionen-Falle

Accepted doctoral thesis by Alexander Schmidt

Date of submission: November 13, 2023
Date of thesis defense: Dezember 20, 2023

Darmstadt, Technische Universität Darmstadt

Erklärungen laut Promotionsordnung

§ 8 Abs. 1 lit. c PromO

Ich versichere hiermit, dass die elektronische Version meiner Dissertation mit der schriftlichen Version übereinstimmt.

§ 8 Abs. 1 lit. d PromO

Ich versichere hiermit, dass zu einem vorherigen Zeitpunkt noch keine Promotion versucht wurde. In diesem Fall sind nähere Angaben über Zeitpunkt, Hochschule, Dissertationsthema und Ergebnis dieses Versuchs mitzuteilen.

§ 9 Abs. 1 PromO

Ich versichere hiermit, dass die vorliegende Dissertation selbstständig und nur unter Verwendung der angegebenen Quellen verfasst wurde.

§ 9 Abs. 2 PromO

Die Arbeit hat bisher noch nicht zu Prüfungszwecken gedient.

Darmstadt, November 13, 2023

A. Schmidt

Abstract

The PUMA (antiProton Unstable Matter Annihilation) experiment aims at determining the ratio of neutrons to protons in the nuclear density tail, based on the ratio of annihilated neutrons and protons after the capture of low-energy antiprotons, as a new nuclear structure observable.

The concept of PUMA relies on a transportable experimental setup. It combines a cryogenic Penning trap for the long-term storage and transport of antiprotons after accumulation at the ELENA (Extra-Low ENergy Antiproton) ring at CERN and a detection system for the identification of pions. These pions originate from annihilations of antiprotons with ions either provided by the offline ion source of PUMA at ELENA or the ISOLDE (Isotope Separation On-Line DEvice) facility at CERN.

In this work, the cryogenic Penning trap setup of PUMA has been designed, procured and assembled. The trapping of antiprotons with storage times in the order of 100 days is equivalent to ambient pressures of about 10^{-17} mbar, which can be achieved by cryosorption. Thermal and vacuum simulations have been performed to validate the trap design for production. Assuming a pressure of 10^{-11} mbar at the setup entrance and by the inclusion of a cylinder shutter for aperture blocking, a pressure of 10^{-19} mbar is predicted in the trap. Following the mechanical assembly, the setup is ready for commissioning.

To optimize the ion optics for the antiprotons from ELENA towards PUMA into the Penning trap, ion optical simulations have been performed. By refining acceptance intervals for the ideal deceleration within the pulsed drift tube and optimal potentials on the focusing elements along the beamline, a transmission of 91 % is reached in the simulation. The results of the simulations were then benchmarked with measurements performed on the PUMA antiproton beamline at ELENA.

Antiprotons also offer opportunities beyond the physics program of PUMA, as the interaction of the annihilation products with the residual nucleus can lead to the formation of single-Λ hypernuclei. Microscopic Monte-Carlo simulations within a transport framework were performed and predict the population of a wide range of currently inaccessible hypernuclei with a typical production rate of 10^{-5} per annihilation. These results offer a new prospective towards studying hypernuclei using antiprotons.

Zusammenfassung

Das PUMA (antiProton Unstable Matter Annihilation) Experiment zielt darauf ab, das Verhältnis von Neutronen zu Protonen im Kerndichteschweif als neue Kernstruktur-Observable zu bestimmen, basierend auf dem Verhältnis von annihilierten Neutronen und Protonen nach dem Einfang von niederenergetischen Antiprotonen.

Das Konzept von PUMA beruht auf einem transportablen Versuchsaufbau. Es kombiniert eine kryogene Penning-Falle für die langfristige Speicherung und den Transport von Antiprotonen nach der Akkumulation am ELENA (Extra-Low ENergy Antiproton) Ring des CERNs und ein Detektionssystem für die Identifizierung von Pionen. Diese Pionen stammen aus der Annihilation von Antiprotonen mit Ionen, die entweder von der Offline-Ionenquelle von PUMA an ELENA oder von der ISOLDE (Isotope Separation On-Line DEvice) Einrichtung am CERN bereitgestellt werden.

In dieser Arbeit wurde der kryogene Penning-Fallenaufbau von PUMA entworfen, beschafft und zusammengebaut. Das Speichern von Antiprotonen über Zeiträume in der Größenordnung von 100 Tagen entspricht einem Umgebungsdruck von etwa 10^{-17} mbar, der durch Kryosorption erreicht werden kann. Um das Fallendesign für die Produktion zu validieren, wurden thermische und Vakuum-Simulationen durchgeführt. Unter der Annahme eines Drucks von 10^{-11} mbar am Eingang des Aufbaus und unter Einbeziehung eines Zylinder-Shutters zur Blockade der Öffnung wird ein Druck von 10^{-19} mbar in der Speicherfalle vorhergesagt. Nach der mechanischen Montage ist der Aufbau nun bereit für die Inbetriebnahme.

Zur Optimierung der Ionenoptik für die Antiprotonen von ELENA hin zu PUMA und in die Penning-Falle wurden ionenoptische Simulationen durchgeführt. Durch Verfeinerung der Akzeptanzintervalle für die ideale Abbremsung in der gepulsten Driftröhre und der optimalen Potentiale an den Fokussierungselementen entlang der Strahlführung wurde in der Simulation eine Transmission von 91 % erreicht. Die Ergebnisse der Simulationen wurden dann mit Messungen an der PUMA-Antiprotonenstrahlführung an ELENA verglichen.

Antiprotonen bieten auch Möglichkeiten, die über das Physik-Programm von PUMA hinausgehen, da die Wechselwirkung der Annihilationsprodukte mit dem Restkern zur Bildung von Einzel-Λ-Hyperkernen führen kann. Mikroskopische Monte-Carlo-Simulationen in einem Transport-Framework wurden durchgeführt und sagen die Population eines breiten Spektrums von derzeit unzugänglichen Hyperkernen mit einer typischen Produktionsrate von 10^{-5} pro Annihilation voraus. Diese Ergebnisse bieten eine neue Perspektive für die Untersuchung von Hyperkernen mit Antiprotonen.

Contents

List of Figures

List of Tables

1. Introduction

1.1. Nuclear structure theory

The atomic nucleus is a system composed of protons and neutrons which has a typical size of a few femtometers (fm) and is bound by the effective interaction between nucleons. It emerges as a residual force from the fundamental strong interaction between quarks and gluons as constituents of the nucleons. The latter is typically described in the theoretical framework of quantum chromodynamics (QCD) as a relativistic quantum field theory, which introduces color charge in analogy to electric charge as an additional quantum number for quarks [1]. While the description of the NN attraction via QCD is conceptually possible [2], the resolution of the intrinsic structure of the nucleons is typically not required to describe the phenomena occurring on the energy scales considered in nuclear structure, which are typically below the excitation energy of the Δ-resonance of the nucleons at about 300 MeV. This led to the development of effective models for the description of the nucleus and the nuclear forces, which are only valid for the relevant energy ($\sim$ tens to hundreds of MeV) and length ($\sim$ 1 fm) scales. Within the framework of effective models for nuclear physics, the characterization of the NN interaction and the solution of the quantum mechanical many-body problem are the two essential steps to access global properties of the nucleus, such as ground state energies.

Global properties of the NN interaction can be extracted from properties of bound nuclei and from NN scattering experiments. For very small distances below about 0.5 fm the interaction is strongly repulsive, for distances in the order of 0.5 fm up to about 3 fm the potential is attractive and for distances above 2 fm it quickly drops to zero. These qualitative properties of the nuclear potential can be derived by considering the binding energy per nucleon over the range of stable nuclei. The binding energy already reaches 7 MeV per nucleon for ^{4}He [3, 4] while only increasing slightly to a maximum value of 8.8 MeV per nucleon for ^{62}Ni [4], indicating that the range of the attractive part of the nuclear potential is similar to the size of the ^{4}He nucleus. The short-ranged repulsion arises from the spatial extension of the nucleons, which results from the color neutrality requirement of the strong interaction. As an example, precise spectroscopic data on the S-state energy shift in hydrogen caused by the proton size derive a charge radius of about 0.84 fm [5, 6]. Besides this central part of the interaction, additional contributions arise from a non-central tensor component, which is, *e.g.*, required to explain the non-zero quadrupole moment of the deuteron in its ground state [7], and from a spin-orbit-coupling component, whose finger prints are visible in phase shifts in NN scattering experiments at higher energies [8].

The formal construction of the nuclear interactions for calculations is based on global symmetries, which constrain the operator structure. Besides the requirement of a hermiticity for real eigenvalues, the operator has to be invariant under particle exchange, translation in position and momentum space, rotation, translation in time, time mirroring as well as parity. In its simplest form, a two-body interaction potential

$$V_{\mathrm{NN}} = V_{\mathrm{Z}} + V_{\mathrm{T}} + V_{\mathrm{LS}} \tag{1.1}$$

comprises a central component V_{Z}, a tensor component V_{T} and the spin-orbit component V_{LS} with a linear dependence on the relative momentum. For the construction of realistic NN potentials it is common to include additional terms with a quadratic dependence on the relative momentum. These potentials reproduce experimental NN scattering phase shifts with high precision up to a high energy scale $\Lambda < 300\,\mathrm{MeV}$, beyond which the theory is not applicable anymore. Examples are the Bonn-A/B potentials [9, 10] and the Argonne-V14/V18 potentials [11, 12]. Both groups of realistic potentials are based on the effective meson exchange model, which assumes that the interaction of two nucleons is mediated by the exchange of massive mesons, thus limiting the effective range of the interaction. Depending on the quantum numbers of the mesons, the contribution of their operator structure to the total interaction potential can be determined. While the light pions dominate the long-range behavior of the central and tensor component and σ-mesons cause the medium-range attraction, the heavier mesons cause a part of the short-range repulsion, which is typically enhanced by additional phenomenological regulators fitted to experimental data [13].

As the Bonn and Argonne potentials are strictly two-body potential, based on the fit to NN scattering data, they fail to reproduce ground state energies and the excitation energies of low-lying excited states of light nuclei ($A = 4 \sim 12$), indicating the lack of relevant physics in many-body systems. It was found that the introduction of three-body forces is essential for the description of properties of such few- and many-body systems such as bound nuclei. Realistic implementations are, *e.g.*, the Tucson-Melbourne (TM) [14] or the Illinois 2 and 4 (IL2, IL4) [15] three-body forces, which are then superimposed with the realistic two-body forces from Bonn or Argonne to reproduce the properties of few-body systems.

While the experimental data on NN scattering and bound few-body systems is well reproduced by above potentials and models [16], they do not provide a systematic quantification of uncertainties. A more systematic approach for the construction of a realistic NN interaction potential is the chiral effective field theory (ChEFT) [17, 18]. In its simplest implementation, it considers nucleons and pions as relevant degrees of freedom and adopts the chiral symmetry from QCD, assuming the quarks would have zero mass. It introduces a perturbative expansion with the expansion parameter Q/Λ, so that only a finite number of terms contribute for a given order of the expansion. The soft scale Q typically is set to an external momentum or the pion mass ($\sim 140\,\mathrm{MeV}$) while the hard chiral symmetry breaking scale can vary between $\sim 350\,\mathrm{MeV}$ up to about 1 GeV [19, 20]. The ChEFT NN interaction potential is then expanded in powers ν of the ratio of scales following

$$V_{\mathrm{NN}} = \sum_{\nu} \left(\frac{Q}{\Lambda}\right)^{\nu} f_{\nu}\left(Q, \Lambda\right). \tag{1.2}$$

All terms that contribute have to be invariant under the transformations mentioned in the previous paragraph as well as chiral transformations. In leading order (LO, $\nu = 0$), only an s-wave contact term and static one-pion exchange appear. As a value of $\nu = 1$ is forbidden by parity and time-reversal transformations, the next-to-leading order (NLO, $\nu = 2$) contributes with two-pion exchange terms as well as higher order contact terms. In the next-to-next-to-leading order (NNLO, $\nu = 3$) additional three-body terms are arise naturally in the expansion; and in N^{3}LO also four-body terms emerge. In the perturbative context, it is expected that the contribution of higher orders of the expansion become less relevant, so that it is common to truncate the order of the considered expansion to $\nu = 3$ for practical calculations of medium-mass and heavy nuclei [21, 22]. A sketch of the hierarchy of contributing terms for the ChEFT expansion, assuming only nucleons and pions as degrees of freedom, is depicted in Fig. 1.1. Here, nucleons resonances and heavier exchange mesons are not considered.

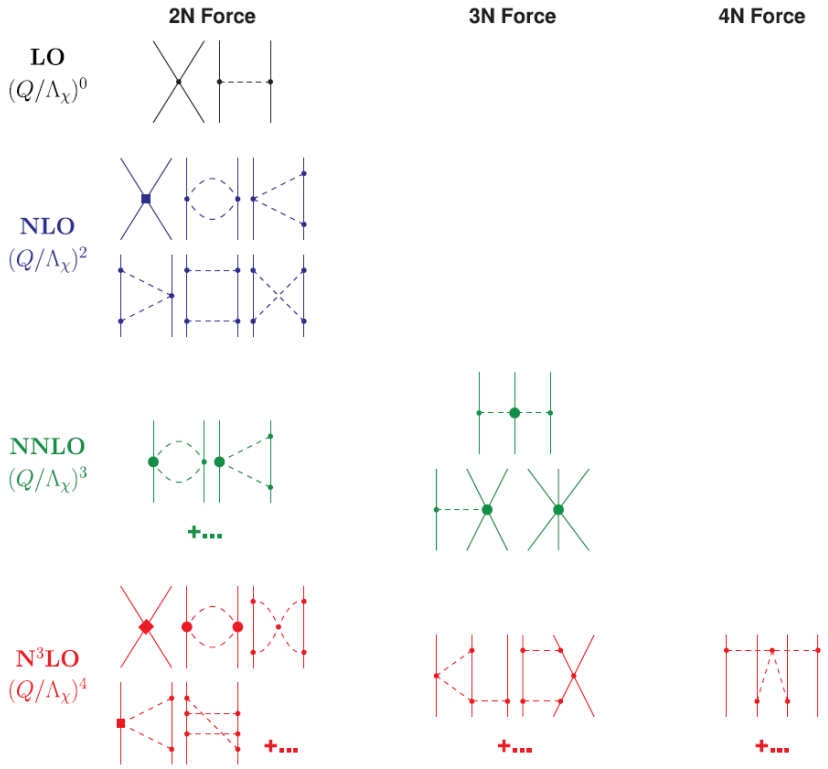

Figure 1.1.: Hierarchy of the nuclear forces in the perturbative expansion in pure nucleon-pion ChEFT. The solid lines represent nucleons and dashed lines pions. The dots and squares indicate interaction vertices, with increasing size for higher order contributions. This figure is reprinted with permission from [18] ©2011 Elsevier.

For the subsequent solution of the quantum mechanical many-body problem the nucleus is modeled as a system of indistinguishable nucleons with spin and isospin as degrees of freedom. The basis of the individual nucleons comprises a spatial, a spin and an isospin part. The many-body basis is then commonly represented by Slater determinants as anti-symmetric product states of the identical nucleon single particle states. One way to provide

an approximate solution for the many-body problem is the introduction of a nuclear mean field, which simplifies the A particle problem to the propagation of a single nucleon in the mean field created by the remaining $A-1$ nucleons. In the Hartree-Fock (HF) models, the mean field is constructed self-consistently as a function of the density, which is given by the sum over the square of the single nucleon wavefunctions, in an iterative scheme based on a variational principle. One frequently used implementation of mean field potentials are the Skyrme potentials [23], which assume zero-range two-body and three-body interactions between two particles, with contributions of a central part and a spin-orbit coupled part. The arising free parameters of the potential are then fitted to experimental data of, *e.g.*, ${}^{16}_{8}\mathrm{O}$, ${}^{32}_{16}\mathrm{S}$ or ${}^{208}_{82}\mathrm{Pb}$ [24]. An extension of the Skyrme potentials is given by the Gogny interactions [25], which include finite-range two body interactions. Due to the fitting of the free parameters to nuclear data, the Hartree-Fock approaches provide good quantitative descriptions of closed-shell nuclei, see Fig. 1.2, but neglect long-range residual interactions such as the pairing interaction of open-shell nuclei, leading to correlations between ground and excited states. These are treated explicitly in extended HF models such as the HF+Bogolyubov (HFB) model [26, 27].

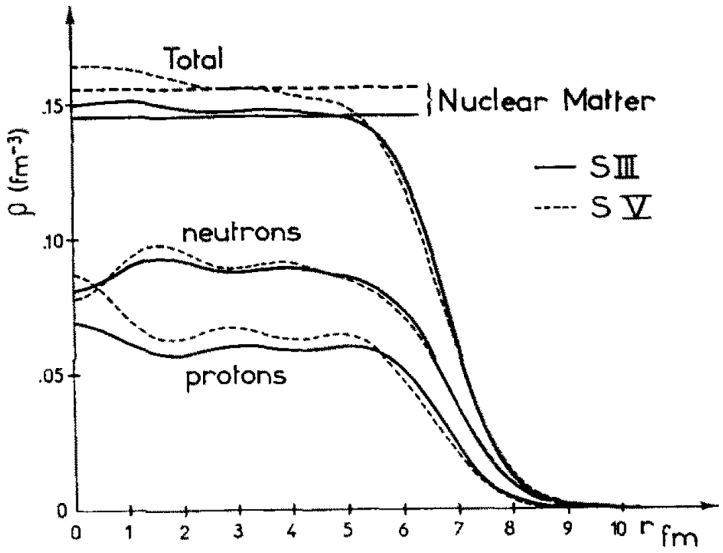

Figure 1.2.: Proton, neutron and total nucleon densities of ^{208}Pb derived in the Skyrme Hartree-Fock framework with the SIII and SV parametrizations of the Skyrme force. This figure is reprinted with permission from [28] ©1975 Elsevier.

In the recent years, a strong emphasis is set on the *ab initio* approach for the solution of the many-body problem. In the context of nuclear structure physics this comprises a complete discussion of all uncertainties, which are induced by the truncation of the interaction potential to a given order of the ChEFT expansion and thus in the order of many-body interactions. Additionally, the inherently infinite basis space needs to be truncated to a finite model space and the statistical uncertainties originating from the fit of the free parameters to experimental data have to be quantified. This uncertainty quantification is typically performed by investigating the convergence of observables with respect to the order of the truncation. In the framework of *ab initio* models, many different approaches

were developed in the last 20 years. Examples are the no-core shell model (NCSM) [29], the Variational Monte Carlo method [30], the Green's function Monte Carlo method [31], many-body perturbation theory methods [32] or the coupled cluster models [33]. These models were initially used for the description of light nuclei up to a mass number of ~ 20, but the recent progress in the computational power and in the development of numerical algorithms to calculate the high-dimensional coupled equations allows the description of heavier nuclei. Recently, the doubly-magic $^{208}_{82}\mathrm{Pb}$ nucleus was investigated in an *ab initio* framework [22], and calculations were employed with coupled-cluster (CC), in-medium similarity re-normalization group (IMSRG) and many-body perturbation theory methods to transform the Hamiltonian in a structure which simplifies calculations. The free parameters of the ChEFT interaction potential, *i.e.*, the low-energy coupling constants related to the contact terms of the expansion, are initially constrained by NN scattering data as well as ground state properties of $^{2}\mathrm{H}$, $^{3}\mathrm{H}$, $^{4}\mathrm{He}$ and $^{16}\mathrm{O}$ to limit the non-implausible parameter space. The obtained 34 non-implausible parametrizations are then weighted with a likelihood measure calibrated on data on $^{48}\mathrm{Ca}$. Predictions for the ground state energy, the electric point-proton radius, the electric dipole polarizability and the neutron skin thickness are obtained as outputs. The latter value will be addressed in Sec. 1.4 as a comparison to experimental values.

The above-mentioned models are used to describe nuclei as an approximation of infinite nuclear matter, which for light nuclei up to $^{40}_{20}\mathrm{Ca}$ is symmetric for protons and neutrons. At the nuclear saturation density $\rho_0 = 0.16\,\mathrm{fm}^{-3}$ the attractive two-body forces and the repulsive three-body forces and short-ranged correlations are balanced, leading to an energetically favored state, which maximizes the binding energy of the nuclei. Moving away from the saturation density in infinite nuclear matter increases the total energy of the system, similarly to the introduction of an asymmetry of protons and neutrons. Figure 1.3 sketches the energy per nucleon as a function of the nucleon density for both symmetric nuclear matter and pure neutron matter in the form of an equation of state (EoS). The energy difference between both curves for a given isoscalar density $\rho = \rho_\mathrm{n} + \rho_\mathrm{p}$ as the sum of the proton and neutron densities $\rho_\mathrm{p,n}$ is given by the symmetry energy $S(\rho)$.

By introducing the asymmetry coefficient $\delta = (\rho_\mathrm{n} - \rho_\mathrm{p})/\rho$ and assuming that δ and ρ are independent, the energy density of asymmetric nuclear matter can then be expanded as

$$\frac{E\left(\rho,\delta\right)}{\rho} = \frac{E\left(\rho,\delta=0\right)}{\rho} + S\left(\rho\right)\,\delta^2 + \ldots . \tag{1.3}$$

This energy density of asymmetric nuclear matter is not only relevant for microscopic systems such as neutron-rich nuclei, but also guides the properties of stellar systems, *i.e.*, neutron stars [34]. As their inner crust is predominantly composed by neutrons and their density is at the same order of magnitude to the nuclear saturation density, their properties are well characterized by the asymmetry term of the nuclear EoS. Even though their masses are similar to the solar mass, their radius is about four orders of magnitude lower than the solar radius because of the very strong gravitational force. This gravitation is compensated by a Fermi pressure P, which arises from the Pauli principle and the required energy to raise its constituent particles into excited states and prevents the collapse of the neutron star into a black hole. This pressure, assuming zero temperature, is directly connected to

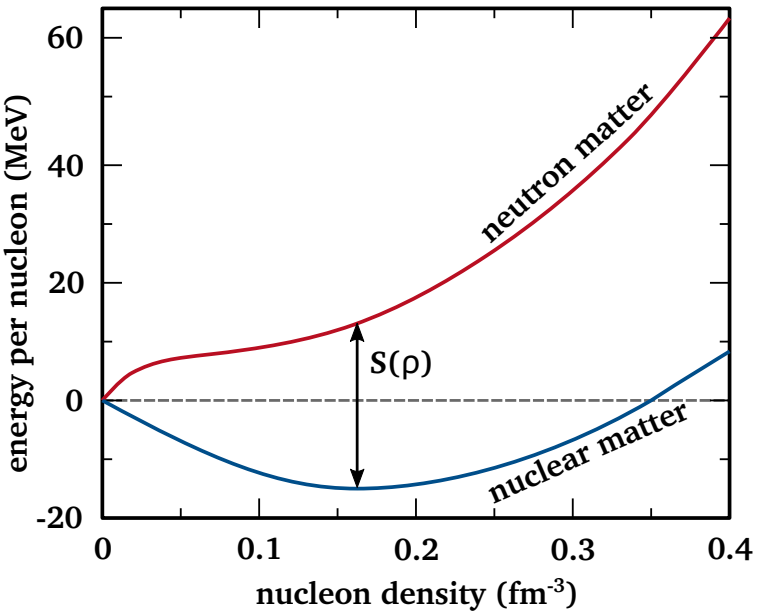

Figure 1.3.: Equation of state for symmetric nuclear and pure neutron matter near the saturation density $\rho_0 = 0.16\,\mathrm{fm}^{-3}$, assuming a temperature $T = 0$. The difference in energy for a given density is given by the symmetry energy $S(\rho)$.

the partial derivative of the energy density with respect to the density via

$$P = \rho^2 \frac{\partial \left(E\left(\rho, \delta\right)/\rho\right)}{\partial \rho}. \tag{1.4}$$

Assuming that a neutron star is composed by pure neutron matter ($\delta = 1$) at zero temperature and evaluating Eq. (1.3) at the saturation density leads to the following relation

$$P\left(\rho_0\right) = \rho^2 \left.\frac{\partial S}{\partial \rho}\right|_{\rho=\rho_0}, \tag{1.5}$$

which directly correlates the pressure of the neutron star with the derivative of the symmetry energy. By expanding the symmetry energy around the saturation density as

$$S\left(\rho\right) = J + L\frac{\left(\rho - \rho_0\right)}{3\rho_0} + \ldots, \tag{1.6}$$

the slope parameter L of the symmetry energy is obtained as $L = 3\rho_0 \left(\partial S\left(\rho\right)/\partial\rho\right)|_{\rho=\rho_0}$.

In the proximity of the nuclear saturation density, the equation of state is constrained by both theoretical calculations [35–37] and experiments [38]. Additional constraints are imposed by astrophysical observations such as gravitational waves from neutron star mergers [39], supernovae [40], neutron star radii and particularly the observation of two-solar mass neutron stars [41–43]. While the latter provide information on the equation of state above the saturation density, the exact properties of the EoS in this density regime remain uncertain. Based on the available data, numerous different parametrizations of the EoS can be obtained [40, 44], which result in different mass-radius relations for neutron stars, as

indicated in Fig. 1.4. Here, the Shen EoS [45] is taken as a reference, and the fit parameters $m*$ as effective nucleon mass, K as incompressibility and $E_{\mathrm{sym}} = S$ as symmetry energy are varied based on ChEFT calculations.

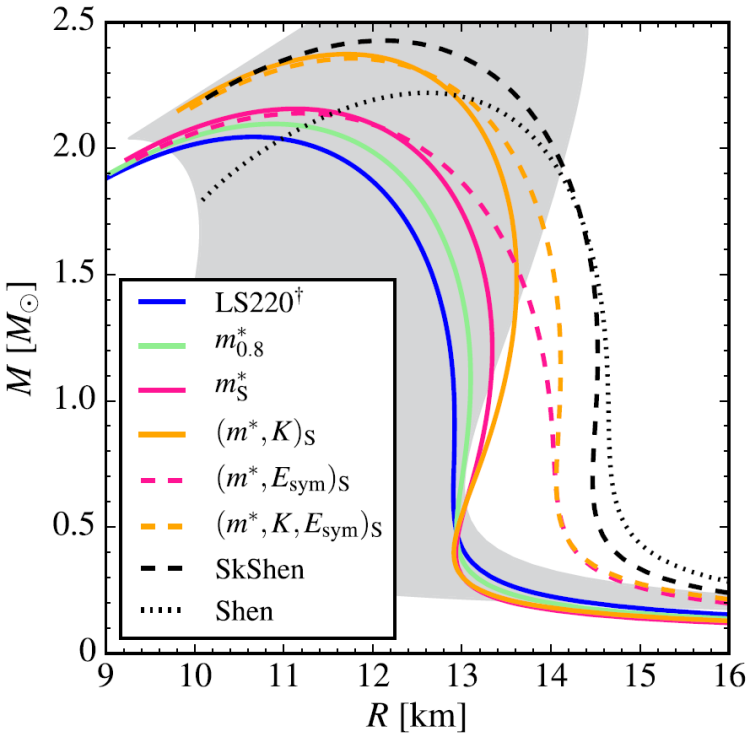

Figure 1.4.: Neutron star mass-radius relation for different parametrizations of the nuclear EoS by Shen. The effective nucleon mass m^*, the incompressibility K and the symmetry energy E_{sym} are varied w.r.t. the original Shen EoS [45]. The gray band is based on ChEFT calculations up to saturation density with an extension to higher densities [46]. This figure is reprinted with permission from [40] ©2020 American Physical Society.

Another approach to derive an equation of state based for asymmetric nuclear on ChEFT is based on many-body perturbation theory (MBPT) around a self-consistent Hartree-Fock state presented in [47]. The considered Hamiltonian comprises two-and three-body interaction constructed in ChEFT up to N^{3}LO with a hard scale $\Lambda = 450\,\mathrm{MeV}$. The model tightly constrains the free energy per particle F/A up to a density of 0.25 1/fm^3 for different proton fractions x and temperatures T, as depicted in Fig. 1.5. At high densities, the theoretical uncertainties of the EFT dominate, as the related energy scales are not properly described by the perturbative expansion for expansion parameters $Q/\Lambda \approx 1$. Due to this, the description of neutron stars, where densities of several saturation densities are predicted, is not possible by a ChEFT EoS based on nucleons and pions and additional degrees of freedom - such as hyperons and nucleonic excitations - have to be included, while at very high densities of about 10 to 20 times ρ_0, a description via QCD in asymptotically free perturbation theory becomes accessible [48].

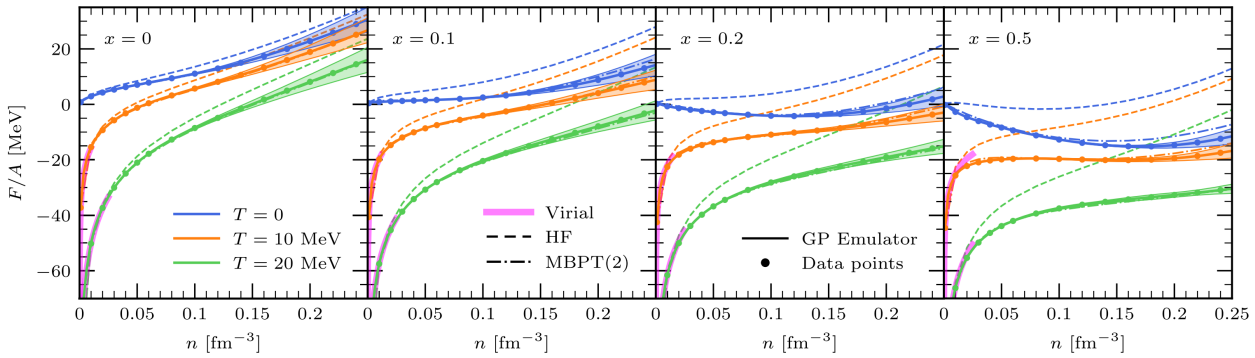

Figure 1.5.: Free energy per particle F/A at N^{3}LO for different proton fractions $x = 0,\, 0.1,\, 0.2,\, 0.5$ and temperatures $T = 0,\, 10,\, 20\,$MeV as a function of the density n. The MBPT results are depicted as dots, and the connecting solid lines are obtained by a three-dimensional Gaussian process regression and the bands display the theoretical EFT uncertainties. For comparison, the results at the Hartree-Fock order (dashed) and the second order (dot-dashed) expansion are given. At low densities $n < 0.025\,\text{fm}^{-3}$, the results are compared to the virial EoS [49]. This figure is reprinted from [47] under CC BY 4.0.

Besides the connection to the Fermi pressure and thus the mass-radius-relation of neutron stars, the symmetry energy and the slope parameter also guide the properties of asymmetric nuclei. The excess of, *e.g.*, neutrons leads to an increase of energy density, which has to be minimized. This minimization is provided by the superposition of two phenomena. On one hand, the central value of the neutron density distribution is increased over the proton central value, leading to a small asymmetry in the core of the nucleus. On the other hand, the neutron density distribution extends to higher radii compared to the proton distribution, causing a layer on the surface of the nucleus, which is predominantly composed by neutrons. This layer is typically characterized by the neutron skin thickness $\Delta r_{\text{np}} = \sqrt{\langle r_n^2 \rangle} - \sqrt{\langle r_p^2 \rangle}$ as the difference of the neutron and proton rms radii.

Getting a consistent and precise value for the neutron skin thickness - in particular for $^{208}_{82}\text{Pb}$ - allows to constrain the range of applicable theoretical models for the description of the nuclear periphery. This constraint is of particular interest, as a wide range of available non-relativistic as well as relativistic models predict a strong correlation of the neutron skin thickness with the symmetry energy slope parameter L of the nuclear equation of state (EoS), see Fig. 1.6. Thus, by precisely determining the neutron skin thickness of ^{208}Pb, a tighter constraint can be put on the asymmetry term of the nuclear EoS.

Due to this correlation, the study of the surface of asymmetric nuclei provides unique information on the asymmetry term of the nuclear equation of state. Providing a precise measurement of the neutron skin thickness would provide a stringent constraint on the slope parameter at saturation density, which would limit the range of applicable EoSs at higher densities occurring in the crust and core of neutron stars. This links systems separated by about 20 orders of magnitude, whose properties are both guided by the nuclear forces.

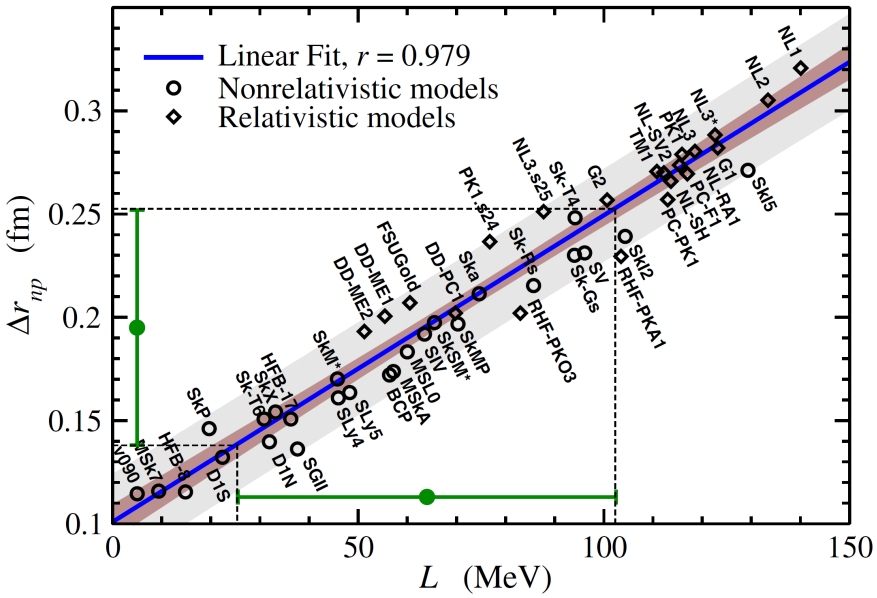

Figure 1.6.: Correlation of the neutron skin thickness Δr_{np} and the slope parameter L of the nuclear EoS based on the different relativistic and non-relativistic theoretical models. This figure is reprinted with permission from [34] ©2011 American Physical Society.

1.2. Charge radii

Experimentally, the nuclear charge distribution, *i.e.*, the proton density profile, can be determined with high precision via elastic electron Coulomb scattering for stable isotopes [50, 51]. By choosing an incident electron momentum of about 200 to 800 MeV/c, where the de-Broglie wavelength of the point-like electrons is smaller than the size of the nucleus, the structure of the nucleus can be resolved while minimizing inelastic scattering. Here, the electron interacts predominantly with the protons via electromagnetic interaction, thus probing the proton distribution inside the nucleus. The measured elastic scattering cross section, depicted for the case of $^{208}\mathrm{Pb}$ in Fig. 1.7, is then related to the charge density profile via the charge form factor $F_{\mathrm{c}}\left(\mathbf{q}^2\right)$ with the momentum transfer $\mathbf{q}$ following the equation

$$\left(\frac{\mathrm{d}\sigma}{\mathrm{d}\Omega}\right)_{\mathrm{exp}} = \left(\frac{\mathrm{d}\sigma}{\mathrm{d}\Omega}\right)_{\mathrm{Mott}} \cdot |F_{\mathrm{c}}\left(\mathbf{q}^2\right)|^2, \tag{1.7}$$

with the analytic Mott cross section, which assumes elastic electron scattering on a spinless and point-like nucleus. The form factor is then connected to the charge distribution via the Fourier transformation

$$F_{\mathrm{c}}\left(\mathbf{q}^2\right) = \int \mathrm{d}^3\mathbf{r}\ \rho_{\mathrm{c}}\left(\mathbf{r}\right) \mathrm{e}^{i\mathbf{q}\mathbf{r}}, \tag{1.8}$$

where the charge distribution corresponds to the convolution of the finite-size proton form factor $f_{\mathrm{p}}(r)$ and the point-proton density ρ_{p}, which is derived in theoretical models.

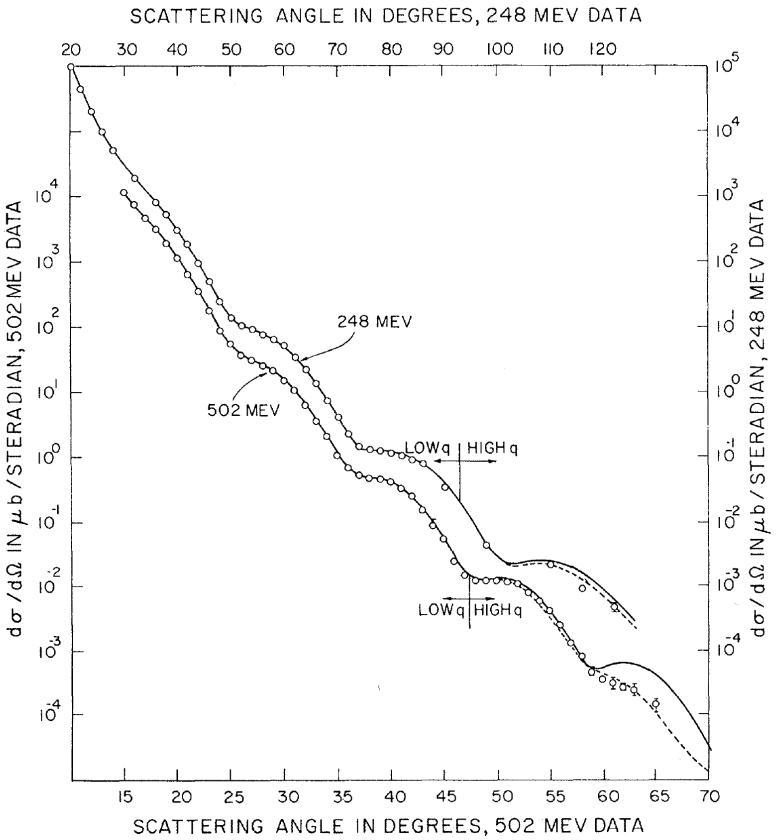

Figure 1.7.: Experimental elastic electron scattering cross sections on ^{208}Pb for electron energies of 248.2 and 502.0 MeV (circles) compared to theoretical cross sections (solid lines). The figure is reprinted with permission from [50] ©1969 American Physical Society.

While the elastic electron scattering allows a precise measurement of the full charge distribution in stable nuclei, the conventional method cannot be applied to unstable nuclei with a short lifetime of less than a few minutes. An alternative approach to allow the use of unstable nuclei as targets for elastic scattering experiments is the self-confining radioactive isotope ion target (SCRIT) method at the RIKEN radioactive ion beam facility, where radioactive ions are confined within an electron storage ring [52]. Longitudinally, the ions are confined by an axial potential well, and the bypassing electron beam creates a transverse focusing effect for radial confinement. Proof-of-principle experiments have already been performed with stable nuclei and the investigation of short-lived nuclei is planned.

Up to this point, only moments of the charge distribution of short-lived nuclei can be determined precisely, with the most common moment being the root mean square (RMS) charge radius, which is given by

$$\sqrt{\langle r_c^2 \rangle} = \sqrt{\int \mathrm{d}^3\mathbf{r}\; r^2 \rho_\mathrm{c}\left(\mathbf{r}\right)}. \tag{1.9}$$

Experimentally, the most common technique to determine rms charge radii of unstable nuclei is laser spectroscopy [53–55]. An overview over the range of nuclei investigated

by laser spectroscopy is depicted in Fig. 1.8. Here, hyper-fine transition frequencies are measured with high accuracy, which are then compared to a stable reference isotope. The isotope shift in the transition frequencies $\delta\nu^{A,A'}$ is caused by two complementary effects: the mass shift, induced by the higher or lower number of neutrons in the nucleus, and the field shift, which is sensitive to the difference of the rms radii of the charge distributions $\delta\langle r_c^2\rangle^{A,A'}$. Here, the mass shift (MS) is given by

$$\delta\nu_{\mathrm{MS}}^{A,A'} = K_{\mathrm{MS}}\frac{m^{A'} - m^{A}}{m^{A'}m^{A}}, \tag{1.10}$$

with the mass shift constant K_{MS}. The field shift (FS) in contrast is caused by a difference in the overlap of the electron wave function $\psi_e(r)$ and the nuclear charge distribution and is given by

$$\delta\nu_{\mathrm{FS}}^{A,A'} = \frac{Ze^2}{6h\epsilon_0}\,\Delta|\psi_e(0)|^2\,\delta\langle r_c^2\rangle^{A,A'}, \tag{1.11}$$

with $\Delta|\psi_e(0)|^2$ as the change in electron density at the nucleus between the two atomic levels of the transition and $\delta\langle r_c^2\rangle^{A,A'}$ as the difference in rms charge radii between the two isotopes.

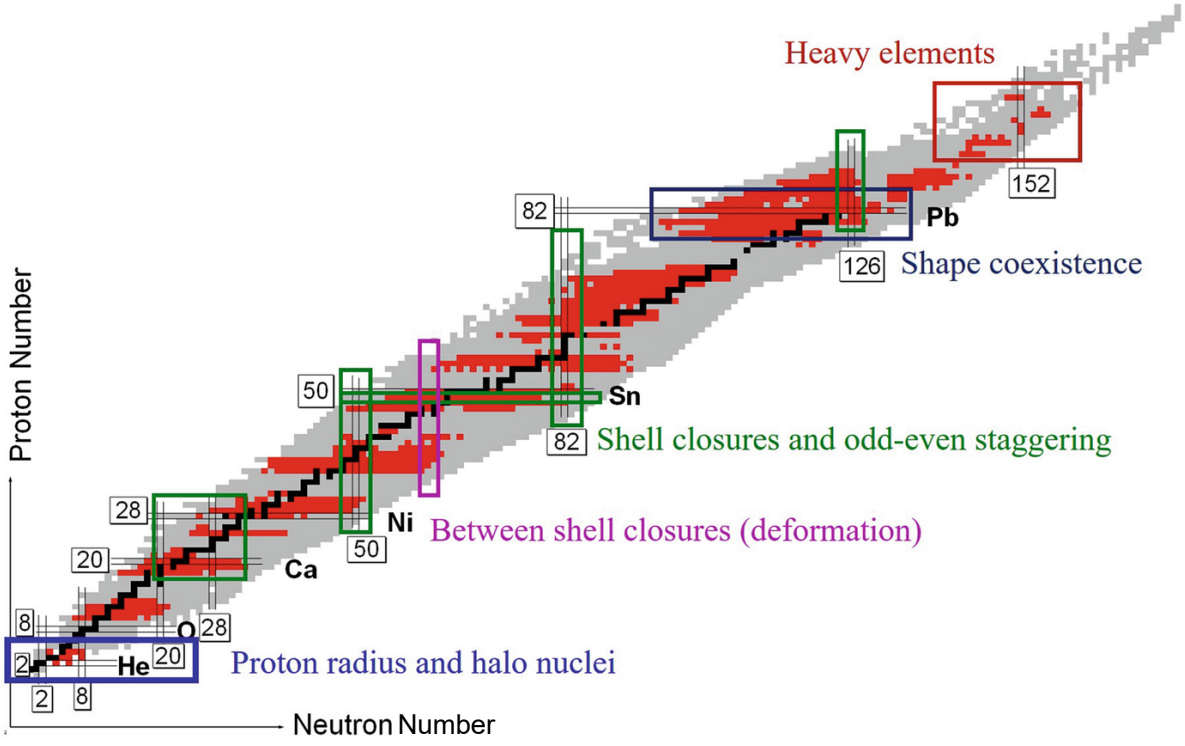

Figure 1.8.: Overview over the isotopes measured via laser spectroscopy in red. Specific regions of interest with high number of measured isotopes are highlighted. This figure is reprinted with permission from [56] ©2023 Springer Nature.

Similarly to the electron laser spectroscopy, experiments are performed with exotic atoms, which replace the light electron with a heavier negatively charged particle, such as a muon.

Due to the higher mass of the muon, its wavefunction is contracted compared to electrons, thus increasing the sensitivity to the nuclear structure. This method has been successfully applied to medium mass and heavy nuclei [57–59], allowing the extraction of rms charge radii by measuring transition frequencies with high precision and modeling the nuclear charge distribution via a two-parameter Fermi distribution. Recent focus is set on light system such as muonic helium and hydrogen [60–64].

1.3. Neutron density distributions and matter radii

While the nuclear proton density distribution and rms radius can be investigated by probes that are sensitive to the electromagnetic interaction, the neutron density is only accessible via elastic scattering of spin-polarized electrons [65–68]. Here, the parity violation of the weak interaction, mediated by the exchange of a heavy Z^0 boson with a mass of about 90 GeV/c^2, causes an asymmetry A_{PV} in the scattering cross sections $\sigma_{\mathrm{f,b}}$ for longitudinally polarized electrons with forward (f) and backward (b) helicity, respectively, when the dominant elastic scattering on protons due to the Coulomb interaction is taken into account. This asymmetry is sensitive to the ratio of the weak form factor $F_{\mathrm{w}}\left(\mathbf{q}^2\right)$ as the Fourier transform of the weak charge density, and the charge form factor via

$$A_{\mathrm{PV}} = \frac{\sigma_{\mathrm{f}} - \sigma_{\mathrm{b}}}{\sigma_{\mathrm{f}} + \sigma_{\mathrm{b}}} \propto \mathrm{C}\,\mathbf{q}^2 \frac{F_{\mathrm{w}}\left(\mathbf{q}^2\right)}{F_{\mathrm{c}}\left(\mathbf{q}^2\right)} \tag{1.12}$$

with a constant C and the momentum transfer $\mathbf{q}^2$ assuming the Born approximation, while additional Coulomb effects have to be taken into account for heavier nuclei. As the neutron has a weak charge of -0.99 while the proton weak charge is only 0.07, the measured asymmetry at the fixed scattering angle of 5° allows the fit of neutron density distribution reproducing this value, which then finally allows to derive the neutron rms radius as depicted in Fig. 1.9. As only a single angle is considered, the derived asymmetry of $A_{\mathrm{PV}} = 550 \pm 16\,(\mathrm{stat.}) \pm 8\,(\mathrm{syst.})$ parts per billion derived by the PREX-II experiment at Jefferson Lab [68] allows a wide range of neutron density profiles, and only the rms neutron radius can be extracted without explicit model dependence. The measurement uncertainty directly relates to the uncertainty of the derived rms neutron radius. Additional measurements at other momentum transfers would allow a more precise determination of this value. Complementary measurements are performed at the Stanford Linear Accelerator Center (SLAC), which focus on the precise measurement of weak neutral current interactions mediated by Z bosons [69].

In case of elastic scattering with hadronic probes, *i.e.*, mostly protons, at intermediate energies of tens of MeV, the scattering process is dominated by the strong interaction [70–72]. Due to the isospin-independence of the strong interaction the elastic scattering thus probes the entire nuclear matter distribution rather than the weak charge distribution, which then allows to derive the neutron density profile by subtracting the proton distribution obtained by *e.g.*, elastic electron scattering, see Fig. 1.10. The dominant source of uncertainties in this approach to determine the neutron distribution and rms radius originates from the optical potentials used to model the strong interaction. However, the main advantage is the

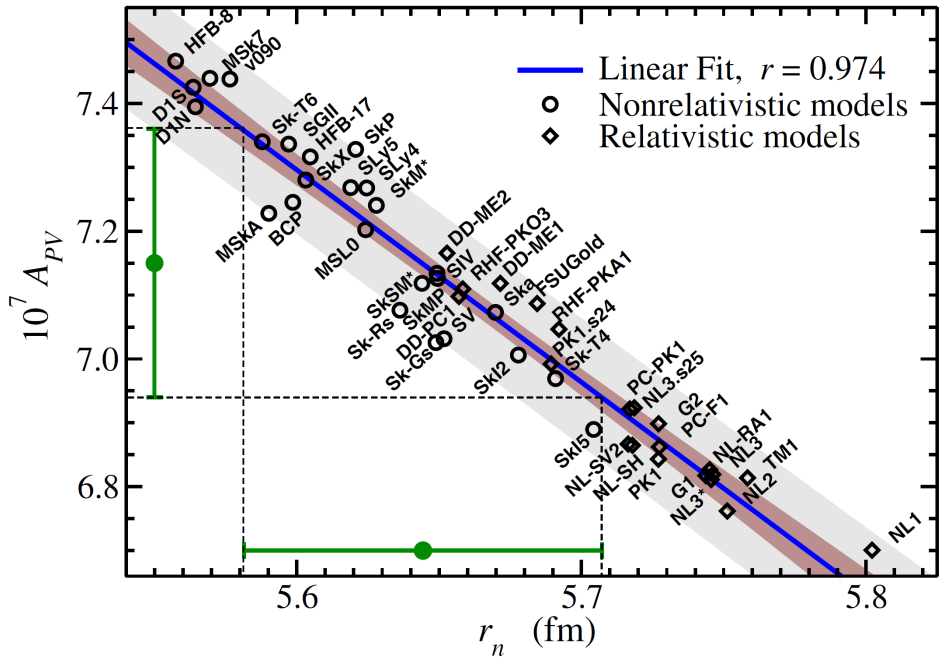

Figure 1.9.: Correlation of the weak scattering asymmetry A_{PV} and the rms neutron radius r_{n} based on the different relativistic and non-relativistic theoretical models. This figure is reprinted with permission from [34] ©2011 American Physical Society.

applicability of this approach for short-lived nuclei via scattering on a hydrogen target in inverse kinematics, if the intensity of the ion beam extends about 10^4 particles per second for a precise measurement [73].

An alternative approach to determine the matter radius is the measurement of the coherent pion photoproduction cross sections [75–77]. Here, the incident photon energy is set to 180 - 240 MeV to excite a virtual Δ resonance, while the cross sections for the Δ excitation are identical for protons and neutrons. In the coherent reaction, the nucleus remains in its ground state, so that all nucleons contribute equally to the reaction amplitude, thus probing the entire nucleus. The deexcitation of the Δ resonance occurs via the emission of a π^0, which is identified via its 2γ decay with large solid-angle photon detectors, while the ground state mass can be separated from excited states via an invariant mass measurement. Based on the measured cross sections of the π^0, theoretical calculations have to be considered to remove the contribution of final state interactions of the produced pions with the residual nucleus and to consider the Δ propagation inside the nucleus. Then, the underlying pion-nucleus interaction is modeled by a complex optical potential [78], which also accounts for inelastic scattering of pions and is obtained through fits to pion-nucleus scattering data, so that the form factor of the nuclear matter distribution can be determined.

While all of above methods are focused on the determination of the neutron rms radius and provide an approximate profile of the neutron density, the details of the neutron distribution remain undisclosed [79]. This is particularly relevant for the low-density tails, which contribute only weakly to the scattering cross section and collective excitations.

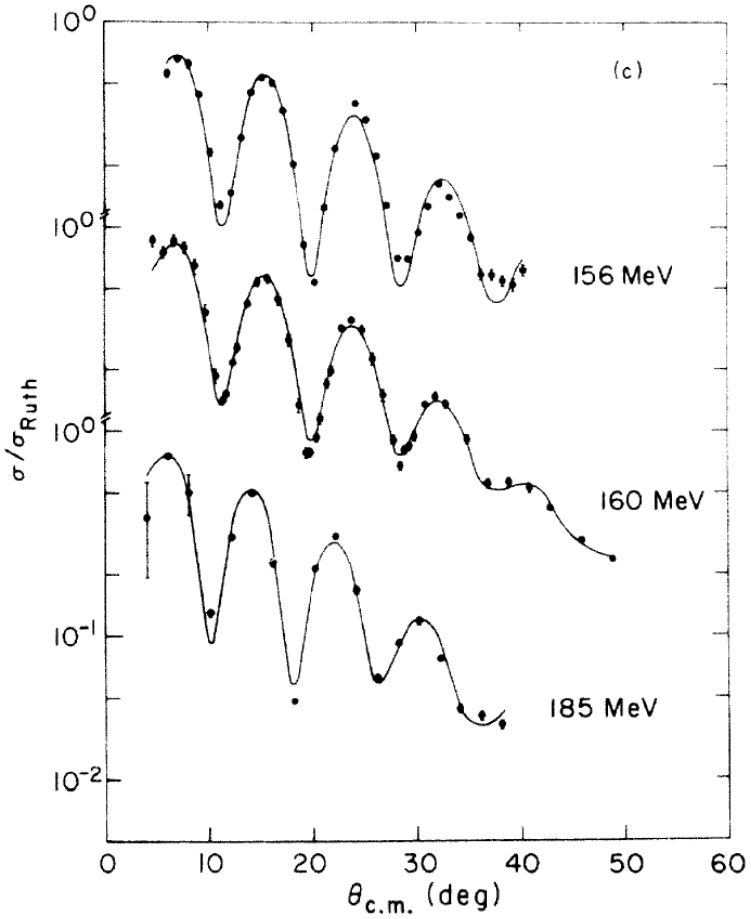

Figure 1.10.: Differential scattering cross section divided by the Rutherford cross section for elastic proton scattering on ^{208}Pb at 156, 160 and 185 MeV. The solid lines indicate fits including optical potentials, while the black dots represent the experimental data. This figure is reprinted with permission from [74] ©1974 American Physical Society.

1.4. Neutron skins and halo nuclei

Based on the mentioned experimental techniques and the appropriate theoretical models, the extension of the proton and neutron distribution inside a nucleus of interest can be obtained. A special focus is set on the rms radii of both nucleon profiles, as they are used to characterize the thickness of the neutron skin Δr_{np} in neutron-rich nuclei. The classical reference for neutron skin measurements is the stable doubly-magic and spherical $^{208}_{82}\mathrm{Pb}$ nucleus with a large neutron excess, and an overview over its derived neutron skin thickness based on different experimental approaches is given in Table 1.1. While the charge rms radius of 5.5 fm is precisely known via electron scattering and muonic atom data, the obtained neutron rms radius derived from parity-violating electron scattering is about 0.1 fm higher than the values derived from proton elastic and inelastic scattering, coherent pion photoproduction and exotic atoms as well as the *ab initio* prediction.

Table 1.1.: Neutron skin thickness of ^{208}Pb as determined by different experimental approaches. The uncertainties comprise both the statistical and the systematical experimental contributions. It has to be highlighted that the uncertainties induced by the theoretical models used to fit the data are not stated. The last line presents the prediction of recent *ab initio* calculations.

Approach	Observable	Value in fm	Ref.
Parity-violating electron scattering	Asymmetry coefficient	0.28 ± 0.07	[68]
Coherent pion photoproduction	Differential cross section	0.15 ± 0.04	[77]
Proton elastic scattering	Differential cross section	0.21 ± 0.06	[80]
Pionic atoms	SI level shifts and widths	0.18 ± 0.05	[81]
Antiprotonic atoms	SI level shifts and widths	0.16 ± 0.06	[82]
Inelastic polarized proton scattering	Electric dipole polarizability	0.16 ± 0.03	[83]
Ab initio prediction	-	0.17 ± 0.03	[22]

While neutron skins occur in principle in every nucleus with a neutron excess, their thickness is typically limited to about 0.2 fm in heavy nuclei such as $^{208}\mathrm{Pb}$ and to about 0.4 fm in light neutron-rich nuclei [84, 85]. However, in several nuclei close to the limit of stability, *i.e.*, with very high proton-to-neutron asymmetry close to the driplines, measurements of the interaction cross section indicate a matter radius that is significantly larger than for other nuclei along an isotopic chain. Historically, the first experiment indicating this increase in interaction cross section was performed by Tanihata *et. al.* at the Lawrence Berkeley National Laboratory (LBNL) [86]. It was found that the determined rms matter radius of $^{11}\mathrm{Li}$ of 3.3 fm is about 0.8 fm larger than the matter radii of $^{6,7,8,9}\mathrm{Li}$. As the charge radius of the Li isotopic chain is mostly constant at around 2.5 fm, the resulting difference in matter and charge radius of $^{11}\mathrm{Li}$ is much higher than expected, indicating the existence of a two-neutron halo. Here, two s-wave neutrons are weakly bound to the $^{9}\mathrm{Li}$ core of the nucleus, with a separation energy of only 0.3 MeV. This low binding energy and low angular momentum of the two halo neutrons allow a very large spatial extension of the respective orbital, where the small overlap with the core of the nucleus is sufficient to keep the neutrons bound by the strong interaction, even though the majority of the wave function extends further from the core than the 2-3 fm range of the strong interaction due to quantum tunneling.

Following this initial observation, the halo character of several other nuclei has been indicated based on interaction radius or nucleon removal energy measurements [87–90]. However, neutron halos are also indicated in medium-mass nuclei such as $^{37}\mathrm{Mg}$, where a $1n$-removal reaction together with a measurement of the measured parallel momentum distribution were performed. The one halo neutron is expected to occupy a p-wave single particle state [91]. Such p-wave halos are suppressed compared to the s-wave halos by the additional centrifugal barrier induced by the angular momentum l, but still exhibit a divergent behavior of the rms orbital radius for very low single particle energies of the halo neutron. To confirm the p-wave halo character, complementary measurements are required.

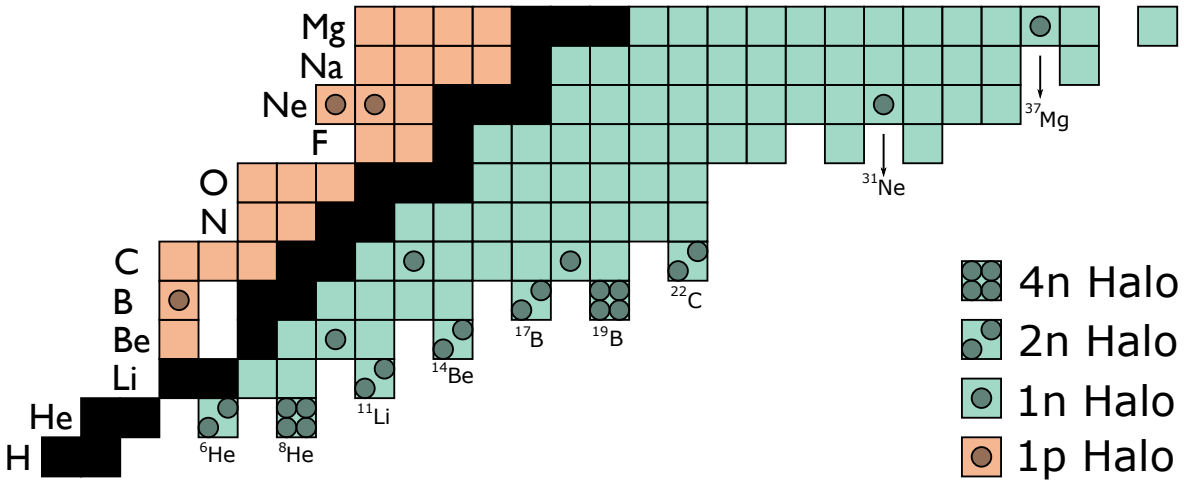

Figure 1.11.: Overview over the indicated proton and halo nuclei in the low-mass region of the nuclear chart. This figure is reprinted from [92] under CC BY 4.0.

Similarly to neutron p-wave halos, which are suppressed by the angular momentum barrier, proton halos are suppressed compared to neutron halos due to their additional Coulomb barrier. Besides this suppression, proton halos require an excess of protons to populate states with very small single particle energies, which limits the range of possible proton halo nuclei to the very light and neutron-deficient region of the nuclear chart, compare Fig. 1.11. An example for a potential proton halo nucleus is ^{8}B, whose charge rms radius is expected to be about 0.7 fm larger than the neutron radius [93]. Additional experiments are required to confirm the 1-proton halo character of ^{8}B.

Theoretically, halo nuclei can be described in the framework of a halo effective field theory (EFT) [94]. It is based on a pionless description of a few-body system, where the core is assumed to be structure-less in leading order and the full nucleus is treated as a few-body system of the core and the valence nucleons. For the calculation, independent operators are assumed for the core and the halo nucleons. Similarly, *ab initio* approaches can be applied to halo nuclei [95], providing complementary information to the halo EFT.

Both nuclear halos as well as neutron skins are phenomena which occur in the density tails of nuclei with a pronounced proton-to-neutron asymmetry. The investigation of their properties such as the neutron skin thickness or the interaction radii via experiments is challenging, limiting the precision of the experimental results. Simultaneously, nuclear theory cannot provide uniform predictions on these properties due to a lack of precise and diverse data to fit the free parameters of their respective models. Consequently, more precise measurements of charge and matter rms radii are required to set proper references for nuclear theory.

1.5. Antiprotonic atoms

Hadronic probes in the form of protons or pions have already been extensively used to study the matter and charge distribution of nuclei via scattering [80, 81]. Besides elastic scattering [96], antiprotons offer additional ways to study nuclear properties [82, 97]. One particular approach is the formation of antiprotonic atoms: If antiprotons and atoms or ions are overlapped at low relative momentum, the antiproton losses energy by collisions with atomic electrons. If the energy of the antiproton is low enough, it can be captured through a knockout of one atomic electron in the Coulomb potential. The capture occurs in a bound antiprotonic orbital at the same distance to the nucleus as the knocked-out electron [98]. The corresponding capture orbital has to have spatial overlap with the initial electron orbital, and due to energy and momentum conservation the binding energy of the antiproton has be similar to the binding energy of the knocked-out electron. Thus, the capture process typically occurs in a highly excited antiprotonic orbital with a principal quantum number

$$n_{\bar{\mathrm{p}}} \approx n_{\mathrm{e}^-} \cdot \sqrt{\frac{\mu_{\bar{\mathrm{p}}}}{m_{\mathrm{e}^-}}} \tag{1.13}$$

with the principal quantum number n_{e^-} of the knocked-out electron, the electron mass m_{e^-} and the reduced antiproton-atom mass $\mu_{\bar{\mathrm{p}}}$. Because of the higher number of available substates, the antiproton is predominantly captured in a high angular momentum state following the statistical distribution $P(l) \propto (2l+1)\, e^{\alpha l}$ with the free parameter α that is fitted to experimental data [99].

Following the capture, the antiproton deexcites towards its ground state orbital following the selection rules for radiative electric dipole transitions ($\Delta n = 1$, $\Delta l = \pm 1$) and Auger transitions [100, 101]. Together with the high abundance of circular (n, $l = n - 1$) states in the initial capture orbital, this cascade leads to a population of circular states during the deexcitation. For sufficiently high transition energies exceeding the ionization energy of a bound electron, Auger transitions are dominant. These occur mostly between higher states which overlap with the electron orbitals, until the electron cloud is mostly or fully stripped, while radiative X-ray transitions are then dominant between lower states. The transition energies are fully described by quantum electrodynamics (QED) as they arise from the electromagnetic (EM) interaction of the antiproton and the stripped nucleus, see Fig. 1.12. However, due to the contracted radial wave functions, the antiproton orbitals start to overlap with the nuclear wave function for a principal quantum number $n \approx 2 \ldots 9$, which leads to two additional effects.

Firstly, the proximity of the antiproton to the nucleus gives rise to shifts and broadening in the transition frequency induced by the strong interaction for low-lying transitions with very small overlap [102, 103]. These shifts compared to the pure EM transitions are then used to determine properties of the $\bar{\mathrm{p}}$N force by introducing phenomenological optical potentials, which model the strong interaction. Here, it was found that the $\bar{\mathrm{p}}$N force has a strong absorptive component, indicated by a deep imaginary part of the potential both for antiprotonic atom- as well as scattering-experiments, and that the interaction is strongly localized to the nuclear periphery with weak sensitivity to the core of the nucleus [104–107].

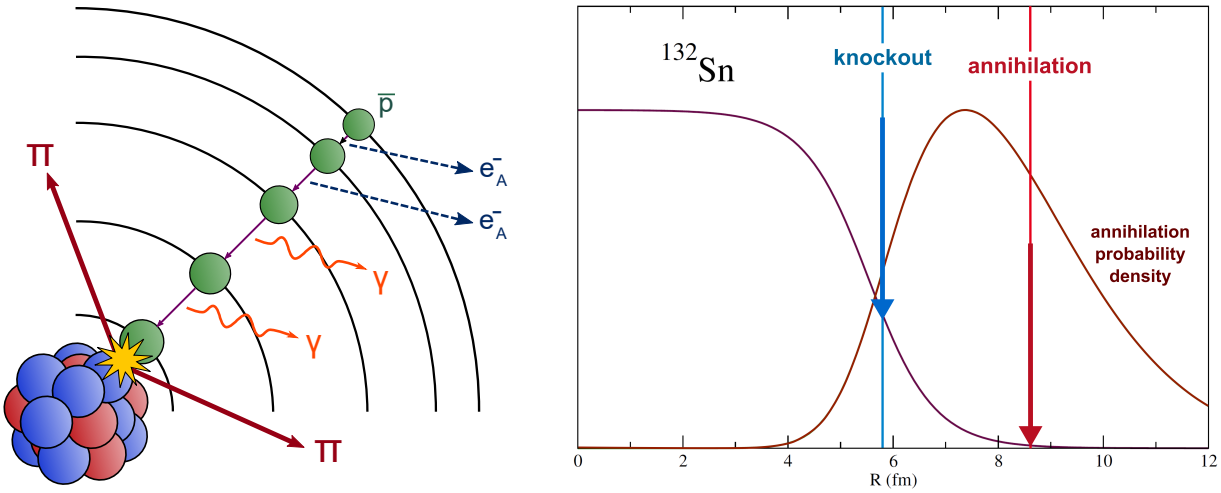

Figure 1.12.: Schematic depiction of the antiprotonic cascade and annihilation following the production of an antiprotonic atom (*left*) and comparison of the simulated region of sensitivity of nucleon removal reactions and peripheral antiprotonic annihilations for the example of ^{132}Sn (*right*). The right figure is adapted from [92] under CC BY 4.0.

Secondly, with increasing overlap of the antiprotonic and nuclear wavefunction, the antiproton will eventually annihilate with a nucleon on the surface of the nucleus. Due to the strong imaginary part of the interaction, the probability for an annihilation is already high for a small overlap, so that only a few percent of antiprotons are able to penetrate into the core of the nucleus [108]. Based on the overlap of the wave functions and the considered absorptive part of the $\bar{\mathrm{p}}$A interaction, a probability density $\phi\,(r)$ for the annihilation as a function of the distance to the core of the nucleus r can be defined, as depicted in Fig. 1.12 for the case of $^{132}\mathrm{Sn}$. Here, the mean radius of annihilation is calculated via

$$\langle r \rangle = \frac{\int_0^\infty r\,\phi\,(r)\;\mathrm{d}\vec{r}}{\int_0^\infty \phi\,(r)\;\mathrm{d}\vec{r}} \tag{1.14}$$

and is about 2 - 2.5 fm larger than the half-density radius, which is the typical radius of sensitivity for proton-knockout reactions (p,2p) [109, 110]. This sensitivity to the low-density tail is a global feature for the annihilation based on the formation of antiprotonic atoms and yields information of the properties in the nuclear periphery.

In particular, the peripheral annihilation yields information about the ratio of protons and neutrons on the surface of the nucleus, as the total charge is conserved. The total energy of about 2 GeV for antiproton-proton and antiproton-neutron annihilations is translated into the production of light mesons and their kinetic energy. The majority of mesons are pions (π^+, π^-, π^0), which are produced in about 80 % of annihilations, while the branching ratio of more exotic mesons such as kaons and antikaons (K^+, K^-), which always occur paired to conserve strangeness, is in the order of about 5 % [111]. A summary table for the branching ratios for antiproton-proton and antiproton-neutron annihilations is found in the attachments. By detecting all charged mesons originating from an isolated annihilation process, it is possible to then identify if the annihilation occurred with a proton or a neutron.

One of the first experiments, which focused on the detection of charged pions originating from the annihilation of stopped antiprotons on solid target plates of copper, titanium, tantalum and lead inside a hydrogen bubble chamber, was performed by Bugg *et. al.* at Brookhaven National Laboratory (BNL) and published in 1973 [112]. For the $^{208}\mathrm{Pb}$ nucleus, they determined that the annihilation with a neutron is 2.34 times as likely as the annihilation with a proton, while the ratio of neutrons to protons in the nucleus is $N/Z = 1.54$. This indicated that the ratio of neutron and proton densities is higher than N/Z in the low-density tail at $< 20\,\%$ of the central density, which together with a similar rms radii for protons and neutrons was interpreted as a neutron halo.

Starting from 1982 up to 1996, the low-energy antiproton ring (LEAR) at CERN was used to perform experiments with low-energy antiprotons, with a minimum kinetic energy of $\sim$ 5.3 MeV. In that time period, studies of the scattering of antiprotons on hydrogen [113–115] and deuterium [116, 117] and the potential existence of a bound antiproton-proton baryonium atom [118] were performed. Additionally, a dedicated series of experiments was aimed at investigating properties of antiprotonic atoms [82, 97, 119–124].

The first group of those experiments with antiprotonic atoms focused on the detection of the antiprotonic X-rays emitted in the cascade, in particular on the last detectable X-rays before absorption [82, 119, 120, 124]. As these transitions are affected by the strong interaction due to the overlap with the nuclear wavefunction, the induced level shifts and broadenings of the level widths are sensitive to the nuclear density under the assumption that the strong interaction potential is proportional to the nuclear density in first order [125]. By assuming an antiproton optical interaction potential $V_{\mathrm{opt}} = \bar{a} \cdot (\rho_{\mathrm{p}} + \rho_{\mathrm{n}})$ with the complex antiproton scattering length $\bar{a} = 2.5 + i \cdot 3.4$ [125] and a simplified two-parameter Fermi distribution for both neutron and proton density, the neutron skin thickness for a wide range of stable nuclei has been derived in [124], see Fig. 1.13. Here, only the statistical uncertainty is considered, while estimates of the uncertainties of the model are not included. The data indicate that the neutron skin thickness Δr_{np} increases approximately linearly with the neutron-to-proton asymmetry $\delta = (N - Z)/A$, which is consistent with theoretical predictions derived by HFB models.

The second group of experiments focused on the detection of light annihilation products such as pions, kaons but also individual protons and neutrons [121, 123]. The detection and identification of the charged pions as well as protons was performed with the CALLIOPE magnetic spectrometer [126], comprising position-sensitive gas proportional chambers, scintillators for time-of-flight characterization and threshold Cherenkov detectors in six identical modules. By determining the resulting total charged pion and proton cross sections, it was inferred that the final state interactions of the annihilation products with the residual nucleus can be modeled via a series of incoherent πN, NN and ΔN interactions within the intranuclear cascade (INC) framework [121].

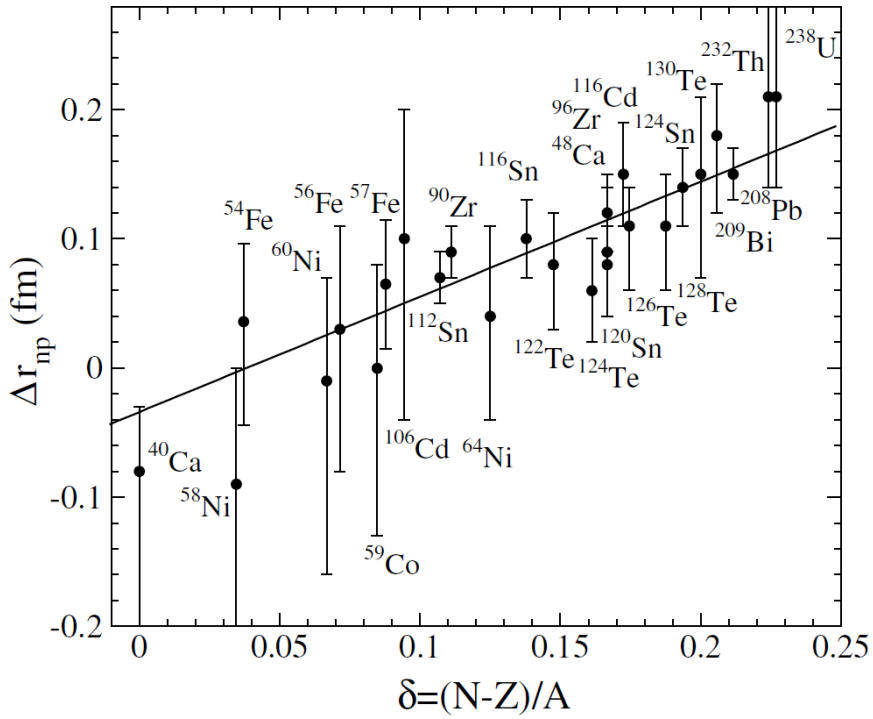

Figure 1.13.: Neutron skin thickness Δr_{np} depending on the nucleonic asymmetry δ as derived from antiprotonic X-ray data. Only statistical uncertainties are given. This figure is reprinted with permission from [124] ©2004 Elsevier.

Besides the detection of light annihilation products, also the residual nucleus after the annihilation can be investigated, especially if a radioactive nucleus is produced in the final state [97, 122]. For this so-called radiochemical method, a dedicated double-arm fission-fragment spectrometer was used [127]; and a special focus is set on the $(Z_{\mathrm{T}}-1,\ N_{\mathrm{T}})$ and $(Z_{\mathrm{T}},\ N_{\mathrm{T}}-1)$ nuclei, where $Z_{\mathrm{T}},\ N_{\mathrm{T}}$ represent the initial target proton and neutron number, respectively. Such nuclei are assumed to be produced in ultra-peripheral annihilations, in which all pions do not interact with the residual nucleus, so that the relative yield of $(Z_{\mathrm{T}}-1,\ N_{\mathrm{T}})$ and $(Z_{\mathrm{T}},\ N_{\mathrm{T}}-1)$ nuclei is sensitive to the neutron-to-proton ratio in the nuclear density tail. The measurements indicated a neutron halo in $^{232}\mathrm{Th}$, as the yield of $^{231}\mathrm{Th}\ (N-1)$ was about 8 times higher than the yield of $^{231}\mathrm{Ac}\ (Z-1)$ [122].

While all of above experimental approaches provide insight in the antiproton-nucleus interaction potential and the structure of the target nuclei, they are all conceptually limited to stable targets. The characterization of the neutron-to-proton ratio in the density tails in short-lived nuclei with a higher asymmetry would provide additional insight in the properties of low-density asymmetric nuclear matter, which is weakly constrained by experiments. The determination of the proton-to-neutron ratio on the nuclear surface, especially for exotic isotopes with a pronounced neutron skin or nucleonic halo, is the goal of the antiProton Unstable Matter Annihilation (PUMA) experiment at the European Organization for Nuclear Research (CERN) [92].

1.6. The PUMA experiment

In contrast to the previous experiments with antiprotonic atoms at LEAR with stable targets, the PUMA experiment uses a different approach to initiate the formation of antiprotonic atoms with the exotic nuclei of interest. These nuclei with a pronounced proton-to-neutron asymmetry have to be produced in a nuclear reaction and are only available at radioactive ion beam facilities (RIBFs) such as the Isotope Separator On-Line DEvice (ISOLDE) facility at CERN. Due to the short lifetime of such isotopes, which is typically in the range of s down to a few ms, the formation of antiprotonic atoms has to be performed on-site. This requires a reservoir of slow antiprotons at the RIBF, which first has to be accumulated at the only facility for slow antiproton experiments - the Antimatter Factory at CERN. It comprises the Antiproton Decelerator (AD) ring and the Extra-Low ENergy Antiproton (ELENA) ring. Thus, to produce and investigate antiprotonic atoms with exotic nuclei, the PUMA experiment is split into three steps: Firstly, a sufficiently large reservoir of antiprotons has to be accumulated at the Antimatter Factory and stored in the PUMA setup. Secondly, the experimental setup together with the reservoir is transported to ISOLDE, see Fig. 1.14. Finally, radioactive antiprotonic atoms are formed at ISOLDE and their annihilation products are detected and identified. In the following, the concept of the experiment is introduced to motivate this work. A detailed description of the full PUMA experiment and its setup is presented [92].

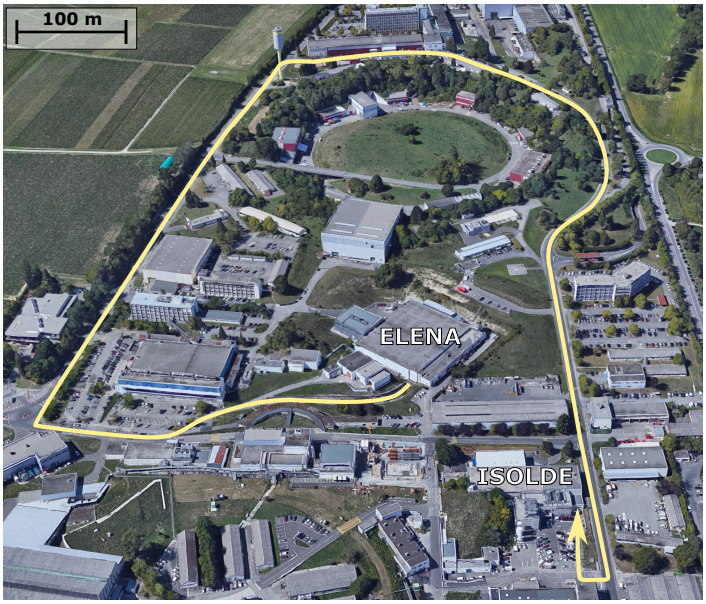

Figure 1.14.: Foreseen path for the transport of the trapped antiprotons in the PUMA setup from the Antimatter Factory to ISOLDE. The figure is reprinted from [92] under CC BY 4.0.

To combine all three steps, PUMA uses a fully transportable experimental setup, which combines a Penning trap assembly, for the antiproton capture and storage at ELENA and the initialization of the formation of antiprotonic atoms with nuclei of interest at ISOLDE, as well as a time-projection chamber (TPC) detector combined with a plastic scintillator barrel, for the detection and identification of the pions produced in the peripheral annihilations.

To provide a large and stable reservoir of antiprotons, the Penning trap design has to minimize the losses of antiprotons through annihilations, both on the trap electrodes and on residual gas molecules. While the former can be minimized by precise alignment of the trap with the magnetic field and the implementation of trapping techniques, the latter requires an extreme high vacuum.

Both the Penning trap and the detection system rely on a strong magnetic field, which is provided by a warm bore solenoid with a homogeneous magnetic field of 4 T. The field arises from superconducting niobium-titanium coils. In order to reach superconductivity at a cryogenic temperature, two sets of coldheads and helium cryo-compressors are used. A sketch of the trap and detection assembly is depicted in Fig. 1.15. The dimensions of the time-projection chamber and the plastic scintillator barrel are fixed based on the simulations performed in [99].

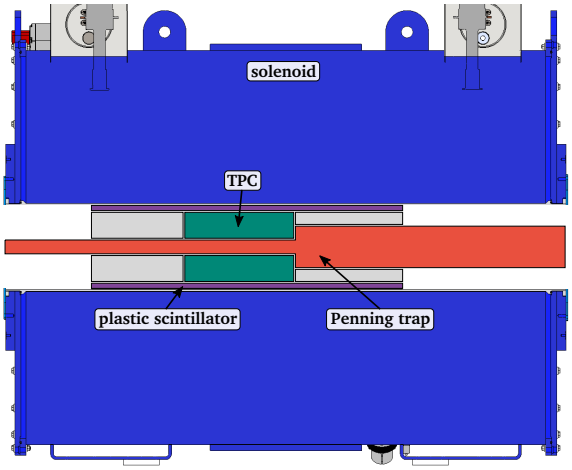

Figure 1.15.: Schematic depiction of the Penning trap and detection system within the warm bore of the PUMA solenoid. The gray shaded area represents mechanical support pieces for the detection system.

The solenoid, the trap assembly and the detector are mounted inside a stainless-steel frame of (3.5 x 1.9 x 2.8) m together with the equipment to operate the components. Besides this main frame, a second smaller frame of (1.8 x 1.9 x 2.8) m comprising a cooling water chiller and a battery pack for powering the full system during the transportation is connected to the main frame during transport and can be disconnected during operation at ELENA and ISOLDE. A schematic overview of the two frames, which form the transportable experimental setup of PUMA, is depicted in Fig. 1.16.

At the Antimatter Factory of CERN, the full experimental setup is mounted at the end of the LNE51 beamline. A top view of the full beamline assembly in the experimental vault is depicted in Fig. 1.17. It consists of an electrostatic deflector to bend antiproton bunches into the experimental vault of PUMA and three ELENA-type electrostatic quadrupole doublets for beam tuning. Following the last quadrupole doublet of LNE51, the remaining beamline and assemblies inside the experimental hall are in responsibility of the PUMA experiment.

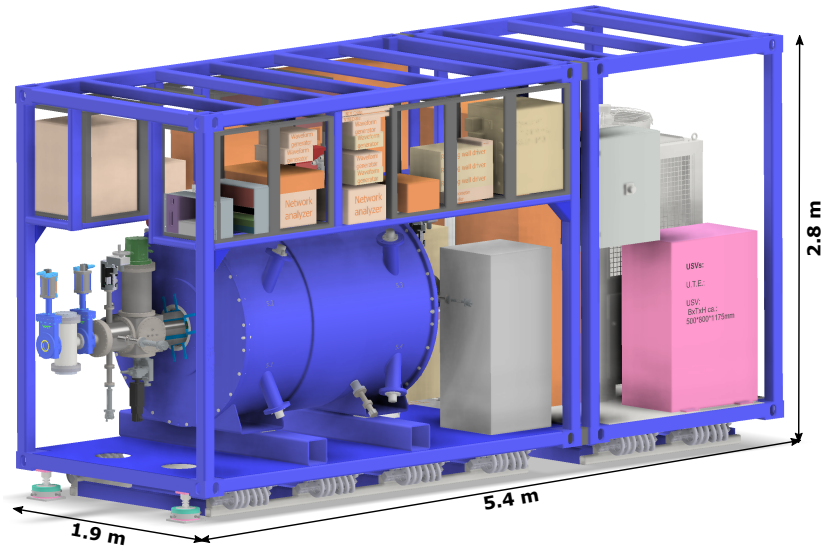

Figure 1.16.: 3D model of the two connected PUMA frames. For simplicity, most electronic devices are replaced by cuboidal placeholders.

The main purpose of the PUMA beamline is to effectively guide the antiprotons into the Penning trap, while decelerating the antiprotons from an initial energy of 100 keV to trapping energies of about 200 eV with two pulsed drift tubes (PDTs). After the first deceleration stage in the high-voltage (HV) PDT, the antiprotons are guided through the beamline by einzel lenses, whose potentials have to be optimized to minimize antiproton losses along the flight path. By increasing the antiproton transmission into the trap, the total number of antiproton bunches that have to be accumulated is minimized.

Besides the straight antiproton line, an additional offline ion source beam line is mounted in parallel inside the experimental hall. This beamline comprises a commercial SPECS IQE 12/38 electron impact ionization source, which ionizes gas molecules and atoms to low charge numbers, a multi-reflection time-of-flight (MR-ToF) spectrometer for isotopic purification of produced ions [128] and a radiofrequency quadrupole (RFQ) for accumulation and bunching.

After the purification and bunching, the ions are bend into the antiproton beamline by two electrostatic quadrupole benders and injected into the PUMA experiment to perform measurements with already trapped antiprotons. The experiments with stable reference nuclei are not only used as a benchmark for the measurement principle and the detection system, but also allow systematic studies of the evolution of the proton-to-neutron ratio along isotopic chains. The requirement for these measurements, similarly to the measurements with unstable nuclei performed at ISOLDE, is the provision of a stable reservoir of trapped antiprotons as well as the generation of an overlap of antiprotons with an incoming ion bunch to initialize the production of antiprotonic atoms. Both aspects set stringent requirements on the Penning trap setup, in particular on the antiproton and ion manipulation and the long-term storage of high antiprotons numbers, which is limited by the repulsive space charge of the equally charged particles and annihilations with residual gas in the setup.

Based on these requirements for the setup, the final design and first assembly of the PUMA Penning trap are presented and supported by simulations in Ch. 2. In Ch. 3, the capture of antiproton bunches coming from the ELENA ring into the trap is investigated by the means of ion-optical simulations, with a special focus on the transmission rate to estimate the total accumulation time.

Chapter 4 of this thesis then presents simulations which investigate the use of trapped antiprotons for the production of hypernuclei. Here, transport simulations are performed to estimate the production of free and bound Λ-baryons following an initial annihilation process through final state two-body interactions of the annihilation products with the residual nucleons.

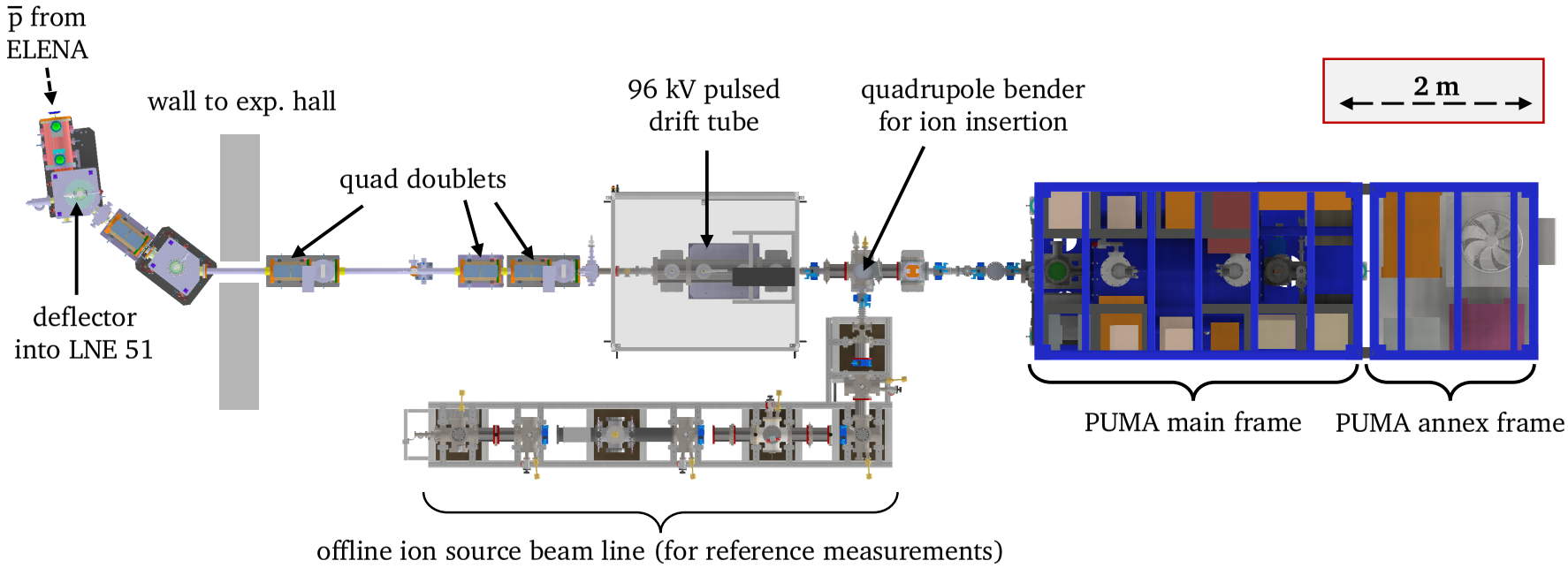

Figure 1.17.: Top view of a 3D model of the PUMA LNE51 and offline ion source beamlines at ELENA. The quadrupole doublets are used to focus the antiprotons into the focal point of the pulsed drift tube, which decelerates the antiprotons to 4 keV. The offline ion source beamline provides isotopically pure ion bunches for measurements with stable nuclei.

2. The PUMA Penning trap and cryostat assembly

The capture and trapping of antiprotons in the PUMA Penning trap is the first essential step for the production of antiprotonic atoms. After the injection into the Penning trap, the antiprotons have to be trapped and cooled with electrons, before they can be overlapped with ions to initiate the formation of antiprotonic atoms. This introduces three main challenges:

(1) 3-dimensional confinement of the antiproton ensemble with the trap fields

(2) extreme high vacuum (XHV) to minimize the annihilations with residual gas

(3) flexibility for optimal mixing and manipulation of antiprotons, electrons and ions

The final modeling and implementation of the Penning trap and cryostat system, which accomplishes these requirements, is presented in this chapter. This model has been derived via several iterations of adjustments based on mechanical, thermal and vacuum simulations as well as discussions with the CERN vacuum group.

In Sec. 2.1, Penning traps as a tool to store and investigate both individual charged particles and high particle numbers are introduced. A particular focus is set on high-density trapping, where the stored particles behave as a non-neutral plasma, and techniques to manipulate this plasma. Section 2.2 presents the final mechanical design of the PUMA trap and cryostat setup and provides details on the geometry and choice of material of the setup components. In Sec. 2.3 the mechanical stress simulation for the final setup is displayed, and the deformation of the components due to gravity is analyzed. Section 2.4 presents the thermal simulation of the setup, which derives the temperature profile in its equilibrium state. This temperature profile is then used in Sec. 2.5 as an input for the vacuum simulations. After introducing the behavior of residual gas in ultra-high vacuum and in particular in cryogenic systems, the simulated profile of the residual gas density up to the PUMA trap is displayed. Section 2.6 documents the process of the first successful mechanical assembly of the setup as a benchmark of the assembly process. Finally, the operation scheme of the PUMA Penning trap for the accumulation of antiprotons and the formation of antiprotonic atoms is sketched in Sec. 2.7 .

2.1. Penning traps for charged single- and many-particle trapping

2.1.1. Penning traps and single-particle motion

Penning traps combine electrostatic and magnetic fields to provide 3-dimensional confinement of charged particles. In the traditional design by H. G. Dehmelt, which was inspired by a vacuum gauge designed by F. M. Penning, an electric field is produced by hyperbolic electrodes in a quadrupolar configuration. Practically, this configuration is realized by two hyperbolic endcap electrodes on the same potential and a single hyperbolic ring electrode between the endcaps on another potential to create a potential difference V_0. Together with the trap radius r_0 and the half-length z_0, the harmonic quadrupolar trap potential is given by $\Phi_\mathrm{T}(r,z) = V_0/4d^2 \cdot (2z^2 - r^2)$ where $d^2 = (2z_0^2 - r_0^2)/4$ is called characteristic trap size. The resulting electric field acts confining in z-direction and deconfining in the perpendicular radial plane. To compensate the deconfinement in the radial plane, a constant magnetic field $\vec{B_\mathrm{T}} = B\vec{e_z}$ is applied along the axis of confinement. In practice, this magnetic field is provided by a solenoid electromagnet. A sketch of a hyperbolic Penning trap is depicted in Fig. 2.1.

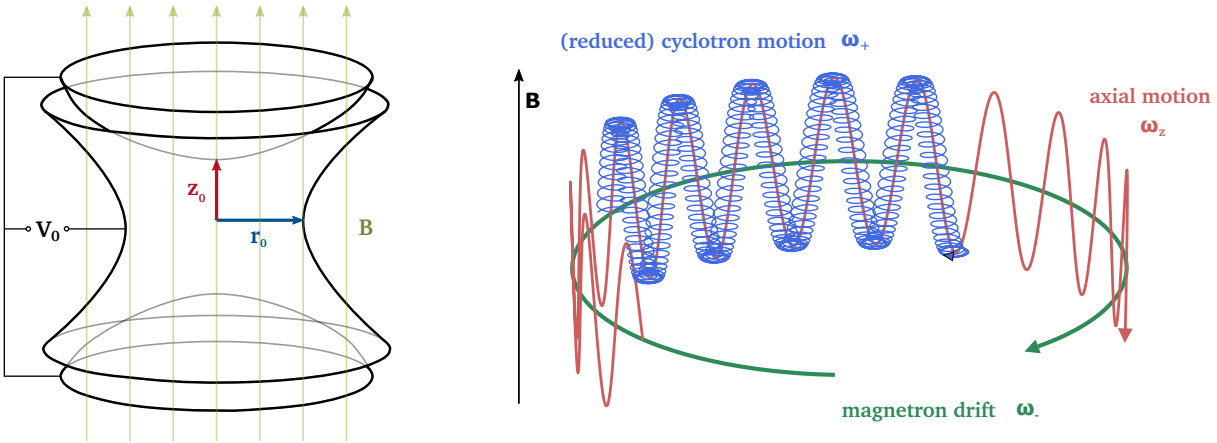

Figure 2.1.: Sketch of the hyperbolic Penning trap geometry (*left*) and the 3-dimensional motion of a single trapped particle (*right*). The magnitudes of the amplitudes of the three eigenmotions - axial, magnetron and reduced cyclotron motion - are set arbitrarily for better visibility. The frequencies follow the ordering $\omega_+ >> \omega_z > \omega_-$.

In absence of additional superimposed fields, the force acting on a trapped particle is the Lorentz force, which fully determines the equation of motion (EoM) for charged particles of mass m and charge q [129]. With the electric trap field $\vec{E_\mathrm{T}} = -\vec{\nabla}\Phi_\mathrm{T}$, the EoM is given by

$$\vec{F_\mathrm{L}} = q \cdot \left(\vec{E_\mathrm{T}} + \dot{\vec{x}} \times \vec{B_\mathrm{T}}\right) = m\ddot{\vec{x}}. \tag{2.1}$$

As the magnetic field is applied along the z-axis, only the radial velocity components contribute to the magnetic force, so that the longitudinal motion is independent of the

magnetic field and fully defined by the trap potential. Splitting the EoM in the Cartesian coordinates, one obtains

$$\begin{aligned} \ddot{x} &= \omega_\mathrm{c}\dot{y} + \tfrac{\omega_\mathrm{z}^2}{2}x, \\ \ddot{y} &= -\omega_\mathrm{c}\dot{x} + \tfrac{\omega_\mathrm{z}^2}{2}y, \\ \ddot{z} &= -\omega_\mathrm{z}^2 z \end{aligned} \tag{2.2}$$

with the cyclotron frequency $\omega_\mathrm{c} = qB/m$ and the axial oscillation frequency $\omega_\mathrm{z} = \sqrt{qV_0/md^2}$. While the longitudinal motion is a pure harmonic oscillation with the frequency ω_z, the radial motion in the x-y-plane is coupled, leading to an epicycloid trajectory in the radial plane. By introducing the reduced cyclotron frequency ω_+ and the magnetron frequency ω_-, which are given by

$$\omega_\pm = \frac{1}{2}\left(\omega_\mathrm{c} \pm \sqrt{\omega_\mathrm{c}^2 - 2\omega_\mathrm{z}^2}\right), \tag{2.3}$$

and the corresponding radii r_+ and r_-, the arbitrary phases ϕ_+ and ϕ_- as well as the axial amplitude of motion a_z and phase ϕ_z, the full 3D motion of a charged particle (see Fig. 2.1) is expressed by:

$$\begin{aligned} x\left(t\right) &= r_+ \sin\left(\omega_+ t + \phi_+\right) + r_- \sin\left(\omega_- t + \phi_-\right), \\ y\left(t\right) &= r_+ \cos\left(\omega_+ t + \phi_+\right) + r_- \cos\left(\omega_- t + \phi_-\right), \\ z\left(t\right) &= a_z \sin\left(\omega_\mathrm{z} t + \phi_z\right). \end{aligned} \tag{2.4}$$

In the radial plane, two motions overlap: a slow magnetron drift motion, which arises from the crossed electric and magnetic field, and a fast reduced cyclotron motion as circular motion of a charged particle around magnetic fields lines. For trapping, it is necessary that the square root in Eq. (2.3) is real, which gives rise to a stability criterion for trapping:

$$\omega_\mathrm{c}^2 > 2\omega_\mathrm{z}^2 \quad \Leftrightarrow \quad \frac{|q|}{m} > \frac{4|V_0|}{B^2}. \tag{2.5}$$

Consequently, sufficiently strong magnetic fields are required to compensate for the deconfining electric field. In the case of the ISOLTRAP measurement Penning trap, the electrostatic potential well has a depth V_0 of about 10 eV, while the magnetic field is at about 6 T. With a trap radius of $r_0 = 13\,\mathrm{mm}$ and a half-length of $z_0 = 11.18\,\mathrm{mm}$, the resulting axial oscillation frequency is $\omega_\mathrm{z} = 618\,\mathrm{kHz}$ for the example of a $^{124}\mathrm{Sn}^+$ ion, while the cyclotron frequency is $\omega_\mathrm{c} = 4.64\,\mathrm{MHz}$. In case of the PUMA experiment with a magnetic field of 4 T, a trap radius of $r_0 = 20\,\mathrm{mm}$ and a half-length of $z_0 \approx 50\,\mathrm{mm}$, the corresponding frequencies for antiprotons are $\omega_\mathrm{z} = 6.45\,\mathrm{MHz}$ and $\omega_\mathrm{c} = 0.38\,\mathrm{GHz}$.

While the cyclotron frequency is not a directly measurable eigenfrequency for trapped charged particles due to the overlapped magnetron motion, the pure cyclotron frequency can be derived by a precise measurement of at least two of the three eigenfrequencies via the invariance theorem

$$\omega_\mathrm{c}^2 = \omega_\mathrm{z}^2 + \omega_+^2 + \omega_-^2. \tag{2.6}$$

It is of particular interest to determine the cyclotron frequencies of trapped particles, as it is directly linked to the particles charge and mass, while the only additional contribution

is given by the magnetic field. If the magnetic field is precisely known, the mass of the particle can be determined with the highest precision that can be reached today. As an example, the Baryon Antibaryon Symmetry Experiment (BASE) recently determined the ratio of the charge-mass ratio of antiprotons and protons with an uncertainty of 16 parts per trillion. Both the proton [130] and antiproton [131] charge-mass ratios are derived from ultra-precise cyclotron frequency measurements using image-current detectors for the axial frequency and tunable cyclotron detectors for the reduced cyclotron frequency at cryogenic temperatures to reduce electrical noise to a minimum. While such measurements yield unrivaled precision, they can only be performed for stable or long-lived ions, as they require continuous measurements over time periods of months. For a precise measurement of masses of unstable ions with Penning trap, other destructive techniques are applied [132, 133].

2.1.2. Non-neutral plasmas and Brillouin limit

The trapping of high particle numbers, as in the case of PUMA for antiprotons, is strongly affected by the Coulomb repulsion of the equally charged particles. The repulsion effectively reduces the confining trap potential, limiting the density of particles that can be stored in a Penning trap to the Brillouin density limit n_B [134, 135]. It only depends on the magnetic field and the mass of the trapped ion species and is reached if the trapped particle ensemble is forced to rotate at the frequency $\omega_\mathrm{c}/2$ by an external drive. It is given by

$$n_\mathrm{B} = \frac{\epsilon_0 B^2}{2m} = 4.2 \cdot 10^{10}\,\mathrm{cm}^{-3} \quad \text{for} \quad B = 4\,\mathrm{T}\,\text{and}\,m = m_p. \tag{2.7}$$

While this limit represents the stationary point, at which the confining magnetic force equals the repulsive Coulomb and centrifugal forces, real trap setups are limited to a few % of this maximum value [136, 137]. This is typically caused by field imperfections. In case of the PUMA experiment, up to about 10^9 antiprotons are supposed to be trapped in a trapping volume of about 10 cm^3, corresponding to a density of $n \sim 1 \cdot 10^8\,\mathrm{cm}^{-3} < 0.01\,n_\mathrm{B}$.

For high ion numbers, it is common to describe the entire ensemble of ions as a non-neutral plasma (NNP) [138, 139]. The description of a trapped ensemble of particles as a NNP is valid if the Debye length λ_D, which depends on the ensemble temperature T, the central ensemble density n_0 and the charge of the ions q and is given by

$$\lambda_\mathrm{D} = \sqrt{\frac{\epsilon_0 k_\mathrm{B} T}{2 n_0 q^2}} \approx 30\,\mu\mathrm{m} \quad \text{for} \quad T = 4\,\mathrm{K}\ \text{and}\ n_0 = 1 \cdot 10^8\,\mathrm{cm}^{-3} \tag{2.8}$$

is much smaller than the dimensions of the particle ensemble, which is typically in the order of a few mm. The Debye length characterizes the diffuseness of the homogeneously charged ensemble on the edges and describes the shielding of the internal space charge field Φ_sc from external fields.

Including the surface diffuseness of the NNP due to temperature effects, a realistic density profile is given by

$$n\left(r,z\right)=n_0\cdot\exp\left(\frac{q\Phi\left(r,z\right)+m\omega\left(\omega_\mathrm{c}-\omega\right)r^2/2}{k_\mathrm{B}T}\right)\quad\text{with}\quad n_0=\frac{m\omega\left(\omega_\mathrm{c}-\omega\right)}{2\pi q^2}\tag{2.9}$$

with the total electric potential $\Phi\left(r,z\right)=\Phi_\mathrm{sc}\left(r,z\right)+\Phi_\mathrm{T}\left(r,z\right)$ as the sum of the space charge potential $\Phi_\mathrm{sc}\left(r,z\right)$ and the trap potential $\Phi_\mathrm{T}\left(r,z\right)$ as well as the plasma bulk rotation frequency ω. In an unperturbed NNP, this bulk rotation frequency corresponds to the $\vec{E}\times\vec{B}$ drift frequency $\omega_\mathrm{E\times B}$. If the bulk rotation frequency ω is increased to $\omega=\omega_\mathrm{c}/2$ by an external excitation, the central density n_0 is maximized, leading to the Brillouin density introduced at the start of the section.

The bulk rotation frequency also guides the angular momentum L of the plasma, which is given by

$$L=m\omega r^2+qBr^2/2c.\tag{2.10}$$

Due to conservation of the angular momentum in absence of perturbations, also the mean quadratic radius $\langle r^2\rangle$ is conserved, which keeps the plasma confined indefinitely assuming an ideal trap setup. However, real Penning trap setups suffer from imperfections such as misalignment of the magnetic field and the electric potential axis or collisions with residual gas molecules. These imperfections are often modeled via a drag torque τ_D, which leads to a decrease of the bulk rotation frequency and an increase of the mean square radius, limiting the storage time [140, 141]. To compensate the drag torque, a counteracting torque has to be applied to avoid a loss of the trapped particles. Experimentally, this torque is implemented by a rotating electric field, which arises from an azimuthally segmented ring electrode. In case of four equal azimuthal segments, a rotating dipole field is generated by applying a sine wave RF potential to each segment, which is shifted by 90° with respect to its neighbors following

$$\Phi_i\left(t\right)=A_\mathrm{RW}\cos\left(i\pi/2+2\pi f_\mathrm{RW}t\right)\quad\text{for}\quad i=0,1,2,3.\tag{2.11}$$

Similarly, eight segments can be used for a dipole field by shifting the phase of neighboring segments by 45° or a quadrupole field with a 90° phase shift. Due to the more accurate approximation of a real sine wave by eight segments compared to four segments for a dipole field, higher order spatial harmonics caused by the finite segment size are suppressed, so that higher segment numbers are generally favored [142]. While the initial use of this rotating field or rotating wall (RW) technique is the compensation of the drag torque, it can also be used to steer the radial expansion of the NNP by overcompensating the drag torque as $\tau_\mathrm{RW}>\tau_\mathrm{D}$. In this case, the mean square radius can be decreased, leading to a compression up to about 13 % of the Brillouin density limit for electrons [140].

The RW technique is the standard approach to confine high particle numbers in cylindrical Penning traps indefinitely, but the induction of the additional rotating field also induces heating, increasing the NNP temperature and thus diluting the density profile. To compensate for the heating, a cooling mechanism has to be introduced. In the case of PUMA,

the cooling is performed by sympathetic cooling with electrons, which are provided by a field-emission point and cool themselves to ambient temperature via emission of cyclotron radiation in the strong magnetic field of the Penning trap. The antiprotons are then cooled via Coulomb collisions with the electrons, which gradually decreases their temperature towards an equilibrium temperature, at which the RW heating and the sympathetic cooling balance. The cooling is more efficient for higher electron numbers and a high initial temperature difference. The typical time scale for the cooling is in the order of seconds for electron cooling of ions [143] and antiprotons [144].

In contrast to the single-particle regime, in which a harmonic potential is essential for the analytic description of the eigenmotions, a simpler square potential is sufficient for axial trapping in the NNP-regime and is often favored due to a simpler fabrication of the trap electrodes. In its simplest form, such a square potential can be produced by three linearly stacked cylindrical electrodes, which are kept at distance by an insulator material. This trap type is also called Penning-Malmberg trap, and a sketch is depicted in Fig. 2.2. Then, by applying a voltage between the two outer ring electrodes and the central electrode, the square potential is produced. This geometry has the main advantage, that the on-axis opening does allow for simple particle injection and also optical access, *e.g.*, for laser spectroscopy. Besides, by stacking higher numbers of cylindrical ring electrodes with suitable lengths and applied potentials, it is also possible to approximate a harmonic potential well [145]. For these reasons, the PUMA experiment makes use of a cylindrical multi-ring Penning trap geometry, which could be operated both with harmonic or square potentials, as detailed in Sec. 2.2.1.

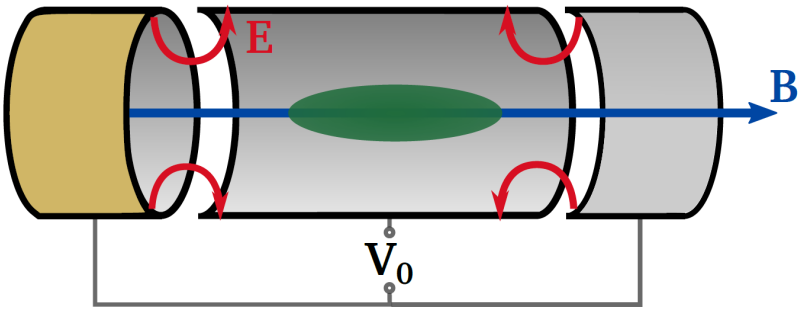

Figure 2.2.: Schematic depiction of the simplest Penning-Malmberg trap geometry with two short open-endcap electrodes and a longer central electrode.

2.2. Mechanical design of the PUMA trap and cryostat

For the trapping and storage of antiprotons in the PUMA Penning trap, a cryogenic setup is required to prevent losses of antiprotons on residual gas, and a detailed discussion of the impact of the residual gas density on the storage time of antiprotons is presented in Sec. 2.5. The trap system has to be operated at a temperature of about 4 K, which can only be achieved in a dedicated setup composed by three temperature stages: (*i*) the 4 K stage comprising the Penning trap, (*ii*) the 50 K stage as buffer between the room temperature

components and the 4 K stage as well as (*iii*) the 300 K stage which includes the vacuum components. The names are based on the estimated operation temperature of the stages. An overview over the full system with color-coded temperature stages is depicted in Fig. 2.3. Here, the two-staged pulsed-tube coldheads, which cool the cold stages, and the mechanical transition pieces between the stages are highlighted separately. A detailed description on the mechanical design of the setup components follows below.

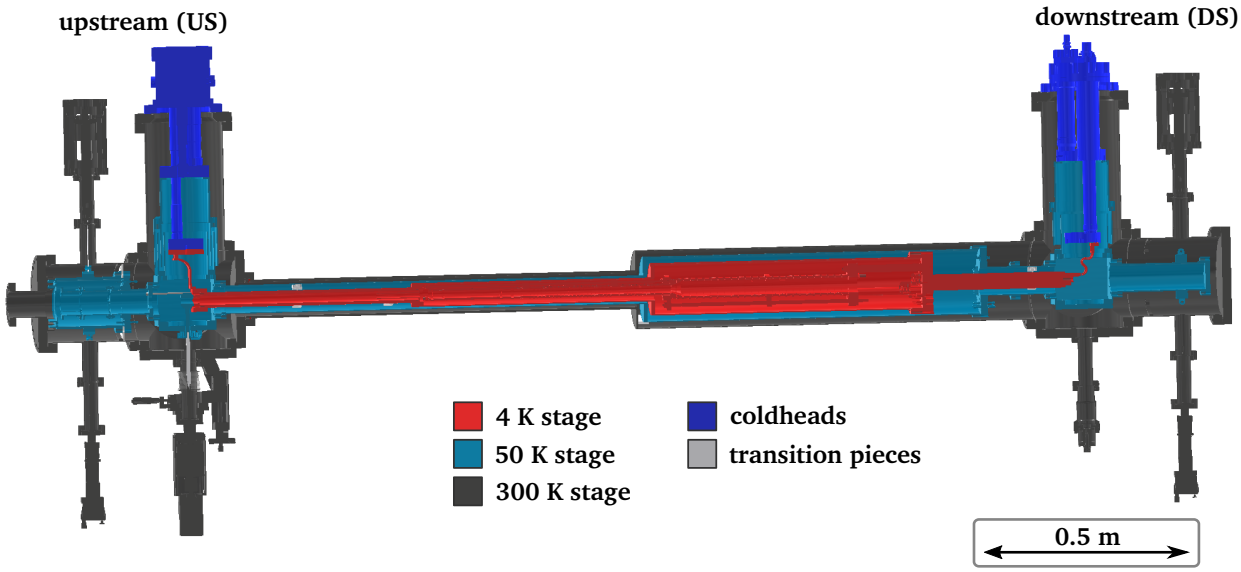

Figure 2.3.: Half-section view of the PUMA Penning trap and cryostat assembly. The different temperature stages are color-coded.

2.2.1. The Penning trap system and the 4 K assembly

For the PUMA experiment, the Penning trap setup has to fulfill two main tasks: the accumulation and long-term storage of antiprotons to provide a reservoir of trapped antiprotons for experiments as well as the overlapping of slow antiprotons with ions to initiate the formation of antiprotonic atoms. To prevent an interference between the two processes, the antiproton storage and formation of antiprotonic atoms will be spatially separated. This separation requires a high flexibility in the axial potential shaping to allow for a transfer of antiprotons from the storage region into the antiprotonic atom formation region. Additional flexibility is required in the latter region, as antiprotons and ions with opposite charge have to be trapped simultaneously. To account for these requirements, the PUMA Penning trap setup consists of two aligned cylindrical multi-ring Penning traps, which are used for the antiproton storage and the overlapping of antiprotons and ions, respectively. Additionally, a pulsed drift tube (PDT) is mounted right in front of the double-trap setup, which is used to decelerate the incoming antiprotons and ions from about 4 keV down to trapping energies of 100 to 200 eV. Due to the initial energy spread of the antiproton bunches of $\sigma_{\mathrm{E}} = 100\,\mathrm{eV}$, this allows for the trapping of the majority of the bunch. An overview over the full trap tower is depicted in Fig. 2.4. The specifications of its components are detailed below. The presented 3D-CAD model is generated with the Autodesk Inventor 2020 Professional software.

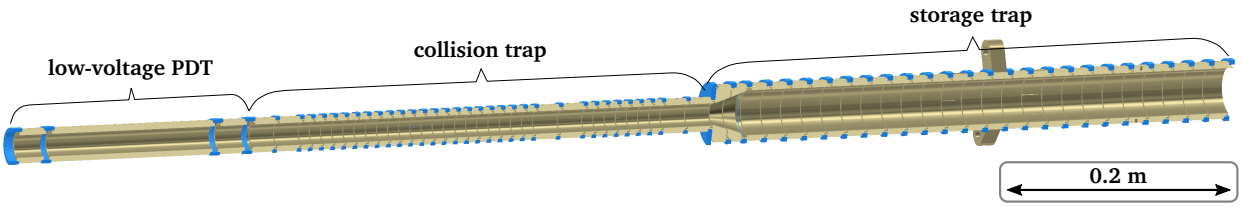

Figure 2.4.: Half-section view of the double-Penning trap assembly of PUMA, including the low-voltage pulsed drift tube (PDT).

All 60 electrodes are made from oxygen-free electronic (OFE) copper and are plated by a layer of silver with a thickness of 2 to 4 µm and a layer of gold with a thickness of 1 to 2 µm, similarly to other cryogenic Penning trap setups [146–149]. This plating protects the electrodes from corrosion by oxidation and reduces patch potentials, which induce anomalous heating [150]. The intermediate silver layer prevents a migration of gold atoms into the bulk copper. As electrical insulators between neighboring electrodes, sapphire (Al_2O_3) rings with high thermal conductivity are used, as they allow for an effective cool-down of the trap tower. A summary of the thermal properties of the implemented materials is presented in Appendix A. Including the pulsed drift tube electrode, a total of 13 different electrode geometries are implemented in the PUMA trap assembly. The corresponding technical drawings are added in Appendix B.

Each electrode has a cylindrical shape and includes wedges for the stacking of the sapphire insulator rings. This is highlighted in the half-section view of an antiproton storage trap electrode stack depicted in Fig. 2.5. In addition, the wedges shield the insulators from charging up and guide the field lines between neighboring electrodes. Besides these full-ring electrodes, on which the axially confining potentials is applied, also azimuthally segmented electrodes are implemented. Here, four- and eight-fold segmented electrodes are used to provide the opportunity of both a dipole and a quadrupole RF excitation such as the rotating wall compression. For all segmented electrodes, the arc length of the segments is equal to provide a smooth approximation of the actual multipole electric field. In azimuthal direction, the electrodes are insulated from each other by the use of ruby (Al_2O_3 with Cr admixture) spheres of 1.5 mm diameter, which are inserted in groves milled into the electrodes before segmentation, see Fig. 2.5.

The storage trap electrodes have a diameter of 40 mm and an inner length of 17 mm to reduce field imperfections and higher order field components in the multi-ring geometry [145]. Additionally, the diameter of 40 mm was chosen to maximize the trapping volume for the accumulation and storage of antiprotons. The full storage trap is composed of a total of 22 unsegmented electrodes and one four- as well as one eight-fold segmented RW electrode, providing a high flexibility in the shaping of the axial potential to trap and manipulate both antiprotons and electrons. Within the storage trap, an effective trapping volume of about 10 cm^3 can be provided, allowing for the trapping of up to 10^9 antiprotons. The storage trap stack is depicted in Fig. 2.6. The central electrode of the stack, which will be kept at ground potential, also includes three protrusions with a through hole in an angle of 120°. The protrusions connect the electrode radially to the support bars of the trap support

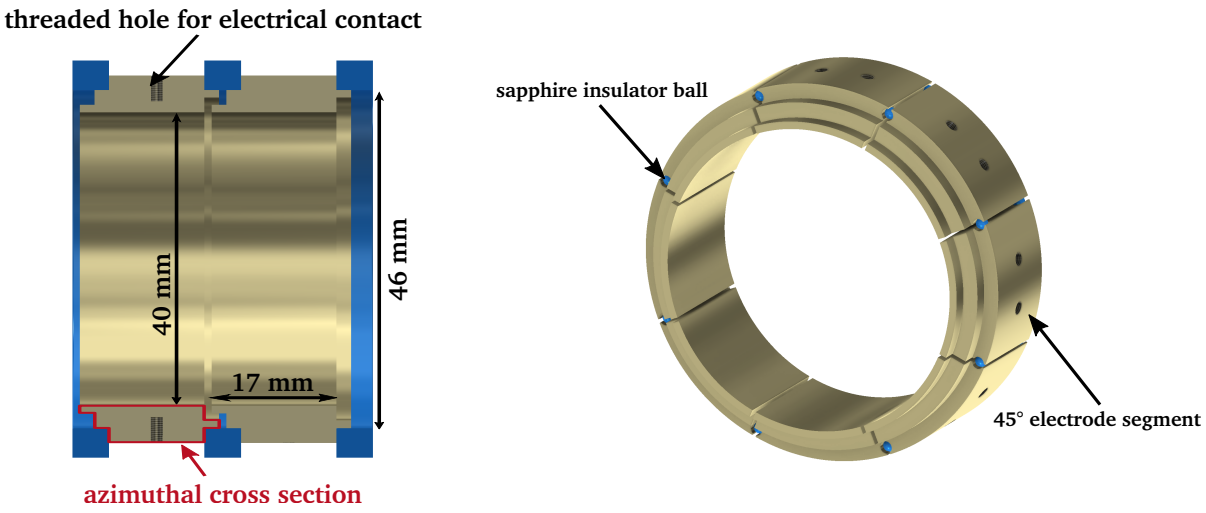

Figure 2.5.: Half-section view of an electrode and insulator ring stack for the storage trap (*left*) and front view of the eight-fold segmented rotating wall electrode (*right*).

frame for additional support of the structure. The copper electrodes were manufactured by the mechanical workshop of the institute of nuclear physics of the TU Darmstadt, electro-polished by Poligrat Deutschland GmbH and plated by Drollinger Metallveredlungswerke GmbH. The additional task of segmentation of the RW electrodes via electro wire cutting was performed by the fine mechanics workshop of the Max-Planck institute for nuclear physics in Heidelberg.

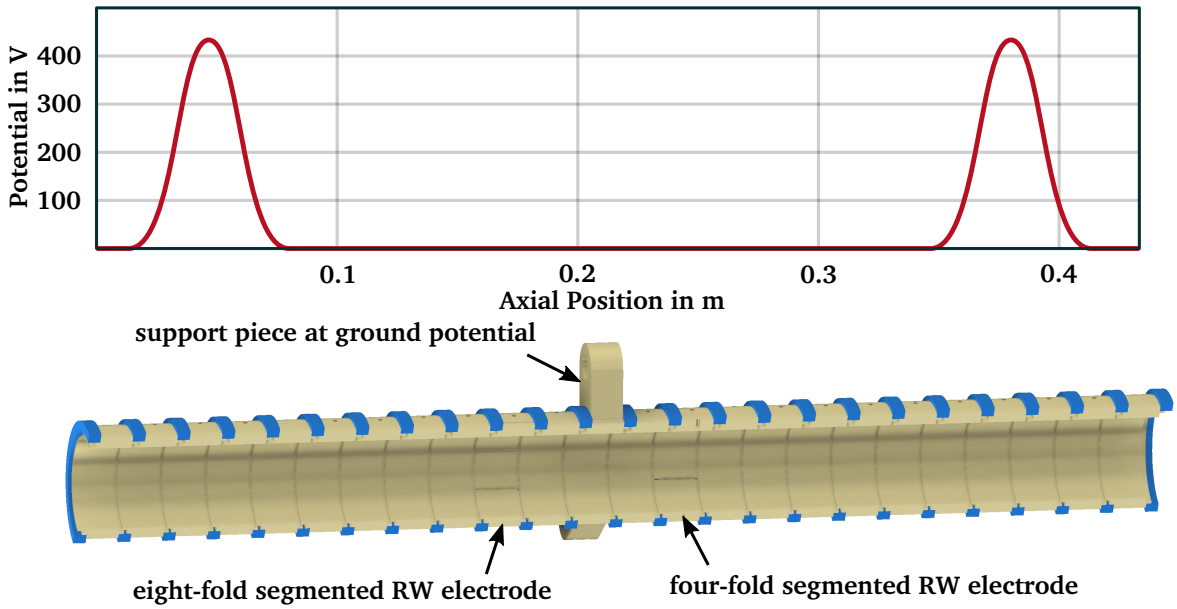

Figure 2.6.: Half-section view of the storage trap electrode stack (*bottom*) and axial square potential for antiproton trapping (*top*).

In contrast to the storage trap, in which each electrode has the same length and diameter, the collision trap, in which a fraction of the stored antiprotons is overlapped with ions of

interest, uses smaller electrodes with a diameter of 20 mm and a length of 9 mm for the potential shaping and additional longer transition electrodes. It comprises two distinct trapping regions, as indicated in Fig. 2.9, which are connected to each other and the storage trap via the transition electrodes. They are only used for particle transport and radial support, similarly to the central electrode of the storage trap. The first and smaller trap region is composed by a single eight-fold segmented RW electrode and three collision trap ring electrodes on either side of it for the axial potential. In the following, this trap region is denoted as the antiproton preparation region, as it is used as an intermediate storage region for the cooling of the fraction of antiprotons that has been extracted from the reservoir in the storage trap. In the second trap region, which in the following is denoted as the collision region, the ions are first captured before the antiprotons are inserted to initialize the formation of antiprotonic atoms. As this region requires the confinement of both negatively charged antiprotons as well as positively charged ions, the axially confining potential has to be bipolar.

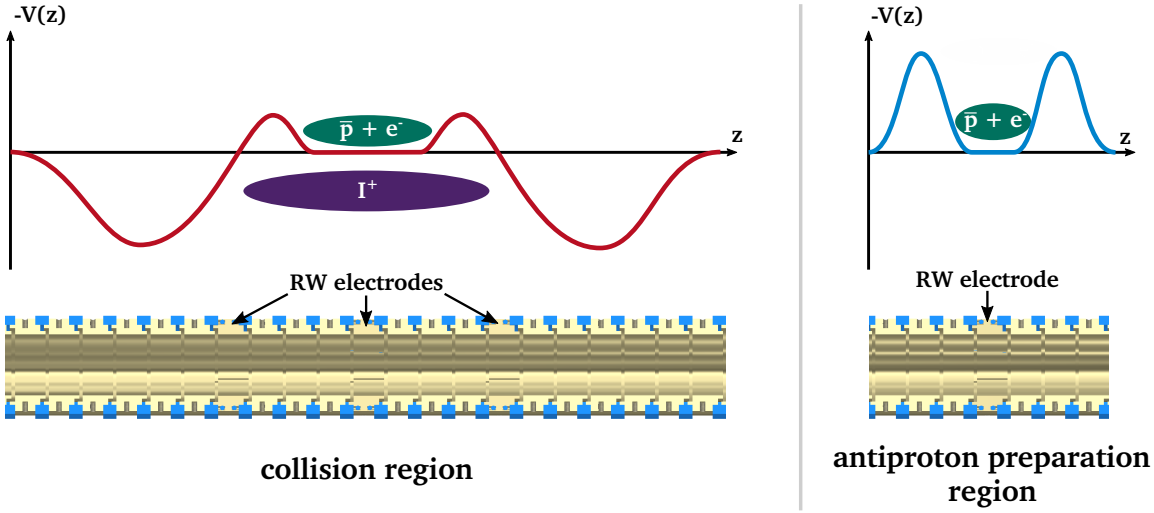

Figure 2.7.: Potential shapes in the two trap regions of the collision Penning trap. The collision region uses a nested bipolar potential for the simultaneous trapping of ions (I^+) and antiprotons ($\bar{p}$).

A sketch of this nested potential and the electrode configuration in the collision region as well as in the antiproton preparation region is depicted in Fig. 2.7. A nested potential involves the danger of longitudinal separation of the oppositely charged species, as it inevitably induces shallow potential wells in axial direction. To prevent this separation, an additional source of axial heating in the form an RF excitation can be implemented after the two species are overlapped.

The reduction of the diameter of the collision trap electrodes compared to the storage trap is mainly caused by external spatial constraints induced by the detection system, whose outer radius limited by the warm bore diameter of the solenoid, as it has to be placed in the strong magnetic field for the identification of the pions produced in the annihilation process. Based on simulations performed by S. Zacarias, which are summarized in [99], it was found that the highest detection efficiency is reached for an inner detector diameter of 100.5 mm,

limiting the outer diameter of the vacuum chamber in the region of the detector to 100 mm. Due to this external constraint, all components inside the solenoid bore exhibit a step-profile in radial extension, with a minimized radius in the upstream half of the cryostat and trap. This is sketched in the half-section view of the trap system inside the solenoid depicted in Fig. 2.8. The position of the two trap regions in the collision trap stack is also adjusted to the detection system, which requires annihilations in the axial center of the time-projection chamber (TPC) for a maximized solid-angle for detection.

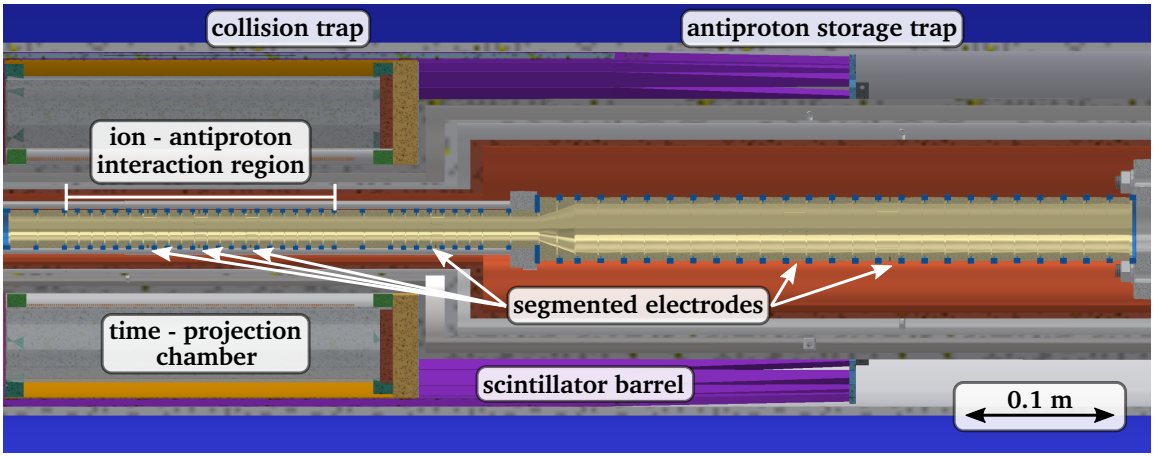

Figure 2.8.: Half section view of the trap and detection system within the solenoid bore.

Right in front of the collision trap stack, the second pulsed drift tube (PDT) for the deceleration form 4 keV down to 150 to 200 eV is mounted. It has a diameter of 20 mm, similarly to the collision trap electrodes. In contrast to the first high-voltage PDT in the PUMA antiproton beamline, this low-voltage PDT does not cause a significant increase in transverse emittance, even though the longitudinal energy is reduced by another factor of 20 to 25, as the strong magnetic field forces the particles on circulating orbits around the magnetic field lines due to the Lorentz force, as seen in the ion optics simulation in Sec. 3.3. It has a length of 146 mm, which is about a factor of 5 shorter than the first HV PDT, because the reduction of energy by a factor of 25 leads to a five-fold reduction in bunch length. Assuming the initial deceleration does not increase the bunch length, a similar time interval for a successful second deceleration will be available as in the first PDT.

As the transition between the collision and storage trap, two conically shaped electrodes are implemented. Their outer diameter is equal to the storage trap electrodes of 50 mm, while the inner radius is linearly adjusted to reduce the diameter from 40 to 20 mm over the length of two storage trap electrodes. The full cylindrical Penning trap tower can be assembled by combining the low-voltage PDT with its grounded neighbor electrodes, the collision trap with its two trap regions, the conical connection electrodes and the storage trap. For radial as well as axial support of the horizontally mounted tower, an aluminum support system is used, which is based on three endcap plates and bars. The plates are attached to the first grounded electrode of the PDT, the first conical electrode with larger diameter and the last electrode of the storage trap via the sapphire insulator rings and are connected by three bars between each plate. At the upstream end of the support tower, three alignment pins are installed, which will allow for an alignment the trap tower within the 4 K

copper trap chamber in groves. On the downstream end, the endcap plate is connected with the trap base flange via three aluminum mounting bars. The trap tower and the aluminum support are depicted in Fig. 2.9.

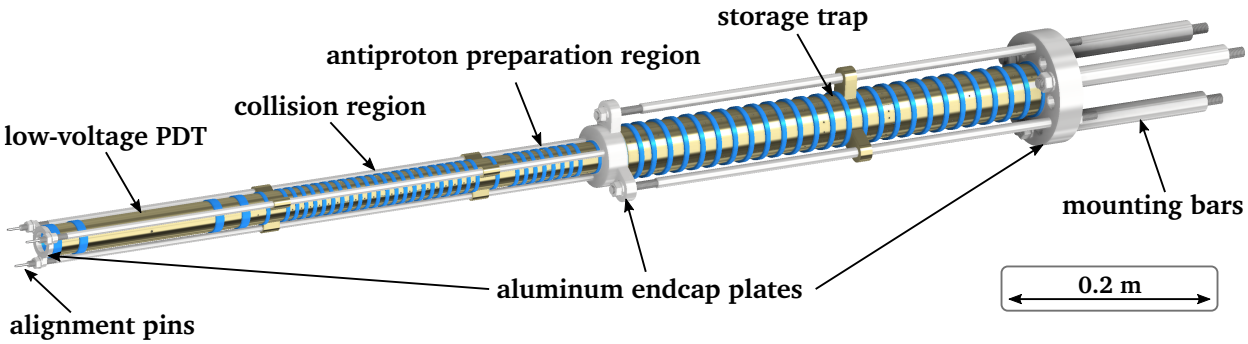

Figure 2.9.: Overview over the PUMA Penning trap tower and its aluminum support.

The trap base flange supports the downstream end of the trap tower and houses the electrical feedthroughs towards the next temperature stage for the trap electrodes as well as the cold field emission sources for the electrons, and a front view of the flange is depicted in Fig. 2.10. To provide a backup it was decided to install two field emitters in parallel. Each field emitter requires one HV pin feedthrough, while another five single-pin feedthroughs are added for the low-voltage PDT ($\times 1$) and the non-destructive diagnostics in the storage trap ($\times 2$) and the collision trap ($\times 2$). This non-destructive diagnostic of trapped particle ensembles is based on RF excitation on one individual electrode and pickup of the induced signal on a second electrode. The general concept of this idea is described in [151] and its implementation for PUMA in [152]. The remaining electrodes for the static potential wells and particle transfer (47 in total) as well as the segmented ring electrodes for the rotating electric fields (36 segments in total) are mounted onto two SUB-D HD 78 pin feedthroughs, while separating the DC potentials on one multipin feedthrough and the RF potentials on the second one. The multipin feedthroughs are rated up to a potential difference to ground and neighboring pins of 500 V and a current of 3 A, which is sufficient for the foreseen trapping energies in the order of 200 eV, while the single copper pin feedthroughs are suited for HV operation up to 5 kV and 25 A. The latter specifications are required for the operation of the low-voltage PDT at a potential of about 4 kV and the electron field emission points with potentials in the order of 1.5 kV.

To connect the trap electrodes (DC as well as RW) with the multipin-feedthroughs, Kapton-insulated Manganin (alloy of $\sim$ 84 % Cu, 12 % Mn and 4 % Ni) wires with a diameter of 0.14 mm are used, which have a significantly lower thermal conductivity than pure copper wires. They are screwed onto the electrodes and electrode segments with M2x3 screws and on the opposite end crimped onto pins of the 78 pin SUB-D HD sockets. The cables are rated up to a DC potential of 1 kV, which is sufficient for the use with the trap electrodes, and the small diameter reduces the heat transfer of the cables into the trap. For the HV components, Manganin wires of 0.25 mm diameter are used, as they are rated up to 6 kV. These cables are similarly screwed onto the respective electrodes and are connected to the single-pin feedthroughs via push-pin connectors made from a copper beryllium (CuBe) alloy.

Due to the closed design of the base flange, ions as well as residual gas molecules can only access the Penning trap from the upstream end. This half-closed trap design provides significant improvements with respect to pressure and temperature compared to open trap assembly such as HITRAP at GSI [153]. The implications on the temperature and pressure profile of the trap tower are detailed in the sections 2.4 and 2.5. On the rear side of the feedthrough flange, a 360 mm long cylinder of 42 mm diameter is screwed into a threaded hole, which acts primarily as a large thermal conductance for the cool-down of the trap and extends the 4 K stage towards the downstream coldhead. The connection between this extension bar and the 4.2 K stage of the coldhead is provided by a flexible custom copper thermal strap from Technology Applications, Inc. (TAI) based on high purity OFE copper braids, whose length is chosen to compensate for the thermal contraction of the 4 K stage. They are depicted on the downstream (DS) end of Fig. 2.11.

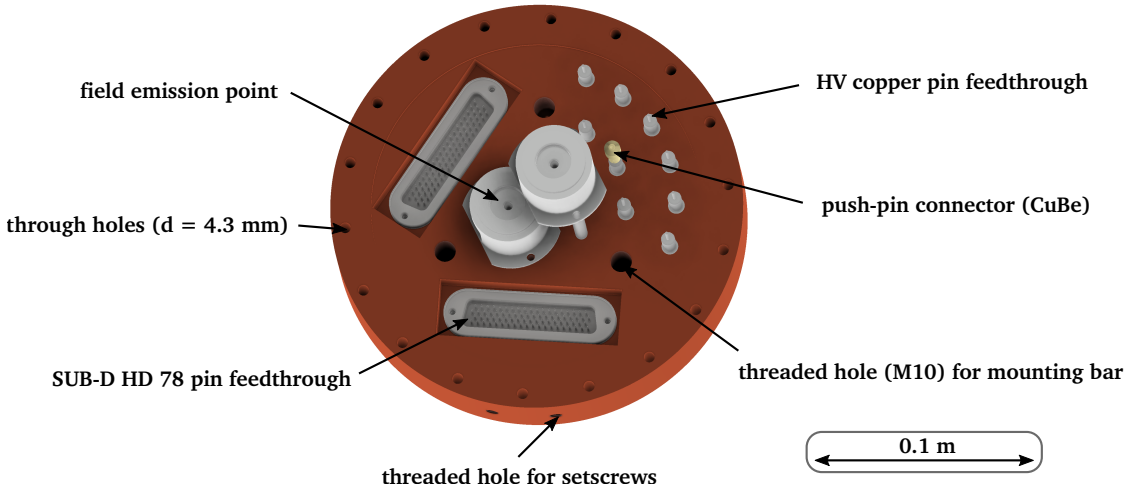

Figure 2.10.: Front view of the Penning trap base flange. The through holes are used for screwing the base flange onto the trap chamber, while the setscrews in the outer surface are used to fix the HD 78 pin feedthroughs in place.

To thermally shield the Penning trap tower from the environment, the tower is mounted into a OFE copper chamber, which follows the radial step-profile of the trap assembly. A half-section view of the trap tower within the chamber is shown in Fig. 2.11. On the downstream end, it is screwed onto the base flange via 18 M5 screws. A standard screwed connection is sufficient, as both components are already placed in a UHV environment. To support the upstream end of the trap tower, the copper chamber features three set holes for the alignment pins. They have a conical opening for an easier assembly of the trap tower, which has a length of about 1.3 m from the base flange to the alignment pins, and a depth of 15 mm that is sufficient to compensate for the different thermal contraction of the aluminum pins compared to the copper of the chamber. On the upstream end of the trap chamber, the 4 K entrance tube is screwed into a threaded hole. This entrance tube in itself is a hollow copper cylinder with a length of 554 mm, an outer diameter of 40 mm and an inner diameter of 25 mm, which primarily acts as a thermal conductance towards the upstream cryostat and as a pressure conductance barrier to improve the vacuum at the trap entrance. Due to the high aspect ratio of 1:22 between inner diameter and length, all particles that enter

the tube with an angle larger than 2.6° will hit a wall before they can pass the tube. As the tube is at cryogenic temperature, the particles have a high probability of sticking to the inner surface of the tube, so that the amount of residual gas particles entering the trap region is significantly reduced. To further enhance the effect of pressure reduction in the trap region, an additional OFE copper conductance barrier is mounted on the rear end of the entrance tube, thus right in front of the trap tower. With an inner diameter of 11.25 mm and a length of 113 mm, the acceptance angle is further reduced to 1.9°. The effect of both these components is also presented in section 2.5.

To connect the entrance tube to the upstream coldhead, two additional components are required. Firstly, a cuboid is screwed onto the upstream face of the entrance tube via four countersunk screws. This cuboid has a central round opening to let the antiprotons and ions enter the cryostat, which is surrounded by four threaded holes, which are used for polyether ether ketone (PEEK) threaded rods as mechanical connection between the temperature buffer stage and the 4 K stage. On the top surface of the cuboid, two threaded holes are placed for the connection to the copper blades as connection towards the coldhead. Similarly to the braided copper straps for the downstream coldhead, a flexible connection to the upstream coldhead is used to decouple the mechanical vibration of the pulsed-tube cooler and to compensate for thermal contraction during cool-down. While the braided straps offer an excellent conductivity, the risk of particle release into the vacuum system due to friction between the individual copper wires right in front of the entrance of the cryostat entrance was evaluated as too severe. Instead, thin copper blades of 0.3 mm thickness are stacked on top of each other so that the stack effectively acts as a spring. This concludes the components implemented in the 4 K stage of PUMA, and an overview over the full system is depicted in Fig. 2.11.

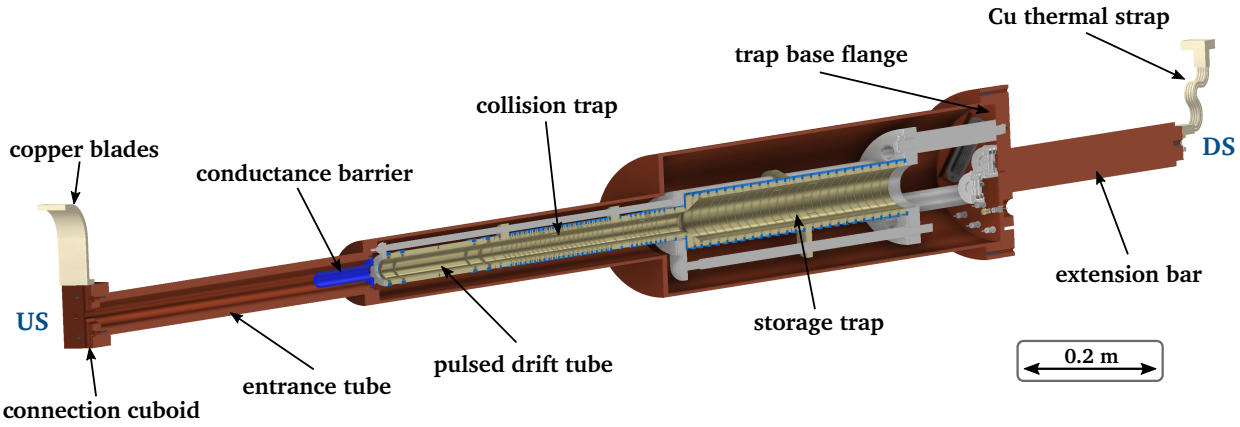

Figure 2.11.: Half-section view of the complete 4 K stage of the PUMA trap setup. The colors of the upstream (US) copper blades and of the downstream (DS) copper thermal strap are set to beige for better visibility. In addition, the conductance barrier inside the entrance tube is highlighted in blue.

2.2.2. The 50 K stage

The main purpose of the 50 K stage is to minimize the heat input into the 4 K stage, especially via thermal radiation. To effectively shield the 4 K stage, the solid angle for thermal radiation from room-temperature components has to be minimized, as a full cover is not possible due to the need of accessibility for antiprotons and ions. The second important task of the 50 K stage is the mechanical support and precise alignment of the embedded trap setup with the magnetic field lines via the alignment system based on linear feedthroughs. Finally, the buffer stage needs to include electrical feedthroughs for the Penning trap and field emission electrodes, as the cables have to be guided from the cryogenic stage towards the vacuum chamber.

To thermally shield the trap chamber from the vacuum tube, an aluminum tube is used. In the narrow part, the tube has an inner diameter of 70 mm and outer diameter of 74 mm, while the wider part has an inner and outer diameter of 166 mm and 170 mm. To mechanically support the trap chamber, a total of 9 ball transfer units (BTUs) in 4 sets are screwed into the pipe's inner surface. An explanation of the working principle of the BTUs is given in Sec. 2.2.4. The first upstream set, which is mounted close to the entrance of the tube, includes three BTUs at the same axial position, which are mounted at an azimuthal angle of 120° with respect to each other. Here, the top BTU is aligned with the vertical axis, while the lower two BTUs are offset by 60° with respect to the vertical axis. The second set of two BTUs, which is mounted in the same way as the lower two BTUs of the first set and located 24 cm behind the first set, also support the entrance tube of the 4 K stage. The remaining two sets support the trap chamber at the location of the storage trap and are placed in a similar manner as the second set of BTUs.

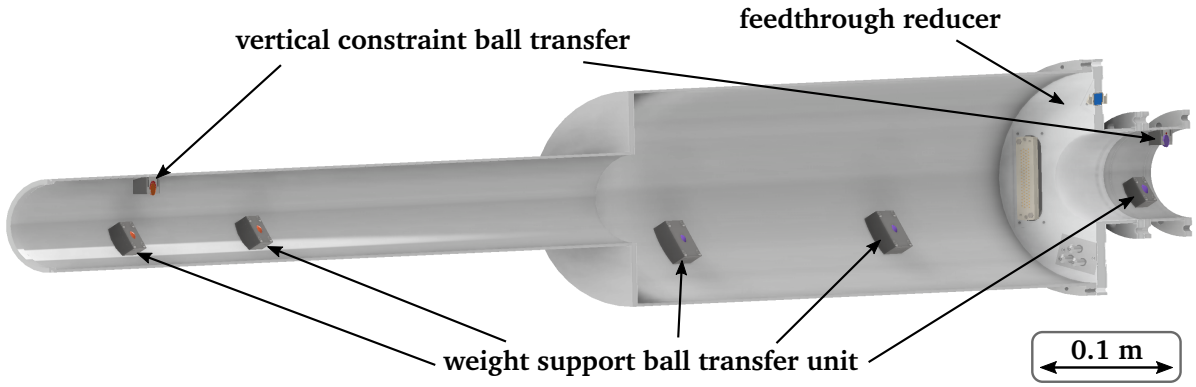

Figure 2.12.: Half-section view of the 50 K aluminum tube with the ball transfer units for weight support and the electrical feedthroughs for the trap electrodes.

To close the aluminum tube on the wide downstream end, a reducer piece is installed which also includes the electrical feedthroughs for the electrodes of the 4 K stage. Here, the same type of feedthroughs, cables and plugs are used as in the 4 K stage. However, as welding of the feedthroughs onto the bulk aluminum is not possible, the feedthroughs are spot-welded onto stainless-steel plates of 2 mm thickness, which are then screwed onto the aluminum component. The reducer limits the inner diameter back to 70 mm and is connected to a short aluminum tube that includes another set of three BTUs, which are

installed similarly to the first set. While the bottom two BTUs of all five set are mainly used for mechanical support of the system while reducing the thermal conductivity, the upper two transfer units are specifically installed for the transport of the system. By limiting the vertical degree of freedom, damages induced by vibrations during transport are prevented. A half section view of the aluminum step tube, feedthrough reducer and short support tube including the BTUs is depicted in Fig. 2.12.

While the step-profile tube is screwed onto the feedthrough reducer via M4 screws, the upstream end of the narrow section does not include holes for screwing. Instead, a groove is milled into the outer surface of the tube, which has a semicircular profile with a diameter of 4 mm and a central offset from the front face of 6.8 mm. To connect the tube to the upstream component, a removable flange ring is first placed around the shallow part of the tube. Then, a snap ring of 4 mm diameter is inserted into the groove, which extends the outer diameter by 2 mm at the position of the groove. Finally, the removable flange ring is pulled over the snap ring so that the front face of the tube and the ring are aligned. This requires a dedicated profile of the flange ring, which is depicted in Fig. 2.13. The concept of a removable flange is used due to spatial constraints. A similar solution will also be used for the main vacuum chamber of the 300 K stage.

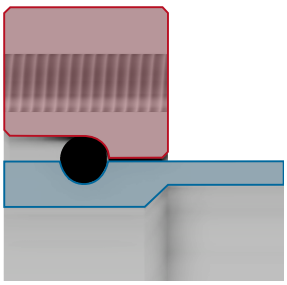

Figure 2.13.: Profile of the removable flange assembly on the upstream end of the aluminum step tube. The profile of the flange is highlighted in red and the tube profile in blue, while the snap ring is in black color.

On the front and rear end of the 4 K stage weight support chamber, hollow cuboids are attached that act as a connection piece between the alignment components, the coldheads and the main chamber, see Fig. 2.14. The cuboids are identical and open in axial and vertical direction for attaching neighboring components via screwing, while the horizontal faces are closed. Towards the top, the connection towards the intermediate cold stage of the coldheads is installed. Similarly to the case of the 4 K stage, a non-rigid mechanical and thermal connection via copper braids is chosen to prevent the emission of particles due to vibrations induced by the coldheads. In addition, a chicane structure without mechanical contact is mounted between the coldhead and the cuboids, which reduces the flow of residual gas into the cryogenic volume by absorbing the gas on the cold surfaces. In case of the upstream coldhead, the chicane pieces are based on a total of four concentric cylinders with increasing diameters, while the downstream coldhead uses a chicane based on a cylinder and an obround piece with a line segment length of 10.5 mm along the longitudinal axis. This straight-line segment is used to compensate for the thermal contraction of the aluminum chamber from the initial location to the thermal anchor PEEK plate.

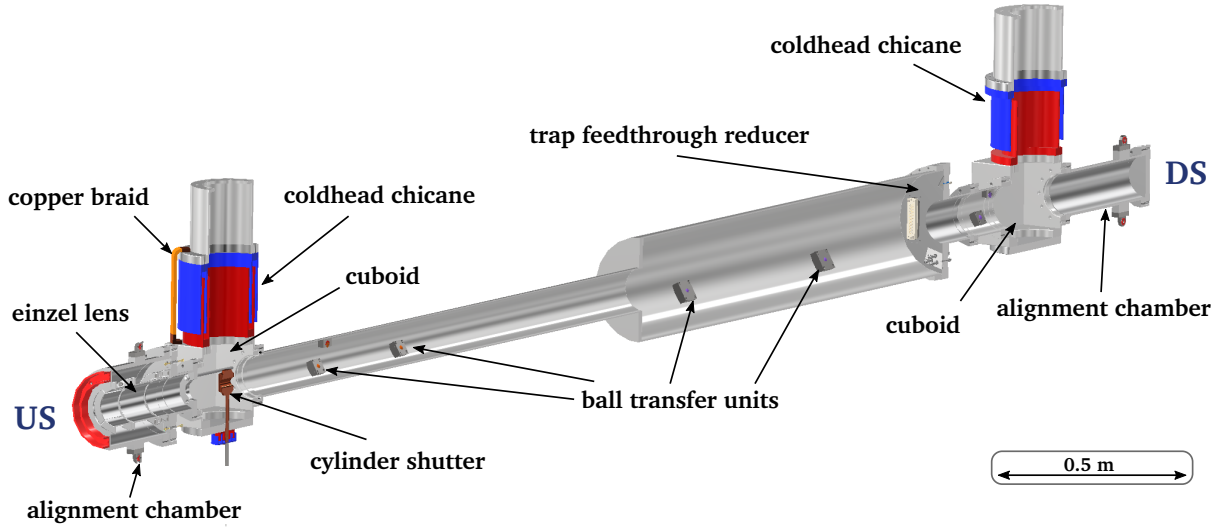

Figure 2.14.: Half-section view of the full assembly of the 50 K stage.

In axial direction, the cuboids are attached to the alignment chambers, which are connected to the horizontally and vertically mounted linear feedthroughs via aramide fiber wires. On the downstream end of the 50 K assembly, a simple tube with an outer diameter of 74 mm is used, which is closed at the rear end by a blind flange and has four azimuthal protrusions in a 90° angle. The suspension pieces for the aramide wire are screwed onto the flat square-shaped surface of the protrusions. It is composed of a stainless-steel main body with countersunk holes for screwing into the alignment chamber and two arc-shaped extrusions, in between which the stainless-steel suspension piece for the alignment wire is mounted. While of the arcs and the suspension piece have an M6 through hole, the second arc includes a threaded holes for M6 screws, so that the position of the suspension piece between the arcs is fixed.

In contrast to the simple tube design for the downstream suspension, the upstream alignment chamber serves a double function as it also houses an einzel lens assembly for focusing of antiprotons and ions into the Penning trap. The dimensions of the electrodes are similar to the ones mounted inside the antiproton beamline and one of the grounded electrodes is split into four segments of 90° arc length for horizontal and vertical steering. To apply the steering and focusing voltages onto the five electrode segments, single-pin copper feedthroughs are mounted onto a reducer base flange, on which the einzel lens tower is mounted. The pins are again spot-welded onto stainless steel plates and screwed onto the aluminum flange and the 0.25 mm diameter Manganin wires are connected via CuBe pushpin connectors. The alignment chamber is then screwed onto the base flange, so that the einzel lens is encapsulated, still allowing ion optical access. To fit the thermal anchor PEEK plate as fix point for thermal contraction in between the chamber and the flange, both pieces are milled to provide four grooves, in which the PEEK plate is inserted. In addition, the flat front face of the alignment chamber features four M4 through holes, which are used to install a chicane piece at the upstream end of the 50 K stage, which is comparable to the chicanes of the upstream cryostat connection. The setup of the alignment chamber is shown in Fig. 2.15.

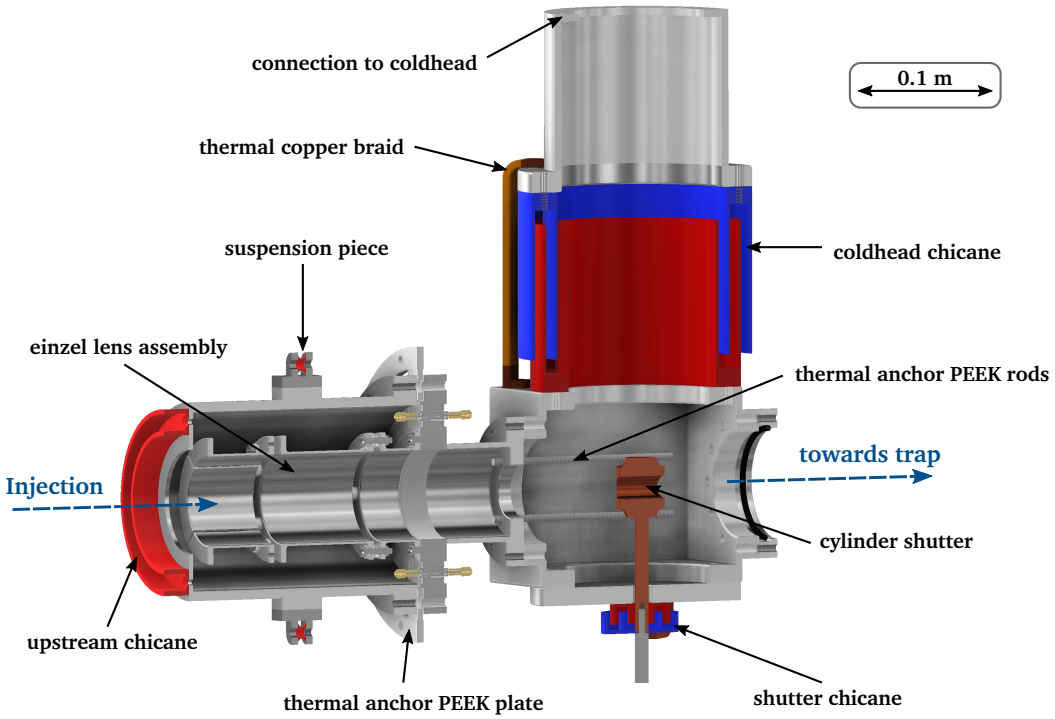

Figure 2.15.: Half-section view of the upstream 50 K assembly up to the removable flange of the main tube.

While the downstream cuboid is closed on the lower surface via a blind flange, the front cuboid features a bottom flange with a central bore hole of 14 mm diameter as well as threaded holes on the bottom surface. Through this bore hole, a cylindrical copper element is inserted into the interior of the cuboid, which is mounted on a long support bar of 10 mm diameter. This element acts as a cylinder shutter, which is placed right in front of the 4 K cryostat entrance and can be rotated into two configurations with a rotary feedthrough (Pfeiffer Vacuum, magnetically coupled, motorized) at room temperature. The cylinder includes a circular bore hole, which allows a passage of particles into the trap, while it blocks the opening after a rotation by 90°. In the latter configuration, the cylinder includes a flattened front surface for the installation of a simple pickup-plate, which is used for detection of incoming antiproton an ion signal. A sketch of the two orientations is depicted in Fig. 2.16.

As the bore hole of the cuboid flange also would provide access for particles to enter the cuboid and the 4 K cryostat, another small chicane is installed between the flange and the cylinder shutter mounting bar. Via the external chicane the shutter is also thermally coupled to the other 50 K components using a copper braid. In the foreseen configuration, the cylinder shutter is placed about 1 mm away from the 4 K entrance cuboid, which features a negative profile for optimized positioning. This limits the degree of freedom of the shutter to about 2 mm in each direction, which can be tuned by a x-y-z precision table (VAb UHV precision manipulator KPM 12-50)). Figure 2.15 summarizes the above-mentioned components of the 50 K stage upstream of the step tube in a half-section view.

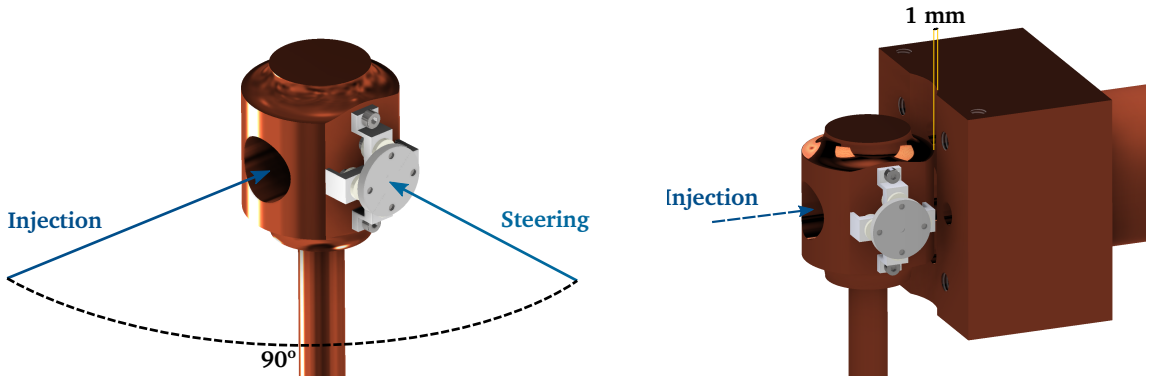

Figure 2.16.: Sketch of the two orientations of the cylinder shutter for injection of ions and antiprotons into the trap and steering of the particles while blocking the aperture of the 4 K region (*left*) and placement of the shutter relative to the 4 K stage entrance cuboid (*right*).

2.2.3. The room-temperature vacuum system

As the final layer of the setup, the room-temperature vacuum system serves the purpose of providing an extreme high vacuum in the surroundings of the cryogenic stages to ultimately reduce the flow of residual gas molecules into the trap volume. The requirements on the pressure inside the vacuum chamber are particularly rigid at the upstream side of the solenoid, as the only opening of the trap chamber is located at this end.

Similarly to the low-temperature stages, the main vacuum chamber, which is mounted in the bore of the solenoid, has a step-profile in radius. Around the storage trap, back towards the downstream coldhead, the chamber is based on a standard CF200 pipe made from 316L stainless steel with an outer diameter of 204 mm and ends of with CF200 flange made from 316LN stainless steel. Inside the tube, two ball transfer units are placed for a weight support towards the center of mass of the cryogenic stage. In the narrow region, the diameter is reduced to 100 mm to be able to fit the time-projection chamber (TPC) around the tube. It is not possible to use a standard non-removable flange on the upstream end of the chamber, as the detector has to be pulled onto the chamber during assembly of the system. To keep the 100 mm diameter over the full length, a removable flange is used - similarly to the aluminum step tube of the 50 K stage. In contrast to the aluminum tube however the front surface of the tube is not flat, as a vacuum seal is required to contain the extreme high vacuum inside the system. Instead, a custom cutting edge is lathed into the front face, which also requires customized copper O-rings as well as the same cutting edge on the connected zero-length reducer flange, which marks the transition from the custom shape back to standard CF200. To provide sufficient cross section of the seal ring, the inner diameter of the vacuum chamber is set to 89 mm, leaving about 5 mm space for the lathing of the cutting edge.

At the rear end of the chamber, a CF200 six-way cube is connected to the chamber flange. It surrounds the 50 K cuboid, whose dimensions are chosen so that they just fit through the 200 mm bore of the cube. On the top port, a pulsed-tube coldhead (Sumitomo SRP-182E2S) is installed with a CF200 tube of 333 mm length to accommodate for the length of the cooling

stages, a CF200 to CF160 zero-length reducer and finally the coldhead, which mounted on the CF160 port. One flange of the CF200 tube is rotatable, so that the coldhead can be oriented in a way that the external helium lines can be installed comfortably. The cooling power of the coldhead is given in Table 2.1. The left port (looking in beam direction) is closed off with a CF200 blind flange, while the right port is used as a feedthrough flange for the connections of the trap and field emission electrodes. While the SUB-D HD 78 pin feedthroughs are again used for the trap electrodes, the in-vacuum single-pin feedthroughs are here translated to three SHV connectors for the low-voltage PDT and the field emitters and six SMA connectors for the non-destructive diagnostics on the air side of the flange. On the bottom port, a CF200 to CF40 zero-length reducer and a CF40 full-metal angle valve are mounted, which provide access for an external pumping station for the room temperature pump-down. Finally, on the back port of the cube, the room-temperature alignment chamber with its four arms and linear feedthroughs is attached. While the bottom and the two horizontal ports use precision linear feedthroughs with a precision of 0.01 mm and a 50 mm stroke (VAb UHV precision linear feedthrough MLSM 40-50), the top port includes a special heavy load precision feedthrough with the same precision and stroke, but the additional feature of accepting an axial force of up to 500 N (VAb UHV precision linear feedthrough LDL 40-50). Together with the same feedthroughs at the upstream alignment chamber, they act as a suspension for the cryogenic system, which is the only mechanical connection between the 50 K stage and the 300 K stage, apart from the two BTUs located in the center of mass of the cryogenic assembly.

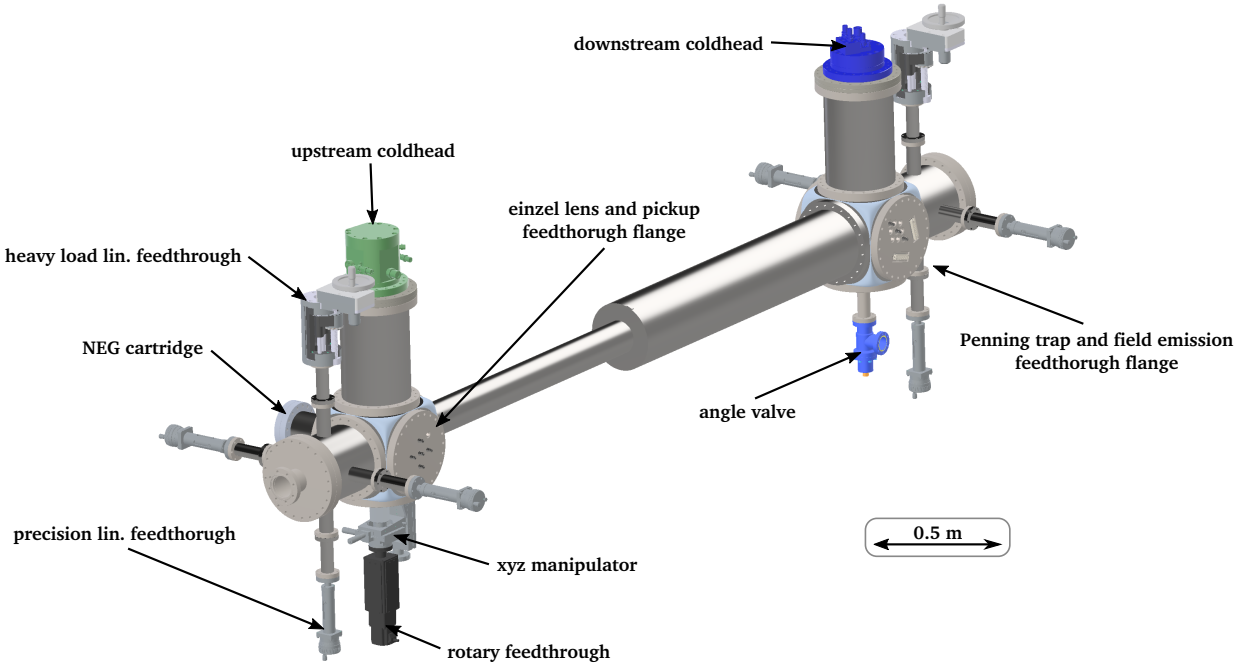

Figure 2.17.: Full view of the 300 K vacuum system of the experimental setup. The different coldheads are colored in green and blue for better visibility.

The front of the main chamber is connected to a similar CF200 six-way cube via the custom zero-length reducer flange. The top port is again used for the mounting of a second pulsed-tube coldhead (Sumitomo SRP-082E2) via a 333 mm long CF200 pipe and a CF200 to CF160 zero-length reducer. The cooling power of the coldhead is also given in Table 2.1. On the front port, a mirror of the downstream alignment chamber and the corresponding linear feedthroughs is mounted, but the foremost port is covered by a CF200 to CF63 reducer nipple, compared to the blind flange at the rearmost port on the opposite end of the setup. The components mounted onto the bottom port via a CF200 to CF40 zero-length reducer belong to the cylinder shutter assembly and comprise a precision x-y-z manipulator (VAb UHV manipulator KPM 12-50) with 25 mm horizontal and 50 mm vertical stroke for the precise alignment of the shutter with respect to the 4 K stage, and a rotary feedthrough for rotating the shutter. Looking in beam direction, the right port of the cube is again occupied with electrical feedthroughs, *i.e.*, five SHV to feedthroughs for the einzel lens as well as a single SMA feedthrough for the shutter pick-up plate. Finally, the left port is occupied by a non-evaporable getter (NEG) pump (SAES Capazitorr Z 1000), which is connected via a CF200 to CF100 zero-length reducer and 150 mm long CF100 pipe and acts as a static pump during the full operation and provides excellent pumping speed of 1000 l/s for hydrogen as main hazard of residual gas, as detailed in Sec. 2.5. An overview over the entire vacuum assembly is depicted as a half-section in Fig. 2.17.

2.2.4. Thermal contraction and conductivity between the stages

Achieving an extreme high vacuum requires the Penning trap to be operated at cryogenic temperatures. The required cooling of the components is either provided by a liquid helium heat bath as used, *e.g.*, in the LHC [154] or strong solenoids as in the case of ISOLTRAP [155], or by dry cold head cryocoolers. While systems based on a liquid helium bath, together with a liquid nitrogen buffer at about 80 K, have the main advantage that they can operate for several hours to days without electrical power, a regular re-filling of the coolants is required due to constant evaporation. In addition, safety regulations at CERN advise the use of a cryogen-free setup for PUMA, as the risk of an explosion due to a sudden expansion because of clogging of the liquid coolant during transportation cannot be ruled out entirely. Consequently, the PUMA setup uses coldhead cryocoolers produced by Sumitomo Cryogenics for both the solenoid and the trap system.

Table 2.1.: Summary of the nominal cooling power of the Sumitomo cold head cryocoolers used in the PUMA setup. The appendices -F100H and -F70H indicate the corresponding helium compressor models fabricated by SHI Cryogenics.

Component	Model	Power [W] at 43 K	Power [W] at 4.2 K
Solenoid	RDK-408D2-F70H	40	1.0
	RDK-408D2-F70H	40	1.0
Trap System	SRP-182E2S-F100H	36	1.5
	SRP-082E2-F70H	40	1.0

As indicated in the overview of the coldhead specification in Table 2.1, all used coldheads are two-stage cryocoolers with a main stage at 4.2 K and a temperature buffer at 43 K, while the coldheads themselves are mounted onto the room-temperature vacuum chamber. Here, the 50 K stage aims at minimizing the thermal load onto the trap, which is caused both by thermal radiation, whose power input $P_{\mathrm{th,rad}}$ scales with the difference of the fourth power of the temperatures $T_{\mathrm{H}}^4 - T_{\mathrm{L}}^4$ with "H" indicating the higher and "L" the lower temperature. Additional load arises from thermal conduction, which depends on the materials connecting the different stages as well as the cross section for heat transfer and the temperature difference. While a high thermal conductivity material is required for the assembly of the cold stages, so that the heat is effectively transferred towards the coldhead stages, the weight support pieces in the form of ball-transfer units (BTU), which thermally connect the stages, are made from low conductivity material to reduce the heat load. An overview over full trap and cryostat assembly is depicted in Fig. 2.20 in the form of a half-section view of the 3D-CAD model.

As indicated in the previous description of the three stages of the system, each stage is mostly composed of a single material. For the vacuum system, the material of choice is low-permeability stainless steel (AISI 316L and 316LN). In case of the 50 K stage, aluminum (EN AW-6082 and -6061) is used due to low mass and thermal conductivity of about 60 W/m K, as indicate in [156]. Finally, the Penning trap electrodes as well as the surrounding cryochamber are made from oxygen-free electric (OFE) copper with at least 99.99 % purity, as it provides a very high thermal conductivity of about 1000 W/m K even for cryogenic temperatures [156], while only the trap support rings and bars are composed of EN AW-6061 aluminum.

The BTUs as weight support between the different stages comprise a housing from non-magnetic stainless steel (AISI 316LN), while the thermal contact towards the lower temperature stage is created with zirconium oxide (ZrO_2) spheres of grade 10 sphericity according to DIN 5401. Due to the spherical geometry, the contact area and thus the heat transfer is minimized. To further reduce the heat transfer, the main contact sphere of about 10 mm diameter is embedded into a reservoir of small ZrO_2 spheres of 2 mm diameter inside the housing. A half-section view of the BTU is depicted in Fig. 2.18.

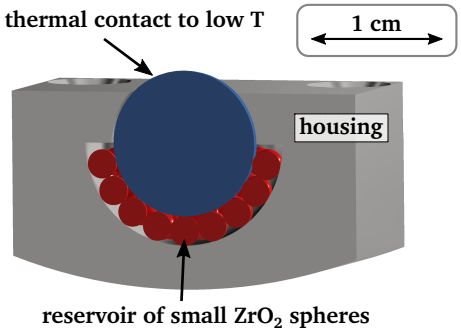

Figure 2.18.: Half section view of the ball transfer units for weight support and minimal heat transfer. The lower surface of the housing is rounded to fit the inner diameter of the respective tube.

For the cryogenic aluminum and copper components, also the thermal contraction has to be considered. Due to the geometry of the setup, the linear extension along the trap and solenoid axis is mainly affected. The aluminum chamber and the copper chamber have a total length of about 3.016 m and about 2.306 m, respectively. The available data on the thermal expansion of aluminum [157] and copper [158] at cryogenic temperatures is taken into account. Figure 2.19 depicts the normalized thermal contraction $L_T - L_{293\,\mathrm{K}}/L_{293\,\mathrm{K}}$ for the two used metals, from which the absolute contraction is calculated to be:

$$\begin{aligned} \Delta L_{\mathrm{Al},\,50\,\mathrm{K}} &= -4.073 \cdot 10^{-3} \cdot L_{\mathrm{Al},\,293\,\mathrm{K}} = -4.073 \cdot 10^{-3} \cdot 3016\,\mathrm{mm} = -12.3\,\mathrm{mm}, \\ \Delta L_{\mathrm{Cu},\,4\,\mathrm{K}} &= -3.256 \cdot 10^{-3} \cdot L_{\mathrm{Cu},\,293\,\mathrm{K}} = -3.256 \cdot 10^{-3} \cdot 2306\,\mathrm{mm} = -7.5\,\mathrm{mm}. \end{aligned} \tag{2.12}$$

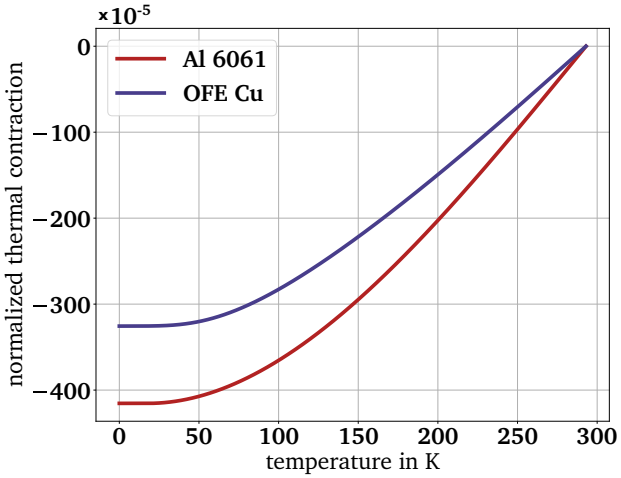

Figure 2.19.: Plot of the normalized linear thermal contraction $L_T - L_{293\,\mathrm{K}}/L_{293\,\mathrm{K}}$ relative to room temperature for Al-6061 and OFE-Cu.

This thermal contraction during cool-down of the setup also affects the geometry of the system, as it induces position shifts with respect to the room temperature vacuum chamber. The 4 K stage is fully embedded within the 50 K buffer stage without direct mechanical contact to the room-temperature components, so it only includes a fixed mechanical reference towards the 50 K stage via four threaded rods made from polyether ether ketone (PEEK) at the entrance of the chamber as fix point for the contraction. In case of the 50 K stage, the chamber has a mechanical connection towards the room temperature stage via the alignment system, composed of the four linear feedthroughs on the front and rear end of the setup. This connection is based on aramide fiber wires with low thermal conductivity of only 0.05 W/m K and very high tensile strength, so that they can carry the weight of both cryogenic stages. The thermal properties of the aramide fiber are summarized in Appendix A. Besides this, an additional rigid fix point for contraction is required. For this, a PEEK plate at the base flange of the einzel lens assembly of the 50 K stage is used, which still allows an angular adjustment of the cryostat in the order of $\sim 0.1^\circ$ (*i.e.*, 5 mm in horizontal and vertical direction over 3 m length) with the alignment system. The coarse alignment of the trap and cryogenic system with respect to the magnetic field is performed with the support frame of the vacuum assembly. A weight budget of the full system is presented in Appendix C.

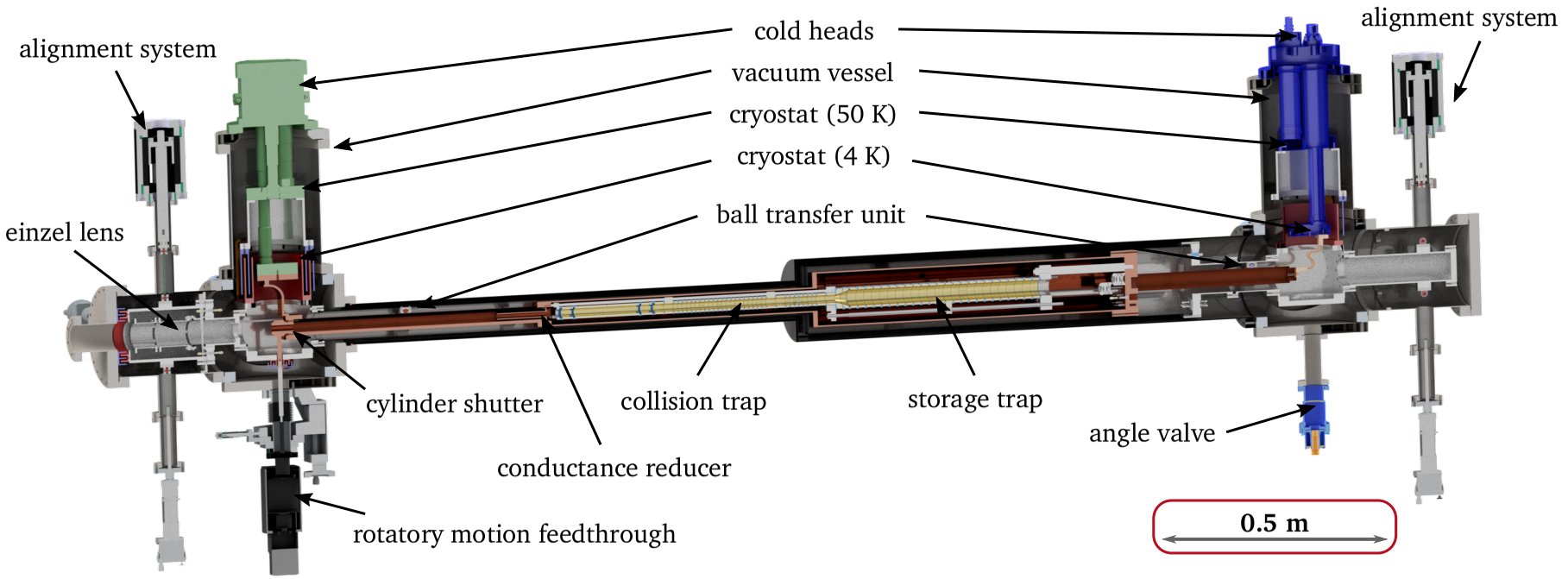

Figure 2.20.: Half section view of the PUMA cryostat assembly. The main components affecting the operation of the system are highlighted.

2.3. Mechanical stress simulations

In a first step to benchmark the cryostat design, a mechanical stress simulation is performed to investigate the deformation of the components exposed to gravity. A particular focus is set on the displacement of the trap tower, as it will influence the alignment of the trap with respect to the magnetic field of the PUMA solenoid.

The mechanical simulation is performed in the 3D-CAD software Autodesk Inventor 2020 Professional, which was also used for the 3D modeling of the cryostat and trap assembly. The software includes a package for the analysis of mechanical stress and displacement based on scalable loads and forces and calculates the physical displacement on a three-dimensional grid over the full model.

As the assembly comprises components which differ in size by about three orders of magnitude, which causes difficulties in the generation of the 3D mesh and the calculation of the mechanical properties, only a simplified model is used for the simulation. It omits small components such as the electrical feedthroughs, the copper braids and blades as coldhead connections or the ball transfer units and replaces them by bulk components with similar physical and mechanical properties. As the main focus is set on the trap tower and the cryogenic components, both coldhead, the angle valve and the cylinder shutter table and feedthrough are fully removed. A half-section view of the simplified model is depicted in Fig. 2.21.

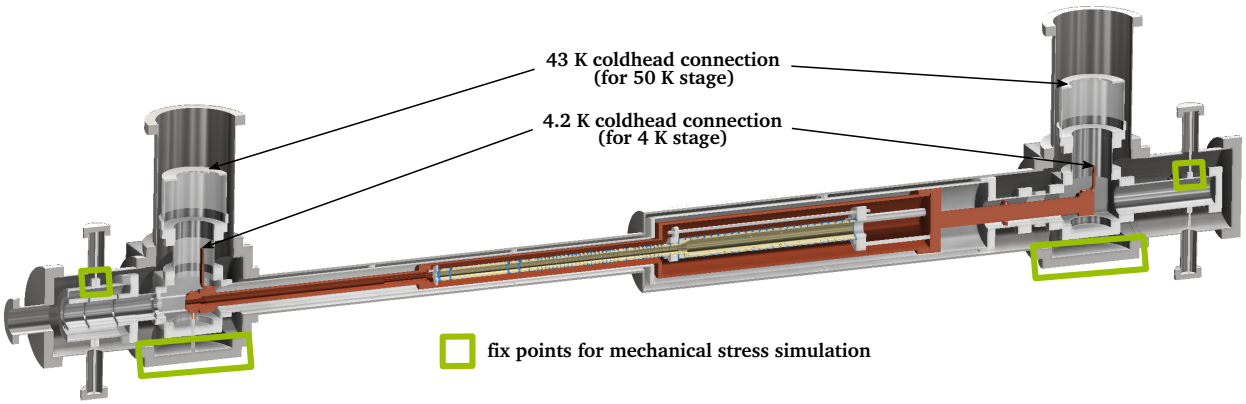

Figure 2.21.: Half-section view of the simplified model of the PUMA trap and cryostat setup for mechanical simulations in Inventor and thermal simulations in COMSOL. The fix points for the stress simulation in Inventor are highlighted with red boxes.

After the definition of the simplified reference model, the starting parameters of the simulation have to be set. As a load, only the gravitational force is considered. In addition, fix points of the assembly have to be defined. In case of the vacuum setup, the fix points are set on the flat surfaces of bottom ports of the CF200 cubes. For the 50 K stage, the fix points are defined on the top connection ports of the alignment chambers, while the 4 K stage is fixed only relative to the 50 K stage.

Based on these initial conditions, the displacement of the system has been simulated, and the result is depicted in Fig. 2.22. Here, the 3D model comprises a strongly magnified depiction of the calculated displacement to identify the regions with the strongest deformation. From that it can be concluded that the deformation is most pronounced for the collision trap aluminum support bars with absolute displacement due to gravity in the order of 100 µm, as indicated by the color code. Over the full assembly, the calculated displacement due to gravity is mostly colored in deep blue, indicating values in the order of few µm up to tens of µm. These values are negligible compared to deviations that arise even during the fabrication process of the setup components, where tolerances of ∼10 µm up to ∼100 µm were demanded.

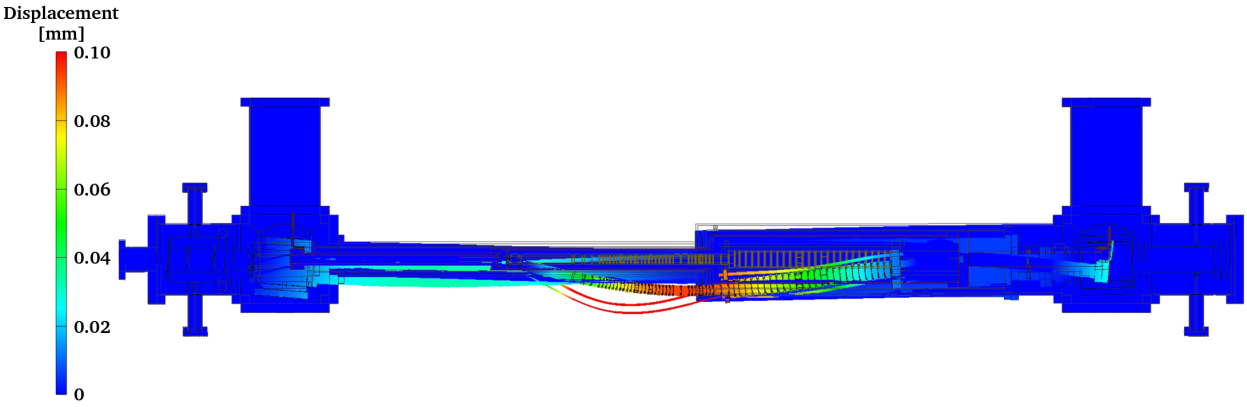

Figure 2.22.: Mechanical displacement of the trap and cryostat components as simulated within Inventor. The depicted displacement in the model is strongly magnified to identify the locations where the largest displacement occurs.

For the trapping of particles, the deformation of the trap with respect to the magnetic field lines gives rise to static field asymmetries. Based on the central deformation of about $\Delta z \approx 100\,\mu\text{m}$ for the trap tower, the induced angle θ between the electric field axis and the magnetic field axis can be estimated as $\theta = 2\Delta z / l_{\text{trap}} \approx 0.2\,\text{mrad}$ with the trap tower length $l_{\text{trap}} = 1090\,\text{mm}$. Based on this angle, a shift in the antiproton cyclotron frequency of $\Delta\omega_{\text{c}} \approx 29\,\text{Hz}$ compared to the nominal value of $\omega_{\text{c}} = 0.38\,\text{GHz}$ can be derived, following the equations presented in [129]. This deviation of about 70 ppb is lower than the typical frequency stability of waveform generators such as the Keysight 33600A Trueform Waveform Generator at 1 ppm [159], so that the shift in cyclotron frequency is negligible.

In the NNP regime, the field misalignment gives rise to a drag torque, which increases the NNP mean square radius over time [142]. Phenomenological model for this background torque have been developed [141, 160], but the exact impact of the misalignment on the drag torque is not yet understood. To compensate the drag torque induced by the field imperfection, the rotating wall electrodes are implemented. The amplitude and frequency of the applied potentials can then be tuned to provide a counteracting positive torque, so that the simulated misalignment of trap axis and magnetic field lines can be tolerated.

2.4. Thermal simulations

Based on the cryostat and trap setup detailed in Sec. 2.2, the thermal profile of the three different stages is investigated by simulations. These are performed with the COMSOL Multiphysics software (version 5.5), which allows the usage of several physics modules, *e.g.*, for electrical, mechanical, fluid, acoustic and thermal applications. It is based on the (numerical) solution of coupled partial differential equations (PDEs) and a finite-element mesh, which is superimposed on the geometry of the setup. An appropriate size of the mesh depends on the size of the components of the setup and a smaller mesh does lead to more precise data while requiring more computation time. In case of the PUMA setup, the size of the components ranges from millimeters for electrical feedthroughs and cables up to meters for the vacuum chambers, which makes the choice of a proper mesh challenging. To simplify and accelerate the simulation it is decided to omit the detailed structure of the electrical feedthroughs, threaded holes, mechanical feedthroughs, ball transfer units as well as vacuum pumps, as they only weakly affect the temperature profile of the Penning trap tower. Additionally, the thermal braid and blades for thermal contact towards the coldheads are replaced by bulk components with similar effective cross section to reduce the required resolution. The model is similar to the one used for the mechanical simulations presented in the previous section, see Fig. 2.21.

This simplified 3D model, conceived with the Autodesk Inventor software, is then imported into COMSOL Multiphysics. While the geometry of the model is kept, the materials of the individual components have to be specified individually. For many common materials such as aluminum and stainless steel the internal data base of COMSOL provides the required thermal parameters such as thermal expansion coefficient, heat capacity and thermal conductivity, while the remaining materials - *i.e.*, sapphire, PEEK, OFE copper and aramide - have to be added manually. Their properties are taken from [161–164] and summarized in Appendix A. In the next step, the required physics modules are implemented. In case of the thermal simulation, these are the packages "Surface-to-Surface Radiation (*rad*)" and "Heat Transfer in Solids (*ht*)", which COMSOL summarizes to the "Heat Transfer with Surface-to-Surface Radiation" multiphysics module. It requests the definition of the required boundary and starting conditions for the simulation such as the initial temperature, the contact pressure between neighboring surfaces as well as the surface emissivity and asperity.

It is assumed that all components start at room temperature (300 K), and the cryogenic stages are cooled through the coldhead connection heat baths indicated in Fig. 2.21, which are at 43 K for the intermediate stage and 4.2 K for the low-temperature stage with the corresponding cooling powers as specified in Table 2.1. For the trap a copper bar with an effective area of 220 mm^2 is assumed as a connection towards both coldheads, which is consistent with the area of the downstream thermal strap from Technology Applications, Inc., and the upstream bladed connection, while the thermal conductivity towards the 43 K heat bath is limited by an effective cross section of 1000 mm^2 of the aluminum connector, while the copper braid connection and blade structure are omitted for simplicity. The thermal conductivity of aluminum at 50 K with about 60 W/m K [157] is approximately one order of magnitude lower than for copper at the same temperature (about 800 W/m K [158]), and copper braids with a surface area of about 300 mm^2 are used for the connection to the

intermediate coldhead stage in the real setup. As the heat flux density q in W/m^2 is proportional to the thermal conductivity k and the temperature gradient ∇T via $q = -k\nabla T$, the simulation provides a conservative temperature profile as it underestimates the power $q \cdot A$ with the effective area A that can be drawn by the cold stage. For all touching surfaces that are screwed, a contact pressure of 0.2 bar and a mean asperity of 0.25 µm, corresponding to polished surfaces, are assumed, while for the remaining surfaces an asperity of 2 µm is set.

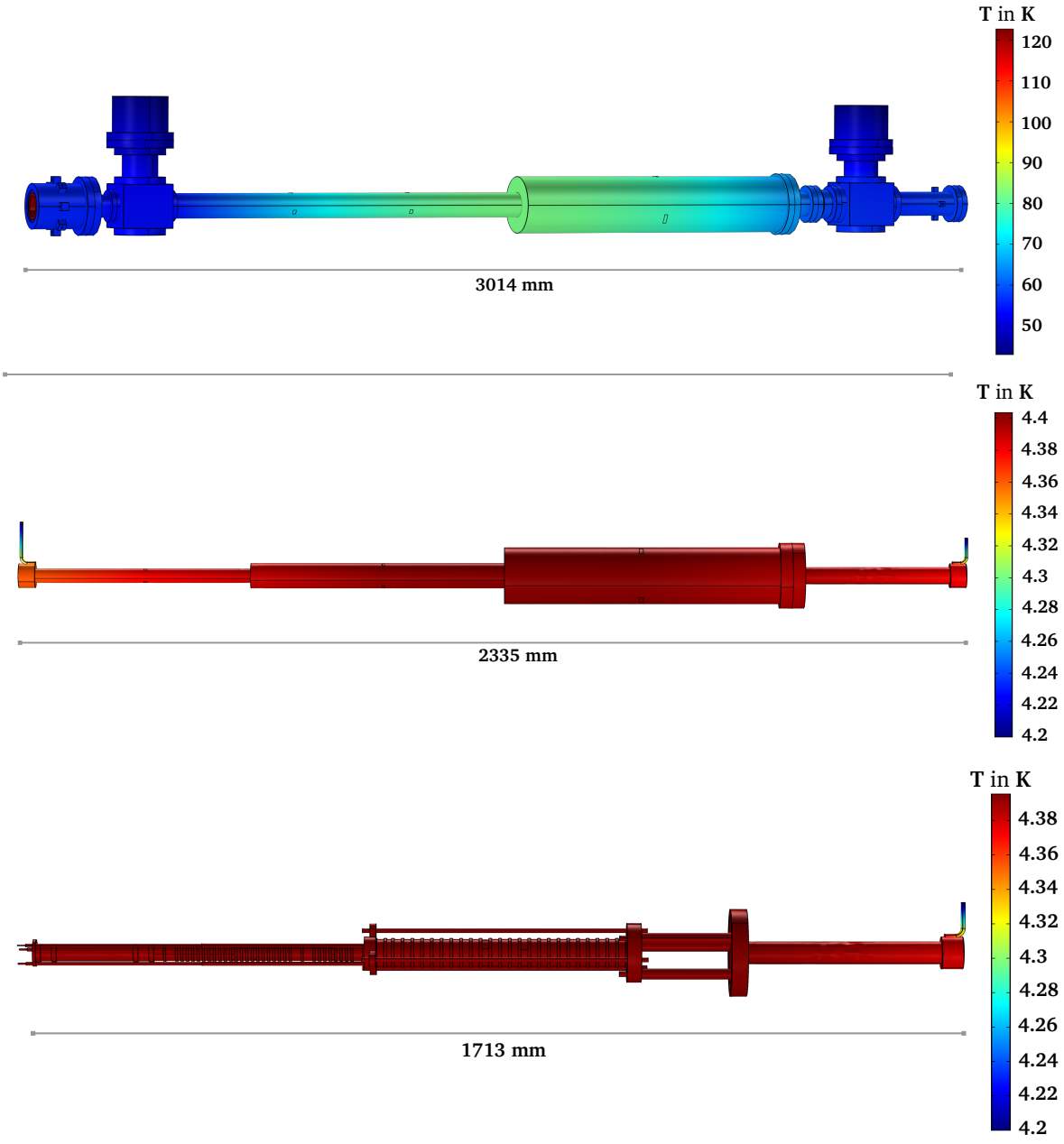

Figure 2.23.: Equilibrium temperature profiles of the 50 K buffer stage (*top*), the full 4 K setup (*middle*) and the Penning trap tower including its connection towards the downstream coldhead (*bottom*).

In the first step, a stationary simulation is performed to determine the equilibrium state. A single tetrahedral mesh was chosen for the full assembly, which has a minimum element size of 0.8 mm to resolve the smaller remaining components such as the sapphire insulator rings of the trap and a maximum element size of 28.2 mm for larger components such as tubes and flanges. Based on this mesh, the equilibrium temperature profiles for the 50 K buffer stage, the full 4 K stage and specifically the trap are obtained and depicted in Fig. 2.23.

In case of the 50 K stage, a significant gradient in temperature is observed between the center towards the extremities with the coldhead connections. While highest temperatures of about 120 K are only reached right at the open entrance of the stage, *i.e.*, at the einzel lens assembly, and quickly drop back to ambient temperature of about 55 K, the center of the stage is significantly warmer than the extremities with a temperature of about 85 K. Here, the radiative heat input from the surrounding vacuum chamber is very high due to the large surface area and cannot fully be compensated by the cooling power of the coldhead.

For both the full 4 K stage as well as the Penning trap tower the gradient in temperature is very shallow over the full length. The heat input from the surrounding buffer stage is low enough to be compensated by the cooling power of the coldheads, even though the buffer stage is not uniformly at about 50 K. The main increase in temperature arises at the actual coldhead connections with an increase by about 0.15 K, while the full remaining assembly stays at temperatures between 4.35 and 4.4 K. This uniform temperature of 4.4 K over the full length of the cryogenic system will also be used for the vacuum simulations in Sec. 2.5.

In case of the 4 K stage, the equilibrium temperature of the system is mainly limited by the effective surface area of the copper braids and blades as connection to the coldheads, as indicated by the color gradient in the simulations. By the use of braids with additional cords, this temperature could be lowered further. In contrast to that, the temperature of the 50 K stage is mostly limited by the thermal radiation from the 300 K stage in the center of the assembly, as well as the upstream opening of the system towards the room-temperature antiproton beamline. As the impact of the 50 K stage temperature on the trap temperature is simulated to be negligible, the 85 K at the center of the 50 K stage are tolerated.

In this equilibrium state, the power consumption through the coldhead connection surfaces is also calculated. At the upstream coldhead, 12.76 W and 0.27 W are drawn at the 42 K and 4.2 K stage, while the downstream coldhead draws 17.27 W and 0.16 W, totaling at about 30 W at the intermediate stages and 0.43 W at the cold stages. Compared to the available cooling power of 76 W and 2.5 W, a sufficient margin is available for the real setup including the omitted details.

As a next step, the cool-down of the system as a function of time should be investigated via simulations. A dedicated test run with the 3D geometry used for the equilibrium state did not converge, so that the implementation of a simplified 2D geometry would be necessary. The obtained time-dependence could then be compared to cool-down times observed at the ALPHA experiment, where the equilibrium temperature of their trap assembly is reached after several hours [165].

2.5. Vacuum simulations

For PUMA, the ambient temperature, *i.e.*, the temperature of the trap, is simulated to be at 4.4 K. The main incentive of this low temperature is a prolongation of the storage time of the antiprotons in the PUMA trap. As antiprotons annihilate on any nuclear matter, the storage time of antiprotons τ is predominantly limited by the pressure of residual gas molecules P and the ambient temperature T. It is assumed that the capture of antiprotons on molecular hydrogen is the dominant source of losses in the cryogenic system, and the corresponding capture cross section is given by

$$\sigma = 3\pi a_0^2 \sqrt{\frac{27.2\,\mathrm{eV}}{E}}, \tag{2.13}$$

with the Bohr radius of the hydrogen atom $a_0 = 5.3 \cdot 10^{-11}$ m and the kinetic energy of antiproton E in the center-of-mass frame. With the antiproton velocity $v = \sqrt{2E/m_{\bar{\mathrm{p}}}}$ and the density of the hydrogen gas n_{H}, the antiproton capture rate Γ is given by

$$\Gamma = 1/\tau = n_{\mathrm{H}} v \sigma. \tag{2.14}$$

The resulting antiproton storage time τ as inverse of the capture rate is thus inversely proportional to the residual gas density and follows the relation

$$\tau = \frac{1}{n_{\mathrm{H}} v \sigma} = \frac{1}{n_{\mathrm{H}}}\, 5.2 \cdot 10^{8}\,\mathrm{s\,cm^{-3}}. \tag{2.15}$$

Considering the ideal gas equation $pV = Nk_{\mathrm{B}}T$ together with the effective cryostat volume V and the Boltzmann constant k_{B}, the antiproton storage time as a function of the residual gas pressure P and temperature T can thus be estimated via

$$\tau[\mathrm{days}] \approx 6 \cdot 10^{-16} \cdot T[\mathrm{K}]/P[\mathrm{mbar}]. \tag{2.16}$$

While the storage time increases with the temperature due to a reduction of the capture cross section, it decreases with the residual pressure due to the lower number of gas molecules to annihilate with. To maximize τ it is thus necessary to find the balance between pressure and temperature. As conventional room-temperature vacuum systems reach pressures down to a few 10^{-10} mbar, the achievable storage times are limited to a few ms. For cryogenic setups however, even though the temperature is lower by a factor of about 75, a pressure of below 10^{-17} mbar can be reached, as demonstrated by the BASE experiments for low antiproton numbers [166]. Such low pressures lead to antiproton storage times in the order of several years, which are also targeted for the PUMA experiment.

2.5.1. Gas flow and pressure in cryogenic XHV setups

To prevent the annihilation of antiprotons between their production and the delivery to the experiments, both the Antiproton Decelerator and the ELENA ring as well as all transfer lines at the Antimatter Factory are operated at an ultra-high vacuum with pressures in the order of 10^{-10} to 10^{-11} mbar. At such low pressures, the flow of the residual gas molecules

is described by a free molecular flow, which implies that the mean-free path of the gas molecules is much larger than the dimensions of the setup. In first order, the particles then move in straight lines and only interact with the surfaces of the setup.

In this molecular flow regime, residual gas molecules pass flow from the higher-pressure region of the PUMA antiproton beamline into the lower pressure PUMA trap chamber without interacting with other residual gas molecules. This flow is mainly limited by the entrance tube of the cryostat and the conductance barrier as two long cylindrical pipes, for which the conductance C is given by

$$C = 0.476\,(T/M)\,r^3/L\ [\mathrm{l/s}]\,, \tag{2.17}$$

with the residual gas temperature T in K and molar mass M in g/mol as well as the pipe inner radius r and length L in cm [167]. For the case of molecular hydrogen gas with $M = 2\,\mathrm{g/mol}$, assuming it is thermalized to 4 K after entering the cryostat aperture, the entrance tube limits the conductance to about 8.6 l/s, and the conductance barrier to about 3.8 l/s, if the no surface adsorption is considered. Besides limiting the conductance, the inner radius and length of the cylindrical pipes also guide the angular distribution of the gas molecules flowing from the high-pressure region into the low-pressure region. Figure 2.24 depicts the angular distribution for the aspect ratios of $L/r = 2,\ 10$. In case of large aspect ratios, the flow into the low-pressure region - in the figures on the right-hand side of the pipe - is strongly directed towards the center axis of the conducting pipe with almost no flow in radial direction [168]. Due to this so-called beaming effect, it can be assumed that in the case of the PUMA cryostat all gas molecules that pass through the cryostat entrance tube and the conductance pipe pass through the trap tower without interacting with the trap electrodes and arrive on the feedthrough flange of the 4K stage.

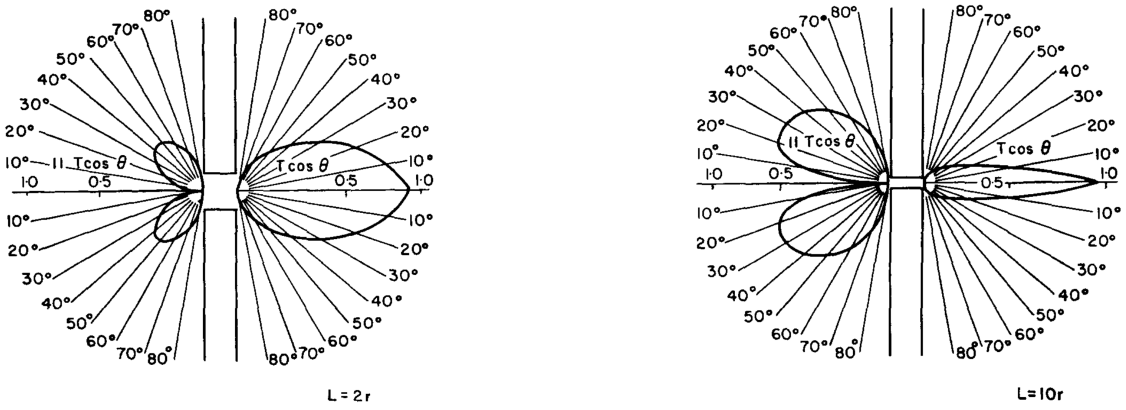

Figure 2.24.: Angular distribution of the molecular flow through cylindrical pipes with length-to-radius ratios $L/r = 2$ (*left*) and $L/r = 10$ (*right*). This figure is reprinted with permission from [168] ©2004 Elsevier.

While at room-temperature this interaction with the surface of apertures is predominantly a collision or a temporary adsorption followed by an isotropic emission, this interaction changes drastically at cryogenic temperatures, where the effect of cryopumping comes

into play. This cryopumping combines two distinct mechanisms in cryocondensation and cryosorption. The former is based on intermolecular Van-der-Waals forces, which are strong enough to keep the molecules bound at low temperatures. It is dependent on gas species and its saturation vapor pressure P_v, which describes the equilibrium pressure of gas- and condensate phase at a given temperature and is the highest for small gas molecules such as Ne, He and H_2. In particular, hydrogen is of interest as it has to the highest saturation vapor pressure with a about 10^{-12} mbar at a temperature of 2 K due to the small molecular size. Cryosorption, on the other hand, is based on the Van-der-Waals attraction between the gas molecules and the surfaces of the system, which is typically much higher than the intermolecular attraction [169]. This process is relevant if the adsorbed quantity of gas molecules is smaller than a full layer covering the surfaces, which in the following is called a monolayer. Due to the stronger attraction the molecules stay bound for much longer time intervals compared to cryocondensation, so that pressures much lower than the saturation vapor pressure can be achieved. The process is the dominant pumping mechanism for PUMA and the key to reach pressures in the order of 10^{-17} mbar. A schematic depiction of the two processes is shown in Fig. 2.25.

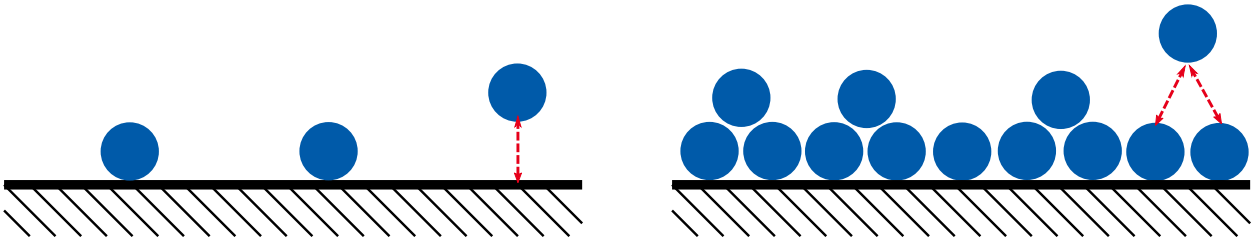

Figure 2.25.: Sketch of the two cryopumping mechanisms: cryosorption (*left*) and cryocondensation (*right*). The figure is reprinted from [92] under CC BY 4.0.

The equilibrium pressure in the cryostat depends on the temperature T, the surface area A and the resulting relative surface coverage $\Theta = S/S_M$ as ratio of the current coverage S and the maximum monolayer capacity S_M. While gases heavier than hydrogen and helium are also pumped by cryocondensation, the former are most effectively pumped by cryosorption. Assuming a surface coverage $\Theta < 1$, the equilibrium pressure is much lower than the saturation vapor pressure, which rises towards P_v for $\Theta \approx 1$. The relation of the equilibrium pressure and the surface coverage is given by adsorption isotherms. For the cryogenic sub-monolayer region the Dubinin-Radushkevich-Kaganer (DRK) equation [170–172] is assumed, which reads:

$$\ln(\Theta) = -D\left[k_B T\left(P_v/P\right)\right]^2. \tag{2.18}$$

Here, D is an empirical constant which depends on the adsorbing surface material and the gas species, which is also called Dubinin-Radushkevich (DR) energy [173] and accordingly has an energy unit (typically eV^{-2}). In the following the focus is set on hydrogen and its isotherms, as it is typically the dominant residual gas species in cryopumped XHV setups.

The adsorption isotherm of H_2 has been measured for pyrex, stainless steel and copper-plated stainless adsorbents, and the resulting isotherms are shown in Fig. 2.26. For all three adsorbents the isotherm is split in three region: (1) the plateau region at high surface

coverage, where $\Theta \approx 1$ and the pressure equals the saturation vapor pressure, (2) a steep drop in pressure for smaller surface coverage $S < S_{\mathrm{M}}$, and (3) the low-pressure and low-coverage region, where the measured values have to be extrapolated towards the pressures relevant for PUMA via the DRK equation. For the definition of a isotherm for the vacuum simulations for PUMA we take the data of the H_2 adsorption isotherm for copper-plated stainless steel at 4.2 K [174], as the PUMA cryostat is composed by copper, and use data taken by Chill, Wilfert and Bozyk at GSI for the cryopumping of hydrogen on stainless steel at temperatures between 7 K and 18 K [175] for the extrapolation towards lower pressures. By this, the equilibrium pressure P of H_2 is calculated as

$$P\left(\Theta, T\right) = P_{\mathrm{v}} \exp\left(-\frac{\sqrt{-\ln\left(\Theta\right)}}{k_{\mathrm{B}} T \sqrt{D}}\right) \tag{2.19}$$

with the saturation vapor pressure $P_{\mathrm{v}} = 4.25 \cdot 10^{-7}$ mbar [176], the maximum monolayer surface density $S_{\mathrm{M}} = 6.45 \cdot 10^{14}\,\mathrm{cm}^{-2}$ and a DR energy of $D = 3075\,\mathrm{eV}^{-2}$. To benchmark the extrapolation, additional measurements are performed by the vacuum group of CERN, which aim at extending the isotherm measurements to even lower surface coverage by the use of dedicated XHV gauges [177].

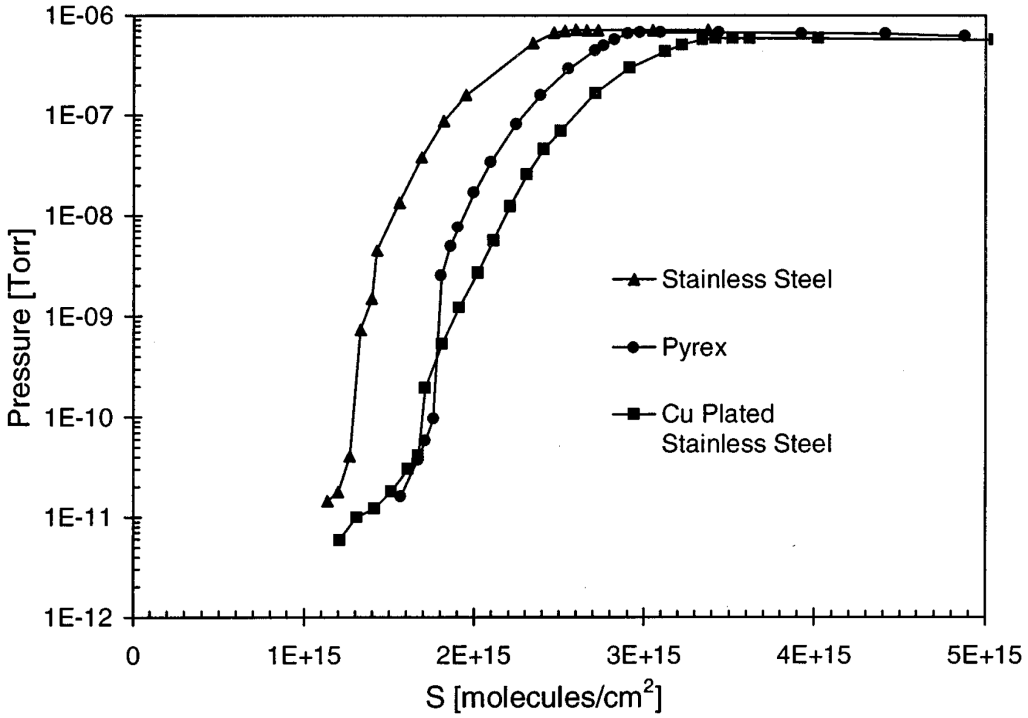

Figure 2.26.: H_2 adsorption isotherms at 4.2 K on pyrex, stainless steel and copper-plated stainless steel. The figure is reprinted with permission from [174] ©1997 American Vacuum Society.

While up to now only adsorption on the cryostat surfaces is considered, also the absorption or gas into the bulk material is also relevant for low-pressure setup. After adsorption on a surface, the gas molecules can migrate into lattice defects and interstitial sites of the bulk material and diffuse within the volume. This diffusion is guided by the diffusion coefficient

d and the particle concentration gradient $\mathrm{d}n_{\mathrm{dif}}/\mathrm{d}x$, causing a particle flow with a flow rate j_{dif}according to Fick's first law

$$j_{\mathrm{dif}} = -d \cdot \mathrm{d}n_{\mathrm{dif}}/\mathrm{d}x. \tag{2.20}$$

The diffusion coefficient is a temperature dependent property of the bulk material, which can be expressed via an Arrhenius law as

$$d\,(T) = d_0 \exp\left(-\frac{E_{\mathrm{dif}}}{RT}\right) \tag{2.21}$$

with the material-dependent diffusion energy E_{dif}, the ideal gas constant R and the empirical diffusion constant d_0. In case of PUMA, the three main materials used for the different temperature stages are stainless steel at 300 K, aluminum at about 50 K as well as copper at 4 K. In case of stainless steel, a huge amount of atmospheric hydrogen dissolves into the steel during the production process, marking the main limitation for the achievable pressure in room-temperature vacuum-systems. To reduce the hydrogen in the bulk of the vacuum chambers, it is common to bake the full assembly at temperatures of 100°C or above to increase the outgassing by diffusion while continuously pumping the system, *e.g.*, with a turbo-molecular pump, reducing the final achievable pressure by up to one order of magnitude. The diffusion coefficient of hydrogen in stainless steel (SS) at room temperature (300 K) is $d_{\mathrm{SS,\,300\,K}} \sim 10^{-9}\,\mathrm{m^2/s}$ [178], compared to $d_{\mathrm{Al,\,50\,K}} \sim 10^{-25}\,\mathrm{m^2/s}$ for aluminum at 50 K [179] and $d_{\mathrm{Cu,\,4\,K}} \sim 0\,\mathrm{m^2/s}$ for copper at 4 K [180]. Consequently, the main source of hydrogen outgassing in the PUMA setup is represented by the room temperature vacuum chambers, which is the reason why the chicanes are installed between the 300 K and 50 K stages of the setup.

2.5.2. Simulation of the residual gas number density and pressure

Based on the setup design and thermal simulations from the previous sections and the outgassing rates and hydrogen isotherms as input data, the pressure profile of the cryogenic stages is analyzed via simulations. Similarly to the temperature profile, the pressure is simulated with the COMSOL Multiphysics software (version 5.5). The rotational symmetry of the on-axis components is used to reduce the setup into a 2D slice with radial symmetry, which significantly improves the simulation times. As an additional simplification, only the on-axis pressure profile up to the 4 K trap base flange is taken into account, as the components behind do not impact the pressure in the trap. As physics module, the "Free Molecular Flow (*fmf*) package is used, which models the propagation of the residual gas in the UHV and XHV environment. The determination of the on-axis pressure profile is performed in a two-step process. In the first step, the pressure profile in the entrance region of the experimental setup, up to the entrance of the 4 K cryostat, is investigated in a first simulation. This simulation aims at extrapolating the pressure from the endpoint of the beamline, which is determined in a separate simulation with the MolFlow+ simulation software, to the cryostat entrance to define proper input parameters for the cryogenic system. Secondly, the pressure profile in the trap is derived based on the input pressure from the first simulation.

For the entrance region a 2D slice of the geometry was considered, which only approximates the complexity of the actual setup, as it omits the horizontally and vertically mounted feedthroughs and pumps and assumes cylindrical symmetry of the cuboid of the 50 K stage. In this simplified system, the upstream 300 K vacuum cube is assumed to be a pipe with an inner diameter of 200 mm, while the 50 K cuboid is represented by a tube with an inner diameter of 40 mm. Additional components that are included are the einzel lens assembly as well as the initial aperture of the CF63 beampipe and the entrance region of the 4 K cryostat with an inner diameter of 25 mm, while the cylinder shutter and the 4 K entrance cuboid are omitted. To mimic the open geometry of the 50 K cuboid towards room temperature via the chicanes an opening in the 50 K tube of 10 mm height is included, which is a conservative estimate of the effective open area between the stages. Finally, the NEG cartridge on the front CF200 cube is also included via a cylinder slice, whose effective area is set to be approximately equal to the cross section of the CF100 tube. While the nominal pumping speed of the cartridge is 1000 l/s, a reduced pumping speed is assumed for the simulation to account for the increase in effective opening angle. The 2D slice in comparison to the actual setup is depicted in Fig. 2.27.

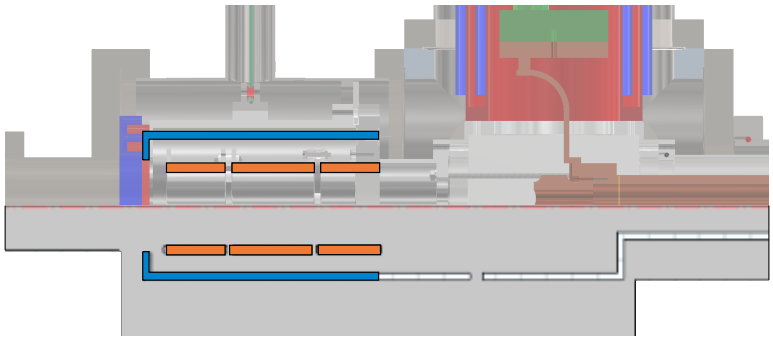

Figure 2.27.: Comparison of the actual upstream front of the cryostat assembly (*top half*) and the corresponding 2D slice implemented in COMSOL (*bottom half*). The einzel lens (*orange*) and the 50 K alignment chamber aperture (*blue*) are highlighted. The cylinder shutter in front of the 4 K stage is omitted.

Prior to the simulation of the pressure profile, the proper initial conditions and input parameter have to be defined. As an input pressure on the upstream CF63 port simulations performed in MolFlow+ [181] predict values in the order of a few 10^{-11} mbar. As outgassing of the room temperature stainless steel components (316L and 316LN) rates of $7 \cdot 10^{11}$ 1/m^{2}s are assumed, which are conservative estimates for unbaked systems, while baked systems reach rates in the order of a few 10^{10} 1/m^{2}s [182]. The effective pumping speed of the implemented pump is assumed as 250 l/s and the temperatures of all components are set according to the values determined in the thermal simulation.

A particularity of the free molecular flow simulations in COMSOL is the usage of particle number densities N/V instead of pressure P as quantity to characterize the amount of residual gas in the setup. This description is more intuitive in the very low-density region, as the thermodynamics interpretation of the pressure as a force acting on a surface becomes inadequate. However, the quantities are connected via the temperature following the ideal gas equation

$$P = \frac{N}{V} k_{\mathrm{B}} T. \tag{2.22}$$

In the following, the simulated number densities will be translated to pressures for orientation.

The result of the simulation of the number density profile in the entrance region of the setup based on the initial conditions described above is depicted in Fig. 2.28. Here, two input pressures of 10^{-10} and 10^{-11} mbar are assumed to investigate the sensitivity to the beamline pressure. Comparing the number density profiles it can be concluded that the lower beamline pressure leads a lower number density over the full range by a factor of about 2 to 3, but not by a full order of magnitude. The effective pressures at the marked position at the setup entrance with a temperature of 300 K are $1.2 \cdot 10^{-10}$ mbar ($P_{\mathrm{in}} = 10^{-10}$ mbar) and $4.6 \cdot 10^{-11}$ mbar ($P_{\mathrm{in}} = 10^{-11}$ mbar). At the entrance of the 4 K cryostat, where a temperature of 50 K is assumed due to a thermalization with the cold components, the resulting pressures are $1.4 \cdot 10^{-11}$ mbar ($P_{\mathrm{in}} = 10^{-10}$ mbar) and $5.6 \cdot 10^{-12}$ mbar ($P_{\mathrm{in}} = 10^{-11}$ mbar). In both cases, the pressures are in the order of about 10^{-11} mbar, which in the following is assumed as input pressure for the subsequent pressure simulations for the cryostat and trap tower.

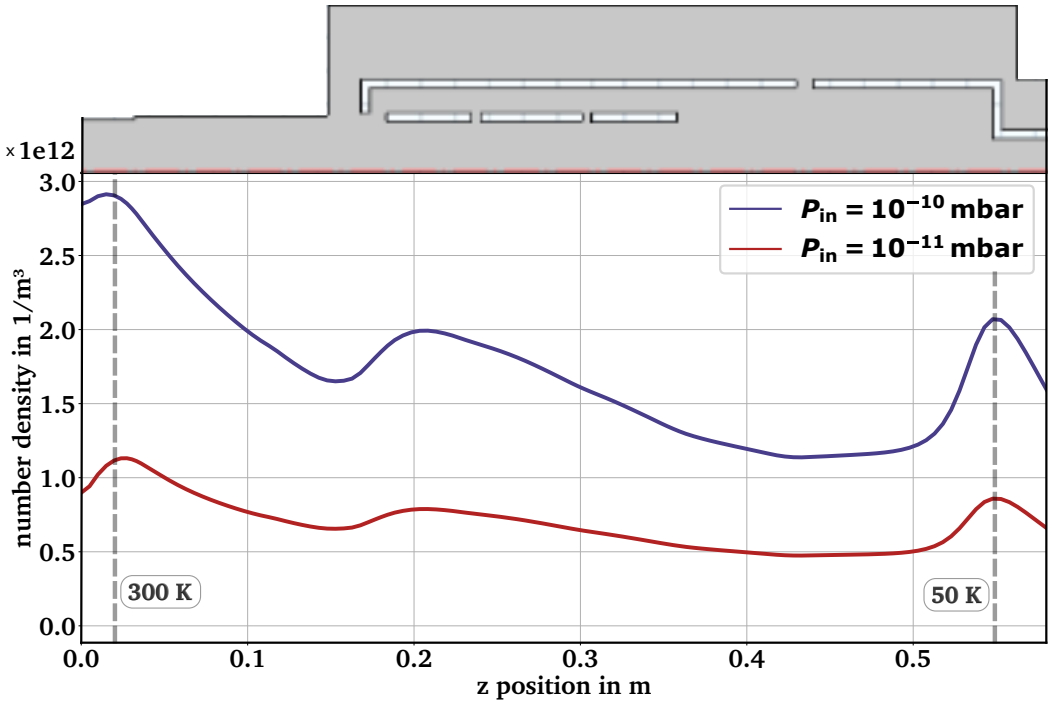

Figure 2.28.: Evolution of the on-axis residual hydrogen gas density in the entrance region of the experimental setup up to the entrance of the 4 K cryostat. For orientation, the 2D slice of the COMSOL model is added on top. Corresponding pressures at the marked points are derived with the mentioned temperatures.

Similarly to the entrance region of the setup, the 4 K cryostat is represented by a 2D slice. As most components along the beam axis are cylindrical symmetric, the slice provides a good approximation. For simplicity, the trap tower is represented by one single polygon,

while the trap support is neglected. The remaining components are the conductance barrier as well as the copper tubes and chambers up to the base flange of the trap, which seals the cryostat on the downstream end. A comparison of the 3D model and the 2D slice is depicted in Fig. 2.29.

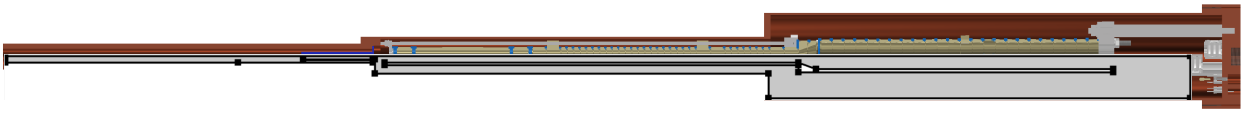

Figure 2.29.: Comparison of the 3D model of the 4 K cryostat assembly (*top half*) and the corresponding 2D slice implemented in COMSOL (*bottom half*).

In contrast to the simulation of the entrance region, the outgassing of the surfaces can be neglected, as the diffusion coefficient is virtually zero for the copper components. At the cryogenic temperature of 4.4 K, which has been derived in the thermal simulations, the surfaces of the system act predominantly via adsorption and desorption. The walls are characterized by three quantities: the sticking factor S, the desorption rate D and the initial adsorbent concentration $n_{\mathrm{ads},0}$. The latter can be estimated to an order of magnitude: assuming that the initial pump down before cool-down leads to a pressure of $p = 10^{-7}$ mbar, the number of particles N in the cryostat volume of $V \approx 10\,\mathrm{l}$ at a temperature of $T = 300\,\mathrm{K}$ is

$$N = \frac{pV}{k_{\mathrm{B}}T} \sim 2.4 \cdot 10^{13}. \tag{2.23}$$

Considering the particles distribute uniformly over the surface area $A \approx 0.75\,\mathrm{m}^2$ of the walls during the cool-down, the corresponding initial adsorbent concentration is

$$n_{\mathrm{ads},0} = \frac{N}{A} \approx 3.2 \cdot 10^{13}\,\mathrm{m}^{-2} \approx 5.3 \cdot 10^{-11}\,\mathrm{mol\,m}^{-2}. \tag{2.24}$$

To keep a safety margin, a conservative value of $5 \cdot 10^{-10}\,\mathrm{mol\,m}^{-3}$ is assumed for the following simulations.

The sticking factor is a dimension-less parameter which describes the probability of a residual gas molecule to stick to the cold cryostat walls instead of being emitted again. While the exact value of the parameter depends on the exact temperature, the surface roughness and the current adsorbent concentration, a first estimate leads to a value of 0.3. For the simulation we assume this sticking factor to be constant, even though measurements indicate a rise in the sticking factor with increasing surface coverage [183]. This conservative approach is appropriate, as the initial surface coverage Θ_0 is at about 10^{-5} and rises only slowly over time within a region where the sticking factor is virtually constant.

Finally, the desorption rate of the cold walls is guided by the isotherm at low temperature and pressure. Following Eq. 2.19 for the pressure as modeled by the DRK isotherm, the desorption rate is calculated with the average thermal velocity v_{av} as

$$D\left(\Theta, T\right) = S \cdot \frac{P\left(\Theta, T\right) v_{\mathrm{av}}\left(T\right)}{4RT}. \tag{2.25}$$

Besides the wall properties, the input pressure at the cryostat entrance remains as last input parameter for the simulation of the on-axis number density of hydrogen molecules. Based on the previous vacuum simulations a value of $P_{\mathrm{in}} \sim 10^{-11}$ mbar is considered as starting value. Similarly to the case of the entrance region of the setup, sensitivity studies are presented and discussed in the following. They investigate the impact of the input pressure, the sticking factor and the time evolution of the derived values for the number density.

Figure 2.30 depicts the results of the on-axis number density along the 4 K cryostat for the input pressure of 10^{-11} mbar and a sticking factor of 0.3 for different points in time. Over the full storage trap tower the number density is below 20 cm^{-3}, which corresponds to a pressure of 10^{-17} mbar at 4.4 K, even after 100 days, while the pressure in the pulsed drift tube and the collision trap is below 10^{-16} mbar. Generally, the degradation of the number density over time primarily affects the entrance tube and conductance barrier, as the particles entering the cryostat are effectively captured by their cold surfaces.

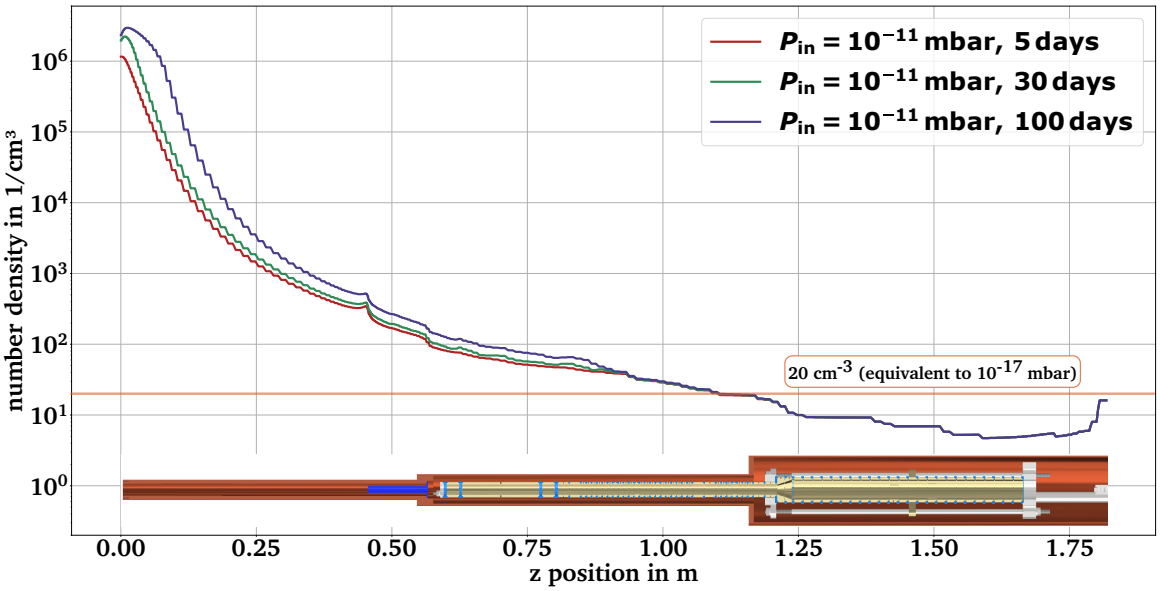

Figure 2.30.: Simulation of the on-axis residual gas density along the 4 K cryostat. The number density of $20\,\mathrm{cm}^{-3}$ is highlighted, as it corresponds to a pressure of 10^{-17} mbar at 4.4 K. For orientation, a half-section view of the cryostat is added.

In Fig. 2.31 simulations of the on-axis number density are presented for different sticking factors of $S = 0.2,\ 0.3,\ 0.4$. While the overall number density in the entrance tube and the collision trap is lower for the higher sticking factor by a factor of about 2 after 100 days, there is no significant effect on the number density in the storage trap. The storage trap stays below 20 cm^{-3}, while the density within the PDT and collision trap only changes weakly, so that the exact value of the assumed sticking factor is not important.

While the vacuum simulations for the antiproton beamline and the setup entrance indicate a pressure of 10^{-11} mbar at the cryostat entrance, imperfections of the real setup, which are not considered in the simulations, could lead to a degradation of the input pressure with respect to the simulated value. To account for this, a simulation is performed for an input pressure of 10^{-10} mbar, and the results of the on-axis number density after 5, 30 and 100 days are compared to the results with an input pressure of 10^{-11} mbar. The results of the simulation are depicted in Fig. 2.32 and it can be concluded that the on-axis number density scales approximately linear with the input pressure, especially in both traps. In the entrance tube, the impact of the higher input pressure is even more pronounced, as the occupancy of the cold surfaces starts to rise significantly, leading to a higher equilibrium pressure after long time periods. In the case of the higher input pressure a number density below 20 cm^{-3} cannot be reached, even in the storage trap. From this simulation it can be concluded that an as low input pressure as possible is desirable, as it significantly improves the long-term stability of the number density and thus pressure in the trap and allows for long antiproton storage times of hundreds of days.

Based on Eq. 2.14, the time-dependent number of stored antiprotons in the storage trap $N_{\bar{\mathrm{p}}}(t)/N_{\bar{\mathrm{p}},0}$ for a residual hydrogen gas density of 20 cm^{-3} is given by the exponential function

$$N_{\bar{\mathrm{p}}}(t)/N_{\bar{\mathrm{p}},0} = \exp\left(3.3 \cdot 10^{-3}\,\mathrm{days}^{-1}\, t\right) = \exp\left(t/301\,\mathrm{days}\right). \tag{2.26}$$

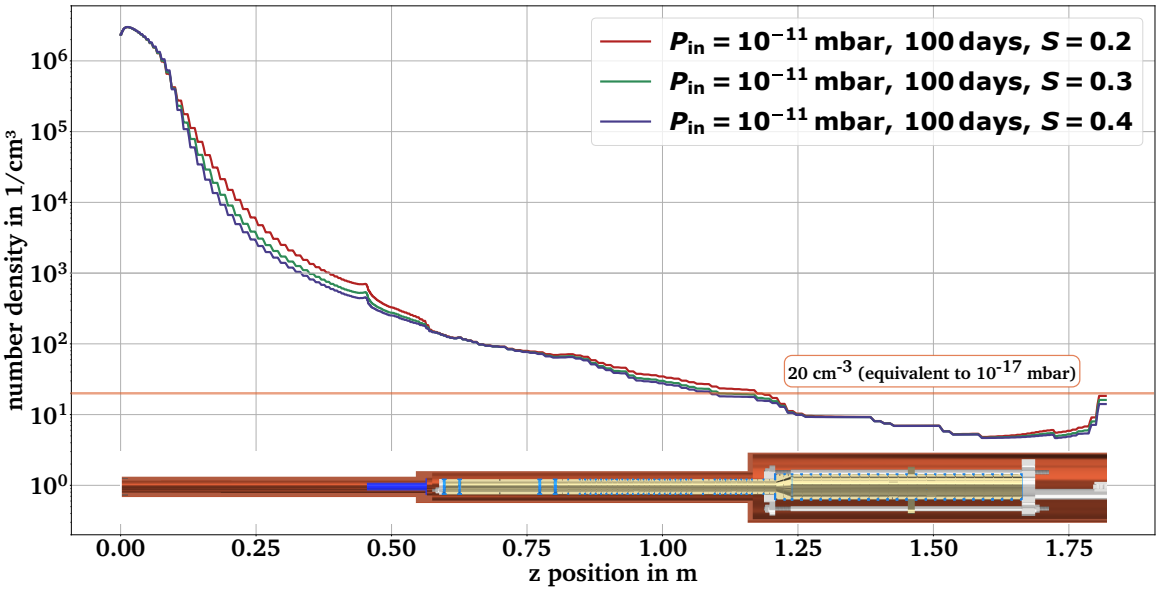

Figure 2.31.: Simulation of the on-axis residual gas density along the 4 K cryostat for varying *sticking factor of* $S = 0.2,\ 0.3,\ 0.4$.

The derived lifetime of $\tau = 301$ days is orders of magnitude higher than is room-temperature UHV setups. As a comparison, the capture rate in the PUMA antiproton beamline can be estimated by assuming a pressure of $P_{\mathrm{line}} = 10^{-10}$ mbar and a temperature of $T_{\mathrm{line}} = 300\,\mathrm{K}$ to be $\Gamma_{\mathrm{line}} = 4.64 \cdot 10^{-3}\,\mathrm{s}^{-1}$, corresponding to a storage time of $\tau_{\mathrm{line}} = 215.4\,\mathrm{s}$. In the single

passing of the antiproton bunch through the beamline, assuming an energy of $E_{\bar{\mathrm{p}}} = 4\,\mathrm{keV}$, corresponding to a velocity of $v\bar{\mathrm{p}} = 8.8 \cdot 10^5\,\mathrm{m/s}$, after deceleration and a flight path length of about $d_\mathrm{f} = 3.5\,\mathrm{m}$, the antiproton bunch spends a time $t_\mathrm{line} = 4\,\mu\mathrm{s}$ within the beamline, so that the number of the antiprotons lost by annihilations with residual gas within the beamline can be estimated to be $1 - N/N_0 = 2 \cdot 10^{-8}$.

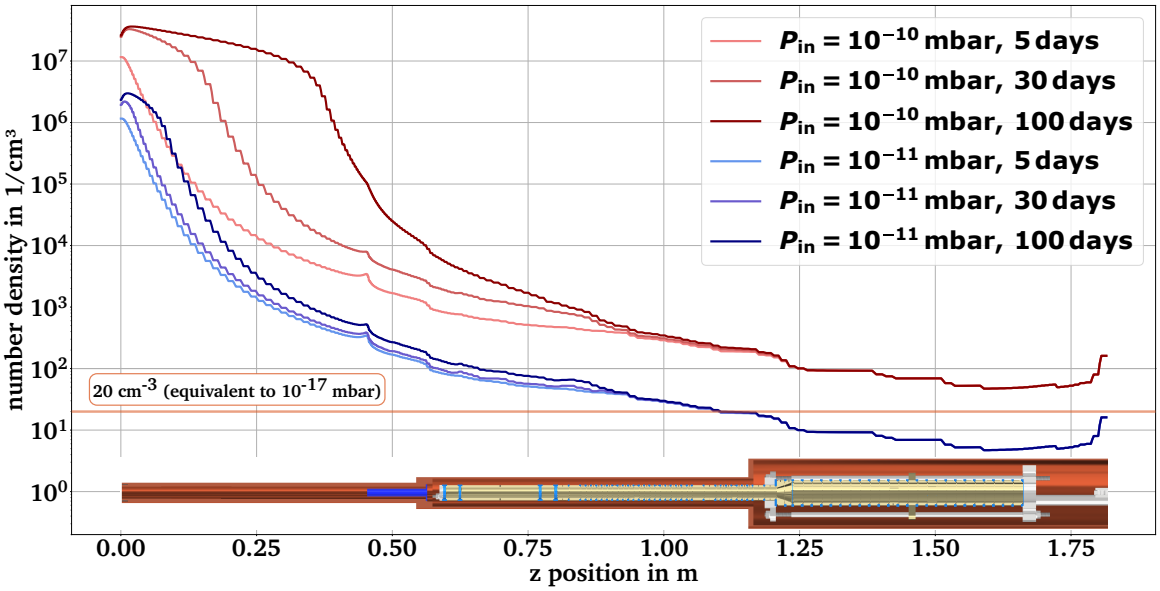

Figure 2.32.: Simulation of the time evolution of the on-axis residual gas density along the 4 K cryostat for different *input pressures* of 10^{-10} and 10^{-11} mbar.

In all presented simulations up to this point, the impact of the cylinder shutter as an aperture blocking the cryostat entrance has been neglected - both in open configuration with a bore hole diameter of 15 mm and in closed configuration - which leads to conservative results. To investigate conceptually the impact of the cylinder shutter on the number density profile in closed configuration, an additional simulation has been performed where the shutter is mimicked by an on-axis aperture blocking 95 % of the opening area of the cryostat. By this, the residual gas molecules only have peripheral access into the cryostat, which limits the open solid angle for transmission into the trap region.

This blocking significantly reduces the residual gas number density over the full length of the cryostat by more than one order of magnitude, so that densities below $20\,\mathrm{cm}^{-3}$ can now be reached over the entire trap tower (see Fig. 2.33). This is effectively caused by preventing the beaming of gas molecules into the trap volume. While the improvement is most pronounced on the extremities with a number density ratio in the order of 50, the improvement over the collision trap only improve by a factor of about 10 due to the open solid angle, so that pressures just below 10^{-19} mbar are reached. In contrast, densities in the order of 10^{-19} mbar are now reached in the storage trap, which would lead to an effective storage time of about 25,000 days, corresponding to about 70 years, following Eq. 2.16. Due to this major improvement in the achievable number density within the cryostat, the cylinder shutter is installed right in front of the cryostat entrance.

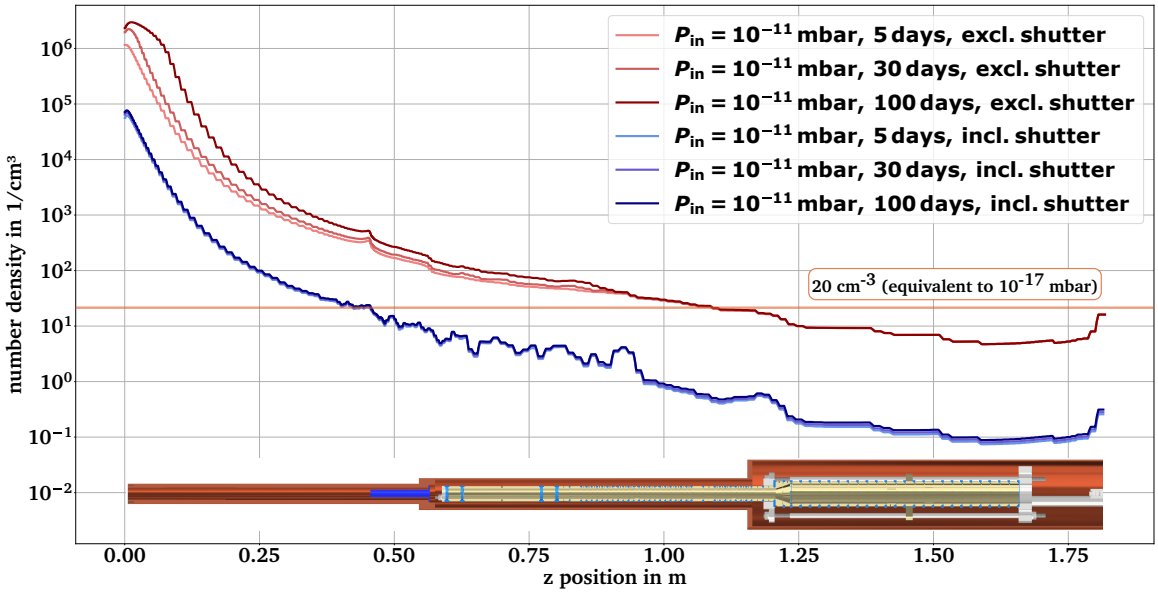

Figure 2.33.: Simulation of the time evolution of the on-axis residual gas density along the 4 K cryostat for an input pressure 10^{-11} mbar including and excluding an *aperture blocking* by the cylinder shutter.

Finally, the effect of a carbon coating on the number density is considered. As discussed in the introduction of the cryopumping mechanisms at the start of the section, the significantly more relevant cryosorption is limited by the available surface area, before a monolayer coverage is reached. This surface can be increased drastically with respect to a flat and polished copper surfaces by applying a carbon coating in the form of a porous, sponge-like layer [184]. However, this increase in surface is in first order only relevant if the coverage of the surfaces approaches the monolayer coverage, so that the equilibrium pressure increases drastically, as indicated by the isotherms depicted in Fig. 2.26. In case of the presented simulations, a significant deterioration of the number density is only observed for the open cryostat and an input pressure of 10^{-10} mbar, while the on-axis number density only increases mildly for the lower input pressure. Thus, to investigate the effect of the carbon coating, the following simulations were performed for an input pressure of 10^{-10} mbar.

As shown in Fig. 2.34, the effect of the coating becomes more prevalent the longer time intervals are considered for the simulation. The overall improvement in pressure over the considered time interval is smaller than a factor of 2 for the additional coating, but is expected to improve if time interval well beyond 100 days are considered. As it is expected that the PUMA cryostat remains sealed during experimental operation as long as no maintenance is required, the longevity of the XHV is an essential premise. Consequently, the entrance tube of the cryostat chamber will be coated with carbon to provide a long-term stability of the setup.

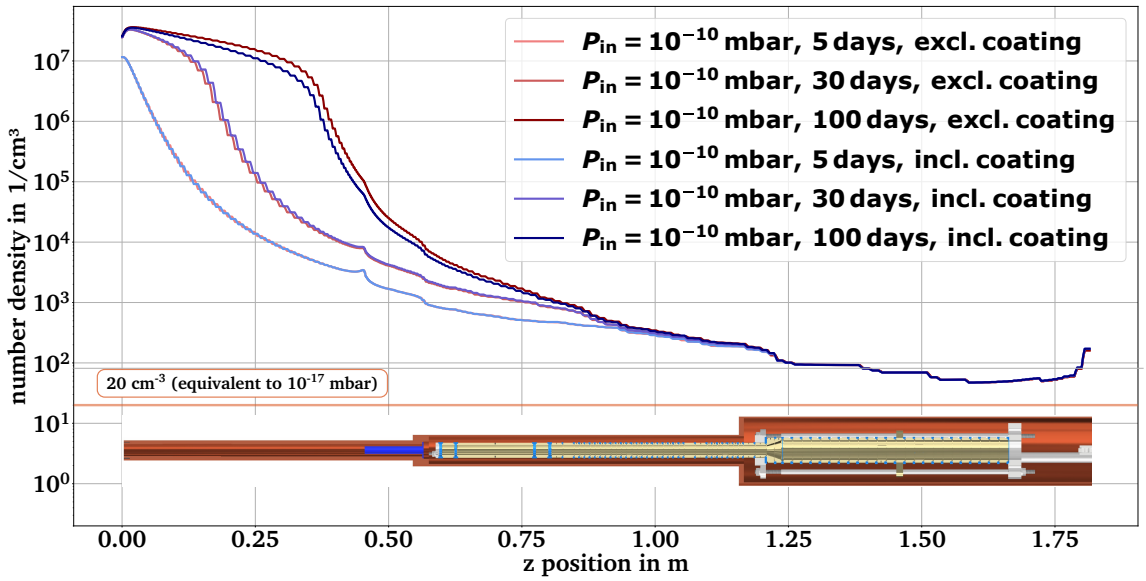

Figure 2.34.: Simulation of the time evolution of the on-axis residual gas density along the 4 K cryostat for an input pressure 10^{-10} mbar including and excluding a *carbon coating* on the inner surface of the entrance tube of the cryostat.

2.6. Mechanical assembly

Following the description of the cryostat and vacuum setup and its components in Sec. 2.2, the mechanical assembly process of the system is documented in this section. Due to the three-staged structure of the setup, the mounting is performed from the inside, *i.e.*, the Penning trap tower and the 4 K cryostat, to the outside vacuum chamber. The full assembly was performed based on the following steps:

1. **Assembly of the rotating wall electrodes:** The first step is the assembly of the azimuthally segmented rotating wall electrodes. The segments are placed on one sapphire insulator ring, kept in place by an additional support cylinder in the center to avoid a collapse.

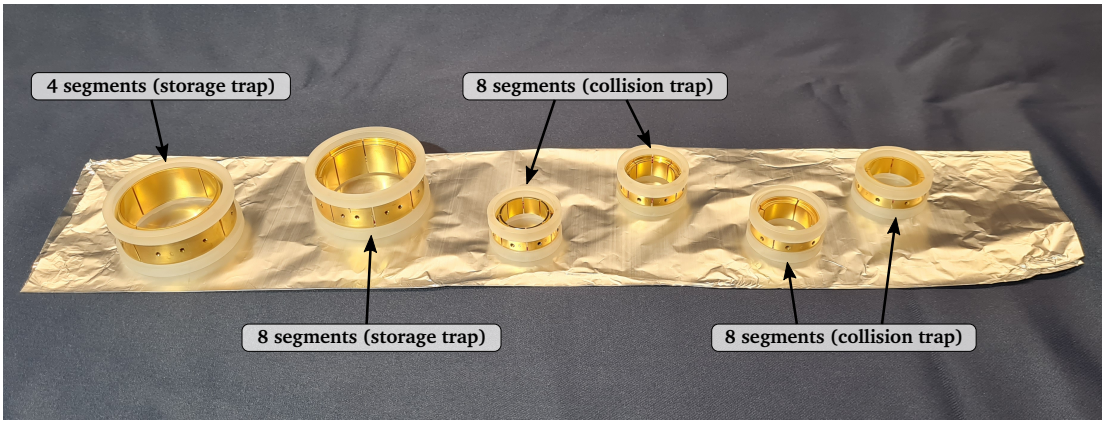

Figure 2.35.: Photograph of the assembled rotating wall electrodes for the Penning trap tower.

In the next step, sapphire (or equivalently ruby) spheres are placed in the axial grooves to electrically insulate the segments and fix their position with respect to the base sapphire ring. Finally, the second sapphire ring is placed on the top to fix the assembly and all segments are checked crosswise with an insulation tester up to 500 V. The six assembled rotating wall electrodes for the collision trap (x 4) and the storage trap (x 2) are depicted in Fig. 2.35.

2. **Assembly of the storage trap:** The following step is the assembly of the storage trap tower within its aluminum support frame. For that, the aluminum support rods are mounted onto the downstream base plate, and a first sapphire insulator ring is placed in the groove of the base plate. Then, ten full electrodes and sapphire rings are mounted, followed by the four-fold segmented RW electrode and another full electrode. Then, the plated aluminum support ring is attached onto the three support bars and pushed onto the last ring electrode, followed by another ring electrode and the eight-fold segmented RW electrode. For the potential shaping, another nine full ring electrodes follow, and the stack is completed by the two conical transition electrodes. The storage trap stack is then fixed longitudinally by the central aluminum base plate. The assembled storage trap is depicted in Fig. 2.36.

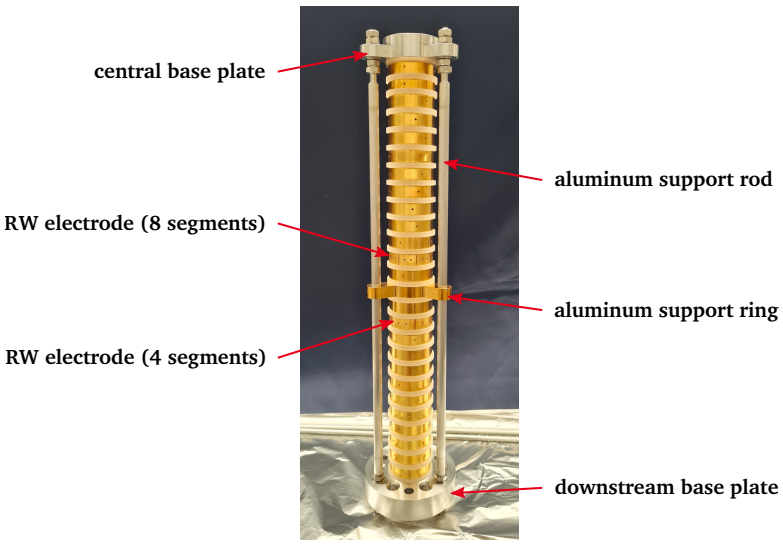

Figure 2.36.: Photograph of the assembled storage trap tower.

3. **Assembly of the full trap:** Following the fixation of the storage trap tower with the central aluminum support plate, the collision trap support bars are screwed into the plate. Then two longer transition electrodes are mounted on the last conical transition electrode, followed by the antiproton preparation section, composed by three short ring electrodes, one eight-fold segmented RW electrode and another three ring electrodes. Another transition electrode is added, before the first collision trap aluminum support ring is installed. Then, the collision section is mounted (6 x ring electrodes, 1 x four segment RW electrode, 3 x ring electrodes, 1 x eight segment RW electrode, 3 x ring electrodes, 1 x four segment RW electrode, 6 x ring electrodes). At the end of the stack, another support ring is installed and a short electrode is added as a distance piece towards the pulsed drift tube stack. It is composed by two grounded front and rear electrodes, two long insulator rings for the HV insulation and the 146 mm long PDT electrode. The full collision trap tower is then closed off with the upstream base plate, which is tightened to axially fix the trap. Finally, the support pins for the upstream weight support are screwed into the aluminum bars to complete the Penning trap tower (see Fig. 2.37).

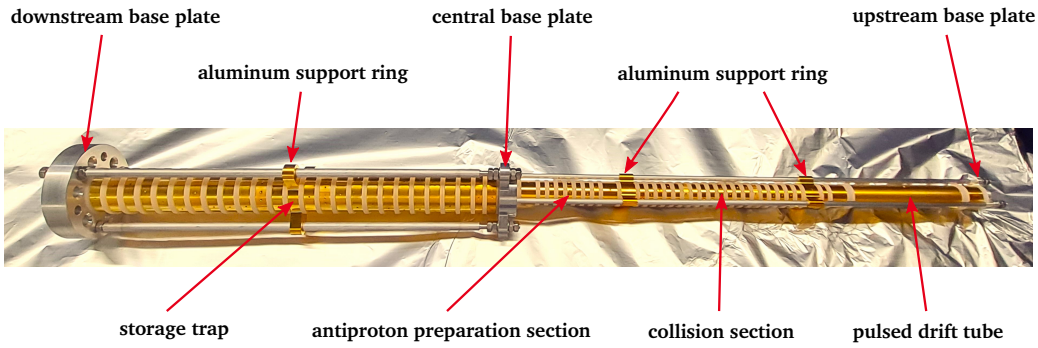

Figure 2.37.: Photograph of the full Penning trap tower.

4. **Insertion of the trap tower in the 4 K copper chamber:** After the assembly of the full trap system, it is mounted on its copper feedthrough flange with three 20 mm diameter aluminum support bars (M10 outer threads) and tightened by two M10 nuts two prevent a loosening of the threaded connection through vibrations. To simplify the following attachment of the surrounding 4 K copper chamber, this mounting is performed vertically (see Fig. 2.38). A set of six screws were arranged in the through-holes of the feedthrough flange for fixing the chamber onto the feedthrough flange before the assembly is again brought in horizontal orientation. To protect the electrical feedthrough pins from damage the feedthrough flange was raised by three sets of aluminum plates.

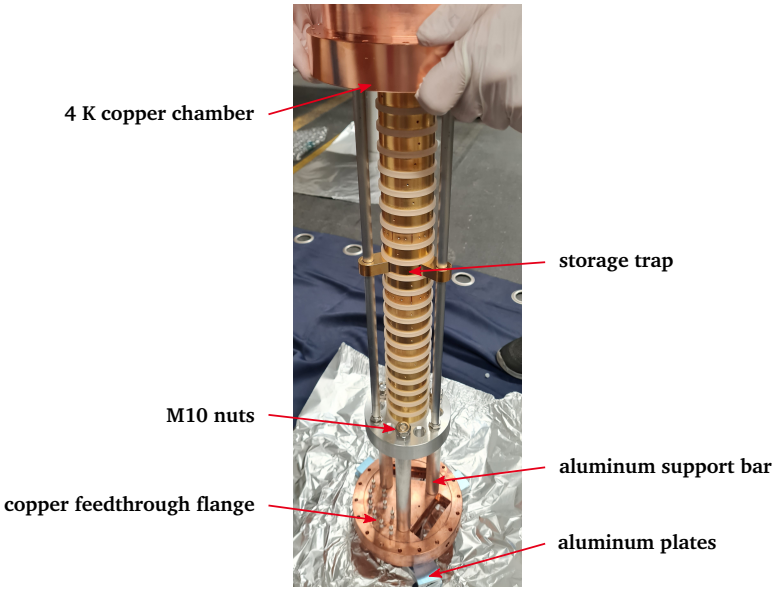

Figure 2.38.: Photograph of the vertical mounting of the 4 K trap chamber. The feedthrough flange on the bottom is raised from the ground to protect the electrical feedthrough pins insulated by ceramics.

5. **Assembly of the full 4 K stage:** After the trap setup is inserted into the 4 K chamber, the remaining copper components can be attached. On the upstream end, the cryostat entrance tube and the conductance barrier are attached. On the downstream end on the other side, the thermal connection bar is screwed into the feedthrough flange. The connection pieces towards the coldheads will be added at a later stage. The full 4 K setup is depicted in Fig. 2.39.

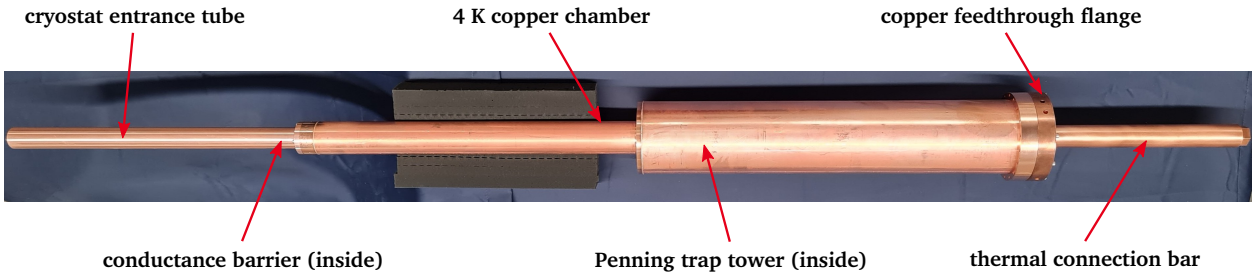

Figure 2.39.: Photograph of the full 4 K setup, excluding the coldhead connection pieces.

6. **Assembly of the ball transfer units and installation in the 50 K tube:** To prepare the insertion of the 4 K stage into the 50 K aluminum chamber, the ball transfer units (BTUs) for the weight support have to be assembled first. For that, the BTU base pieces are filled with small diameter zirconium oxide spheres of 2 mm diameter, and the different larger diameter spheres are inserted on top and fixed by the respective top plates. After their assembly, they are screwed onto the inner surface of the 50 K aluminum chamber. Here, the BTUs are pushed into position with a long thin metal rod, until the screws can be attached from the outer surface. Figure 2.40 shows a photograph of the 50 K chamber with the attached BTUs.

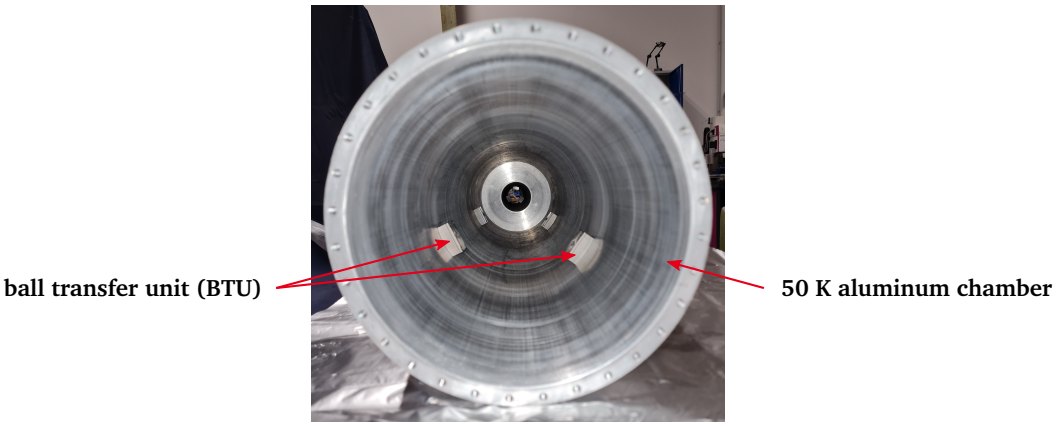

Figure 2.40.: Photograph of the 50 K aluminum chamber with the installed ball transfer units.

7. **Insertion of the 4 K stage into the 50 K stage:** After installation of the BTUs in the aluminum tube, the 4 K stage is inserted into the tube and placed onto the BTUs. After the 4 K stage is pushed in the proper position, the 50 K feedthrough flange and the downstream aluminum tube (including its three BTUs) are attached, so that the 4 K stage rests on all foreseen BTUs. Due to the tight tolerances, the relative position of the two stages is well constrained - even in longitudinal direction. A picture of the 50 K chamber with the inserted 4 K stage is depicted in Fig. 2.41.

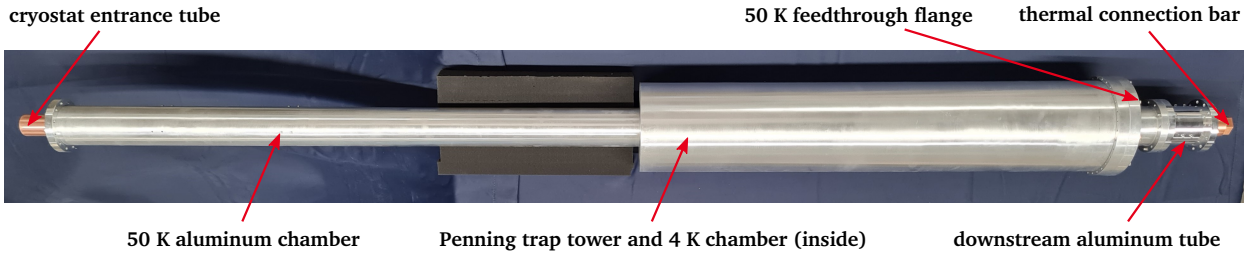

Figure 2.41.: Photograph of the 50 K chamber with the inserted 4 K setup.

8. **Insertion of the cold stages into the main vacuum chamber:** To finalize the assembly of the components that are inserted in the bore of the PUMA solenoid, the two cold stages have to be inserted into the main vacuum chamber. For this, the removable

flange of the aluminum chamber has to be removed first, as the inner diameter of the vacuum chamber is too small. Instead, it has to be attached only after the cold stages are placed inside the vacuum chamber. For the first mechanical assembly presented here, the PUMA solenoid is not included. Instead, the vacuum chamber is fixed between the two lateral CF200 cubes, which are placed on tables for the mounting procedure. Figure 2.42 depicts the view at the upstream and downstream end of the inserted tubes after the insertion into the vacuum chamber.

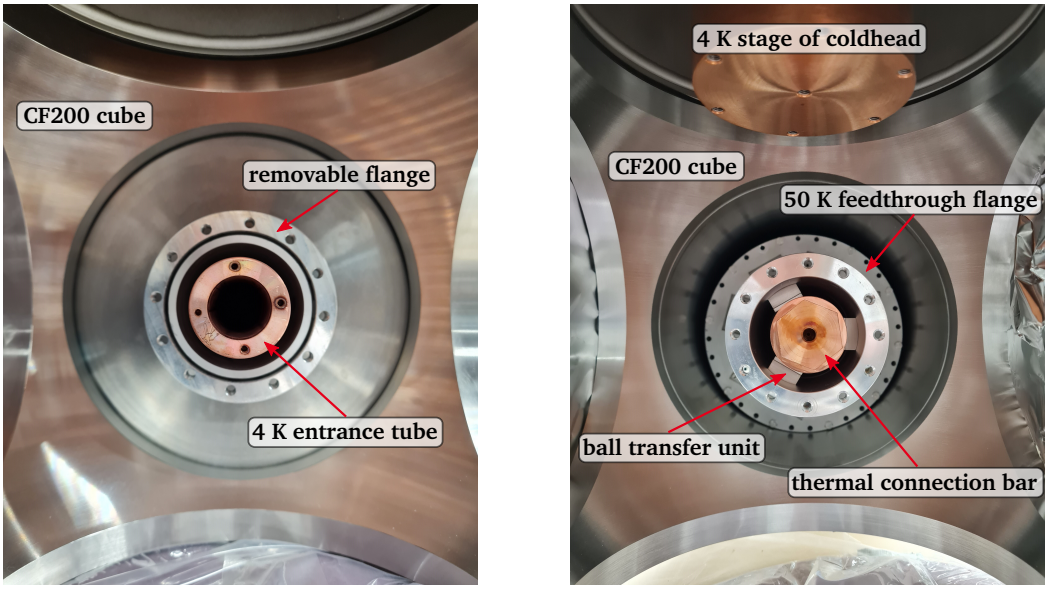

Figure 2.42.: Photograph of the upstream (*left*) and downstream (*right*) view of the layered temperature stages in the vacuum chamber. In case of the downstream end, the 4 K stage of the coldhead is added for orientation.

9. **Assembly of the cryostat alignment system:** To lift the cryogenic stages from the vacuum chamber and provide alignment with the magnetic field lines, the lateral alignment chambers are assembled separately. In case of the downstream chamber, a heavy-load linear feedthrough and a medium-load linear feedthrough are mounted on opposite ports for the vertical positioning, while the horizontal ports are closed off with blind flanges. The suspension pieces for the aramide cords are mounted both on the feedthroughs and the 50 K aluminum chamber, and then then cords are installed and the aluminum chamber is aligned in the center of the vacuum chamber. In case of the upstream chamber, all four linear feedthroughs are mounted and the einzel lens is assembled on its aluminum base flange. Following the installation of the G10 thermal connection ring in the vacuum chamber, the aluminum chamber is inserted and mounted as well as aligned with the aramide cords. Figure 2.43 shows the upstream alignment chamber including all four linear feedthroughs for weight support (top port) and alignment (horizontal and bottom port).

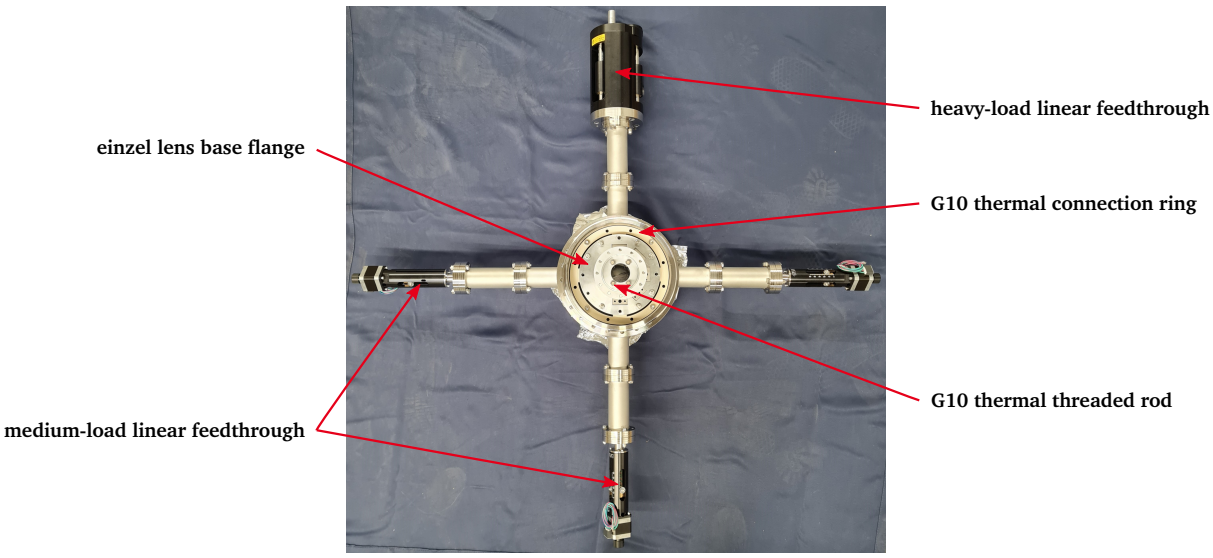

Figure 2.43.: Photograph of the upstream cryostat alignment chamber. The heavy-load feedthrough is mounted on the top port, while the remaining three feedthroughs are used for the precision alignment.

10. **Installation of the 50 K cubes:** Before the alignment systems are mounted onto the CF200 cubes, the 50 K aluminum cubes, which mark the intersection between the main chamber, the coldheads and the alignment chambers, are inserted into the CF200 cubes through the open on-axis ports of the CF200 cubes and screwed onto the main aluminum chamber. A view through the top port of the cube downstream CF200 cube is depicted in Fig. 2.44.

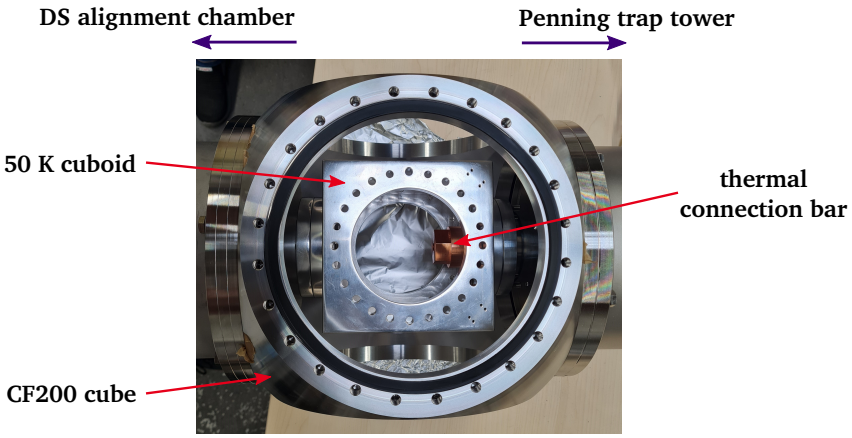

Figure 2.44.: Photograph of the downstream CF200 cube through the top port.

11. **Mounting of the downstream cold head and alignment system:** For the mounting of the downstream alignment chamber, the respective coldhead assembly was installed on the top port. To free the access through the bottom port of the CF200 cube, the setup was lifted by crane via two threaded holes on the coldhead and the alignment chamber was screwed onto downstream port of the cube. After fixing the connection

between the vacuum chamber, the aluminum chamber and cube were attached by tightening the screws through the bottom opening of the aluminum cube. After the connection is tightened, the aluminum cryochamber is lifted with the heavy-load linear feedthrough. Figure 2.45 depicts the craned downstream end of the cryostat after installation of the alignment chamber. Subsequently, the coldhead is dismounted, the chicane pieces towards the coldhead are installed and the coldhead is mounted again on the top port of the cube.

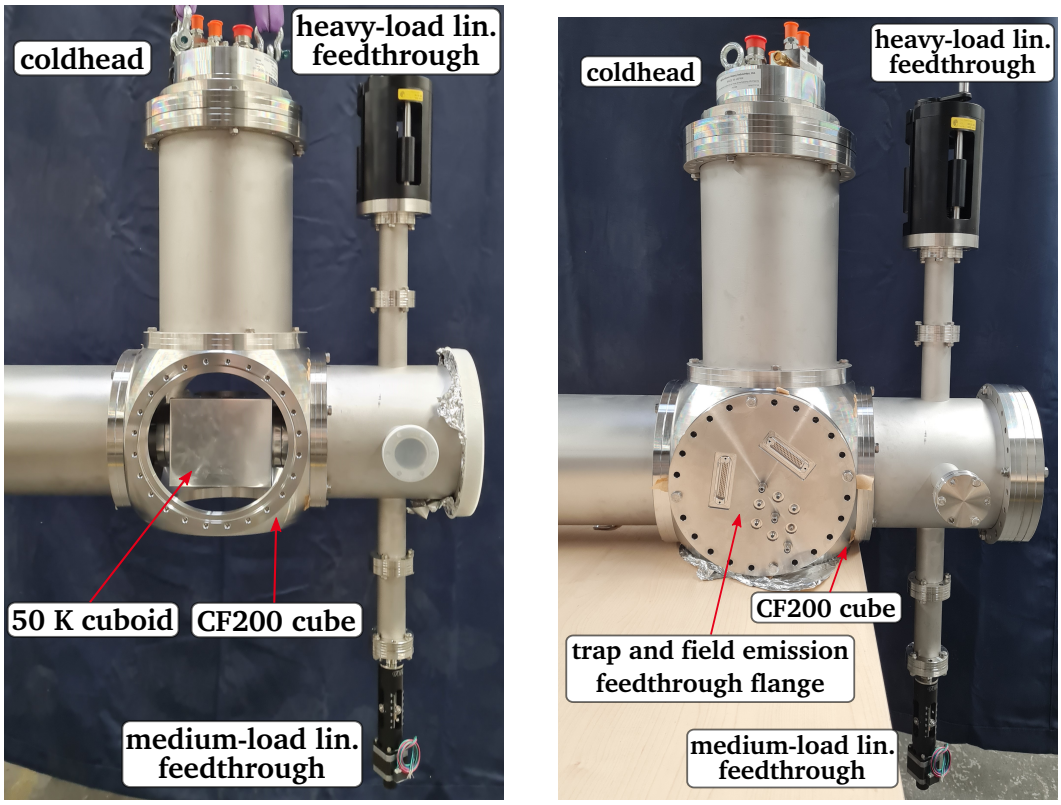

Figure 2.45.: Photograph of the downstream end of the cryostat assembly, including the installed alignment chamber and the coldhead assembly (*left*) and the additional horizontal feedthrough and blind flanges (*right*).

12. **Installation of the horizontal CF flanges on the downstream cube:** On the horizontal ports of the downstream CF200 cube, the electrical feedthrough flange for the trap electrodes and the field emission electron sources and a CF200 blind flange are attached. The remaining open ports of the downstream alignment chamber are also closed off with blind flanges. The resulting assembly is depicted in Fig. 2.45.

13. **Mounting of the upstream cold head and alignment system:** Similarly to the downstream end of the system, the respective coldhead and the alignment chamber are mounted on the upstream CF200 cube. For that, both pieces were mounted separately and craned into position for tightening the screwed connection. After connecting the stainless-steel vacuum chambers, the upstream aluminum chamber and the 50 K aluminum cube have to be connected. For that, the cube and the connected Al trap chamber were slightly lifted through the horizontal open ports of the cube. After

tightening the connection, the trap chamber is aligned with the linear feedthroughs and lifted up from the vacuum chamber. To check that all three stages are electrically and thermally insulated, the resistance between each stage is determined with a Fluke isolation tester at up to 500 V, which indicated no electrical and thus also thermal connection between all stages. The resulting assembly at the upstream cube is depicted in Fig. 2.46.

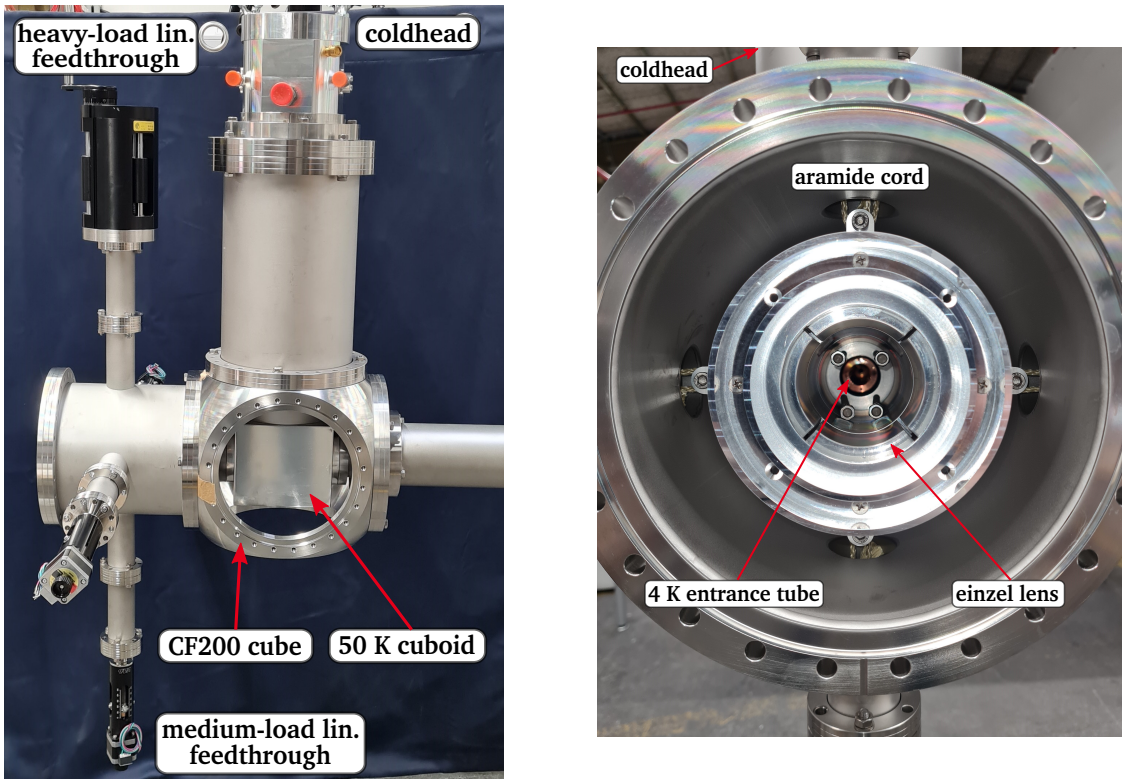

Figure 2.46.: Photograph of the upstream CF200 cube and the mounted alignment chamber and coldhead assembly (*left*) and on-axis view through the upstream end of the assembly (*right*).

14. **Installation of the horizontal CF flanges on the upstream cube:** Following the alignment of the 50 K stage, the horizontal ports of the cube and the front port of the alignment chamber can be installed. On the latter, the CF200 to CF63 reducer is attached, which will connect the setup to the antiproton beamline. The horizontal ports of the cube are closed off with the einzel lens feedthrough flange and a blind flange. The latter replaces the NEG cartridge, which is not installed for the mechanical test assembly to prevent damage. The assembly including the added flanges and reducer are depicted in Fig. 2.47. This marks the final step for the successful mechanical test assembly of the cryostat setup, which is shown in Fig. 2.48.

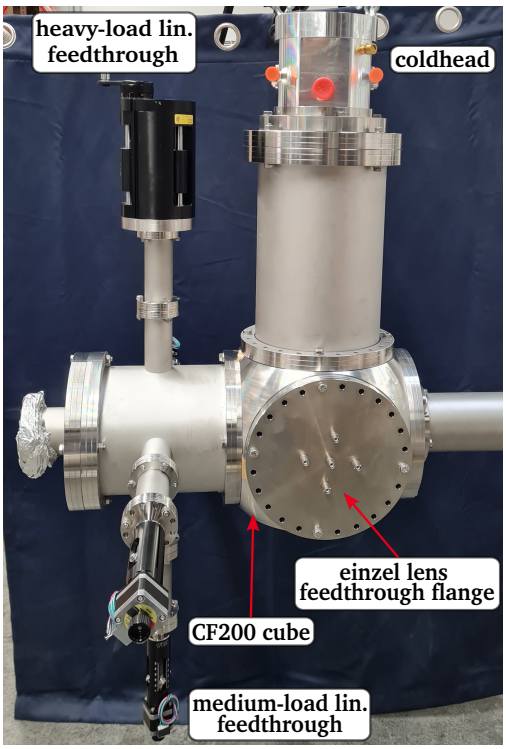

Figure 2.47.: Photograph of the upstream end of the cryostat assembly after installation of the CF flanges.

15. **Installation of the cylinder shutter and the angle valve on the bottom ports of the CF cubes:** The final assembly of the cryostat setup would also require the mounting of the cylinder shutter, its xyz-precision table and its rotary feedthrough on the bottom port of the upstream CF200 cube as well as the mounting of the angle valve for the pump-down on the bottom port of the downstream CF200 cube. As soon as the dedicated support system is finalized and assembled, these remaining components will be added.

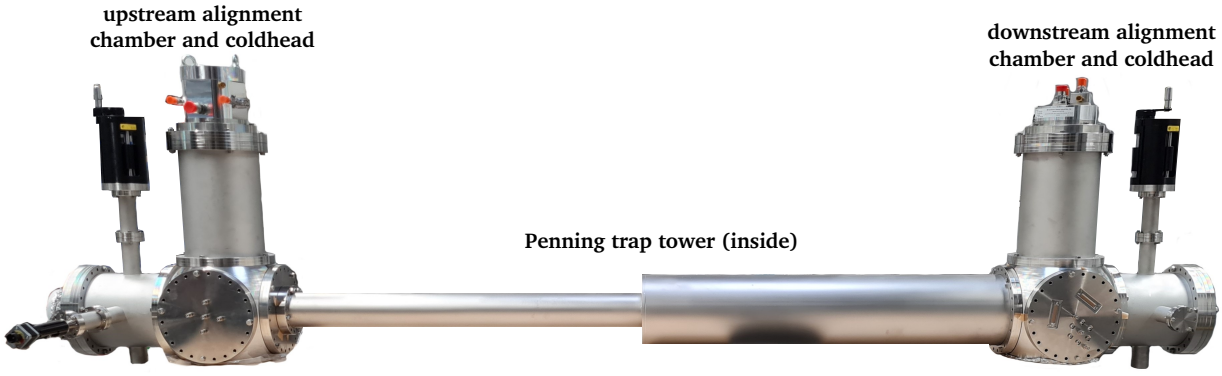

Figure 2.48.: Photograph of the fully assembled cryostat, excluding the bottom ports of the CF200 cubes.

2.7. Trap operation scheme

After introducing the trap and cryostat setup, supported by simulations, and performing the first assembly of the system, the foreseen operation scheme for the trap is sketched in the following. A particular focus is set on the antiproton accumulation in the storage trap, see Sec. 2.7.1, and the mixing of the antiprotons with ions in the collision trap, see Sec. 2.7.2.

2.7.1. Antiproton accumulation in the storage trap

Prior to the formation of antiprotonic atoms by overlapping ions and antiprotons in the collision trap, a reservoir of up to 10^9 antiprotons is accumulated in the storage trap of PUMA. This reservoir is particularly relevant for the experiments performed with short-lived ions at ISOLDE. Assuming the transmission of up to 10^7 antiprotons per bunch coming from the ELENA ring, at least 100 bunches have to be stacked consecutively.

This accumulation of antiprotons by stacking of subsequent bunches requires a dedicated iterative scheme. As the antiprotons enter the storage trap with a kinetic energy of about 200 eV and an energy standard deviation of 100 eV, a buffer of cold particles is required for the initial deceleration and cooling process. In case of the first trapped bunch, this buffer is provided in the form of about 10^8 to 10^9 electrons, which are emitted by the field emission sources and cooled to ambient temperature via the emission of cyclotron radiation. For the following bunches, the mix of the already trapped and cooled antiprotons as well as the electrons acts as buffer. This continuous change of the buffer also affects the cooling time constant for each bunch, which should decrease with increasing number of cold stored antiprotons.

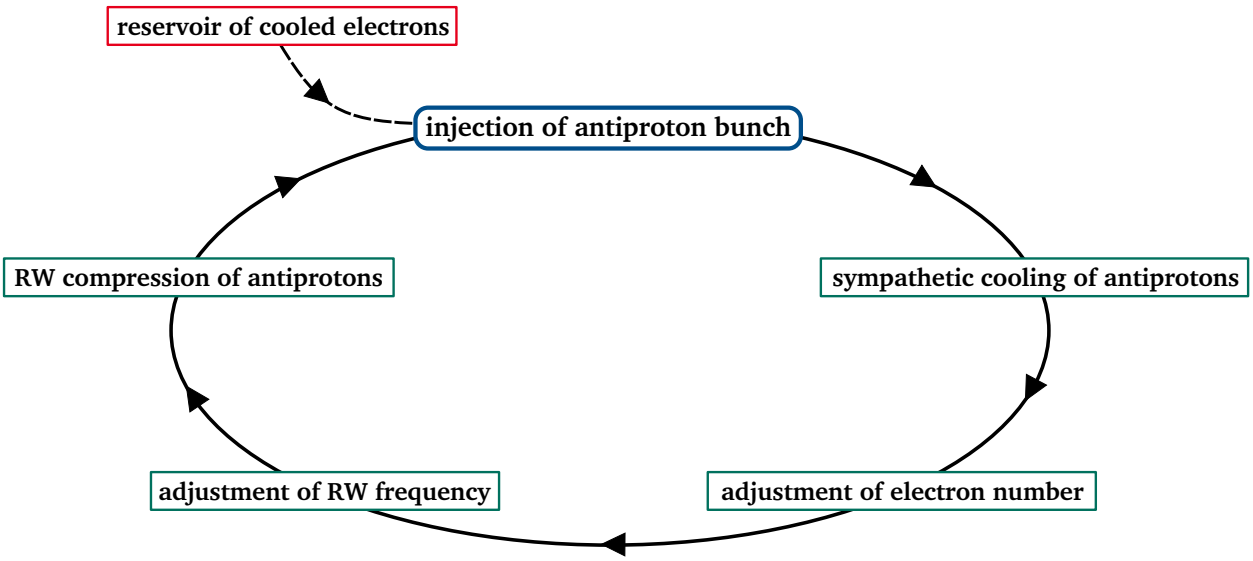

Figure 2.49.: Flow diagram of the workflow during the antiproton accumulation at the Antimatter Factory.

To account for the increased number of antiprotons after the capture of each bunch, several trap parameters have to adjusted. One the one hand, the number of co-trapped electrons has to be increased to provide sufficient cooling power to keep a low equilibrium temperature. On the other hand, the rotating wall frequency and amplitude have to be adjusted to keep radial control over the stored ensemble. A sketch of the full workflow during the antiproton accumulation is depicted in Fig. 2.49. The exact values for the electron number increase and the RW parameter adjustments will be determined during the setup commissioning at the Antimatter Factory.

2.7.2. Antiproton and ion mixing in the collision trap

Following the accumulation and cooling in the storage trap, the formation of antiprotonic atoms in the collision trap can be initiated. This formation process is based on the following steps, which are sketched in Fig. 2.50:

(a) Transfer and capture of $\bar{\mathrm{p}}$: About 10^7 antiprotons from the storage trap are transferred to the antiproton preparation region via ramping of the upstream potential well. Based on the axial bounce frequency f_z of the stored antiproton plasma, the fraction N/N_tot of extracted antiprotons can be chosen by choosing a pulse length t_0 with $t_0 f_\mathrm{z} = N/N_\mathrm{tot}$. Due to the higher bounce frequency of the electrons, almost all electrons will also be removed from the storage trap. This has to be compensated by refilling electrons with the cold field emission point.

(b) Capture and cooling of $\bar{\mathrm{p}}$: After transferring the antiprotons to the preparation region they are cooled by the extracted electrons and compressed by the RW field. A higher density and smaller radius of antiprotons is favored as it increases the production rate of antiprotonic atoms, if the spatial overlap with the ions remains the same. After preparation, the cold antiprotons and electrons are transferred to the collision region and temporarily stored in the downstream end.

(c) Capture of positive ions: Following the deceleration to trapping energies, a bunch of up to about 10^5 ions is captured in the upstream end of the collision region. For this antiproton and ion number, the expected rate of antiprotonic atom formation can be estimated with the capture cross section (compare Eq. 2.13) to be at about 1 kHz. The ion capture process does not induce heating to the antiprotons, as there is no spatial overlap yet.

(d) Transfer of $\bar{\mathrm{p}}$ and ions: To initialize the overlap, both species are then guided towards the center of the collision region by adjusting the potentials on the electrodes.

(e) Overlapping of $\bar{\mathrm{p}}$ and ions: Both species now overlap, and the ions are adiabatically cooled by the antiprotons and electrons. This increases the antiproton temperature, so that they might overcome the shallow confining potential well. While the electron cooling reduces the temperature of both species, the lower ion temperature also induces the risk of recombination. To prevent this, the initial electrons as well as the electrons emitted during the deexcitation of the antiprotonic atoms can be dumped from the mixing region by quickly pulsing the negative potential. An exact determination of the

cooling and recombination rate has to be performed on the real setup to evaluate the need for electron extraction.

(f) RF heating of ions: If the ions are cooled efficiently, they might be lost in the negative potential wells that confine the antiprotons, leading to longitudinal separation. This could be prevented by axial RF heating. The necessity of this heating has to be evaluated during the first overlapping test with stable ions at the Antimatter Factory.

To summarize, this chapter described the cryogenic trap setup of PUMA. The mechanical composition and choice of material for all three temperature stages is motivated based on thermal and vacuum simulation, with the ultimate goal to provide an as long antiproton storage times as possible and to mix antiprotons and ions at low relative energy. Based on these simulations, a pressure of below 10^{-17} mbar can be reached over the full trap tower, if the cryostat aperture is closed off by the cylinder shutter, translating to storage times of hundreds of days. The successful test assembly of the setup is also documented, and the system will be mounted at the antiproton beamline in early 2024, so that the foreseen operation scheme of the trap can be benchmarked.

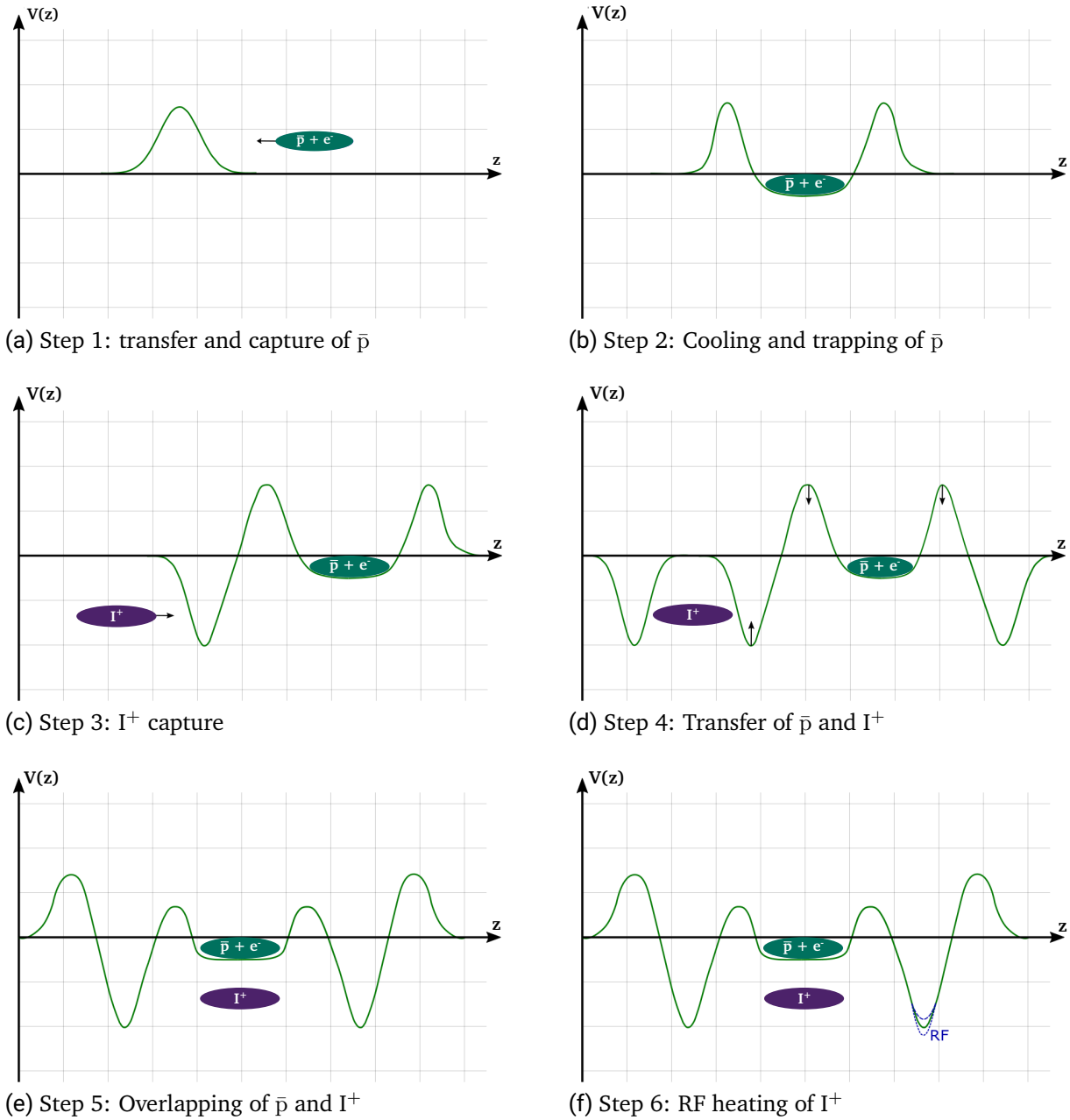

(a) Step 1: transfer and capture of $\bar{p}$

(b) Step 2: Cooling and trapping of $\bar{p}$

(c) Step 3: I^+ capture

(d) Step 4: Transfer of $\bar{p}$ and I^+

(e) Step 5: Overlapping of $\bar{p}$ and I^+

(f) Step 6: RF heating of I^+

Figure 2.50.: Overlapping scheme for positive ions (I^+) and $\bar{p}$ in the collision region of PUMA. This figure is adapted from [92] under CC BY 4.0.

3. Beam optics and antiproton transmission at ELENA

Before the antiproton bunches coming from the ELENA can be trapped and accumulated in the Penning trap assembly, they have to be guided effectively through the PUMA antiproton beamline upstream of the experimental setup to reduce losses and thus minimize the accumulation time. An additional complexity arises from the deceleration of the antiproton bunches within the pulsed drift tube, as a deceleration has strong implications on the transverse bunch profile, which ultimately may lead to significant losses of antiprotons. The ion optical simulations presented in this chapter aim at determining the ion optical properties of an antiproton bunch within the beamline of PUMA to derive the antiproton transmission into the storage trap and to define the locations along the beamline, at which antiproton losses occur. In addition, the impact of the deceleration of an antiproton bunch within the HV PDT on the bunch length and energy spread is investigated. As a benchmark, the simulations are finally compared to experimental data.

In Sec. 3.1, the production and transmission of antiprotons at the Antimatter Factory of CERN is summarized, with a special focus on the antiproton bunch properties at the end of the LNE51 beamline, which yield as input for the following simulations. Section 3.2 then presents the software used for the ion optical simulations and summarizes the implementation of the PUMA antiproton beamline and the definition of input parameter of the antiprotons for their propagation. In Sec. 3.3, the results of the simulations of the deceleration of antiprotons in the HV PDT and the transmission of antiprotons through the full beamline are presented. Finally, in Sec. 3.4, the simulation results are benchmarked with experimental data obtained during the commissioning of the HV PDT with antiprotons.

3.1. Antiproton production and optics at the Antimatter Factory

3.1.1. Antiproton production at the Antimatter Factory

At the Antimatter Factory, antiprotons are produced by impinging bunches of about $1 \cdot 10^{13}$ protons at a kinetic energy of 26 GeV from the Proton Synchrotron (PS) onto a thick Iridium target cylinder. In this process, about $4 \cdot 10^{7}$ antiprotons are produced per bunch, which translates to a rate of about 1 antiproton per 250,000 protons. The antiprotons are then separated from the other produced particles by a magnetic spectrometer, which guides the antiprotons into the Antiproton Decelerator (AD) with an initial energy of about 10 GeV. In the AD, the antiprotons are decelerated over three steps down to an energy of 5.3 MeV,

while the transverse emittance increase due to the deceleration process is compensated by stochastic [185] and electron cooling [186]. As these processes introduce non-conservative forces, they do not oblige Liouville's theorem [187] of emittance conservation under conservative forces and allow for a reduction of the phase space distribution of the antiproton bunch. An explanation of the emittance to characterize particle bunches is given in the following subsection.

Since the installation and commissioning of the Extra-Low ENergy Antiproton (ELENA) ring and the first transfer of antiprotons to experiments in 2021, the antiprotons are regularly decelerated to energies of about 100 keV [188]. Following the extraction from the AD into the ELENA ring, the antiprotons are first chopped into four bunches of up to $1 \cdot 10^7$ particles each, which then are decelerated further in a three-step process down to 100 keV, while the emittance is controlled via electron cooling. Due to the chopping, the ELENA ring can now provide four experiments in parallel with antiprotons, while previously only a single antiproton bunch was available at the AD. An overview of the Antimatter Factory with the two antiproton storage rings and the attached experiments is depicted in Fig. 3.1.

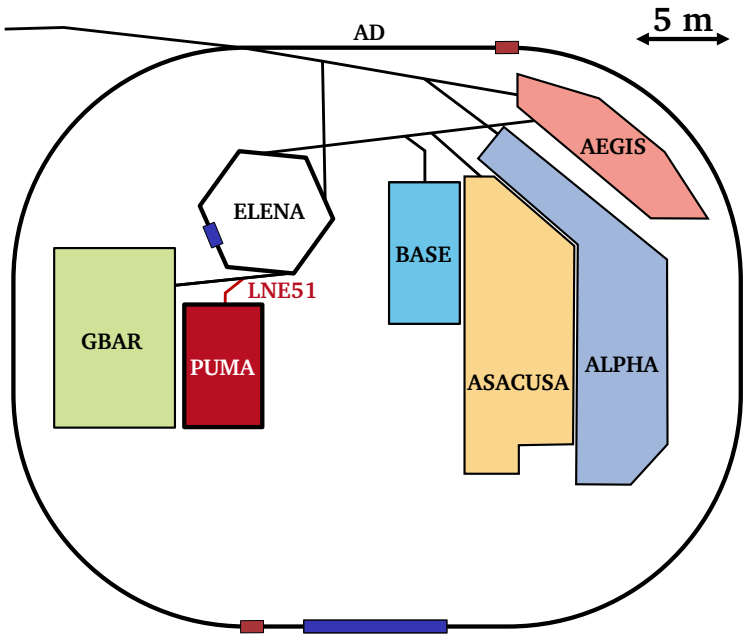

Figure 3.1.: Schematic top view of the Antimatter Factory. The experimental areas are highlighted in colored shading, with dark red shading for the PUMA experiment and the connected LNE51 transfer line. The blue blocks along both storage rings indicate electron cooling devices, while the red blocks along the AD indicate the stochastic cooling pickup and kicker.

Typically, antiprotons are delivered to the experiments every 115 to 120 seconds during normal operation. This time interval between subsequent bunches is mainly caused by the time required to decelerate and cool a produced antiproton bunch within the AD, which typically takes about 100 seconds, while the second stage of the deceleration in the ELENA ring takes about 10 to 15 seconds. Based on the repetition rate and antiproton number per

bunch, up to about $3 \cdot 10^8$ antiprotons can be delivered to an experiment within an hour. In an optimal case, this would allow the accumulation of an antiproton reservoir of 10^9 particles within less than 3.5 h, but losses of antiprotons during the transport into the PUMA prolong this accumulation time.

One of the main sources of losses between the ELENA ring and the connected experiments is an additional deceleration step for the antiprotons from 100 keV to energies below a few keV. This step is required to be able to capture the antiprotons in a trap setup for further studies. Prior to the installation of the ELENA ring, the deceleration of antiprotons from 5.3 MeV to about 5 keV was performed by a degrader foil or atomic collisions in gas cells, which led to antiproton losses in the order of 95 % to 99.9 % due to range-straggling effects [189–191]. Based on the lower final energy in ELENA, the losses in degrader foils were reduced significantly, so that nowadays transmission rates in the order of 50 % can be achieved [192]. In addition, electrostatic deceleration schemes were developed, which make use of a pulsed drift tube [193, 194]. As the deceleration in a PDT does not require interaction with matter, a transmission of up to 100 % can be reached in principle.

The emittance increase induced by this deceleration cannot be directly compensated by a cooling mechanism as in the case of the storage rings. For experiments with a degrader foil, which is typically placed closed to the trap setup and within a magnetic field, this emittance increase is negligible due to the strong focusing of the Lorentz force. In case of the pulsed drift tube setup at PUMA however, the following rest of the antiproton beamline has to account for the increase of emittance.

3.1.2. Antiproton optics in ELENA and the LNE51 transfer line

The emittance is a quantity commonly used in accelerator physics to characterize the distribution of charged particle bunches relative to an ideal particle, which follows a pre-defined reference orbit, characterized by the three coordinates (x_0, y_0, s_0), with s_0 being the longitudinal component along the reference orbit. The radial offset of an individual particle of the bunch relative to the ideal particle is characterized by the transverse offsets (x, y) and the angles (x' and y'), which are typically calculated by the ratio of the transverse velocities $v_{x,y}$ and the velocity component along the flight path v_s. In longitudinal direction, the offset is often defined via the kinetic energy T and the longitudinal offset Δs or energy difference ΔT.

By summarizing the properties of each particle relative to the ideal particle in the three phase space planes x-x', y-y' and T-ΔT, the emittance ϵ along the three spatial coordinates is defined by the surface area of the phase space ellipse. Depending on the convention, the area typically comprises about 40 % of all particles, corresponding to the 1σ-interval of 2D Gaussian distribution, or about 87 % of all particles for the 2σ-interval.

In case of the ELENA ring, nominal transverse 2σ-emittances of $\epsilon_{x,y} = 4\,\pi$ mm mrad for the horizontal plane x and the vertical plane y were foreseen during the planning of the machine [195], while $\epsilon_x = 6\,\pi$ mm mrad and $\epsilon_y = 4\,\pi$ mm mrad are regularly achieved during operation [196]. In longitudinal direction, a 1σ bunch length of 75 ns and a 1σ energy spread of 100 eV were observed in accordance with the nominal values. These emittances

and bunch properties are also valid along the LNE51 transfer line and are thus assumed as input for the ion optical simulations presented below.

While the surface area of the transverse phase space distribution is known in form of the emittances, the exact shape of the bunch along the transfer line and in particular at the end of the transfer line, *i.e.*, at the so-called optical handover point (HOP), has to be tuned by preceding ion optical simulations. These simulations were performed with the software MAD-X by Y. Dutheil from the CERN ion optical department. In MAD-X the antiproton bunch is characterized the emittances ϵ and the Twiss parameters α, β, γ, which characterize the orientation of the phase space ellipse, as indicated in Fig. 3.2. The Twiss parameters and the emittance are connected via the equation

$$\epsilon = \gamma x^2 + 2\alpha x x' + \beta x'^2. \tag{3.1}$$

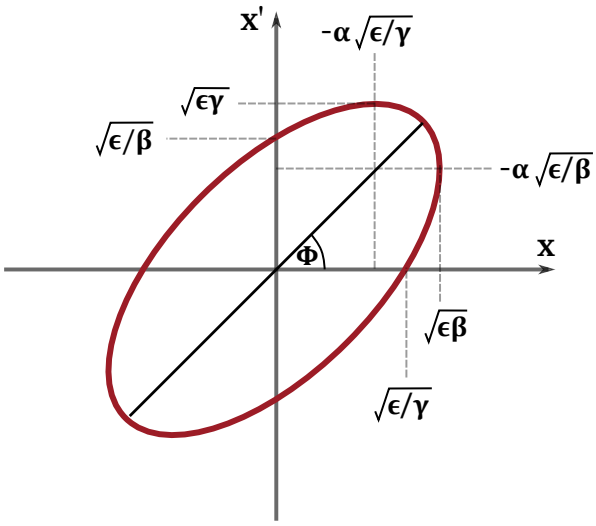

Figure 3.2.: Depiction of a phase space ellipsis of emittance ϵ and the Twiss parameters α, β, γ.

For ion optical simulations in MAD-X it is common to characterize the beam shape along the flight path via the propagation of the Twiss parameters, which can be translated to spatial and angular coordinates following the relations depicted in Fig. 3.2. Including the translation to spatial coordinates, the transverse antiproton bunch profile starting from the extraction from ELENA up to the optical HOP of PUMA has been simulated, and the results are depicted in Fig. 3.3.

At the end of the beamline, the antiproton bunch is focused towards the optical HOP to reach a horizontal bunch width of $\sigma_x \sim 2\,\text{mm}$ and a vertical bunch width of $\sigma_y \sim 1\,\text{mm}$. During discussions it was decided that the bunch should have an upright shape at the optical HOP, characterized by the Twiss parameter $\alpha = 0$, so that the dispersion angles for both planes can be directly calculated with the known emittances to be $\sigma_{x'} = 0.75\,\text{mrad}$ and $\sigma_{y'} = 1\,\text{mrad}$. These four standard deviations will finally be implemented as input for the transverse profile for the following simulations.

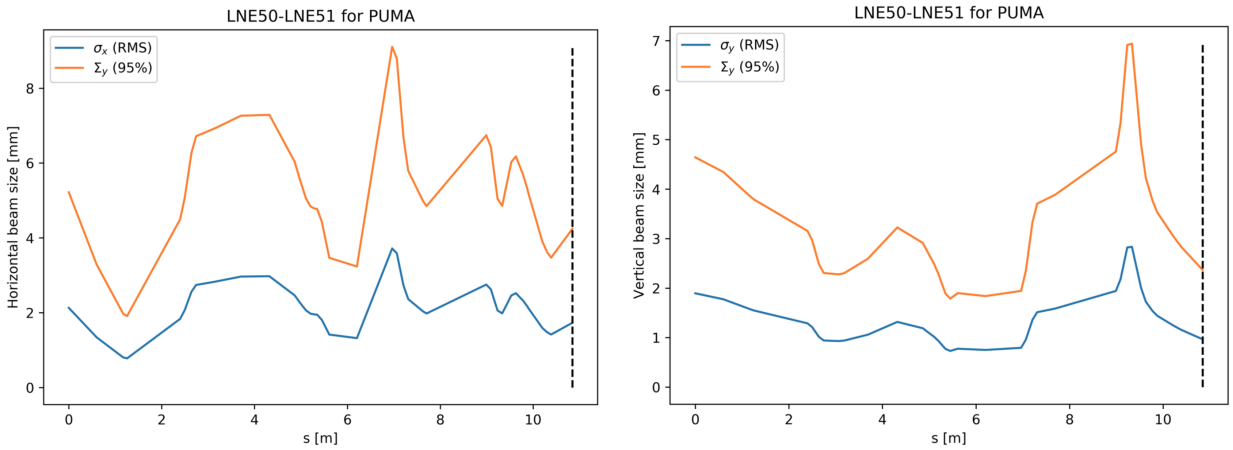

Figure 3.3.: Simulated transverse profile of an antiproton bunch between the extraction from ELENA and the optical HOP of PUMA. The left plot depicts the horizontal profile and the right plot the vertical profile. The figure is reprinted from [92] under CC BY 4.0.

3.2. Implementation of the antiproton beamline in SIMION

3.2.1. The SIMION simulation software

As a simulation program for the antiproton propagation along the beamline the SIMION Ion and Electron Optics Simulator software is used. It can resolve 2D and 3D geometries and calculates electrostatic and / or magnetic potential arrays for given electrodes. Based on the definition of the geometry of the relevant ion optical elements and apertures in a geometry (*gem*) file, the potential arrays of all electrodes are derived within a predefined volume by solving the Laplace equation

$$\nabla^2 V = 0, \tag{3.2}$$

using the defined electrodes and their scalable potential V as boundary conditions. These potential arrays are then defined on a 2D or 3D mesh, whose resolution can be chosen to balance the precision as well as the total simulation time and consumption of resources. Within the workbench volume and the interpolated potentials, the trajectories of individual input particles are then calculated based on the electromagnetic forces.

The latter points mark a clear deviation compared to the previously mentioned MAD-X software, which calculates the propagation of the Twiss parameters as representation of the full phase space distribution. As each particle's trajectory is calculated individually in SIMION, the simulation time scales with the number of considered particles. Rather than considering the full 10^7 antiprotons per bunch, samples of 1.000 up to 10.000 particles, following the obtained input distributions, are considered for the simulations.

While the baseline version of SIMION uses static potentials, it can be extended by user programs to allow for time-dependent and custom electric and magnetic fields as well as custom

calculations and generation of output data. Commonly, the programming language Lua is used for such user programs, which are implemented in the form of workbench programs that are automatically loaded as soon as the workbench is opened. In this workbench program, ten program segments can be addressed: (i) `initialize`, (ii) `init_p_values`, (iii) `flym`, (iv) `tstep_adjust`, (v) `fast_adjust`, (vi) `efield_adjust`, (vii) `mfield_adjust`, (viii) `accell_adjust`, (ix) `other_actions` and (x) `terminate`. For the following simulations, segments (iii), (v), (vii) and (ix) are specifically addressed in the Lua workbench program.

The segment `flym` is used to define reference parameters, such as particle counters for the determination of transmission rates or adjustable potentials which are transferred to the electrodes in a following segment, prior to the start of the actual simulation. As soon as the simulation is finished, the defined reference parameters can then be evaluated, and the transmission rates are printed or written into an output file.

In the segment `fast_adjust` the potentials on the electrodes can be adjusted after every time step. This is particularly relevant for time-dependent potentials as in the case of the two pulsed drift tubes, which have to be switched to ground while the decelerated particles are within the field-free interior. A detailed discussion about the time-dependent pulsed drift tube potentials is given in Sec. 3.2.2.

The segment `mfield_adjust` can be used to implement analytic expressions for a magnetic field inside an empty magnetic potential array rather than using a fully defined 3D magnetic potential array. In case of the PUMA beamline, this segment is used to implement the (axial) magnetic field of the PUMA solenoid, which captures incoming ions and antiprotons by the strong Lorentz force. To get an analytic expression the 3D simulated magnetic field, which is provided by Bilfinger Noell as supplier, is fitted in axial direction with a two-parameter Fermi (2pF) fit, which is given by

$$B\left(z\right) = \frac{B_0}{\exp\left(\frac{z-a}{c}\right)+1} \tag{3.3}$$

with the central magnetic field $B_0 = 4\,\mathrm{T}$ and the two parameters $a = 724.06\,\mathrm{mm}$ and $c = 72.15\,\mathrm{mm}$ (see Fig. 3.4). In this simplistic implementation, only the axial magnetic field is considered, while the horizontal and vertical components are neglected, especially in the fringe field on the solenoid extremities. These components typically lead to a funnel effect, which compresses the incoming ion and antiproton bunches towards the solenoid center axis. Consequently, a conservative estimate of the achievable transmission into the trap will be presented.

Finally, the segment `other_actions` is also called after each time step and is used to define and check criteria for the successful deceleration or transmission at different longitudinal positions along the beamline. For the deceleration, the axial velocity is checked behind the pulsed drift tube. In case of the HV PDT, the axial velocity after deceleration is supposed to be at about 875 mm/µs, corresponding to 4 keV kinetic energy. To account for the energy spread of $\sigma_{\mathrm{kin.\,E}} = 100\,\mathrm{eV}$, velocities between 850 and 900 mm/µs are tolerated, corresponding to an energy interval of $\pm 250\,\mathrm{eV}$, while all particles outside this velocity interval are removed. A similar check is also implemented for the second PDT, where only

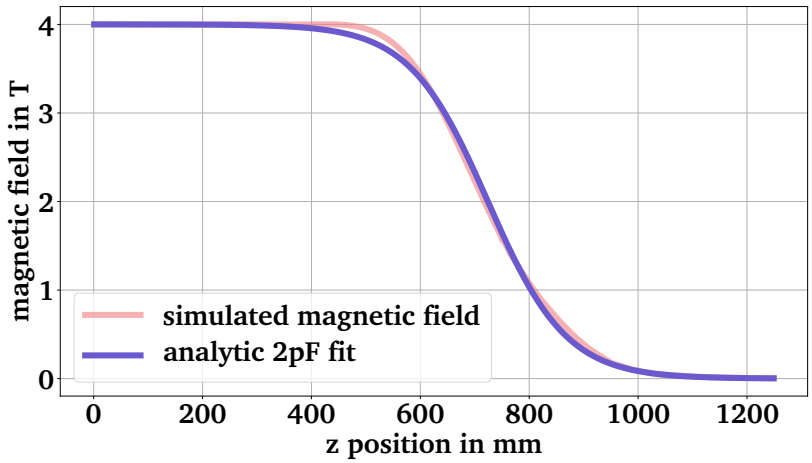

Figure 3.4.: Comparison of the simulated magnetic field for the PUMA solenoid by Bilfinger and the analytic 2pF fit for the analytic implementation in SIMION.

an upper limit of 280 mm/µs - corresponding to a kinetic energy of 400 eV - is set, as all particles below that energy can be trapped effectively. To investigate the transmission and the losses along the beamline, several reference points - mostly tight aperture constraints or the PDTs - along the beamline are defined to check if particles pass through the reference plane without being lost upstream. This allows a clear identification of beamline sections inducing high losses, which could potentially be compensated by proper settings on the ion optical elements. The ultimate reference is the amount of properly decelerated antiprotons that reach the storage trap, and the aim of the presented simulations is a maximization of this number. Besides this, additional beam properties along the beamline are investigated, such as the proper PDT switching time, the energy spread after deceleration, the beam envelope and the transverse beam profile at the cryostat entrance.

3.2.2. Definition of the ion optical components along the antiproton beamline

As final step to prepare the ion optical simulations, the ion optical components along the antiproton beamline of PUMA have to be assembled into a geometry file. The relevant components are the high-voltage einzel lens, the high-voltage pulsed drift tube and the low-voltage einzel lenses along the room temperature beamline and the 50 K einzel lens, the low-voltage pulsed drift tube and the trap electrodes within the cryostat assembly. Additionally tight radial apertures are included in the form of grounded electrodes, on which antiprotons could be lost. Figure 3.5 depicts a slice of the implemented 3D workbench (*bottom*) and its equivalent in the half-section view of the beamline CAD model (*top*).

In the following, a particular focus is set on the pulsed drift and the impact of the deceleration on the ion optical properties of an antiproton bunch. As indicated in the previous Sec. 3.1, the deceleration induces an increase of transverse emittance, in particular in the divergence angles x' and y'. As only the velocity components along the flight path are reduced

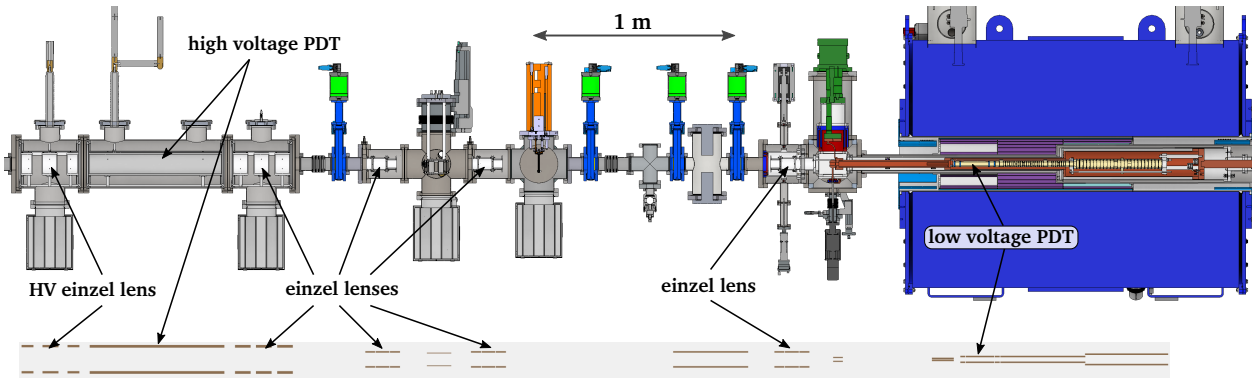

Figure 3.5.: Overview of the ion optical elements in the PUMA antiproton beamline and the implementation in SIMION depicted below. The additional components included in SIMION represent aperture constraints from grounded components within the beamline.

by the PDT, while the radial velocity components remain, the resulting divergence angles increase by the same factor as the velocity decreases, assuming small angle approximation. Considering a deceleration from 100 keV to 4 keV from the PUMA HV PDT, the on-axis velocity is reduced by a factor of 5, leading to an increase in transverse emittance by a factor of 5. At the same time, the bunch length in spatial coordinates is reduced by the same factor. The working principle of the PDT and its impact on the bunch emittance are sketched in Fig. 3.6.

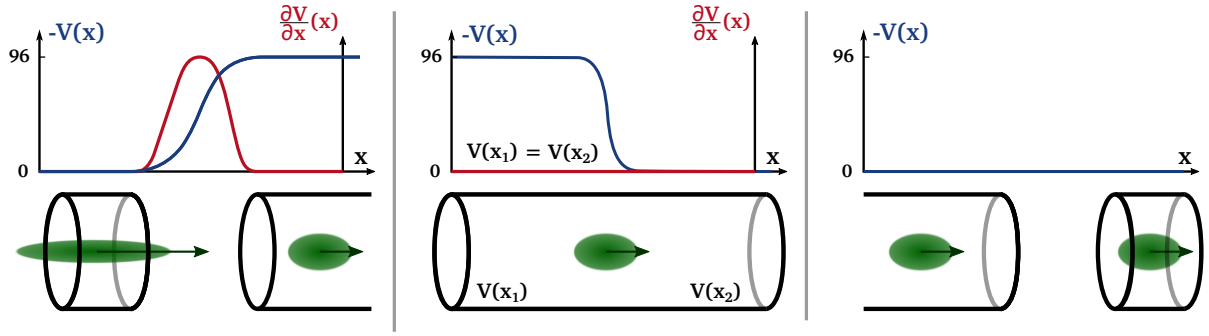

Figure 3.6.: Sketch of the working principle of a pulsed drift tube in three steps: Deceleration at the entrance, switching while the bunch is in the field-free interior and exit at low kinetic energy. The longitudinal contraction and transverse expansion due to the deceleration are illustrated and the potentials are depicted in the co-moving frame of the antiproton bunch.

In first approximation, the time-dependent potentials on the pulsed drift tube are then defined by step function, which is given by

$$V_{\mathrm{PDT}}(t) = \begin{cases} V_0 & \text{for } t \leq t_{\mathrm{pulse}} \\ 0 & \text{for } t > t_{\mathrm{pulse}} \end{cases} \tag{3.4}$$

with the PDT pulsing time t_{pulse} that has to be determined via the simulations. In case of the HV PDT, this time corresponds in first order to the time of flight of the barycenter of a

realistic antiproton bunch from the optical handover point to the center of the pulsed drift tube, while considering potentials of -89 kV at the HV einzel lens and -96 kV at the PDT. For a more realistic representation of the time-dependence of the PDT potentials a pulsing test has been performed with the help of a 1:1000 voltage divider and an oscilloscope. The voltage was measured at the high-voltage electric feedthrough and the potential was switched to ground with a Behlke HTS 1501-20-LC2 switch. The resulting decay curve is depicted in Fig. 3.7 in blue, while the red line represents an analytic multi-exponential fit to the data for an implementation in the Lua workbench program. The measured curve shows a clear oscillatory behavior, especially in the first 300 ns after the switching, which is not expected. It was concluded that the oscillation was caused by reflections within the cable due to an imperfect termination and is thus not considered in the following. The fit thus follows the equation

$$V_{\mathrm{PDT}}(t) = a \cdot \exp(-\lambda t) + b \cdot \exp(-1.01\lambda t) + c \cdot \exp(-1.1\lambda t) \quad \text{for } t > t_{\mathrm{pulse}} \equiv 0 \tag{3.5}$$

with the parameters $a = 5.915 \cdot 10^6\,\mathrm{V}$, $b = -6.631 \cdot 10^6\,\mathrm{V}$, $c = 0.711 \cdot 10^6\,\mathrm{V}$ and $\lambda = 18.229\,\mu\mathrm{s}^{-1}$. While it underestimates the magnitude of the measured potential overshoot of about 20 %, the time constant for the decay and the general behavior are well-reproduced. The exponential decay is then implemented into the Lua program as a replacement for the instantaneous switch to ground to closer resemble the actual setup. It is assumed that the potential decay scales linearly with the potential while the time constant remains and that both PDTs decay with a similar profile.

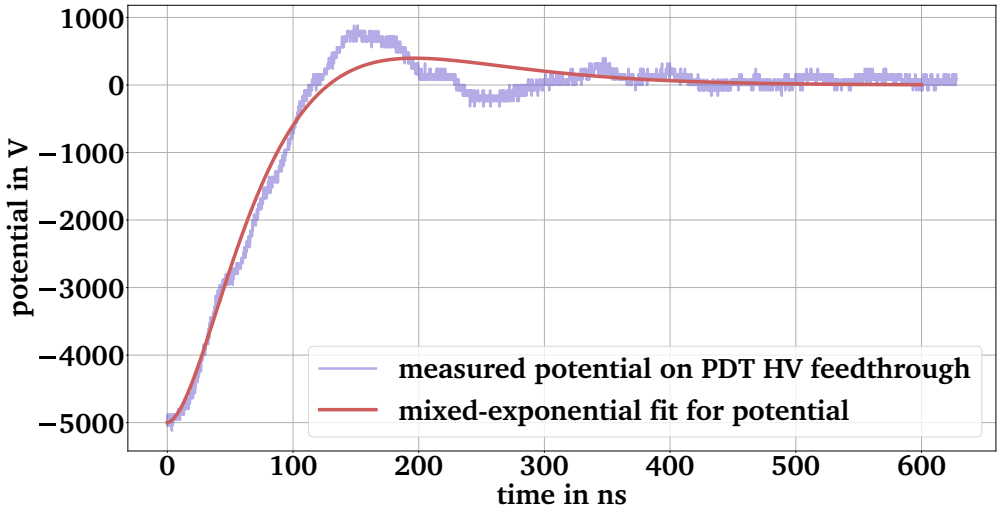

Figure 3.7.: Decay of the PDT potential from an initial value of 5 kV to ground as measured at the HV electrical feedthrough. For an implementation in SIMION, an analytic multi-exponential fit following Eq. 3.5 is used.

Up to this point, only the impact of the PDT on the transverse emittance under the assumption of a successful deceleration has been considered. In practice, this deceleration can only be achieved by a precise timing of the PDT switching from HV to ground, with the time pattern described in Eq. 3.5. The identification of the time interval for successful deceleration will be the first step in the following ion optical simulations.

3.3. Ion optical simulations

3.3.1. Antiproton properties after deceleration in the pulsed drift tube

To investigate the ideal pulsing time for the pulsed drift tube, different values of t_{pulse} are set in the Lua workbench program and the time of flight (ToF) as well as the kinetic energy at a reference point 2 m behind the pulsed drift are measured for each setting. While the kinetic energy provides a direct indication of a proper deceleration, it is not a directly accessible observable in the straight beamline. Because of this, the time of flight is also investigated, as it provides an indirect measurement of the kinetic energy. The reference point is set to 2 m behind the PDT, as the first transmission test measurement presented in Section 3.4 place a time-of-flight detector right at this point, so that a one-to-one correlation can be performed. The results of the ToF-scan are depicted in Fig. 3.8 in the form of heat-map histograms, with yellow and red colors indicating high density and blue indicating zero density at the given time of flight. The plot can be separated into three main regions: (*i*) $t_{\mathrm{pulse}} < 0.1$ µs - if the PDT is switched too early, the PDT is already at ground potential before the antiprotons are decelerated at the PDT entrance, so that a very short ToF is observed, (*ii*) $0.3 < t_{\mathrm{pulse}} < 0.7$ µs - if the PDT is properly switched, the antiprotons are decelerated to 4 keV and not re-accelerated at the exit of the PDT, leading to significantly higher ToFs of about 3.8 µs towards the reference point and (*iii*) $t_{\mathrm{pulse}} > 0.8$ µs - if the PDT is switched too late, the antiprotons are first decelerated at the PDT entrance but then re-accelerated at the exit, so that they pass the 2 m distance to the reference point again at 100 keV, leading to ToFs which are slightly higher than in region (i), but much shorter than in region (ii). In between these three main regimes, transition intervals are observed for $t_{\mathrm{pulse}} \sim 0.2,\ 0.8$ µs, in which only a part of the bunch is decelerated, leading to wide and irregular distributions of the ToFs.

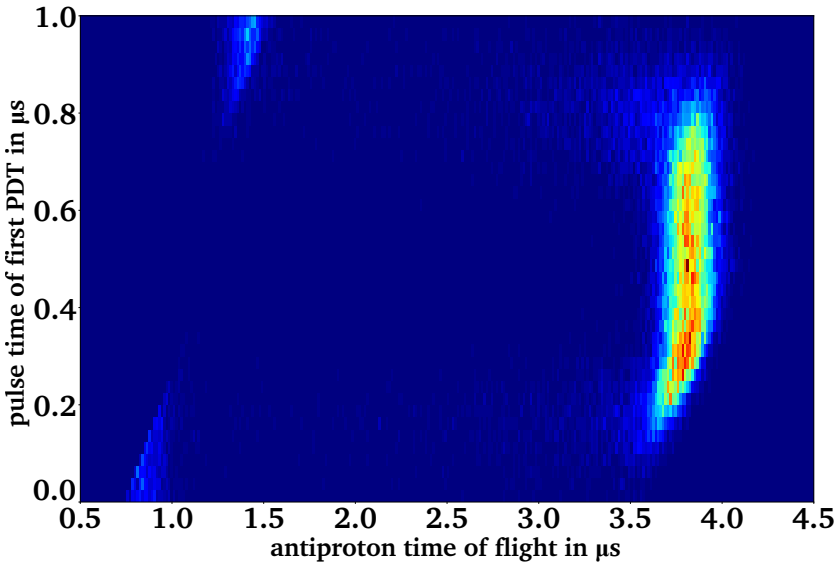

Figure 3.8.: Distribution of the antiproton time of flight to a reference point 2 m behind the PDT for different PDT pulsing times (relative to the initialization at the optical HOP) as a heatmap. Red colors indicate high intensity, while blue colors represent low intensities.

In a first estimate, the difference in time of flight between an antiproton at 100 keV (velocity of about 4380 mm/µs) and at 4 keV (velocity of about 875 mm/µs) over the distance of 2.8 m between the center of the PDT as location of deceleration to the reference point would correspond to about 2.5 µs, which is consistent with the observed difference in ToF and indicates a successful deceleration to 4 keV. This assumption is confirmed by the 2D heat-map histogram of the kinetic energies depicted in Fig. 3.9, where a mean energy of about 4.05 keV is observed in the pulse time interval of region (*ii*).

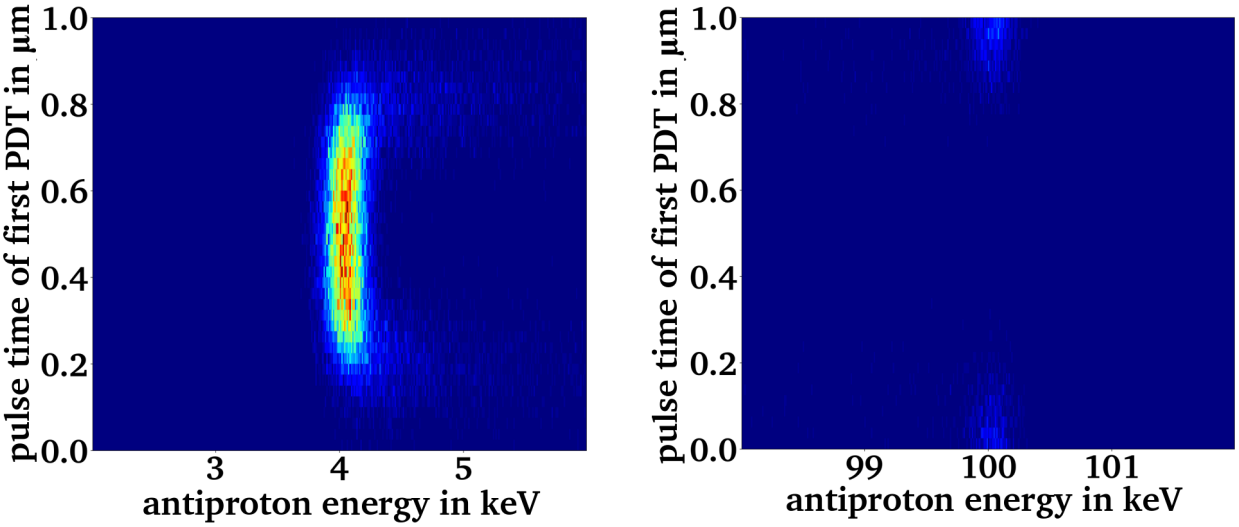

Figure 3.9.: Distribution of the antiproton kinetic energy for different PDT pulsing times (relative to the initialization at the optical HOP).

In the next step, a close look is taken at the distribution of the time of flight of the decelerated antiprotons, assuming a pulsing time of 0.45 µs after the antiproton initialization. The distribution of the ToF at the reference point is then fitted by a Gaussian distribution to derive the standard deviation of the bunch after deceleration, which in first order should remain equal to the input bunch length with $\sigma_{\mathrm{z},0} = 75$ ns. The fit to the simulated distribution is depicted in Fig. 3.10, yielding a central value of $\mu = 3.823$ µs and a standard deviation of $\sigma_{\mathrm{z,RP}} = 89$ ns, which is about 20 % higher than the input bunch length. This increased bunch length presumably originates from the non-instantaneous deceleration, as the fitted potential pulsing is implemented in the simulation. In contrast to the increase in bunch length, the energy width of $\sigma_{\mathrm{kin.E}} = 100$ eV in conserved, as indicated by the Gaussian fit of the kinetic energy depicted in Fig. 3.10.

A particularity of both plots in Fig. 3.8 and 3.9 is the magnitude of the decelerated beam compared to the fast beams, indicated by the width and color of the signals. This change in magnitude originates from the proper focusing of the antiprotons after deceleration, maximizing the signal in this reference plane, while many particles are lost in the case of the fast beams due to insufficient focusing by the low-voltage einzel lenses downstream of the PDT.

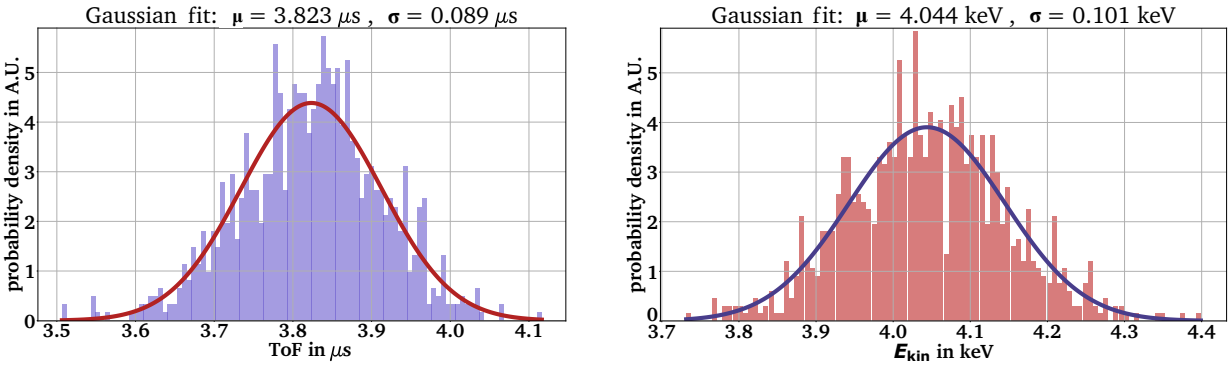

Figure 3.10.: Time of flight (*left*) and kinetic energy (*right*) distribution of the decelerated antiproton bunch at the reference point. A Gaussian fit is performed to determine a bunch length standard deviation of 89 ns and an energy spread with a standard deviation of 101 eV, which is consistent with the input energy spread.

3.3.2. Optimization of the antiproton transmission and envelope

To optimize the transmission of antiproton into the PUMA storage trap, the ideal settings of the electrode potentials on the einzel lenses were determined in a two-step process: firstly, Monte-Carlo simulations with random potential values for the different einzel lens potentials along the beamline were performed to find starting values for the subsequent simplex-type optimization, and secondly to fine tuning of the potentials via the optimization.

In the Monte-Carlo simulations, a potential interval of [-85,-90] kV was allowed for the HV einzel lens (denoted as einzel lens 1), while the three low voltage einzel lenses, denoted by einzel lens 2 to 4, were limited to [0,-4] kV. In each individual simulation, a random set of potentials from the defined intervals is taken and 1000 particles with the derived input distributions are propagated to evaluate the transmission into the storage trap. To define smaller potential intervals with high transmission, the transmission rate is plotted in the form of scatter plots with a combination of two different electrode potentials on the axes. In all plots depicted in Fig. 3.11, a bright yellow color indicates high transmission rates, while blue and white colors correspond to low transmission rates. In the plots, red ellipses are added to indicate regions of high transmission, which are used to define starting values and intervals for the subsequent optimization. These intervals are: *electrode 1:* -88.5 ± 1.5 kV, *electrode 2:* -2.6 ± 0.4 kV, *electrode 3:* -1.5 ± 1.5 kV and *electrode 4:* -2.0 ± 0.5 kV.

In the next step, these intervals are used for the simplex optimization, for which SIMION provides an internal implementation based on the Nelder-Mead downhill routine [197]. This simplex algorithm requests starting values (either upper or lower limits), an initial step size, which is reduced in the proximity of a minimum, and a metric (L) to minimize. For the given case, the metric is set to minimize the losses indicated by $L = 1 - T_{\mathrm{ST}}$ with the transmission T_{ST} into the storage trap (ST). Then, the simplex code varies the first parameter, while keeping all remaining parameters constant, until a local minimum is found. Then, the next parameter is adjusted in a similar fashion. After one iteration over all parameters, the first one is again adjusted to account for the changed voltages on the other electrodes along the beamline. This process is then repeated, until a (local) multi-dimensional minimum is

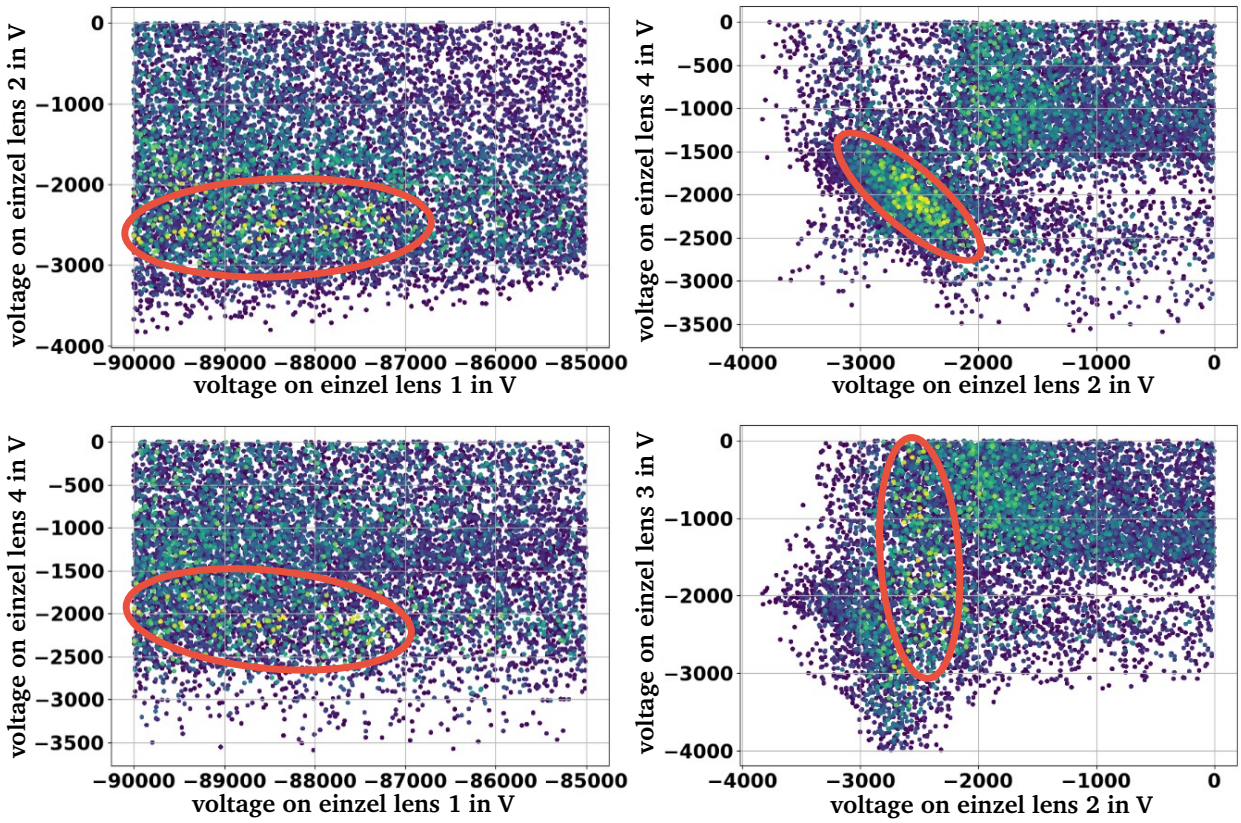

Figure 3.11.: Scatter plot of the transmission rates for different combinations of einzel lens electrode potentials. Bright yellow and green colors indicate a higher transmission.

reached, where no further improvement is reached by varying the voltages. Based on this optimization, voltages of $-89.5\,\mathrm{kV}$ (E1), $-2.7\,\mathrm{kV}$ (E2), $-2.6\,\mathrm{kV}$ (E3) and $-1.75\,\mathrm{kV}$ (E4) for the four einzel lenses in the antiproton beamline were derived. In a final step, also the 50 K einzel lens within the experimental setup is optimized to a value of $-2.2\,\mathrm{kV}$, so that a final antiproton transmission rate of about 90 % is reached. This value is significantly higher than the rates achieved by conventional degrader foils, improving the transmission rate by about one order of magnitude.

Finally, the radial profile of the antiproton bunch along the beamline and the location of antiproton losses are investigated. To do so, the additional transmission reference points along the antiproton beamline are taken into account. Considering the optimized electrode potentials, the respective transmission rates of a sample bunch of 1000 particles are given by: [a] the transmission through the HV PDT: $T_{\mathrm{HV-PDT}} = 1$, [b] the transmission through the quad. bender: $T_{\mathrm{QB}} = 1$, [c] the transmission through the cylinder shutter : $T_{\mathrm{shut}} = 0.996$, [d] the transmission through the conductance barrier: $T_{\mathrm{CB}} = 0.957$, [e] the transmission through the LV PDT: $T_{\mathrm{LV-PDT}} = 0.915$ and [f] the transmission into the storage trap: $T_{\mathrm{ST}} = 0.915$.

These rates indicate that most of the 8.5 % losses occur in between the ball shutter and the conductance barrier as well as in the second low-voltage PDT, while the remaining losses

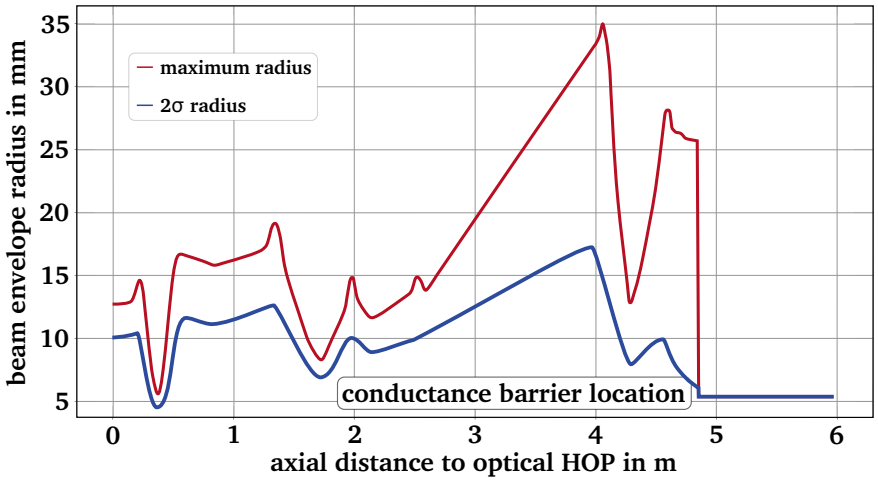

Figure 3.12.: Plot of the radial beam profile of the transmitted antiproton bunch inside the PUMA beamline. While the blue line indicates the 2σ radii of the antiproton bunch for a given axial position, the red line indicates the maximum radial offset of an individual antiproton at the given axial position.

along the beamline are mostly negligible. This conclusion is also supported by the observed beam envelope, which is depicted in Fig. 3.12. For the plot, two different properties are considered: the 2σ environment of the radial distribution of all antiprotons (*blue*) and the maximum offset of an individual antiproton (*red*). In addition, for each axial position, only antiprotons that are not splatted are depicted, so that the number of antiprotons is not constant along the axis. This becomes especially prevalent at the entrance of the conductance barrier with an inner radius of 5.625 mm, as all particles above this radius are considered to be splatted, causing the step-drop at the entrance. The additional losses within the second PDT are predominantly caused by an insufficient deceleration of the antiprotons, as the radial expansion of the beam within the magnetic field remains constant. It is concluded that the losses are caused by the intrinsic energy spread, as the kinetic energy of the lost particles overcomes the 400 eV cutoff.

To summarize, the ion optical simulations indicate decelerated antiproton transmission rates in the order of 90 %, which is about one order of magnitude higher than previous approaches with degrader foils and would lead to more than $5 \cdot 10^6$ trapped antiprotons per bunch. Assuming an ultimate goal of $1 \cdot 10^9$ antiprotons as reservoir for measurements, a total of about 200 bunches needs to be collected, corresponding to about 400 min or less than 7 h of beamtime at ELENA.

3.4. Simulation benchmark with experimental data

The presented ion optical simulations provide a good first estimate of the settings for the ion optical elements along the beamline and indicate transmission rates of close to 100 %, but they assume an idealized geometry of the components, perfect alignment and constant parameters of the input bunch. While these approximations are required to provide a first reasonable order of magnitude estimate in the simulation, a fully realistic simulation

would require a precise knowledge of all properties of the relevant ion optical elements (*i.e.*, displacement and tilt with respect to the simulated geometry, surface and geometry imperfections) and the (shot-to-shot) variation of the position and angle of the incoming bunches of the real setup. As it is almost impossible to determine all parameters within the required precision, measurements have to be performed on the real setup as a benchmark of the simulations.

In this section, the results of first antiproton deceleration and transmission measurements obtained with a reduced antiproton beamline at ELENA are discussed. The focus is set on the results that can be compared directly with the ion optical simulations, while a thorough discussion of the full measurement campaign is presented in [198]. The reduced beamline does not include the experimental setup with the cryostat and trap assembly as well as the last short pumping section with an inner diameter of 63 mm (CF63 vacuum pipe) right in front of the setup, but replaces the latter with a detection cross. This detection cross comprises a micro-channel plate detector for position-sensitive detection, a Faraday-cup for total charge measurements, an energy grid for the determination of the kinetic energy and a Magne-TOF detector with a scaler for time of flight measurements, where the location of the Magne-TOF was used as reference point for the ion-optical simulations for the time of flight and energy scan. Besides these detectors, the beamline currently includes a beam transfer viewer (BTV) right in front of the detection cross, which is based on a tilted phosphorus screen, which is observed by a digital CCD camera. At a later stage, the BTV as a fully destructive diagnostics tool - similarly to the detectors within the detection cross - will be replaced by a secondary electron monitor (SEM) grid, which is transparent for more than 95 % of the beam but still provides a position-sensitive signal. An overview over the reduced beamline is depicted in Fig. 3.13.

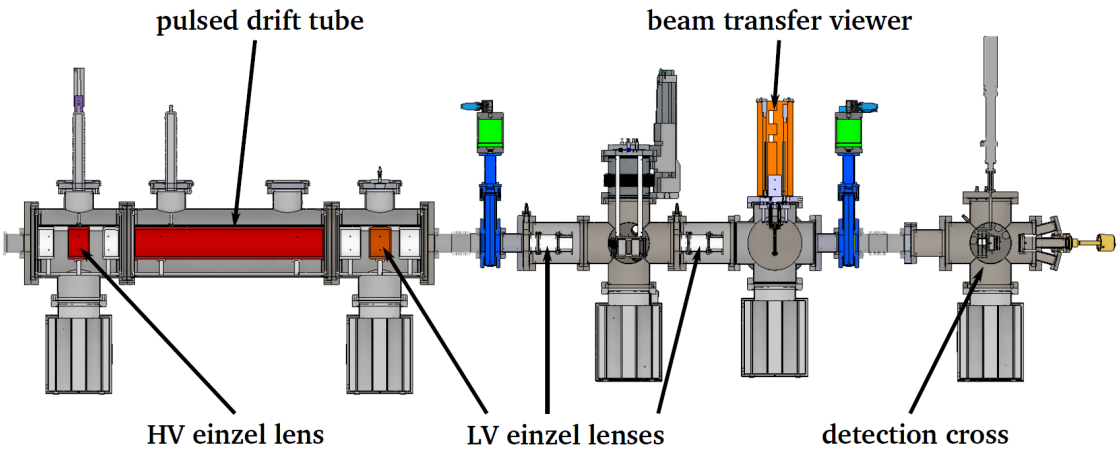

Figure 3.13.: Half-section view of the reduced PUMA beamline.

In the first measurement, the deceleration of the antiprotons was investigated by two different measurements. Firstly, the time of flight of the antiprotons was scanned over different pulsed drift tube pulsing times. This pulsing time is defined relative to a trigger signal "AEX.PUMA", which represents the deflection of the antiprotons from the ELENA ring into the LNE51 beamline and has a negligible shot-to-shot variation with respect to the timing. By setting an adjustable trigger delay and defining an additional wait time in the

scaler, the pulsing time can then be scanned over a reasonable interval, derived from analytic estimates of the time of flight. The signals are then acquired by combining the Magne-TOF detector for the actual time of flight measurement, which only provides a signal at the points in time a pre-defined signal threshold is overcome, with the actual magnitude and length of the induced signal, which is visualized with an oscilloscope. Both signals are then combined in a 2D plot by adjusting the oscilloscope data to the time stamps from the Magne-TOF, while color-coding the signal magnitude. The resulting plot - depicted in Fig. 3.14 - shows a clear difference in the determined time of flight of the decelerated beam compared to un- or re-accelerated antiprotons, as expected by the simulations. Both the width of the time intervals of the pulsing for proper deceleration as well as the absolute time difference in ToF agree very well with the predictions from the simulations, see Fig. 3.10, indicating a successful deceleration to 4 keV.

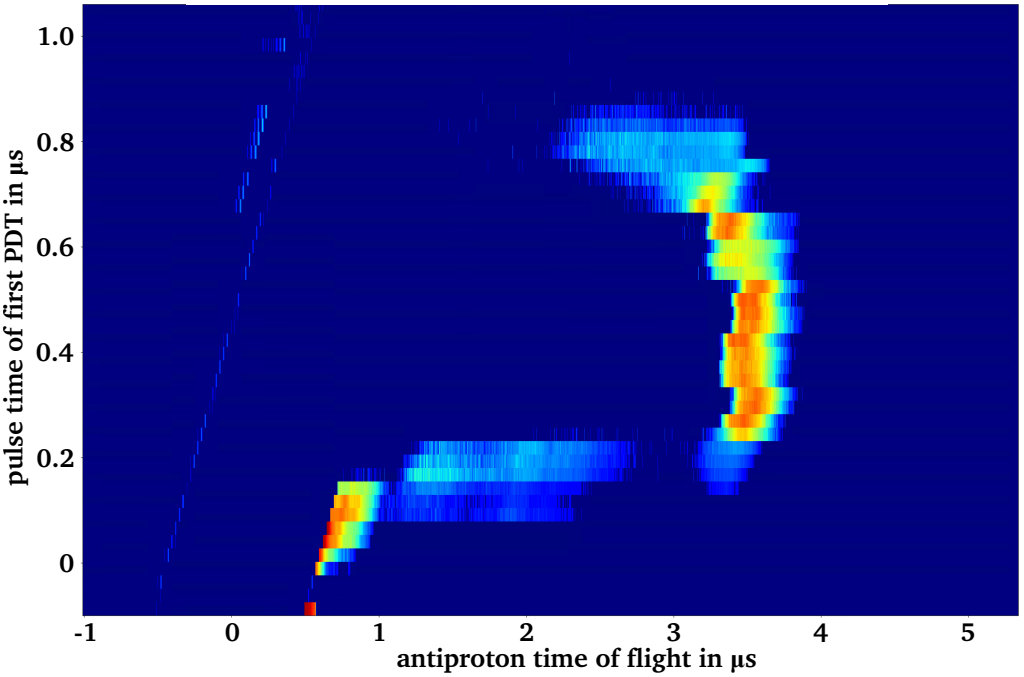

Figure 3.14.: Time of flight scan of the antiproton bunches for different pulsing times of the first PDT. For each pulse time, a spectrum was recorded with an oscilloscope, whose amplitude is indicated by the color code. The faint linearly shifting signal on the left originates from noise induced by the PDT switching, which is suppressed for 1 µs after the first trigger event. The interval of successful deceleration and the observed difference in time of flight are in good agreement with the simulations depicted in Fig. 3.8. For the decelerated and re-accelerated bunches, the oscilloscope signal overlapped with the switching noise, so that the signals cannot be resolved.

This conclusion is also supported by the subsequent energy grid measurement, which is based on applying increasing stopping voltages to the grids while measuring the remaining signal on the Magne-TOF with the oscilloscope. Based on the area under the oscilloscope signal, the relative transmission is then derived as ratio to the maximum signal at zero

blocking voltage. The transmission profile as a function of the stopping voltage does not only provide the central kinetic energy, but also contains information on the energy spread by the width of the transmission decay. The acquired data indicate a mean energy of about 3.9 kV and a width of 150 eV, which in first order is consistent with the simulated values. The increase of the energy spread with respect to the nominal value, which is not predicted by simulations, might be caused by imperfections in the beamline, such as misalignments, causing field imperfections, or induced electrical noise during the fast switching of the PDT.

Finally, the antiproton transmission up to the detection cross was investigated. While typically Faraday cups are used for the measurement of the total charge of a bunch, the annihilations of antiprotons lead to the production of additional charges that ultimately falsify the measured signal from the actual input. Consequently, a direct charge and thus number measurement is not possible, so that a relative measurement is applied instead. Instead of the Faraday cup, the BTV is used for this measurement, as it additionally provides information of the beam shape and position, while providing information on the bunch intensity by the intensity signal on the phosphorus screen.

Another reason for the usage of the BTV is the large acceptance area of the screen, which is particularly relevant for the reference measurement with un-decelerated antiprotons. While the simulations in SIMION predict a small beam diameter both in horizontal and in vertical direction, with an aspect ratio of about 1:1.5 (vertical:horizontal), the observed beamspot of the 100 keV antiprotons exhibits an aspect ratio of about 1:3 (see Fig. 3.15), while the vertical extension is consistent with the simulated values. This significant deviation from the simulation is caused by the (horizontal) dispersion of the antiproton bunch at the optical handover point, which is not considered in the SIMION simulations.

Due to the dispersion, correlations between the horizontal plane and the longitudinal energy spread are present, which introduce deviations from the usual description of the three independent Gaussian distributions along the spatial axes. In the given case, the horizontal dispersion at the optical handover point is at about

$$D_{\mathrm{x}}(s) = \frac{\Delta x}{\Delta p / p_0} = -2\,\mathrm{m}, \tag{3.6}$$

causing an additional horizontal offset Δx depending on the offset Δp from the nominal momentum $p_0 = 13.7\,\mathrm{keV/c}$, corresponding to $E_{\mathrm{kin}} = 100\,\mathrm{keV}$, at the optical handover point. Additionally, the absolute value of the dispersion function is increasing at the optical HOP, which - in absence of other ion optical elements - leads to a higher dispersion further downstream of the beamline. This ultimately leads to the observed horizontal beam spread on the BTV, but it is assumed that the effect on the decelerated bunches is most negligible due to the compensation by the HV einzel lens and the HV PDT close to the HOP.

This compensation is also observed, as the beam spot, which can be achieved with the decelerated bunch, is almost spherical, as depicted in Fig. 3.16. The relative signal strength as indication of the transmission rate is then derived by fitting a Gaussian distribution to the signal above the background and deriving the integrated surface area for both fast and slow antiproton bunches. The resulting ratio of about 0.5 is significantly lower than the

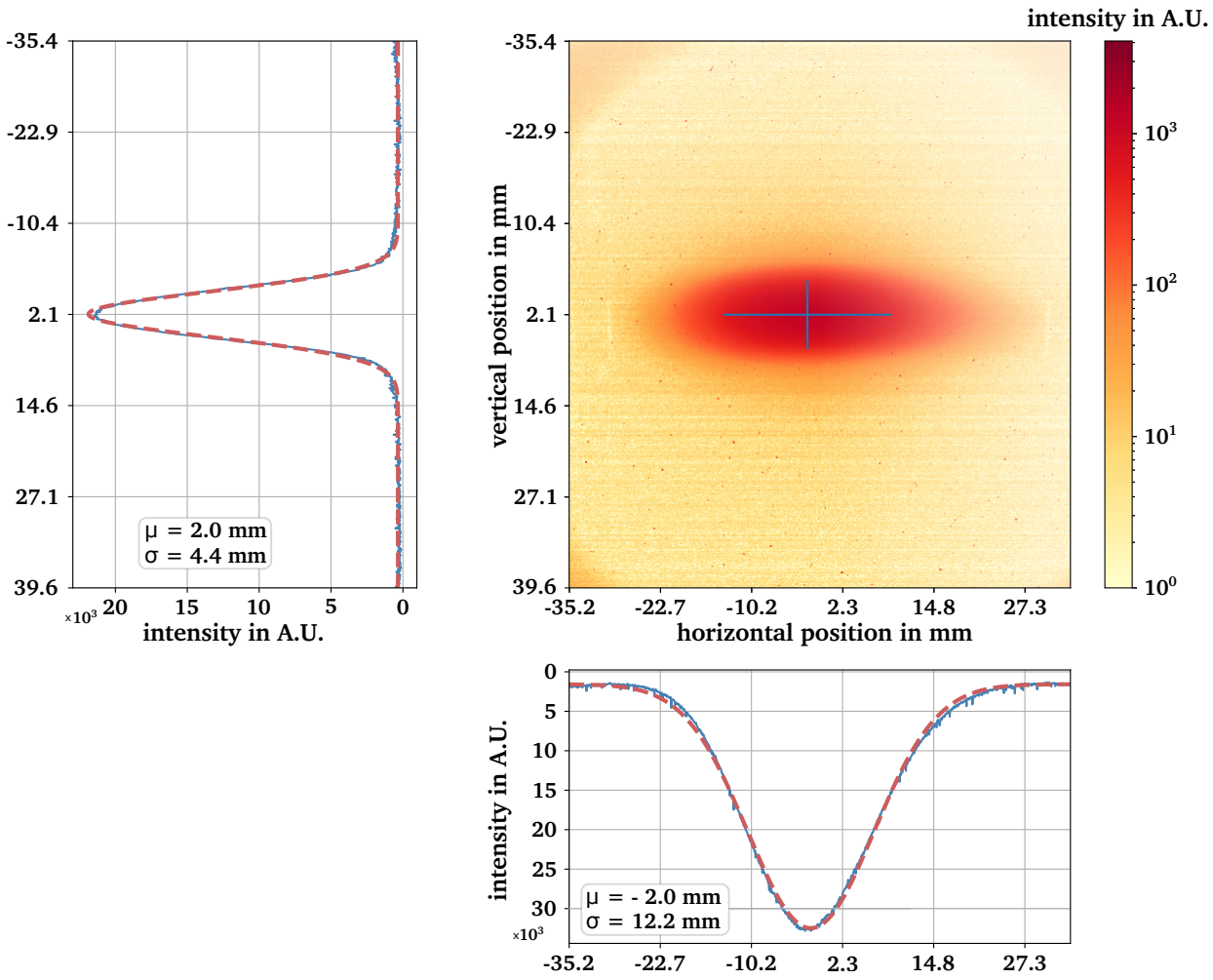

Figure 3.15.: BTV image of the undecelerated antiproton beam at the beam transfer viewer. The horizontal and vertical projection of the intensity around the maximum are added, and the mean value as well as the standard deviation are shown.

prediction of almost 1, indicating antiproton losses along the low-energy beamline, which are presumably caused by a misalignment of the HV components.

For the measurement of the slow antiproton beam, the HV einzel lens was not set to the simulated value of 89 kV, as no signal could be observed on the BTV for that setting. Following a manual scan of different potentials it was found that a signal on the BTV can be observed below 86 kV, while the bunch gets lost for higher potentials. This indicates a misalignment of the HV einzel lens and the pulsed drift tube with respect to the upstream beamline, which could be caused by either a relative tilt or a transverse offset with respect to the nominal beamline. As both HV components act as very strong ion lenses, these misalignments induce strong effects on the nominally straight ion trajectories, as indicated in Fig. 3.17. For this ion optical simulation, the HV einzel lens was shifted horizontally by 1 mm for the center axis, marked by the dashed red line. This small offset already causes a significant deflection into the pulsed drift tube entrance, which propagates downstream to cause some losses on the LV einzel lens electrodes and a bunch barycenter which is offset from the nominal center axis.

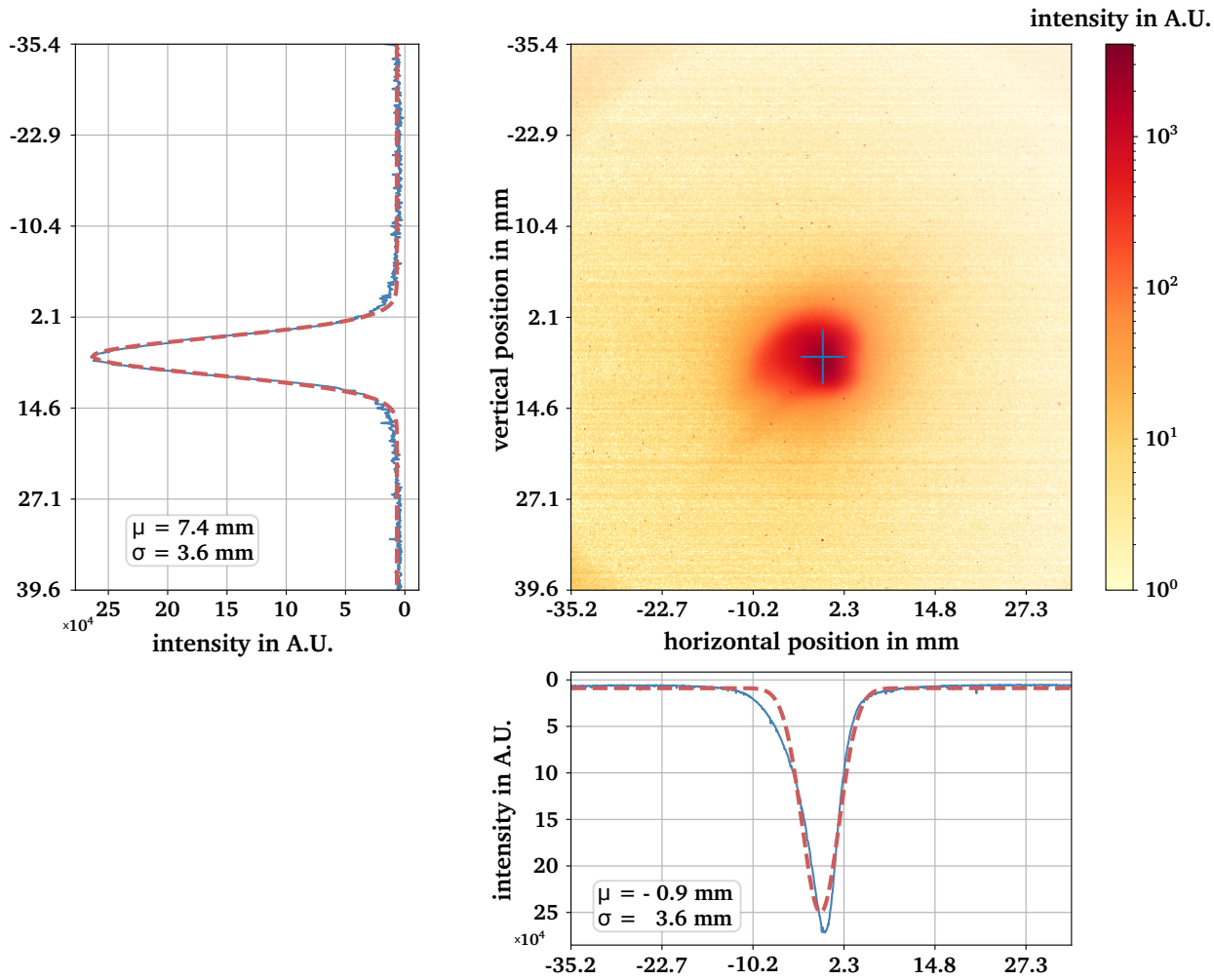

Figure 3.16.: BTV image of the decelerated and focused antiproton beam at the beam transfer viewer. The horizontal and vertical projection of the intensity around the maximum are added, and the mean value as well as the standard deviation are shown.

As already small offsets and tilt angles induce significant deflections, a very precise alignment system for the HV einzel lens and pulsed drift tube assembly would be required to optimize the transmission towards the simulated 100 % to the BTV. At the current stage, such an alignment system is not implemented, and it would require significant design adjustments of the complex high voltage components. As the achieved transmission of about 50 % would only prolong the required accumulation time by a factor of 2 with respect to the estimated 7 h based on the simulations, the adjustments will likely be postponed to the upcoming long shutdown of the CERN accelerator complex, which is used for maintenance of existing setups and installation of new setups.

To summarize, ion optical simulations were performed to determine the path of flight of the antiproton bunches along the PUMA beamline up to the PUMA storage trap. While the idealized simulations predict transmission rates of about 90 %, first tests with a reduced

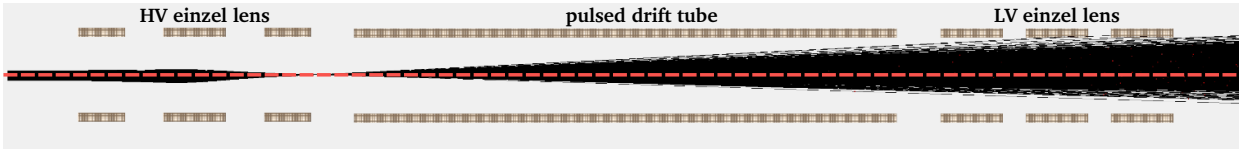

Figure 3.17.: Simulated antiproton trajectories for a horizontal offset of 1 mm for the HV einzel lens. The dashed red line indicates the center axis.

beamline already indicate losses of about 50 %. This hints at imperfections of the real beamline setup, most likely due to misaligned or tilted ion optical components. Still, the observed transmission rates are about one order of magnitude higher than for degrader foils, supporting the use of a pulsed drift tube for the antiproton deceleration.

4. Strangeness production in peripheral antiprotonic annihilations

The PUMA experiment focuses on the detection and identification of the charged pions produced in the annihilation of antiprotons on the nuclear surface. While most pions are directly produced in the annihilation itself, the high total energy of the process also allows the production of heavier mesons, *i.e.*, kaons, η-mesons, ρ-mesons and ω-mesons. The latter three species have lifetimes in the order of $\tau < 10^{-18}$ s, then decay predominately into charged pions of different multiplicity while conserving the total charge [199–201]. They are resolved in the detectors by their pionic decay, as the effective range before decay is in the order of nanometers or below. In contrast to that, the kaons (K^+, K^-, K^0, $\bar{K^0}$) have lifetimes in the order of $\tau \sim 10^{-8}$ s, which is similar to the pion lifetime [202, 203]. They are produced in about 5 % of all annihilations and have a quark composition of $u\bar{s}$, $s\bar{u}$ for K^+, K^- and $d\bar{s}$, $s\bar{d}$ for K^0, $\bar{K^0}$. As strangeness is conserved in QCD processes, kaons are always produced in kaon-antikaon pairs.

Similarly to the pions, the kaons can interact with the residual nucleus in the final state of the annihilation. For pions, these final state interactions are caused by absorption and charge exchange reactions, so that the pion multiplicity and total charge measured in the detector might deviate from the actual multiplicities originating from the annihilation. In case of kaons, the additional reaction mechanism of strangeness exchange is available. By exchanging a strange quark from a K^- or a $\bar{K^0}$ and an up- or down-quark with either a proton or a neutron, a Λ-baryon with valence quarks uds can be produced. It is the lightest strange baryon (hyperon), has an isospin and charge of zero and a mass of about 1115.7 MeV/c^2. In free space, it has a lifetime of $\tau_\Lambda = 2.63 \cdot 10^{-10}$ s and decays via weak decay into a proton or neutron and a pion [204]. After production of a Λ-baryon via strangeness exchange inside a nucleus, the Λ can be bound by the residual nucleus to form a hypernucleus, *i.e.*, a bound system composed of nucleons and at least one strange baryon [205].

In this chapter, the production of hypernuclei in the final state of peripheral annihilations based on antiprotonic atoms is investigated by means of Monte-Carlo simulations. After providing an overview of the interaction of Λ baryons and nucleons and experimental approaches to study this interaction in Sec. 4.1, the simulations, which are performed in a 2-step process, and their results are presented in the sections 4.2, 4.3 and 4.4. The simulations and their results are also summarized in [206]. Finally, a concept for the experimental implementation of the process is discussed and related challenges and chances are highlighted 4.6.

4.1. Strangeness in nuclear physics

The *ab initio* description of nuclei as few- or many-body systems composed by nucleons requires a precise knowledge of the underlying two-body (NN) and three-body (NNN) interactions [29]. They are described by phenomenological boson-exchange models [207, 208] or by potentials derived from chiral effective field theory [209, 210], allowing to precisely reproduce experimental NN scattering data or ground state properties of bound few-body systems.

The introduction of a hyperon (Y) - such as the Λ baryon - into a nucleus requires the additional knowledge of the YN and YNN interactions for a description of the baryonic system. The ΛN two-body interaction has a short attractive effective range [211], which is commonly modeled via the exchange of pions or heavier mesons [212]. Additional contributions to the interaction compared to NN interactions arise from the strangeness exchange via kaons and the strong Λ-Σ coupling due to their small mass difference of just 75 MeV/c^2 [213], compared to the Δ resonance excitation energy for nucleons at about 300 MeV. Based on the typical energy scales for nuclear effective models, it is thus required that the explicit treatment of the Σ is taken into account. Besides the meson exchange approaches, focus is recently also set on the implementation of chiral hyperon-nucleon interactions for *ab initio* calculations [214–216], with potentials derived in LO and NLO, *e.g.*, by the Jülich-Bonn-Munich group [217, 218]. To constrain the contact terms of the perturbative expansion, precision data on ΛN scattering is required.

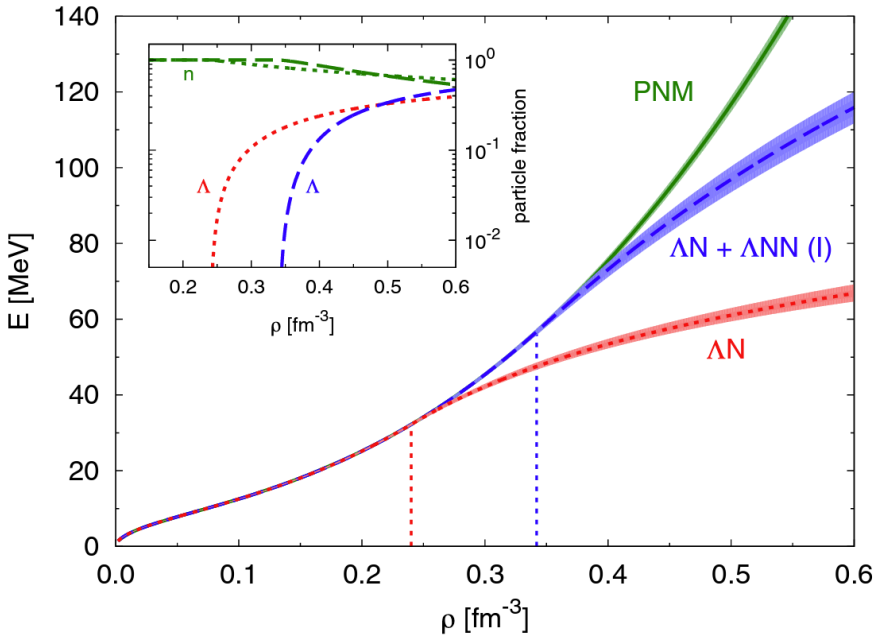

Figure 4.1.: The equations of state for pure neutron matter (PNM, *green*), hypermatter with hyperons interacting via the ΛN two-body interaction alone (*red*) and hypermatter with hyperons interacting via ΛN as well as ΛNN interactions (*blue*). The Λ production threshold densities are highlighted. In the inset, the resulting density-dependent fraction for neutrons and Λs are shown. The figure is reprinted with permission from [219] ©2015 American Physical Society.

Experiments with strange baryons are challenging, as the free Λ-baryon decays on a timescale of 10^{-10} s via the weak interaction into a nucleon and a pion, while heavier strange baryons have even shorter lifetimes. While the same lifetimes are also observed in a nuclear environment, *i.e*, at saturation density ρ_0, the production and decay of Λ-baryons may be in equilibrium in the high-density core of neutron stars ($\rho_{\text{core}} > \rho_0$) [220]. If the strange quark mass is lower than the chemical potential of the up- and down-quarks, the inverse process of strangeness production is facilitated [221]. The introduction of ΛN two-body interactions, derived from ΛN scattering data, leads to a softening of the resulting equation of state with respect to the purely nucleonic form. This implies a weaker slope of the energy density as a function of the baryon density, as depicted in Fig. 4.1. This softer EoS affects the mass-radius relation of neutron stars, limiting the maximum theoretical mass to values that contradict the astrophysical observations of neutron stars with two solar masses [222, 223]. In the literature, this conflict is typically called "hyperon puzzle" [212, 224]. Theoretical calculation based on a model omitting the Λ degrees of freedom indicate that a strongly repulsive ΛNN three-body interaction could resolve the puzzle and stiffen the EoS [212, 225] (see Fig. 4.2), which is consistent with a strong ΛN-ΣN coupling, but sufficient experimental data to constrain the interaction parameters is lacking.

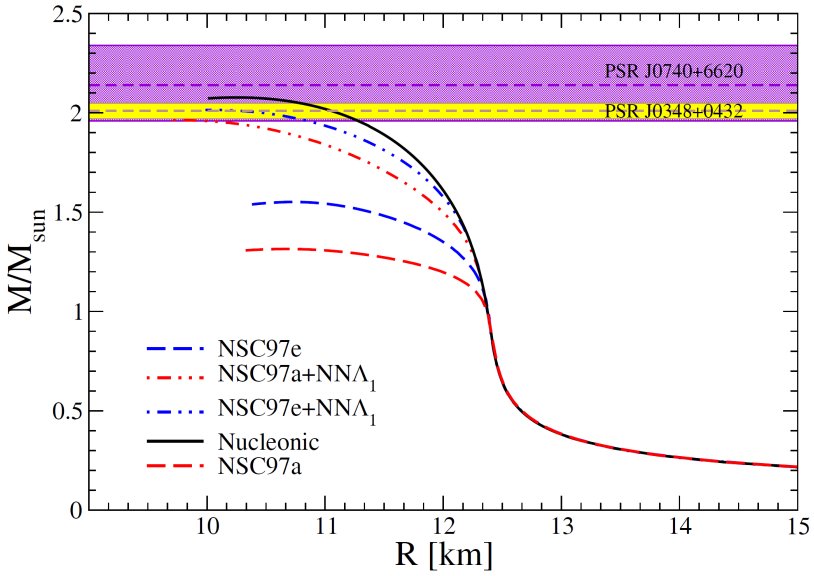

Figure 4.2.: Mass-radius relation for neutron stars for a pure nucleonic EoS (full line), two EoS including ΛN two-body interactions (dashed lines) and additional ΛNN three-body interactions (dashed-dotted lines). For comparison, the determined masses of two recently observed pulsars and their uncertainties are given. This figure is reprinted from [225] under CC BY 4.0.

To provide tighter constraints for the theoretical models both in nuclear environments and neutron stars, dedicated experiments are required. The first of such experiments set the focus on the investigation of the Λp scattering cross section, where the Λ baryons were produced by an incoming kaon- or pion-beam. At the Lawrence Radiation Laboratory, experiments with stopped π^- beams derive an elastic scattering cross section of 22.3$\pm$5.9 mb based on 14 events [226] for a Λ momentum range of 400 to 1000 MeV/c. Subsequent experiments with K^- beam stopped in a propane bubble chamber accumulated 26 scattering events and

derived a similar cross section for a similar momentum range [227]. In a lower momentum interval of 120 to 320 MeV/c, measurements were performed with stopped K^- beams in a hydrogen bubble chamber were performed at CERN and led to 378 elastic Λp scattering events [228]. Besides the meson-induced strangeness production, in a recent experiment, the CLAS collaboration investigated the elastic Λp-scattering following the photon-induced Λ production in a liquid hydrogen target. This provided the first data on Λp-scattering since the 1970s and extracted more precise and accurate cross sections over a momentum range of 900 to 2000 MeV/c [229]. Complementary, Σp scattering was investigated at J-PARC for a momentum range of 400 to 700 MeV/c, yielding about 4500 elastic and 2400 inelastic scattering events [230]. An overview over the scattering cross section derived from experiments and theoretical models is depicted in Fig. 4.3.

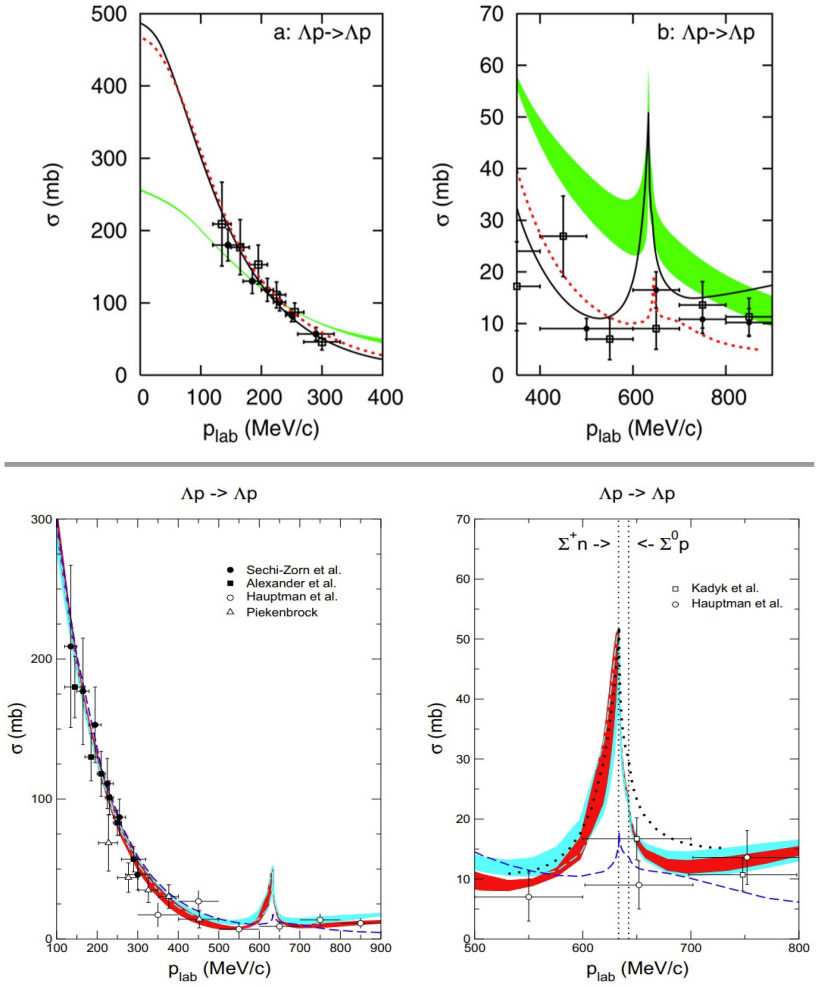

Figure 4.3.: Depiction of the experimental data on Λp-scattering cross sections and the derived theoretical models. The black lines correspond to a Nijmengen boson-exchange model [231] and the colored dashed lines represent the Jülich 04 meson-exchange model [232]. The two top images include a chiral EFT model in LO with hard scale energies $\Lambda = 550 \ldots 700$ MeV as green band and the two bottom images include two chiral EFT models in NLO with hard scale energies $\Lambda = 500 \ldots 650$ MeV as cyan and red band. These figures are reprinted with permission from [233] ©2006 Elsevier and from [234] under CC BY 4.0.

Additional direct constraints on the Λp, $\Lambda\Lambda$ and Λpp interaction are also obtained by the ALICE collaboration at the LHC. They analyzed two- and three-particle correlations in momentum space by means of the femtoscopy technique applied to ultra-relativistic pp collisions at $\sqrt{s} = 13$ TeV and extract several data points along the two-particle Λp and $\Lambda\Lambda$ correlation functions for relative momenta in the range of 0 to 200 MeV/c [235, 236]. The resulting correlation functions are depicted in Fig. 4.4, and the strong increase of the correlation for low relative momenta k^* indicates an attractive Λp interaction, which is in agreement with meson-exchange model predictions, while no strong conclusions could be drawn for the $\Lambda\Lambda$ interaction. In addition, data points along the three-body Λpp correlation function were obtained for normalized mixed momenta up to 400 MeV/c, but the measurements are compatible with a null-hypothesis over the full momentum range [237]. To increase the currently limited statistics, these studies will be continued in upcoming LHC runs.

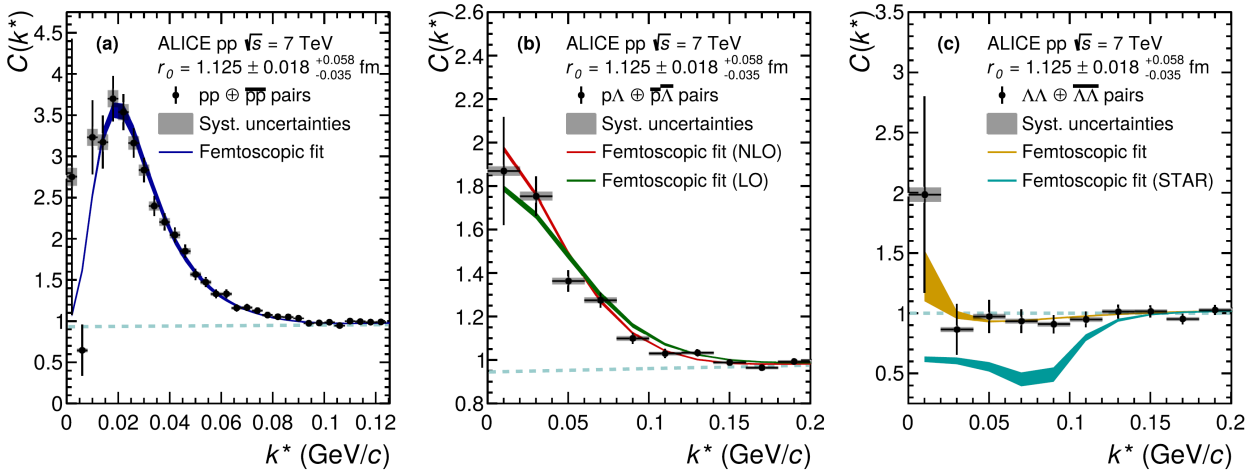

Figure 4.4.: Plot of data points along the $p-p$ (*left*), $p-\Lambda$ (*middle*) and $\Lambda-\Lambda$ (*right*) correlation function, including femtoscopic fits. This figure is reprinted from [238] under CC BY 4.0.

In contrast to the case of protons, precise data on the Λn interaction is not available due to the neutral nature of the neutron and the related detection challenges. While there have been efforts to derive properties of the interaction through the final state interactions of Λ-baryons and neutron in kaon photoproduction from deuterons, which indicated a significant effect on the kaon cross sections [239, 240], no direct Λn scattering data is published.

While previous experiments focused on the interaction of free hyperons with nucleons to constrain, *e.g.*, the ΛN potential, additional properties of the hyperon-nucleon interaction - in particularly within a nuclear environment - can be extracted from the study and spectroscopy of hypernuclei, *i.e.*, bound baryonic systems composing both nucleons and hyperons [205].

Several mean-field models have been developed to describe these hypernuclei [241–253]. Recently, *ab initio* no-core shell models were derived for p-shell hypernuclei [254–257] and quantum Monte Carlo methods have been applied for ground-states of medium-mass

nuclei [258, 259]. In this nuclear environment, the Λ-Σ coupling has to be treated explicitly, as the excitation energy is below the typical cutoff energy for nuclear models of about 300 MeV. However, the lack of experimental spectroscopic data on hypernuclei limits the description of the corresponding interactions and coupling constants, as only about 40 single-Λ hypernuclei have been investigated experimentally [260].

For the experimental study of hypernuclei two main approaches are used: (*a*) the (mesonic) decay spectroscopy of light hypernuclei, where typically the residual nucleus is detected in coincidence with the pion emitted in the weak decay of the bound Λ baryon and (*b*) the γ-ray spectroscopy in combination with a missing-mass measurement, which derives both the ground state energies as well as excitation energies for resolvable excited states. The respective hypernuclei are produced by a strangeness exchange (K^-, π^-) [261–263], a kaon pair creation such as (π^+, K^+) [264–266] or an electromagnetic $(e, e'K^+)$ [267, 268] reaction with a target nucleus. The γ-ray spectroscopy allows to derive an excitation spectrum as depicted in Fig. 4.5, which together with a missing mass measurement allows the assignment of the ground state and selected excited states. By using high-resolution germanium detectors such as the Hyperball Ge detector array [269], even the hypernuclear hyperfine structure can be investigated [270, 271]. This is particularly relevant for constraining the spin-dependent components of the nucleon-hyperon interaction, such as the spin-orbit or tensor forces.

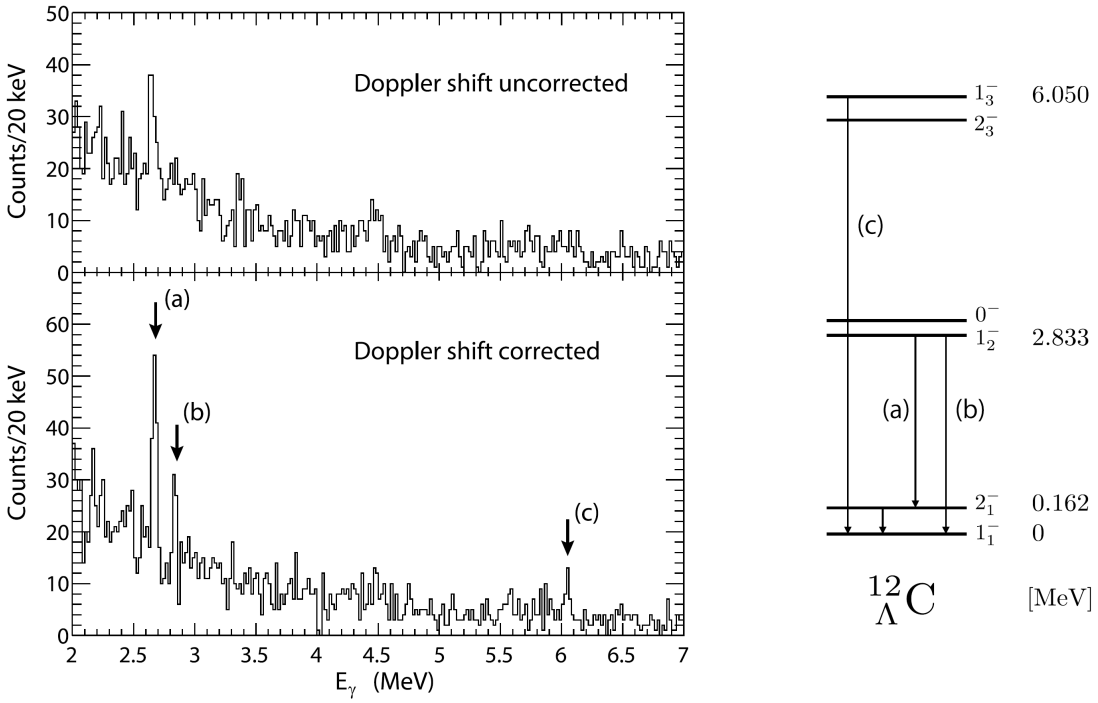

Figure 4.5.: Gamma-ray spectrum of $^{12}_{\Lambda}$C excluding (*top*) and including (*bottom*) the Doppler-shift correction. The corresponding level scheme is depicted on the right, where the measured transitions are indicated. This figure is reprinted with permission from [272] ©2013 Elsevier.

Corresponding experiments with light hypernuclei measured, *e.g.*, the ${}^{7}_{\Lambda}\mathrm{Li}(3/2^{+}, 1/2^{+})$, ${}^{9}_{\Lambda}\mathrm{Be}(5/2^{+}, 3/2^{+})$ and ${}^{16}_{\Lambda}\mathrm{O}(1^{-}, 0^{-})$ spacings [273, 274] as well as the $p_{1/2}$, $p_{3/2} \rightarrow s_{1/2}$ inter-shell transitions in ${}^{13}_{\Lambda}\mathrm{C}$ [275]. For the future, γ-ray spectroscopy is also foreseen for heavier systems up to ${}^{208}_{\Lambda}\mathrm{Pb}$ [272], but currently the information on heavier hypernuclei is limited to ground state properties derived by missing mass measurements. Here, the Λ binding energy and its dependence on the hypernuclear mass has been derived over a wide range of hypernuclei, starting from ${}^{7}_{\Lambda}\mathrm{Li}$ up to ${}^{208}_{\Lambda}\mathrm{Pb}$, extracting the effective depth of the Λ potential as ~ 30 MeV [276]. An overview over all hypernuclei, that have been discovered and measured so far, is depicted in Fig. 4.6. While the low-mass region of the hypernuclear chart up to ${}^{16}_{\Lambda}\mathrm{O}$ is well-studied, the available data on heavier systems is very scarce.

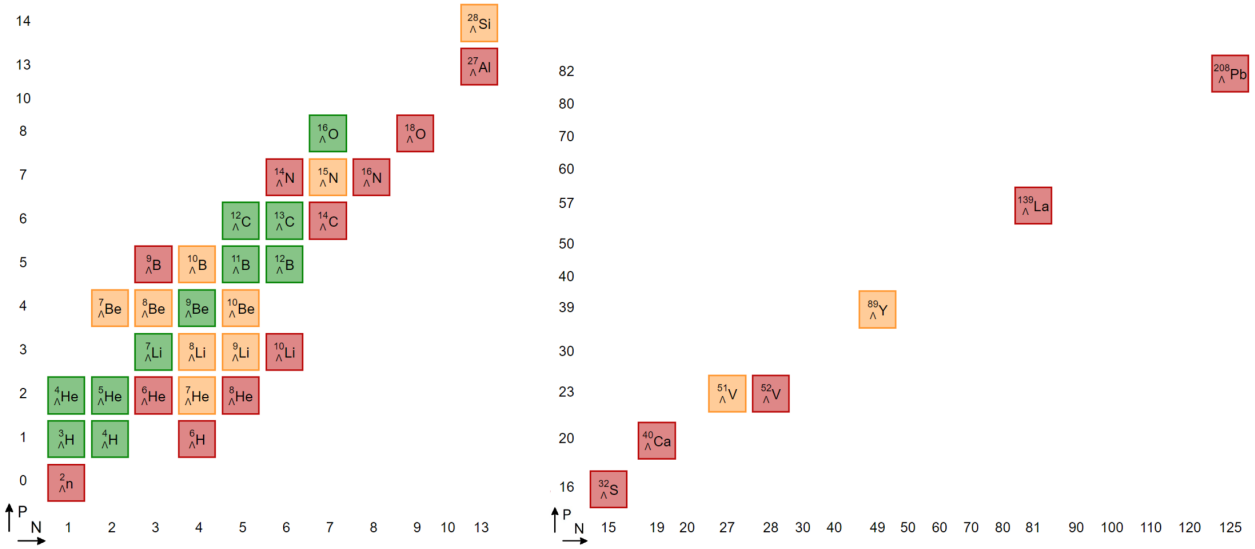

Figure 4.6.: Overview of the currently discovered and investigated hypernuclei. A red color indicates that less than 6 values for that nucleus are published, yellow colors indicate less than 20 values and green represents more than 20 values. The figure has been adapted from [260].

The main reason for the lack of data for heavy hypernuclei is the non-mesonic decay of the Λ via either $\Lambda p \rightarrow np$ or $\Lambda n \rightarrow nn$, in which the virtual pion from the weak decay is absorbed by a nucleon within the nuclear system [277]. The absorbing nucleon might escape the nucleus due to the transferred momentum, but the clear indication of a foregoing hypernuclear formation is lacking compared to the delayed pion-emission of the dominant mesonic decay in light hypernuclei. Starting from a baryon number of $A \sim 20$, the non-mesonic decay is strongly dominant, and the rate relative to the mesonic decay stays almost constant for heavier hypernuclei. This is interpreted as an indication for a short-ranged correlation, in the ΛN and NN interactions, which will be studied in future hypernuclear experiments.

The production of hypernuclei is performed either by a strangeness exchange reaction $(n(K^{-}, \pi^{-})\Lambda, p(K^{-}, \pi^{0})\Lambda)$, a strangeness pair creation $(n(\pi^{+}, K^{+})\Lambda, p(\pi^{-}, K^{0})\Lambda)$ or an electromagnetic reaction $(n(e, e'K^{0})\Lambda, p(e, e'K^{+})\Lambda)$. The cross section for the direct strangeness exchange with a kaon beam is the highest with values of ~ 1 mb, but the preparation of a pure and intense kaon beam is challenging. In case of the pion-induced strangeness

production, the cross section is limited to a few μb, while it drops to tens of nb for the electromagnetic reaction. In the different production reactions also different hypernuclear states are accessible. The strangeness exchange induces a low momentum transfer of only tens of MeV/c, so that substitutional states are populated, where the Λ might occupy an excited state. In contrast, the pion-induced reaction creates high-spin and high-angular momentum nucleon hole states by a high momentum transfer of hundreds of MeV/c, which favors the population of deeply bound states for the Λ baryon. However, all of aforementioned methods are limited to stable target nuclei, so that only hypernuclei with proton and neutron numbers close to the initial nucleus can be produced.

Besides these reaction approaches, strangeness and in particular hypernuclei can also be produced in heavy-ion collisions. This method has already been discussed in the 1970s [278] and became an active field of research in the recent years. At the ALICE experiment at CERN, light hypernuclei up to a baryon number of 4 are detected following ultra-relativistic Pb-p collisions at $\sqrt{s_{\mathrm{NN}}} = 5.02\,\mathrm{TeV}$ [279]. The cross section for the production of heavier hypernuclei decreases by about an order of magnitude for each additional baryon, so that this method is only suited for the production of light nuclei up to helium. Similarly, experiments performed at the HADES experiment at GSI with Ag-Ag collisions at $\sqrt{s_{\mathrm{NN}}} = 2.55\,\mathrm{GeV}$ [280] and at the STAR experiment at Brookhaven National Laboratory with Au-Au collisions at $\sqrt{s_{\mathrm{NN}}} = 3\,\mathrm{GeV}$ [281, 282] observed the production of hyperhydrogen and hyperhelium, and derived their decay branching ratios and lifetimes (see Fig. 4.7) with high precision [280, 283, 284]. Additionally, the HypHI phase 0 experiment [285] and its successor, the WASA-FRS HypHI experiment [286, 287], performed precision spectroscopy of hyperhydrogen based on peripheral heavy ion collisions with $^{6}\mathrm{Li}$ beams at 2 AGeV impinging on a solid carbon target. The use of lighter ions as target and projectile has supplementary been investigated via simulations [288].

A special focus is set on the hypertriton $^{3}_{\Lambda}\mathrm{H}$ as the lightest bound hypernucleus. Its lifetime is expected to be consistent with the free Λ, as supported by above measurements, and theoretical models predict its structure as a hypernuclear halo in the form a Λ orbiting a deuteron core [290]. A dedicated experiment to determine the matter radius of the hypertriton will be performed at GSI/FAIR [291].

For the case of heavier hypernuclei, simulations indicate the population of heavier neutron-rich hypernuclei by fragmentation of collision residues with radioactive ion beams [292]. Based on this initial study, an experiment has been proposed to study the production of neutron-rich hypernuclei via a charge exchange reaction with heavy ion projectiles [293].

Finally, hypernuclei can also be produced by antiproton annihilations through final state interactions of the annihilation products with the residual nucleons, *i.e.*, either via a strangeness-pair production in a pion-nucleon interaction or via direct strangeness exchange with a kaon ($K^{-}p \rightarrow \pi^{0}\Lambda$ and $K^{-}n \rightarrow \pi^{-}\Lambda$). They were firstly observed by the CERN-PS-177 experiment at the low-energy antiproton ring (LEAR) via delayed fission, with an estimated production rate of about 0.3 to 0.7 % per annihilation [294, 295] on Bi and U targets. While this observation was based on stopping antiprotons in a solid target, leading to the formation of antiprotonic atoms, the future PANDA experiment plans to investigate the production of double-Λ hypernuclei via antiproton-nucleus collisions [296]. Following a

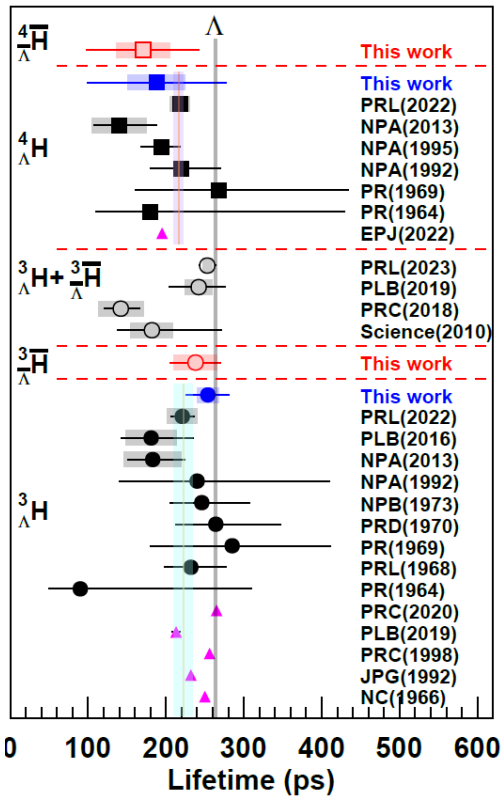

Figure 4.7.: Recent lifetime measurement of ${}^{3}_{\Lambda}\mathrm{H}$, ${}^{3}_{\bar{\Lambda}}\bar{\mathrm{H}}$, ${}^{4}_{\Lambda}\mathrm{H}$ and ${}^{4}_{\bar{\Lambda}}\bar{\mathrm{H}}$ from the STAR experiment and comparison to previous measurements. The figure is reprinted from [289] under CC BY-NC-ND 4.0.

$\Xi^-\bar{\Xi}^-$ pair production in such a collision at ~ 3 GeV/c relative momentum, the Ξ^- can be captured in a secondary target to initiate a double-Λ production via a $\Xi^- p \rightarrow \Lambda\Lambda$ reaction [297].

4.2. Simulation framework

For the following simulations, we consider antiprotonic atoms as a starting point, which are produced with cold and slow trapped antiprotons as provided by the PUMA Penning trap. The focus is set on the peripheral annihilation with low relative momentum and the subsequent propagation of the annihilation products, which occasionally might lead to the production of Λ baryons. These could be captured by the residual nucleus to form a hypernucleus. The simulation framework and code are introduced below.

The simulation of the process is performed by a two-step process. In the first step, the peripheral annihilation of an antiproton on a nucleus with low relative momentum and the subsequent propagation of the annihilation products and potential interaction with the residual nucleons is simulated within the Gießen-Boltzmann-Uehling-Uhlenbeck (GiBUU) transport framework [298]. In the case that the final state interactions lead to the production of a Λ baryon, which is captures by the residual nucleus to form an excited hypersource, the

deexcitation process of this hypersource into a ground state hypernucleus via nucleon-, Λ- and photon emission is performed in the second step with the ABLA++ evaporation and fission code [299]. In the following, both simulation codes and the implementation of the question at hand are detailed.

The GiBUU transport code provides a unified transport framework for elementary reaction on nuclei (*i.e.*, electrons, photons, neutrinos or hadrons on nuclei) as well as heavy-ion collisions in a typical energy range of tens of MeV up to about 40 GeV, guided by the considered cross sections for scattering. It describes the full dynamical evolution of the reaction over time and provides the complete final state after a given time cut. The degrees of freedom in this code are mesons and baryons, whose propagation is calculated via the relativistic Boltzmann-Uehling-Uhlenbeck equation [300] given by:

$$\left[k^{*\mu}\partial_\mu^x + \left(k_\nu^* F^{\mu\nu} + m^* \partial_x^\mu m^*\right)\partial_\mu^{k^*}\right] f\left(x, k^*\right) = \mathcal{I}_{\text{coll}}. \tag{4.1}$$

The equation describes the propagation of the single-particle phase space distribution function $f\left(x, k^*\right)$ with the position x and the kinetic four-momentum $k^* = k - V$. Here, the vector potential V includes contributions from the isoscalar ω meson field, the isovector ρ meson field and the electromagnetic field A via $V = g_\omega\omega + g_\rho\tau\rho^3 + A$ with the isospin projection $\tau = \pm 1$ for protons / neutrons and the meson-nucleon coupling constants g_i, which are taken from the NL parametrizations [301]. The additional parameters in the equation are the field tensor $F^{\mu\nu} = \partial^\mu V^\nu - \partial^\nu V^\mu$ and the effective mass $m^* = m + S$ with the scalar potential $S = g_\sigma\sigma$ expressed by the isoscalar σ meson field and the corresponding coupling constant g_σ. The contribution of binary collisions and resonance decays is added via the collision term $\mathcal{I}_{\text{coll}}$ on the right-hand side of the equation.

While the applicable energy range of GiBUU (MeV to GeV) is well above the energy of the initial antiproton-nucleus collision, which is considered to occur at rest and in the following is set to 10 eV for all considered simulations, the propagation of the mesonic annihilation products with kinetic energies of tens to hundreds of MeV is described properly by the GiBUU equation. To initialize the simulation, the antiproton is defined as a projectile with a kinetic energy of 10 eV and the target nucleus is defined as a target at rest with its center at the origin of the position coordinate system. The distribution of the nucleons for a given proton (Z) and neutron (N) number is determined with the relativistic Thomas-Fermi model [302]. The impact parameter and the initial distance to the nucleus in the direction of flight are individually set for each of the considered target nuclei and aim at reproducing the radial annihilation profile observed in antiprotonic atoms, as detailed in Sec. 1.5. For the examples of the target nuclei $^{16}\mathrm{O}$ and $^{132}\mathrm{Xe}$, which together with $^{40}\mathrm{Ar}$ and $^{84}\mathrm{Kr}$ are considered for the majority of the following simulations, the simulated locations of the annihilation process are depicted in Fig. 4.8, together with a simplified two-parameter Fermi nuclear density and a predicted annihilation distribution derived from quantum electrodynamics (QED), based on the overlap of the antiprotonic orbitals with the nuclear density. For $^{16}\mathrm{O}$, a mixing of $n_{\bar{\mathrm{p}}} = 3, 4$ (20 %, 80 %) is assumed based on absorption width measurements in water targets [119, 120], and for $^{132}\mathrm{Xe}$ a mixing of $n_{\bar{\mathrm{p}}} = 7, 8$ (20 %, 80 %) is interpolated from X-ray intensity measurements on tin isotopes [303]. A diagram of the full workflow of the simulation preparation and evaluation is depicted in Fig. 4.9.

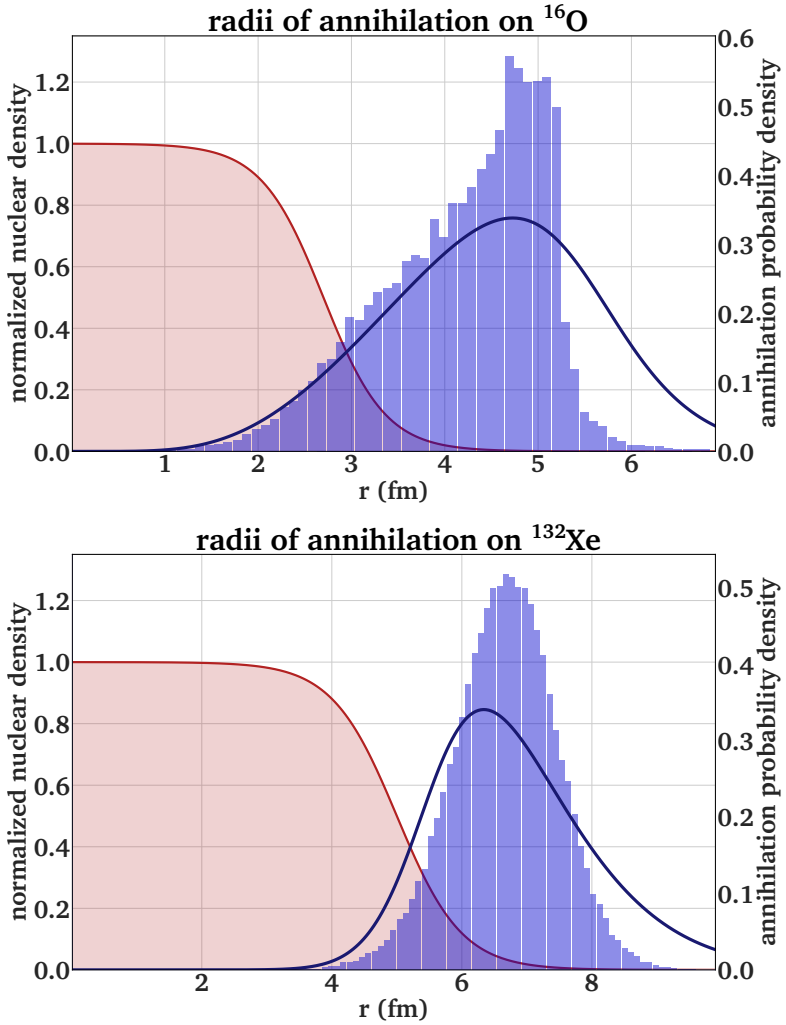

Figure 4.8.: Antiproton annihilation probability density simulated in GiBUU (blue histogram) compared to a prediction based on the antiprotonic radial wave function for absorption (blue line) for the examples of ^{16}O (*top*) and ^{132}Xe (*bottom*), with r as radial distance to the center of the nucleus.

The exact shape of the theoretical distributions cannot be reproduced in GiBUU, as its particle-based picture does not allow an annihilation more than about 3 fm away from the half-density radius. This effect is particularly pronounced for oxygen, where a sharp drop annihilation probability is observed above about 5.2 fm. However, the simulated distributions are set in a way that they reproduce the mean and median values of the calculated distributions, to account for the majority of annihilation events and thus to provide the best approximation possible. However, the underestimation of the amount of super-peripheral annihilations has to be taken into account for the evaluation for the discussion of the simulation results, as these annihilations are expected to suffer weakly from final state interactions, simply due to the smaller solid angle.

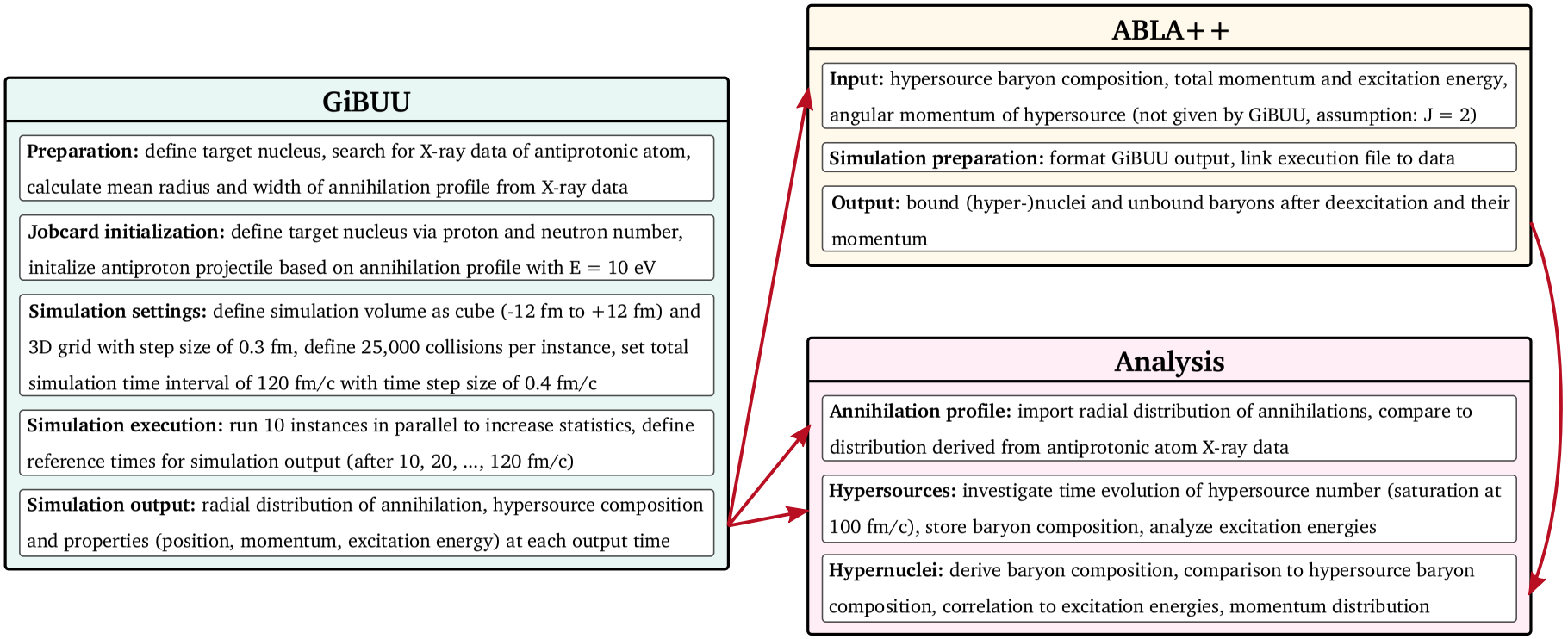

Figure 4.9.: Simulation workflow for the determination of hypernuclei production in peripheral antiproton annihilations.

Due to the exact initialization of the antiproton position with respect to the nucleus, the annihilation process occurs basically immediately after starting the propagation, *i.e.*, after short time intervals $t < 10$ fm/c. The annihilation itself is modeled with phenomenological branching ratios for the annihilation products, as summarized in Appendix D. The mesons produced as products of the annihilation then propagate and interact with residual nucleus, which can lead to the production of a Λ baryon via direct strangeness exchange with a primary kaon (*i.e.*, $K^- n \to \Lambda\pi^-$, $K^- n \to \Sigma^{-,0}\pi^{0,-}$, $K^- p \to \Lambda\pi^0$ and $K^- p \to \Sigma^{+,-,0}\pi^{-,+,0}$) or via s-$\bar{s}$ pair production induced by a pion (*i.e.*, $\pi p \to \Lambda K \pi$ and $\pi p \to \Sigma K \pi$, $\pi n \to \Lambda K \pi$ and $\pi n \to \Sigma K \pi$ for all possible charge combinations). The corresponding momentum-dependent cross sections for the individual processes and their implementation in GiBUU are detailed in [298]. For above mentioned reactions, they are taken from [304] for the pion-induced strangeness pair production and from [305] for the strangeness exchange with kaons. The propagation of all hadrons continues up to the cutoff time, which for the presented simulations is set to 120 fm/c. This limit was derived by considering the time evolution of the Λ baryon production for different cutoff times, and it was found that the number of produced Λs remains virtually constant for longer time steps. Additionally, a similar cutoff time of 130 fm/c was used in [306] for the investigation of double-Λ hypernuclei production at PANDA, where the same saturation in strangeness production is observed.

After the cutoff time, the properties of all remaining baryons are summarized. Based on the particle positions, the baryon density is defined on a three-dimensional grid, which is also used for the calculation of the nuclear mean fields for the propagation itself. For the performed simulations, a cubic grid extending from -16 to +16 fm with a step size of 0.4 fm was used. All particles, for which the baryon density at their position extends the predefined density limit of $\rho_L > 0.01\rho_0$ with the nuclear saturation density ρ_0, are then summarized to a so-called source. In most cases this source only comprises nucleons, but occasionally a produced Λ baryon fulfills this criterion, leading to the formation of a hypersource. This hypersource is interpreted as an excited hypernucleus, and its total energy E_{tot} is calculated as the sum over the single particle energies, composed by the kinetic energy and the local mean field potential. To then derive the excitation energy of the hypersource, the ground state mass M_{GS} of the respective ground state hypernucleus has to be subtracted from the total energy. Due to the lack of precision data, especially for heavier systems, the modified Bethe-Weizsäcker mass formula for hypernuclei, which is fitted to experimental data on hypernuclear binding and separation energies [307], is used. It calculates the hypernuclear binding total energy E_{B}, which represents the mass defect with respect to the sum over the baryon masses of the source. The excitation energy E_{ex} is then given by

$$E_{\mathrm{ex}} = E_{\mathrm{tot}} - M_{\mathrm{GS}} = E_{\mathrm{tot}} - \left(N \cdot m_{\mathrm{n}}c^2 + Z \cdot m_{\mathrm{p}}c^2 + m_{\Lambda}c^2 - E_{\mathrm{B}}\right). \tag{4.2}$$

The resulting excitation energies are typically in the order of 0 to 6 MeV/nucleon for the considered four target nuclei, as depicted in Fig. 4.10. In a few cases, the calculation also led to negative excitation energies, which could arise either from uncertainties in the propagation or the uncertainties of the fitted binding energies. As they are non-physical, they are not considered for further investigation.

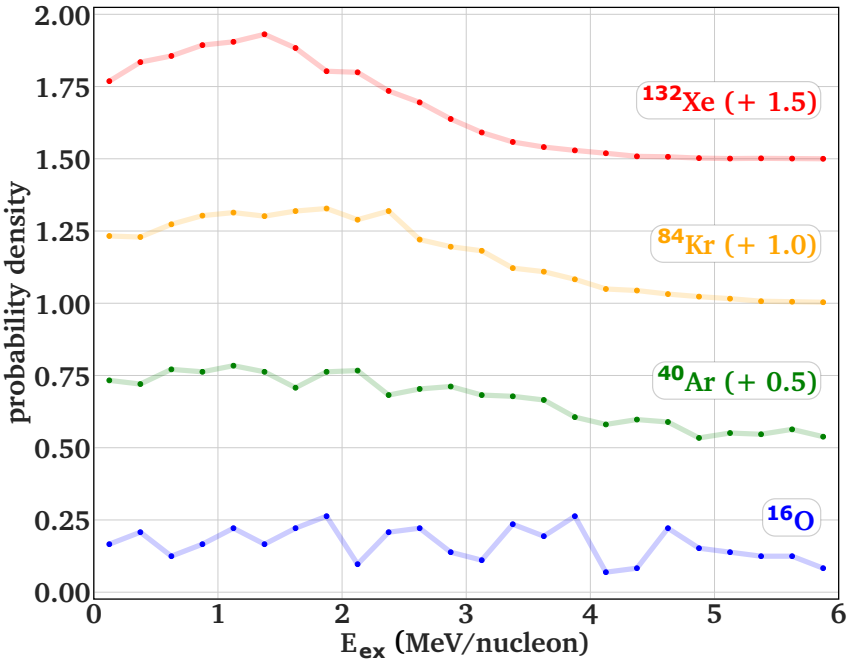

Figure 4.10.: Excitation energies per nucleon of the hypersources as simulated by GiBUU for the four different target nuclei. A vertical offset is added for better visibility.

Following the definition and identification of hypersources within GiBUU, the deexcitation towards ground-state hypernuclei is simulated with the ABLA++ evaporation and fission code. The deexcitation occurs via fission or evaporation of either protons, neutrons or other light particles based on the Weisskopf formalism [308], until the remaining excitation energy drop below the particle evaporation threshold. The decay width from an initial nucleus characterized by its excitation energy and angular momentum $E_\mathrm{i}\,(J_\mathrm{i})$ into a daughter nucleus with excitation energy $E_\mathrm{f}\,(J_\mathrm{f})$ via emission of a particle ν with a kinetic energy E_ν, spin θ_ν and mass m_ν is given by

$$\Gamma_\nu\left(E_\mathrm{i}\right) = \frac{\left(2\theta\nu+1\right)m_\nu}{\pi^2\hbar^2\rho_\mathrm{i}\left(E_\mathrm{i},J_\mathrm{i}\right)}\cdot\int_0^{E_\mathrm{i}-S_\nu-B_\nu}\sigma_\mathrm{c}\left(E_\nu\right)\rho_\mathrm{f}\left(E_\mathrm{f},J_\mathrm{f}\right)\left(E_\nu-S_\nu-B_\nu\right)\,\mathrm{d}E_\mathrm{f}. \tag{4.3}$$

Here, ρ_i and ρ_f are the level densities of both initial and daughter nucleus, $sigma_\mathrm{c}$ is the cross section for the inverse capture process, S_ν is the particle separation energy and B_ν its emission barrier. For a realistic description for charged particles, the latter two parameters are taken from the atomic mass evaluation (AME) from 2016 [309]. From that point on, the remaining energy is dissipated via γ-rays, until the hypernuclear ground state (g.s.) is reached. The code has initially been used to simulate the fission process of heavy nuclei such as $^{181}\mathrm{Ta}$ [310] and $^{208}\mathrm{Pb}$ [311], but the recent implementation of the hypernuclear extension of the Bethe-Weizsäcker mass formula also allowed to investigate the deexcitation of hypernuclei formed in nucleon-induced spallation reactions [312]. Here, the corresponding particle separation energies are calculated as the difference in binding energy between the initial (hyper-)nucleus and the residual (hyper-)nucleus after a potential evaporation.

As an input for the deexcitation calculation, ABLA++ requests the baryonic composition of the hypersource, the total excitation energy, the momentum, the kinetic energy as well as the angular momentum. The latter is not directly accessible in GiBUU, as the nucleons are treated individually, and has to be set manually. For the simulation presented in the following, it is assumed that predominantly states with low angular momentum are populated, and $J = 2$ is set for all deexcitation processes. As a result of the process, the properties of all evaporated particles as well as the residual (hyper-)nucleus are printed into a root-file as output, which in the following is used for the analysis.

4.3. Hypernuclear yields

Both the initial transport simulation in GiBUU and the subsequent deexcitation in ABLA++ provide a wide range of data. In the following, the focus is set on the properties of the populated ground state hypernuclei, especially the baryonic composition. The number of ground state hypernuclei obtained after the deexcitation is then compared to the number of initial annihilation processes to estimate production rates, which are then used to estimate run times of corresponding experiments. As a reference for the obtained yields, previous experimental and simulation studies are taken into account, which obtain Λ production rates per annihilation in the range of about 1 to 3 $\%$, depending on the target nucleus [313, 314].

Based on this expected Λ production rate, the number of initial low-energy collisions simulated in GiBUU was set to 250,000 for each target nucleus. Due to the peripheral initialization of the collision process, about 90 to 95 % of all collisions lead to an annihilation process, while the antiproton passes the nucleus without interaction in the remaining cases. The resulting number of annihilations should lead to an estimated production of more than 2,000 Λ baryons, which subsequently could be captured by the residual nucleons to form a hypersource. This is consistent with the observed Λ production rate in the simulations, which is summarized in Table 4.1 and ranges from about 1.36 % for the light $^{16}\mathrm{O}$ target up to 2.41 % for $^{132}\mathrm{Xe}$. These rates are consistent with previous measurements with stopped antiproton beams at LEAR [294, 295]. While only about 20 % of the produced Λ baryons lead to the production of a hypersource in $^{16}\mathrm{O}$, this ratio rises to almost 50 % for $^{132}\mathrm{Xe}$. This increase in production is caused by the higher number of residual nucleons in the heavier targets, which ultimately lead to a deceleration of the Λ baryon and the capture into the remaining nucleus. It has to be noted that the uncertainties quoted in this table and all following tables is a pure statistical uncertainty, based on the assumption that the production of Λ baryons and hypersources follows a Poisson distribution, as all simulations are performed within the standard parallel-ensemble method over the same time interval.

Table 4.1.: Simulation Statistics of the antiproton annihilations in GiBUU. Hypersources (HS) are excited hypernuclei, which are defined by phase space coalescence. Only statistical uncertainties are presented.

Nucl.	annihilations	Λs	Λ rate in %	HSs	HS rate in %	HS / Λ
^{16}O	223,344	3,039 $\pm$ 55	1.36 $\pm$ 0.02	601 $\pm$ 25	0.27 $\pm$ 0.01	0.198
^{40}Ar	231,893	4,007 $\pm$ 63	1.73 $\pm$ 0.03	1,325 $\pm$ 36	0.57 $\pm$ 0.02	0.331
^{84}Kr	249,731	5,566 $\pm$ 75	2.23 $\pm$ 0.03	2,435 $\pm$ 49	0.98 $\pm$ 0.02	0.437
^{132}Xe	249,858	6,032 $\pm$ 78	2.41 $\pm$ 0.03	2,915 $\pm$ 54	1.17 $\pm$ 0.02	0.483

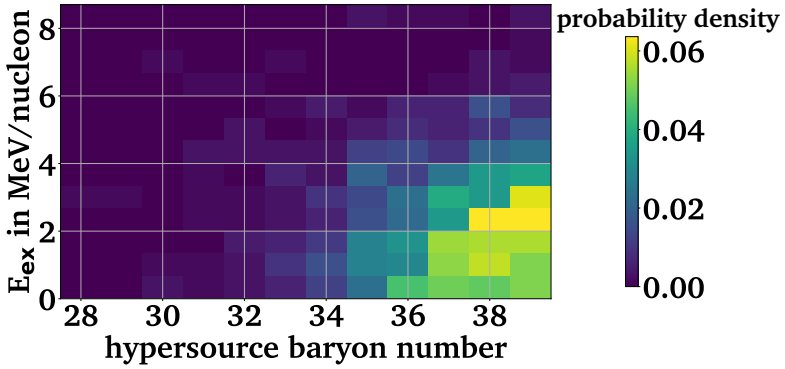

Figure 4.11.: 2D-histogram of the hypersource baryon number and excitation energy distribution for the target nucleus ^{40}Ar.

The excitation energies of the produced hypersources follow the distributions depicted in Fig. 4.10. Typically, the hypersources are produced in a state with a baryon number close to the initial nucleus and with low excitation energy, but occasionally hypersources with significantly lower baryon numbers and higher excitation energies are populated, as indicated in Fig. 4.11. In the subsequent deexcitation simulation in ABLA++, the higher excitation energies will lead either to the population of lighter ground state hypernuclei or the evaporation of the Λ during deexcitation, thus preventing the population of a g.s. hypernucleus. In contrast to that, low excitation energies will lead to final g.s. hypernuclei with baryon numbers close to the initial nucleus. A depiction of the correlation of the initial baryon number of the hypersource and the baryon number after deexcitation, depending on the excitation energy of the hypersource, is depicted in Fig. 4.12, again for the case of ^{40}Ar.

This figure also indicates, that a wide range of baryon numbers A_{gs} for the g.s. hypernuclei is accessible, with a maximum number $A_{\mathrm{gs,max}} = A_{\mathrm{target}} - 1 = 39$ for the case of ^{40}Ar and a significant population of hypernuclei with baryon numbers down to $A_{\mathrm{gs}} \approx A_{\mathrm{target}} - 15$, while lighter hypernuclei (except for free Λ baryons indicated by a baryon number of 1) are only sparsely populated. While this low mass region of hypernuclei is not accessible by annihilations on ^{40}Ar, the use of the lighter ^{16}O target leads to the production of hypernuclei with baryon numbers $A_{\mathrm{gs}} \leq 15$. Similarly, the use of the heavier ^{84}Kr and ^{132}Xe targets provide access to heavier hypernuclei, a region where the hypernuclear properties are currently only sparsely known.

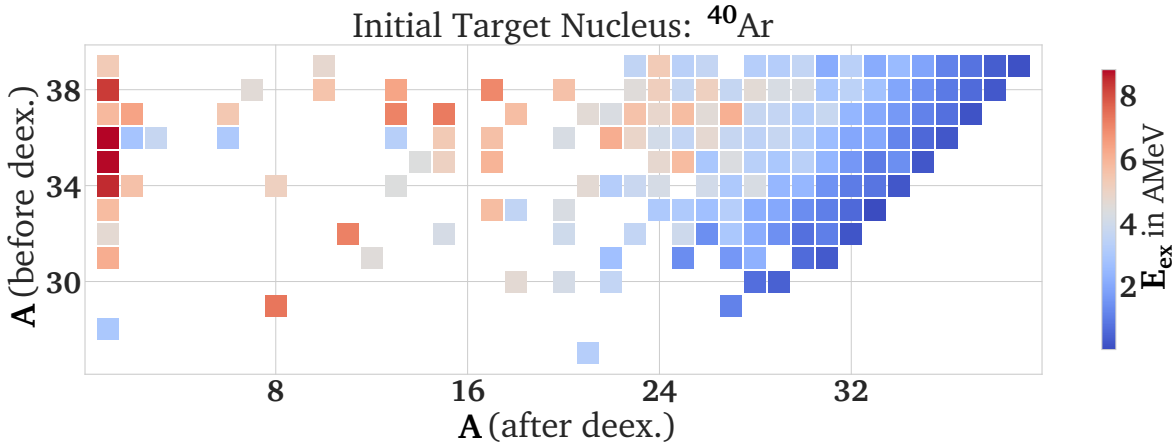

Figure 4.12.: Correlation of the initial baryon number of the hypersources before deexcitation and the final ground state hypernuclei after deexcitation depending on the initial excitation energy for the target nucleus ^{40}Ar. $A = 1$ corresponds to a free Λ, which was emitted during the deexcitation process.

Combining the g.s. hypernuclear yields of the four considered target nuclei, almost the full hypernuclear chart along the valley of stability up to ${}^{131}_{\Lambda}\mathrm{Xe}$ becomes accessible, as depicted in Fig. 4.13. The produced g.s. hypernuclei are here indicated by their proton (Z) and neutron (N) number, and the production rate per annihilation is indicated with the color coding. While for all four targets regions with high production rates of about 1 to 2 per mill for individual hypernuclear isotopes arise, indicated by bright red color, the general rate of production of individual hyperisotopes is in the order of about 10^{-5} per annihilation, with a minimum resolvable production rate of about $5 \cdot 10^{-6}$. The potential production of less abundant hypernuclei is not resolved due to limitation to about 200,000 annihilation events.

The simulations indicate the production of over 200 new hypernuclei in the medium-mass region of the hypernuclear chart. In Table 4.2 the five most abundant g.s. hypernuclei and their production rates are summarized for each target nucleus. The rate of production for a hypernucleus of interest reaches up to a few 10^{-4} per annihilation. Consequently, at least tens of millions antiproton-nucleus annihilations have to be considered to provide sufficient statistics for a significant measurement. In case of the ELENA ring, up to 10^7 antiprotons are provided in a bunch every 120 seconds, so that a measurement of a special hypernucleus could be performed within a few hours for the stable reference nuclei considered. The properties of the produced hypernuclei can then be accessed via spectroscopy. While the light hypernuclei produced for oxygen decay predominantly via meson emission, the non-mesonic decay $\Lambda N \rightarrow NN$ is strongly dominant for the heavier hypernuclei originating from argon, krypton and xenon [315].

In the next step, the momenta of the produced hypernuclei are investigated. Considering a lifetime of about 200 ps, similar to the free Λ, the momentum guides the distance a hypernucleus travels prior to its weak decay. The momenta of the g.s. hypernuclei are provided as an output in ABLA++, and the distribution of the momenta for the hypernuclei is depicted in Fig. 4.14. The typical range of momenta is in the order of a few hundreds

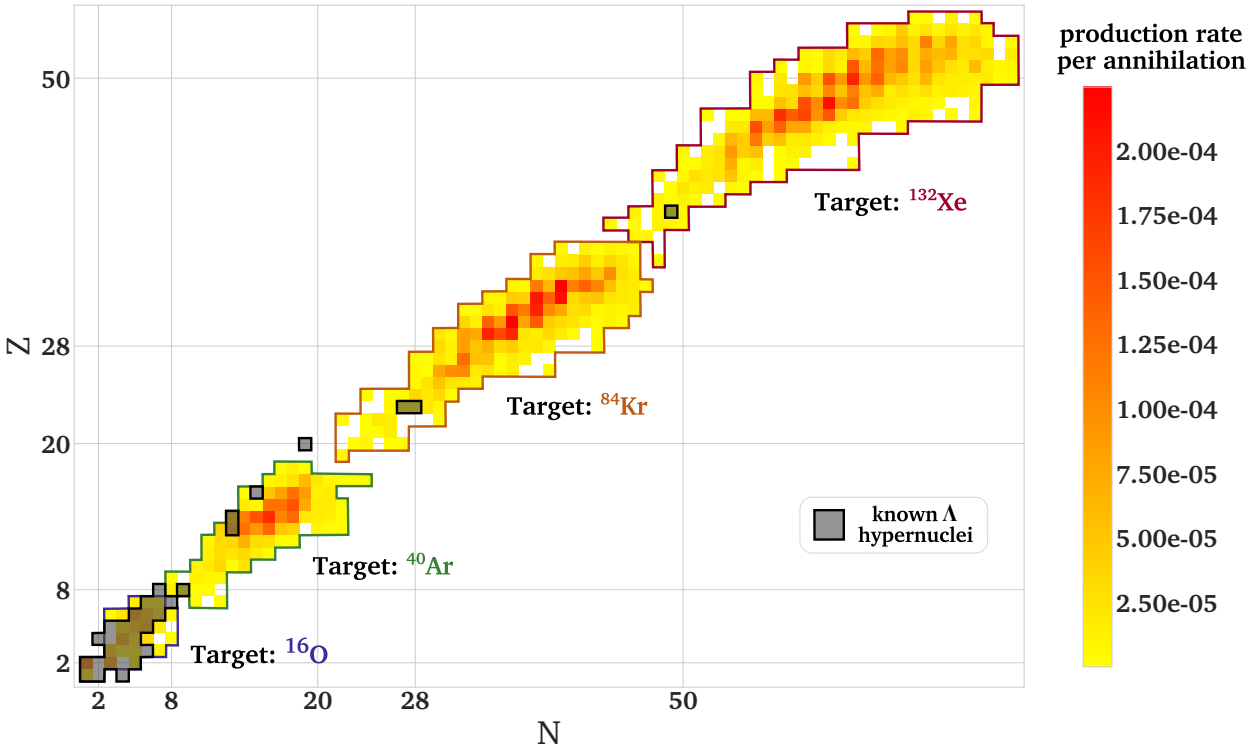

Figure 4.13.: Yields of different hypernuclear isotopes per annihilation on the respective target nucleus. The landscape of already investigated hypernuclei is indicated by gray shading.

of MeV/c with mean values of about 160 MeV/c for hypernuclei from ^{16}O, 220 MeV/c for ^{40}Ar, 320 MeV/c for ^{84}Kr and 370 MeV/c for ^{132}Xe. Assuming that the hypernuclear mass is similar to the mass of the initial nucleus within a factor of two, the effective range before decay can be estimated as about 600 µm for hypernuclei from ^{16}O, 350 µm for ^{40}Ar, 250 µm for ^{84}Kr and 180 µm for ^{132}Xe. It can be concluded that the weak decay of the produced hypernuclei occurs in first order at the location of its production.

4.4. Production mechanism

Following the investigation of the range of accessible hypernuclei and their momenta in the previous section, the production mechanisms leading to the formation of hypersources in GiBUU are investigated. As introduced in Sec. 4.1, the hypernuclei are produced either in a direct strangeness exchange reaction with a kaon produced in the annihilation (*i.e.*, $K^-n \to \Lambda\pi^-$, $K^-n \to \Sigma^{-,0}\pi^{0,-}$, $K^-p \to \Lambda\pi^0$ and $K^-p \to \Sigma^{+,-,0}\pi^{-,+,0}$) or via strangeness pair production in the interaction with a pion originating from the annihilation (*i.e.*, $\pi p \to \Lambda K\pi$ and $\pi p \to \Sigma K\pi$, $\pi n \to \Lambda K\pi$ and $\pi n \to \Sigma K\pi$ for all possible charge combinations).

To determine the dominant strangeness production mechanism, the cross sections for the two different paths were individually set to zero, while the other path remains open including the corresponding momentum-dependent cross sections implemented in GiBUU [298].

Table 4.2.: Most abundant g.s. hypernuclei after deexcitation in ABLA++ for the four reference nuclei.

^{16}O		^{40}Ar		^{84}Kr		^{132}Xe	
nucleus	p in 10^{-5}	nucleus	p in 10^{-5}	nucleus	p in 10^{-5}	nucleus	p in 10^{-5}
$^{10}_{\Lambda}$B	9 ± 2	$^{29}_{\Lambda}$Al	19 ± 3	$^{65}_{\Lambda}$Cu	28 ± 3	$^{109}_{\Lambda}$Ag	21 ± 3
$^{7}_{\Lambda}$Li	8 ± 2	$^{32}_{\Lambda}$Si	15 ± 3	$^{72}_{\Lambda}$Ge	24 ± 3	$^{113}_{\Lambda}$In	19 ± 3
$^{10}_{\Lambda}$Be	7 ± 2	$^{28}_{\Lambda}$Al	15 ± 3	$^{71}_{\Lambda}$Ga	21 ± 3	$^{104}_{\Lambda}$Pd	18 ± 3
$^{11}_{\Lambda}$B	6 ± 2	$^{31}_{\Lambda}$Al	13 ± 2	$^{69}_{\Lambda}$Ga	20 ± 3	$^{106}_{\Lambda}$Pd	16 ± 3
$^{9}_{\Lambda}$Be	5 ± 2	$^{28}_{\Lambda}$Mg	13 ± 2	$^{62}_{\Lambda}$Ni	19 ± 3	$^{107}_{\Lambda}$Ag	16 ± 3

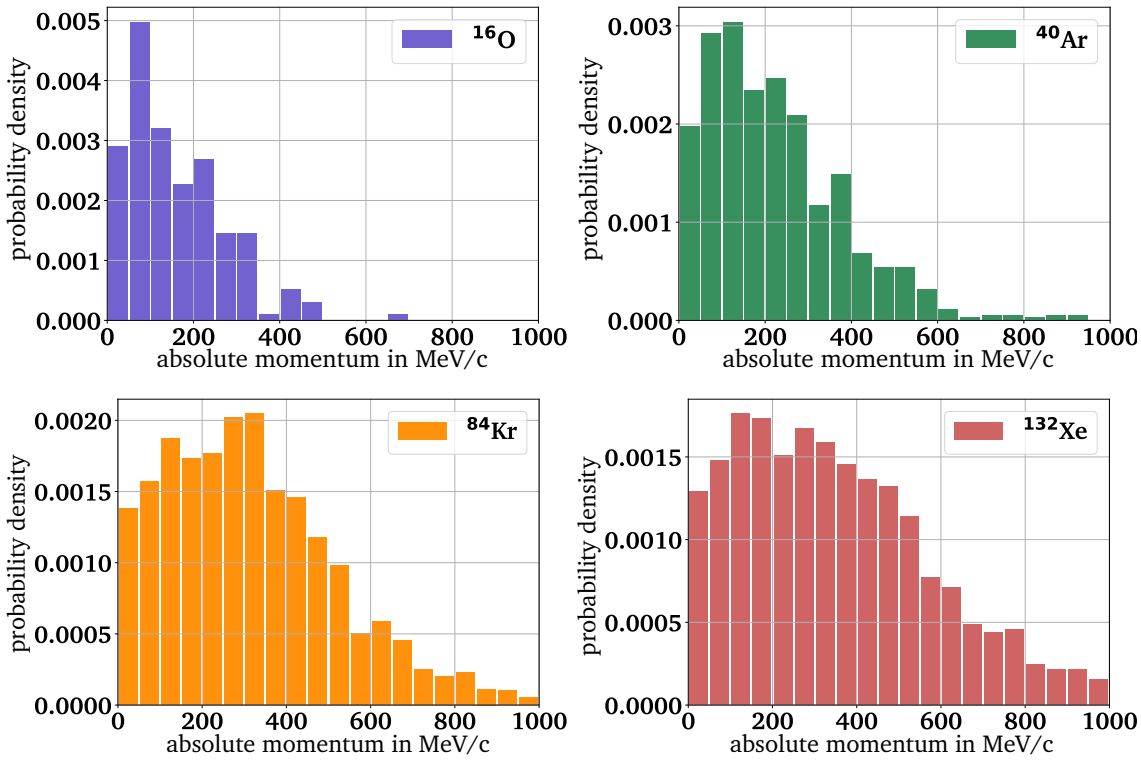

Figure 4.14.: Momentum distribution for the g.s. hypernuclei originating from annihilations on ^{16}O (*left top*), ^{40}Ar (*right top*), ^{84}Kr (*left bottom*), and ^{132}Xe (*right bottom*).

Simulations including the two blocked pathways were performed to derive the resulting rates for Λ and hypersource production for the cases of annihilations on ^{40}Ar and ^{84}Kr. Apart from the blocked cross sections, the same initial conditions for the reactions are considered as in the previous section. The resulting Λ baryon and hypersource production rates are summarized in Table 4.3.

For both nuclei, the direct strangeness exchange is strongly dominant, contributing to about 78 % of Λ baryons and 82 % of hypersources for annihilations on ^{40}Ar and to about 72 % of Λ baryons and 82 % of hypersources for ^{84}Kr. The Λs produced in a direct strangeness exchange have a higher probability of about 40 % to lead to the formation of a hypersource,

Table 4.3.: Simulation Statistics of the strangeness production from antiproton annihilations in GiBUU assuming only strangeness exchange (SE) or non-strange meson interactions (NSMI).

Nucleus	channel	annihilations	Λs	Λ rate in %	HSs	HS rate in %
^{40}Ar	SE	9,230	180 ± 13	1.95 ± 0.15	66 ± 8	0.71 ± 0.09
	NSMI	9,217	50 ± 7	0.54 ± 0.08	14 ± 4	0.15 ± 0.04
^{84}Kr	SE	9,994	230 ± 15	2.30 ± 0.15	102 ± 10	1.02 ± 0.10
	NSMI	9,995	89 ± 9	0.89 ± 0.09	22 ± 5	0.22 ± 0.05

while this probability is at about 25 % for the strangeness pair production. This discrepancy is caused by the lower Λ momentum after a strangeness exchange, leading to a higher probability of staying in the nuclear volume.

Based on the kaon pair production probability of 5 % in an antiproton-nucleon annihilation, about every second kaon leads to the formation of Λ baryon for the heavier hypernuclei. This can be illustrated by considering the effective solid angle of almost 2π for a final state interaction with the residual nucleus following a peripheral annihilation. For smaller target nuclei, the effective solid angle is reduced, leading to a reduction of the Λ production rate per kaon to about 40 % in the case of ^{40}Ar.

The ratio between the direct strangeness exchange and the pion-induced strangeness production is similar for both nuclei, leading to the conclusion that the Λ and hypersource production mechanism is mostly independent from the initial target nucleus, and that the direct strangeness exchange is the dominant mechanism.

4.5. Isotope effect

The four target nuclei considered up to this point (*i.e.*, ^{16}O, ^{40}Ar, ^{84}Kr and ^{132}Xe) as the most abundant isotope of their respective isotopic chain lead to the formation of a wide range of g.s. hypernuclei across the hypernuclear chart. However, it is expected that the baryonic composition of the hypernuclei is strongly correlated with the proton and neutron number of the initial target isotope. In case of the argon chain, the symmetric ^{36}Ar isotope with equal proton and neutron number is also stable, even though the natural abundance is only at about 0.3 %. Similarly, the stable xenon isotope with the lowest neutron number is ^{124}Xe with an abundance of about 0.1 %. Both these isotopes have a lower neutron number than the previously considered isotopes, and the impact of the lower initial neutron number on the hypernuclear yields is investigated.

As the initial nucleon number of the neutron-deficient isotopes is only smaller than the nucleon number of the most abundant isotope by 10 $ or less, it is expected that the overall simulation statistics (*i.e.*, strangeness and hypernuclei production rate) remain at the same level. This is also observed in the simulation, where the absolute rate of hypernucleus

production remains at about 0.55 % for $^{36}\mathrm{Ar}$ and 1.14 % for $^{124}\mathrm{Xe}$. However, the yield of individual hyperisotopes differs significantly, is indicated in Fig. 4.15.

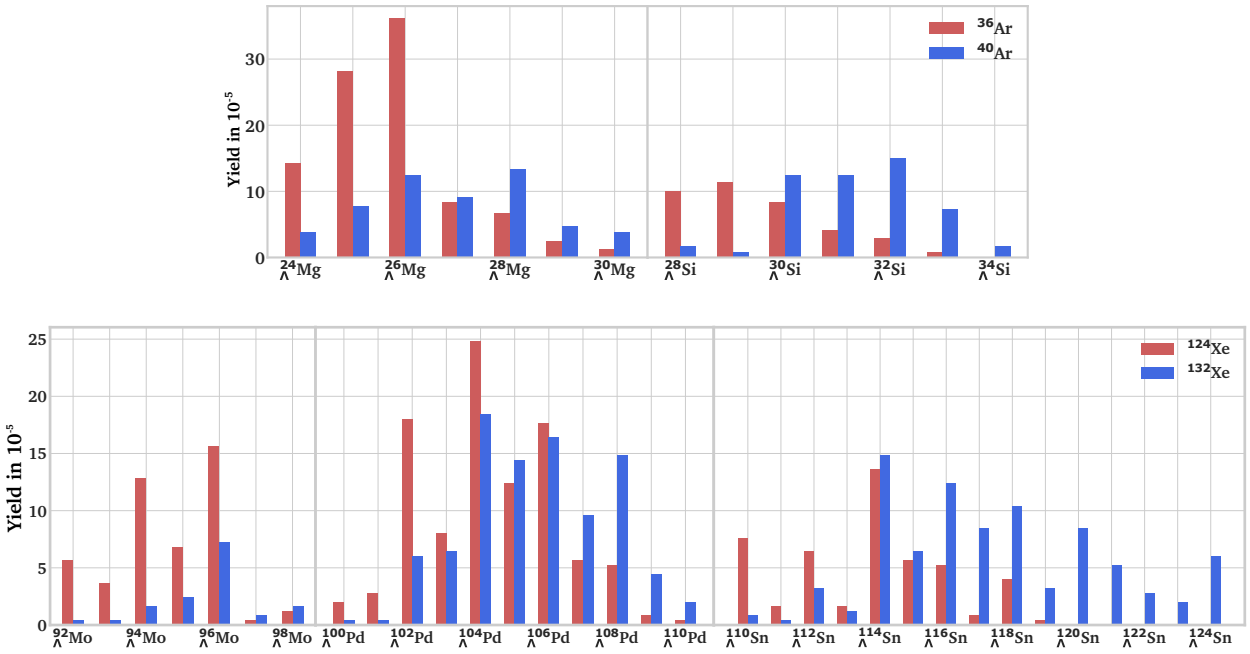

Figure 4.15.: Impact of the initial target nucleus on the yields along different hyperisotopic chains. The neutron-deficient ^{124}Xe favors the production of lighter and more neutron-deficient isotopes in the $_{\Lambda}$Mo and $_{\Lambda}$Pd chains, while ^{132}Xe provides high yields in neutron-rich and heavy isotopes along the $_{\Lambda}$Pd and $_{\Lambda}$Sn chains. A similar behavior is also observed in the yields from ^{36}Ar and ^{40}Ar.

In this figure, the production rate per annihilation of different isotopes along hyperisotopic chains are depicted for both the neutron-deficient and the most abundant initial target isotopes. In case of $^{36}\mathrm{Ar}$ and $^{40}\mathrm{Ar}$, the yields along the $_{\Lambda}\mathrm{Mg}$ ($Z = 12$) and the $_{\Lambda}\mathrm{Si}$ ($Z = 14$) chains are plotted, and the neutron-deficient $^{36}\mathrm{Ar}$ target leads to a strong enhancement in the production of the more neutron- and proton-deficient isotopes along the magnesium chain. This effect is even more pronounced in the case of $^{124}\mathrm{Xe}$ and $^{132}\mathrm{Xe}$, where the lighter xenon isotopes strongly enhances the production of the neutron-deficient $_{\Lambda}\mathrm{Mo}$ ($Z = 42$) chain, while the $^{132}\mathrm{Xe}$ target leads to a higher abundance of neutron-rich $_{\Lambda}\mathrm{Sn}$ ($Z = 50$) isotopes. Overall, the use of the neutron-deficient target isotopes leads to the population of the neutron-deficient hyperisotopes, even though the barycenter of high production rates shifts to slightly lower proton numbers, leading to a low abundance of hyperisotopes with a baryon number $N_{\mathrm{i}} - 1$ with the initial target nucleus nucleon number N_{i}. To summarize, the use of the stable isotopes with the highest and lowest neutron number as targets yield the possibility to cover a wide range of hypernuclei along hyperisotopic chains.

4.6. Experimental implementation

In the previous sections, the production of hypernuclei based on peripheral annihilations is discussed. The simulated rates of production are in the order of 10^{-5} per annihilation for individual hyperisotopes and a wide range of currently undiscovered hypernuclei can be populated by combining different stable target nuclei. In this section, an idea for the implementation of a corresponding experiment is discussed.

Similarly to the PUMA experiment, the requirement of low-energy antiprotons for the formation of the antiprotonic atoms leaves the Antimatter Factory of CERN as only facility for such an experiment. As the ELENA ring provides up to 10^7 antiprotons per bunch, the produced number of an individual hypernucleus of interest is in the order of tens to hundreds - assuming that about 50 % of the antiprotons are transmitted to the experiment and form an antiprotonic atom. Considering that an antiproton bunch is provided every two minutes, several thousands of a specific hypernucleus of interest are produced every day.

The actual number of detectable hypernuclei is additionally limited by the pionic weak decay rate of the hypernucleus of interest, which is in the order of a few percent for hypernuclei with a baryon number of $A > 25$ [315] as well as the detection efficiency. To characterize a produced hypernucleus, a multi-detector setup is required, which allows the measurement of the γ-rays emitted during the deexcitation of the hypernuclei as well as the weak decay pion and the residual nucleus to perform an invariant mass measurement of the ground state mass. Each of these particles require a dedicated detector. A schematic overview over the foreseen experimental apparatus is depicted in Fig. 4.16.

In case of the charged decay pions, the charge and mass are derived from their curvature within a strong magnetic field based on the induced signals on silicon tracker layers (80 µm thickness each) and a low-gain avalanche detector (LGAD) with picosecond resolution for the timing information and the momentum reconstruction. Similarly to the PUMA experiment, a large-acceptance detector has to be placed radially around the antiproton trapping volume, in which the antiprotonic atoms are formed. As the weak decay pions typically have momenta in the order of 100 MeV/c [316], the pion detection system has to be mounted within the vacuum chamber to prevent losses between the production location and the detector, thus maximizing the detection efficiency.

For prompt γ-ray detection, the vacuum chamber has to be surrounded by a plastic scintillator array with a sensitivity to the typical photon energies of MeV for the hypernuclear transitions. Possible scintillator materials would be cerium-doped gadolinium aluminum gallium garnet (GAGG(Ce)) or cerium-doped lanthan bromide (Ce:$LaBr_3$), whose performances in nuclear gamma-ray spectroscopy were investigated in [317].

Finally, the decay recoil nucleus has to be detected by an axial time-projection chamber, placed downstream of the hypernuclear site of formation. The active volume of the detector, which houses the drift gas, is separated from the XHV in the vacuum chamber by a $\sim$ 30 nm thick silicon nitride membrane. Based on this thickness, the energy loss of the stripped recoil nuclei by inelastic collisions with electrons can be calculated via the Bethe-Bloch formula

$$-\frac{\mathrm{d}E}{\mathrm{d}x} = \frac{4\pi n z^2}{m_\mathrm{e} c^2 \beta^2} \cdot \left(\frac{e^2}{4\pi\epsilon_0}\right)^2 \cdot \left[\ln\left(\frac{2m_\mathrm{e}c^2\beta^2}{I(1-\beta^2)}\right) - \beta^2\right]. \tag{4.4}$$

Here, z and β are the charge number and the velocity of the recoil nucleus, $n \approx 1.2 \cdot 10^3\,\mathrm{nm}^{-3}$ is the electron density of the membrane material and $I \approx 100\,\mathrm{eV}$ its mean excitation potential. Additional contributions to the energy loss arise from nuclear interactions within the membrane. The expected energy loss for the stripped recoil nuclei is simulated with the stopping and range of ions in matter (SRIM) simulation code [318]. Assuming the simulated mean momenta of the g.s. hypernuclei from Sec. 4.3, the absolute energy loss through the membrane can be derived. As an estimate, the residual nucleus after decay is assumed to be fully stripped and differs from the initial target nucleus only by a neutron number smaller by 1, and the resulting energy loss through the 30 nm thick membrane is summarized in Table 4.4.

Table 4.4.: Energy loss of the weak decay recoil nuclei in the 30 nm thick silicon nitride membrane of the axial time-projection chamber with contributions of energy loss from interaction with electrons (index e) and nuclei (index n).

Nucleus	p [MeV/c]	E_kin [keV]	$-\frac{\mathrm{d}E}{\mathrm{d}x}_\mathrm{e}$ [keV/nm]	$-\frac{\mathrm{d}E}{\mathrm{d}x}_\mathrm{n}$ [keV/nm]	$-\mathrm{d}E_\mathrm{tot}$ [keV]
$^{15}\mathrm{O}^{8+}$	160	910	1.0	< 0.1	30
$^{39}\mathrm{Ar}^{18+}$	220	660	1.0	0.3	39
$^{83}\mathrm{Kr}^{36+}$	320	660	0.8	1.3	63
$^{131}\mathrm{Xe}^{54+}$	370	560	0.9	2.6	105

Based on the results it can be concluded that the majority of the produced weak decay recoil nuclei should be able to penetrate through the membrane to enter the sensitive detection volume, especially in the range of lighter recoil nuclei up to a mass number of A $\sim$ 50. As expected, the relative energy loss is higher for the heavier recoil nuclei originating from annihilations on $^{132}\mathrm{Xe}$, where hypernuclei produced in a very low-momentum state might not be detectable due to absorption in the TPC membrane.

After the recoil nucleus passes through the detector membrane, it ionizes the drift gas and the electrons drift towards the pad plane for amplification and detection. In the strong axial magnetic field, the ion's trajectory is curved due to the Lorentz force, and its charge-to-mass ratio can be derived from a momentum and magnetic rigidity measurement. This requires a very good position resolution of better than 100 µm for the detector to resolve the tracks curvature. The full reconstruction of the ion's momentum and charge-to-mass ratio based on the observed tracks requires a dedicated scheme, which will not be detailed in this work.

The full detector is comprised of three detection systems for the γ-rays, the decay pions and the recoil nuclei, surrounding the antiprotonic atom formation volume in the center of system. Here, the antiprotons, which previously would be cooled and decelerated in a buffer trap, would be overlapped with stable target nuclei, rather than using exotic ions as in the case of the PUMA experiment. This increases the rate of observable annihilations significantly and also led to the choice of the considered target nuclei for the performed

simulations. The full setup would be placed within the warm bore of a strong solenoid. For the sketch, the bore diameter of the PUMA solenoid is considered, which could be re-used for the hypernuclear experiments after the PUMA experiment has successfully performed all foreseen measurements.

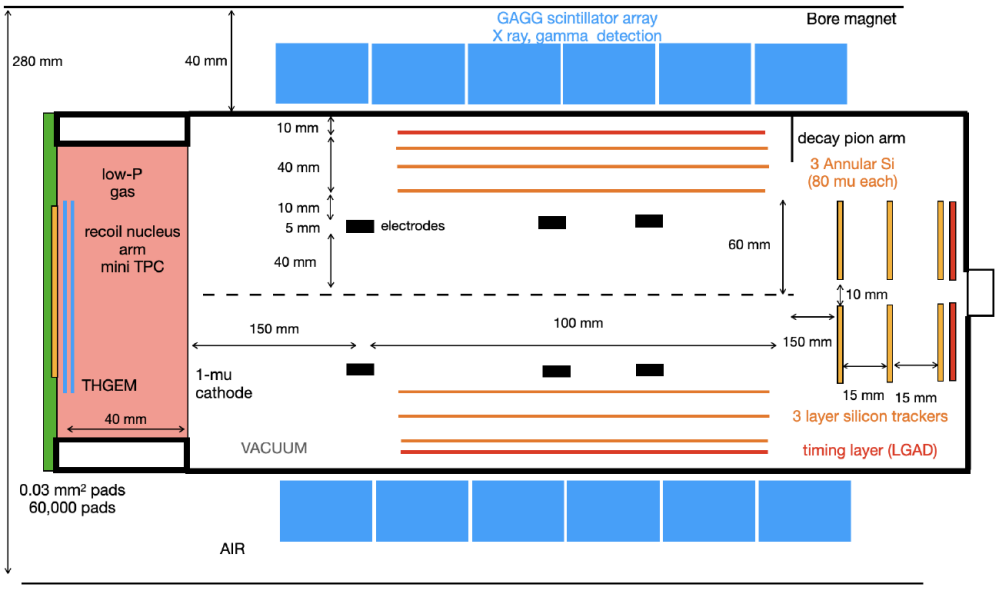

Figure 4.16.: Sketch of the multi-detection system foreseen for hypernuclear studies based on low-energy antiprotons. The dimensions of the components are not in scale. A detailed description of the subsystems is given in the text. Figure by courtesy of Prof. Dr. Obertelli.

Based on the successful detection of the decay pion and the recoil nucleus as well as measuring their masses (m_π, M_N) and momenta ($\vec{p_\pi}$, $\vec{p_\mathrm{N}}$), the initial hypernucleus can be reconstructed via an invariant mass measurement. The hypernuclear mass M_HN is then given by

$$M_\mathrm{HN}^2 = m_\pi^2 + M_\mathrm{N}^2 + \sqrt{m_\pi^2 + p_\pi^2 c^2}\sqrt{M_\mathrm{N}^2 + p_\mathrm{N}^2 c^2} + 4\vec{p_\pi}\vec{p_\mathrm{N}}. \tag{4.5}$$

To now estimate the resolvable count rate of a specific hyperisotopes with a production rate $p_\mathrm{HN} = 10^{-5}$ per annihilation, the antiprotonic atoms formation probability $p_\mathrm{AA} = 0.5$, the pionic weak decay branching ratio $p_\mathrm{pwd} = 0.05$ (assuming $A < 50$ for the produced hypernucleus) and the detection efficiency have to be added. Preliminary simulations indicate an efficiency of $\epsilon_\pi = 0.78$ for the pion detection and tracking. In case of the recoil nucleus, due to the strong magnetic field, the probability to be boosted towards the downstream detector is $p_\mathrm{b} = 0.5$. The probability of the recoil nucleus to enter the TPC and to lead to the formation of a resolvable track is estimated to $p_\mathrm{t} = 0.6$, and the probability to correctly identify the recoil nucleus and its momentum is estimated to be $p_\mathrm{id} = 0.5$, leading to a total recoil nucleus detection efficiency of $\epsilon_\mathrm{nuc} = p_\mathrm{b} p_\mathrm{t} p_\mathrm{id} = 0.15$. Consequently, the resolvable count rate per annihilation p_tot is given by

$$p_\mathrm{tot} = p_\mathrm{HN} \cdot p_\mathrm{AA} \cdot p_\mathrm{pwd} \cdot \epsilon_\pi \cdot \epsilon_\mathrm{nuc} \approx 3 \cdot 10^{-8} \tag{4.6}$$

Assuming that each antiproton bunch of ELENA provides $5 \cdot 10^6$ antiprotons and up to 720 bunches of antiprotons are provided by ELENA every day, the absolute number of resolvable hypernuclei per day is given by $N_{\mathrm{HN,day}} \approx 100$. This number corresponds to a conservative estimate, as the lowest simulated hypernucleus production rate of 10^{-5} per annihilation and a high baryon number of A $\sim$ 40, leading to a small pion decay branching ratio, were considered for this estimate. For lighter and more abundant hypernuclei, this number could be increased by up to two orders of magnitude.

In this chapter, the production of single-Λ hypernuclei from the peripheral annihilation of an antiproton following the formation of antiprotonic atoms has been investigated. The simulations were performed in two steps and indicate the production of a wide range of undiscovered hypernuclei with a typical production rate of a few 10^{-5} per annihilation. A special focus was set on their baryonic composition, which can be tuned by considering different isotopes of the stable gaseous target nuclei, and their momenta, which have to exceed a few tens of MeV/c so that the pionic decay recoil nucleus can be detected. A preliminary scheme for a dedicated experiment to study the formation of hypernuclei based on their production in antiprotonic atoms at the Antimatter Factory has been worked up, and the implementation and construction of the experimental components is in reach within the next years.

5. Conclusion and outlook

The PUMA experiment at CERN aims at probing the ratio of neutrons to protons in the density tail of stable and unstable nuclei using low-energy antiprotons [92]. Currently, the experiment is under construction. This thesis contributes to PUMA via the development of the Penning trap system as the core of the transportable experimental setup.

As the first part of this thesis, the cryogenic trap assembly of PUMA has been developed and constructed. The double Penning trap assembly requires cooling to cryogenic temperatures to provide an extreme high vacuum (XHV) of about 10^{-17} mbar, corresponding to a residual gas density of less than 20 particles per cm^3, which can only be achieved via cryosorption. The cryostat and trap assembly, which includes a conductance barrier for a reduction of the conductance into the trap volume and a cylinder shutter for the blocking of the cryostat aperture, has been designed. The resulting temperature and pressure profile along the setup has been investigated via simulations performed in COMSOL 2015 to assure that the requirements can be fulfilled. The thermal simulations indicate that the full trap tower and its surrounding copper chamber are cooled to a temperature of 4.4 K by the two coldheads of system. The subsequent pressure simulations are split in two different stages. In the first step, the evolution of the on-axis residual gas number density from the end to the antiproton beamline up to the entrance of the 4 K copper stage has been investigated. The number density is connected to the pressure via the ideal gas equation and the simulation leads to an input pressure in the order of $1 \cdot 10^{-11}$ mbar at the cryostat entrance. From this point on, the evolution of the number density up to the electrical feedthrough flange of the trap tower is simulated in the second step. An open cryostat aperture limits the number density in the collision trap to about 60 cm^{-3}, corresponding to a pressure of $3 \cdot 10^{-17}$ mbar, and achieves pressures below 10^{-17} mbar in the storage trap. The inclusion of the cylinder shutter as aperture blocking improves the number density across the full length of the system by more than one order of magnitude, reaching down to number densities of 0.1 cm^{-3} in the storage trap, which translates to a pressure below 10^{-19} mbar and storage times of about 70 years. After benchmarking the setup with simulations, the first mechanical assembly of the system was successfully performed, and the system is currently under preparation for the first pump-down at room temperature and subsequent tests at cryogenic temperature.

To optimize the transmission of antiprotons into the PUMA trap, ion optical simulations were performed in SIMION. Based on the antiproton bunch properties at the end of the LNE51 beamline, which are described by MAD-X simulations performed by the ion optics department of CERN, the propagation and deceleration of the antiproton bunch were investigated. The simulations indicate an antiproton transmission rate of 91 % into the storage trap, while most of the losses occur at the conductance barrier - right in front of the trap tower - and within the low-voltage pulsed drift tube. To benchmark the ion optical simulations

and the operation of the 96 kV pulsed drift tube, transmission tests were performed with the antiproton beamline at ELENA. Here, the deceleration of the antiproton bunch to 4 keV was shown to be successful based on an excellent agreement of the foregoing ion optical simulation and the measured difference in time of flight up to a mounted detector. In contrast to that, the measured beam intensities at the detector were a factor of two smaller than expected, limiting the transmission to about 50 %. Subsequent conceptional simulations raised the suspicion that the high voltage electrodes are not perfectly aligned, which should be investigated further.

Following the first pressure and trapping tests on the cryogenic trap assembly at Darmstadt, the cryostat and trap will be transported to CERN for the assembly of the full experimental setup in spring 2024. There, the trap assembly and the detection system will be mounted within the bore of the PUMA solenoid and the setup will be connected to the antiproton beamline of PUMA. Initially, the antiproton transmission into the trap will be optimized and the antiproton trapping and accumulation scheme as well as the detection system will be benchmarked. After successful trapping of antiprotons over a time span of days, the first transportation tests and physics experiments with stable ions are foreseen at the Antimatter Factory in autumn 2024, before experiments with unstable nuclei can be performed at ISOLDE in 2025.

The potential benefit of low-energy antiprotons goes beyond the physics of neutron skins and halos at the core of the PUMA experiment, as the interaction of the annihilation products with the residual nucleus can lead to the production of Λ baryons and single-Λ hypernuclei. To estimate the range of accessible hypernuclei and their production rates, simulations were performed in a two-step process [206]. In the first step, the initial annihilation and the subsequent production and capture of Λ baryons was investigated in GiBUU. The obtained rates of Λ production range from 1.36 % per annihilation for a $^{16}\mathrm{O}$ target up to 2.41 % for $^{132}\mathrm{Xe}$. They predominantly arise from direct strangeness exchange with kaons produced in the annihilation and agree well with the rates obtained at the previous PS-177 experiment at LEAR. Based on a coalescence criterion, these Λ baryons are then attributed to a hypersource as an excited hypernucleus with production rates of 1.2 % per annihilation or below. In the second step, the deexcitation of the hypersource via particle evaporation and γ-ray emission is simulated in ABLA++. The resulting ground state hypernuclei cover a wide range of the hypernuclear chart, providing access to over 100 currently undiscovered hyperisotopes, and the typical production rates are in the order of 10^{-5} to 10^{-4} per annihilation. This range can be further improved by considering the full range of accessible isotopes as targets for the initial annihilation. Based on the promising simulation results, the concept for a dedicated experiment was introduced and the key features of the required setup were outlined. It was concluded that the simulations indicate a strong potential for the study of hypernuclei produced by peripheral antiproton annihilations and that the implementation of the corresponding experiment is at reach within the next years.

Bibliography

[1] W. Marciano and H. Pagels. "Quantum chromodynamics". In: *Phys. Rep.* 36.3 (1978), pp. 137–276.

[2] S. Aoki. "Nucleon-nucleon interactions via lattice QCD: Methodology: HAL QCD approach to extract hadronic interactions in lattice QCD". In: *Eur. Phys. J. A* 49 (2013), pp. 1–12.

[3] S. Brunner et al. "Determination of the ^{4}He mass in a Penning trap". In: *Eur. Phys. J. D* 15 (2001), pp. 181–188.

[4] M. Wang et al. "The AME 2020 atomic mass evaluation (II). Tables, graphs and references". In: *Chin. Phys. C* 45.3 (2021), p. 030003.

[5] M. Niering et al. "Measurement of the hydrogen 1s-2s transition frequency by phase coherent comparison with a microwave cesium fountain clock". In: *Phys. Rev. Lett.* 84.24 (2000), p. 5496.

[6] J.-P. Karr, D. Marchand, and E. Voutier. "The proton size". In: *Nat. Rev. Phys.* 2.11 (2020), pp. 601–614.

[7] G. F. Newell. "The electric quadrupole moment of the deuteron". In: *Phys. Rev.* 78 (6 June 1950), pp. 711–714.

[8] J. L. Gammel and R. M. Thaler. "Spin-orbit coupling in the proton-proton interaction". In: *Phys. Rev.* 107.1 (1957), p. 291.

[9] R. Machleidt, K. Holinde, and C. Elster. "The Bonn meson-exchange model for the nucleon—nucleon interaction". In: *Phys. Rep.* 149.1 (1987), pp. 1–89.

[10] R. Machleidt. "The meson theory of nuclear forces and nuclear structure". In: *Advances in nuclear physics*. Springer, 1989, pp. 189–376.

[11] R. B. Wiringa, R. A. Smith, and T. L. Ainsworth. "Nucleon-nucleon potentials with and without Δ (1232) degrees of freedom". In: *Phys. Rev. C* 29.4 (1984), p. 1207.

[12] R. B. Wiringa, V. G. J. Stoks, and R. Schiavilla. "Accurate nucleon-nucleon potential with charge-independence breaking". In: *Phys. Rev. C* 51 (1 Jan. 1995), pp. 38–51.

[13] S. R. Beane, T. D. Cohen, and D. R. Phillips. "The potential of effective field theory in NN scattering". In: *Nucl. Phys. A* 632.3 (1998), pp. 445–469.

[14] S. A. Coon et al. "The two-pion-exchange three-nucleon potential and nuclear matter". In: *Nucl. Phys. A* 317.1 (1979), pp. 242–278.

[15] S. C. Pieper et al. "Realistic models of pion-exchange three-nucleon interactions". In: *Phys. Rev. C* 64.1 (2001), p. 014001.

[16] S. C. Pieper, R. B. Wiringa, and V. R. Pandharipande. “Ground state of ^{16}O”. In: *Phys. Rev. Lett.* 64 (4 Jan. 1990), pp. 364–367.

[17] S. Weinberg. “Phenomenological lagrangians”. In: *Phys. A* 96 (1979).

[18] R. Machleidt and D. R. Entem. “Chiral effective field theory and nuclear forces”. In: *Phys. Rep.* 503.1 (2011), pp. 1–75.

[19] L. Coraggio et al. “Reduced regulator dependence of neutron-matter predictions with perturbative chiral interactions”. In: *Phys. Rev. C* 87 (1 Jan. 2013), p. 014322.

[20] R. Machleidt and F. Sammarruca. “Chiral EFT based nuclear forces: achievements and challenges”. In: *Phys. Scr.* 91.8 (2016), p. 083007.

[21] J. Hoppe et al. “Probing chiral interactions up to next-to-next-to-next-to-leading order in medium-mass nuclei”. In: *Phys. Rev. C* 100.2 (2019), p. 024318.

[22] B. Hu et al. “Ab initio predictions link the neutron skin of ^{208}Pb to nuclear forces”. In: *Nat. Phys.* 18.10 (2022), pp. 1196–1200.

[23] T. H. R. Skyrme. “The effective nuclear potential”. In: *Nucl. Phys.* 9.4 (1958), pp. 615–634.

[24] D. Vautherin and D. Brink. “Hartree-Fock calculations with Skyrme’s interaction. I. Spherical nuclei”. In: *Phys. Rev. C* 5.3 (1972), p. 626.

[25] P. Ring and P. Schuck. *The nuclear many-body problem*. Springer Science & Business Media, 2004.

[26] M. Baranger. “Self-Consistent field theory of nuclear shapes”. In: *Phys. Rev.* 122 (3 May 1961), pp. 992–996.

[27] A. Faessler, P. U. Sauer, and M. M. Stingl. “Hartree-Fock and Hartree-Bogolyubov calculations in p shell nuclei”. In: *Z. Phys. A* 212.1 (1968), pp. 1–31.

[28] M. Beiner et al. “Nuclear ground-state properties and self-consistent calculations with the Skyrme interaction: (I). Spherical description”. In: *Nucl. Phys. A* 238.1 (1975), pp. 29–69.

[29] B. R. Barrett, P. Navrátil, and J. P. Vary. “Ab initio no core shell model”. In: *Prog. Part. Nucl. Phys.* 69 (2013), pp. 131–181.

[30] T. Ohgoe and M. Imada. “Variational Monte Carlo method for electron-phonon coupled systems”. In: *Phys. Rev. B* 89.19 (2014), p. 195139.

[31] A. Lovato, N. Rocco, and R. Schiavilla. “Muon capture in nuclei: An ab initio approach based on Green’s function Monte Carlo methods”. In: *Phys. Rev. C* 100.3 (2019), p. 035502.

[32] B. S. Hu, Q. Wu, and F. R. Xu. “Ab initio many-body perturbation theory and no-core shell model”. In: *Chin. Phys. C* 41.10 (2017), p. 104101.

[33] G. Hagen et al. “Emergent properties of nuclei from ab initio coupled-cluster calculations”. In: *Phys. Scr.* 91.6 (2016), p. 063006.

[34] X. Roca-Maza et al. “Neutron skin of ^{208}Pb, nuclear symmetry energy, and the parity radius experiment”. In: *Phys. Rev. Lett.* 106.25 (2011), p. 252501.

[35] K. Hebeler and A. Schwenk. “Chiral three-nucleon forces and neutron matter”. In: *Phys. Rev. C* 82 (1 July 2010), p. 014314.

[36] S. Gandolfi, J. Carlson, and Sanjay Reddy. “Maximum mass and radius of neutron stars, and the nuclear symmetry energy”. In: *Phys. Rev. C* 85 (3 Mar. 2012), p. 032801.

[37] T. Krüger et al. “Neutron matter from chiral effective field theory interactions”. In: *Phys. Rev. C* 88 (2 Aug. 2013), p. 025802.

[38] J. Birkhan et al. “Electric dipole polarizability of ^{48}Ca and implications for the neutron skin”. In: *Phys. Rev. Lett.* 118 (25 June 2017), p. 252501.

[39] L. Baiotti. “Gravitational waves from neutron star mergers and their relation to the nuclear equation of state”. In: *Prog. Part. Nucl. Phys.* 109 (2019), p. 103714.

[40] H. Yasin et al. “Equation of state effects in core-collapse supernovae”. In: *Phys. Rev. Lett.* 124 (9 Mar. 2020), p. 092701.

[41] J. Antoniadis et al. “A massive pulsar in a compact relativistic binary”. In: *Science* 340.6131 (2013), p. 1233232.

[42] E. Fonseca et al. “Refined mass and geometric measurements of the high-mass PSR J0740+6620”. In: *Astrophys. J. Lett.* 915.1 (July 2021), p. L12.

[43] R. W. Romani et al. “PSR J1810+1744: Companion darkening and a precise high neutron star mass”. In: *Astrophys. J. Lett.* 908.2 (Feb. 2021), p. L46.

[44] M. F. O’Boyle et al. “Parametrized equation of state for neutron star matter with continuous sound speed”. In: *Phys. Rev. D* 102 (8 Oct. 2020), p. 083027.

[45] H. Shen et al. “Relativistic equation of state of nuclear matter for supernova and neutron star”. In: *Nucl. Phys. A* 637.3 (1998), pp. 435–450.

[46] K. Hebeler et al. “Equation of state and neutron star properties constrained by nuclear physics and observation”. In: *Astrophys. J.* 773.1 (2013), p. 11.

[47] J. Keller, K. Hebeler, and A. Schwenk. “Nuclear equation of state for arbitrary proton fraction and temperature based on chiral effective field theory and a Gaussian process emulator”. In: *Phys. Rev. Lett.* 130.7 (2023), p. 072701.

[48] G. Chapline and M. Nauenberg. “Asymptotic freedom and the baryon-quark phase transition”. In: *Phys. Rev. D* 16 (2 July 1977), pp. 450–456.

[49] C. J. Horowitz and A. Schwenk. “The virial equation of state of low-density neutron matter”. In: *Phys. Lett. B* 638.2-3 (2006), pp. 153–159.

[50] J. Heisenberg et al. “Elastic electron scattering by ^{208}Pb and new information about the nuclear charge distribution”. In: *Phys. Rev. Lett.* 23.24 (1969), p. 1402.

[51] B. Frois et al. “High-momentum-transfer electron scattering from ^{208}Pb”. In: *Phys. Rev. Lett.* 38.4 (1977), p. 152.

[52] K. Tsukada et al. “First elastic electron scattering from ^{132}Xe at the SCRIT facility”. In: *Phys. Rev. Lett.* 118.26 (2017), p. 262501.

[53] G. Ewald et al. “Nuclear charge radii of ^{8,9}Li determined by laser spectroscopy”. In: *Phys. Rev. Lett.* 93.11 (2004), p. 113002.

[54] J. Ketelaer et al. “TRIGA-SPEC: A setup for mass spectrometry and laser spectroscopy at the research reactor TRIGA Mainz”. In: *Nucl. Instrum. Methods A* 594.2 (2008), pp. 162–177.

[55] R. Neugart et al. “Collinear laser spectroscopy at ISOLDE: new methods and highlights”. In: *J. Phys. G Nucl. Part. Phys.* 44.6 (2017), p. 064002.

[56] W. Nörtershäuser and I. D. Moore. “Nuclear charge radii”. In: *Handbook of Nuclear Physics*. Ed. by Isao Tanihata, Hiroshi Toki, and Toshitaka Kajino. Singapore: Springer Nature Singapore, 2020, pp. 1–70.

[57] D. G. Ravenhall, R. Herman, and B. C. Clark. “Nuclear charge distribution in calcium from electron scattering and muonic X-rays”. In: *Phys. Rev.* 136.3B (1964), B589.

[58] D. Kessler et al. “Muonic X-rays in lead isotopes”. In: *Phys. Rev. C* 11.5 (1975), p. 1719.

[59] C. Piller et al. “Nuclear charge radii of the tin isotopes from muonic atoms”. In: *Phys. Rev. C* 42.1 (1990), p. 182.

[60] K. Pachucki. “Proton structure effects in muonic hydrogen”. In: *Phys. Rev. A* 60.5 (1999), p. 3593.

[61] R. Pohl et al. “Muonic hydrogen and the proton radius puzzle”. In: *Annu. Rev. Nucl. Part. Sci.* 63 (2013), pp. 175–204.

[62] C. E. Carlson. “The proton radius puzzle”. In: *Prog. Part. Nucl. Phys.* 82 (2015), pp. 59–77.

[63] J.-P. Karr and D. Marchand. “Progress on the proton-radius puzzle”. In: *Nature* (2019), pp. 61–62.

[64] A. Antognini, F. Kottmann, and R. Pohl. “Laser spectroscopy of light muonic atoms and the nuclear charge radii”. In: *SciPost Phys. Proc.* (2021), p. 021.

[65] T. W. Donnelly, J. Dubach, and I. Sick. “Isospin dependences in parity-violating electron scattering”. In: *Nucl. Phys. A* 503.3-4 (1989), pp. 589–631.

[66] C. J. Horowitz. “Parity violating elastic electron scattering and Coulomb distortions”. In: *Phys. Rev. C* 57.6 (1998), p. 3430.

[67] D. H. Beck and R. D. McKeown. “Parity-violating electron scattering and nucleon structure”. In: *Annu. Rev. Nucl. Part. Sci.* 51.1 (2001), pp. 189–217.

[68] D. Adhikari et al. “Accurate determination of the neutron skin thickness of ^{208}Pb through parity-violation in electron scattering”. In: *Phys. Rev. Lett.* 126.17 (2021), p. 172502.

[69] R. Wang. “Parity violation in electron scattering in the E158 experiment at SLAC”. In: *J. Phys. Conf. Ser.* 2386.1 (2022), p. 012068.

[70] B. Buck. “Calculation of elastic and inelastic proton scattering with a generalized optical model”. In: *Phys. Rev.* 130 (2 Apr. 1963), pp. 712–726.

[71] S. Hama et al. “Global Dirac optical potentials for elastic proton scattering from heavy nuclei”. In: *Phys. Rev. C* 41 (6 June 1990), pp. 2737–2755.

[72] G. Hagen and N. Michel. “Elastic proton scattering of medium mass nuclei from coupled-cluster theory”. In: *Phys. Rev. C* 86 (2 Aug. 2012), p. 021602.

[73] L. A. Riley et al. “Thick-target inverse-kinematics proton scattering from ^{46}Ar and the N = 28 shell below ^{48}Ca”. In: *Phys. Rev. C* 72.2 (2005), p. 024311.

[74] W. T. H. Van Oers et al. “Optical-model analysis of p^+ ^{208}Pb elastic scattering from 15-1000 MeV”. In: *Phys. Rev. C* 10.1 (1974), p. 307.

[75] V. Girija et al. “Coherent pion photoproduction”. In: *Phys. Rev. C* 27.3 (1983), p. 1169.

[76] B. Krusche and S. Schadmand. “Study of non-strange baryon resonances with meson photoproduction”. In: *Prog. Part. Nucl. Phys.* 51.2 (2003), pp. 399–485.

[77] C. M. Tarbert et al. “Neutron skin of ^{208}Pb from coherent pion photoproduction”. In: *Phys. Rev. Lett.* 112.24 (2014), p. 242502.

[78] M. Gmitro, S. S. Kamalov, and R. Mach. “Momentum-space second-order optical potential for pion-nucleus elastic scattering”. In: *Phys. Rev. C* 36 (3 Sept. 1987), pp. 1105–1117.

[79] G.D. Alkhazov et al. “Nuclear matter distributions in the ^{6}He and ^{8}He nuclei from differential cross sections for small-angle proton elastic scattering at intermediate energy”. In: *Nucl. Phys. A* 712.3 (2002), pp. 269–299.

[80] J. Zenihiro et al. “Neutron density distributions of ^{204,206,208}Pb deduced via proton elastic scattering at E_p = 295 MeV”. In: *Phys. Rev. C* 82.4 (2010), p. 044611.

[81] E. Friedman. “Neutron skins of ^{208}Pb and ^{48}Ca from pionic probes”. In: *Nucl. Phys. A* 896 (2012), pp. 46–52.

[82] B. Klos et al. “Neutron density distributions from antiprotonic ^{208}Pb and ^{209}Bi atoms”. In: *Phys. Rev. C* 76.1 (2007), p. 014311.

[83] A. Tamii et al. “Complete electric dipole response and the neutron skin in ^{208}Pb”. In: *Phys. Rev. Lett.* 107 (6 Aug. 2011), p. 062502.

[84] T. Suzuki et al. “Neutron skin of Na isotopes studied via their interaction cross sections”. In: *Phys. Rev. Lett.* 75.18 (1995), p. 3241.

[85] S. Bagchi et al. “Neutron skin and signature of the N = 14 shell gap found from measured proton radii of $^{17-22}$N”. In: *Phys. Lett. B* 790 (2019), pp. 251–256.

[86] I. Tanihata et al. “Measurements of interaction cross sections and nuclear radii in the light p-shell region”. In: *Phys. Rev. Lett.* 55.24 (1985), p. 2676.

[87] M. Brodeur et al. “First direct mass measurement of the two-neutron halo nucleus ^{6}He and improved mass for the four-neutron halo ^{8}He”. In: *Phys. Rev. Lett.* 108.5 (2012), p. 052504.

[88] P. Descouvemont. “Halo structure of ^{14}Be in a microscopic ^{12}Be + n+n cluster model”. In: *Phys. Rev. C* 52.2 (1995), p. 704.

[89] K. J. Cook et al. “Halo structure of the neutron-dripline nucleus ^{19}B”. In: *Phys. Rev. Lett.* 124.21 (2020), p. 212503.

[90] K. Tanaka et al. “Observation of a large reaction cross section in the drip-line nucleus ^{22}C”. In: *Phys. Rev. Lett.* 104.6 (2010), p. 062701.

[91] N. Kobayashi et al. “Observation of a p-wave one-neutron halo configuration in ^{37}Mg”. In: *Phys. Rev. Lett.* 112.24 (2014), p. 242501.

[92] T. Aumann et al. “PUMA, antiProton unstable matter annihilation - PUMA collaboration”. In: *Eur. Phys. J. A* 58.5 (2022), p. 88.

[93] T. Minamisono et al. “Proton halo of ^{8}B disclosed by its giant quadrupole moment”. In: *Phys. Rev. Lett.* 69.14 (1992), p. 2058.

[94] H. W. Hammer, C. Ji, and D. R. Phillips. “Effective field theory description of halo nuclei”. In: *J. Phys. G: Nucl. Part. Phys.* 44.10 (2017), p. 103002.

[95] G. Hagen, T. Papenbrock, and M. Hjorth-Jensen. “Ab initio computation of the ^{17}F proton halo state and resonances in A = 17 nuclei”. In: *Phys. Rev. Lett.* 104.18 (2010), p. 182501.

[96] Y.-G. LI. “Antiproton-nucleus elastic scattering at intermediate energies”. In: *Chin. Phys. C* 17.9 (1993), pp. 829–834.

[97] A. Trzcinska et al. “Neutron density distributions deduced from antiprotonic atoms”. In: *Phys. Rev. Lett.* 87.8 (2001), p. 082501.

[98] J. S. Briggs, P. T. Greenland, and E. A. Solovev. “The capture of slow antiprotons in noble gases”. In: *J. Phys. B* 32.2 (1999), p. 197.

[99] S. Zacarias. “Probing nuclear density tails with antiprotons at PUMA: Detection and method”. en. PhD thesis. Darmstadt: Technische Universität Darmstadt, 2022, xxi, 114 Seiten.

[100] D. Gotta et al. “X-ray transitions from antiprotonic noble gases”. In: *Eur. Phys. J. D* 47 (2008), pp. 11–26.

[101] G. R. Burbidge and A. H. De Borde. “The mesonic auger effect”. In: *Phys. Rev.* 89.1 (1953), p. 189.

[102] A. Deloff and J. Law. “Strong-interaction effects in antiprotonic atoms”. In: *Phys. Rev. C* 10 (6 Dec. 1974), pp. 2657–2658.

[103] P. Roberson et al. “Strong interaction and mass measurements using antiprotonic atoms”. In: *Phys. Rev. C* 16.5 (1977), p. 1945.

[104] J. Cote et al. “Nucleon-antinucleon optical potential”. In: *Phys. Rev. Lett.* 48 (19 May 1982), pp. 1319–1322.

[105] T. Suzuki and H. Narumi. “Microscopic approach to the antiproton-nucleus optical potential”. In: *Nucl. Phys. A* 426.3 (1984), pp. 413–430.

[106] C. J. Batty et al. “Optical potentials for low energy antiproton-nucleus interactions”. In: *Phys. Lett. B* 142.4 (1984), pp. 241–244.

[107] R. Lazauskas and J. Carbonell. “Antiproton-deuteron hydrogenic states in optical models”. In: *Phys. Lett. B* 820 (2021), p. 136573.

[108] B. El-Bennich et al. “Paris N$\bar{N}$ potential constrained by recent antiprotonic-atom data and $\bar{N}$P total cross sections”. In: *Phys. Rev. C* 79.5 (2009), p. 054001.

[109] I. Tanihata. “Nuclear structure studies using high-energy radioactive nuclear beams: Radii and nucleon momentum distributions of exotic nuclei”. In: *Nucl. Phys. A* 478 (1988), pp. 795–804.

[110] A. D. Martin. “A study of K–mesic atoms”. In: *Nuovo Cimento* 27 (1963), pp. 1359–1378.

[111] E. Klempt, C. Batty, and J.-M. Richard. “The antinucleon–nucleon interaction at low energy: Annihilation dynamics”. In: *Phys. Rep.* 413.4-5 (2005), pp. 197–317.

[112] W. M. Bugg et al. “Evidence for a neutron halo in heavy nuclei from antiproton absorption”. In: *Phys. Rev. Lett.* 31 (7 Aug. 1973), pp. 475–478.

[113] L. Linssen et al. “Measurement of antiproton-proton small-angle elastic scattering at low momentum”. In: *Nucl. Phys. A* 469.4 (1987), pp. 726–748.

[114] P. Kroll and W. Schweiger. “Analysis of low-energy antiproton-proton forward scattering”. In: *Nucl. Phys. A* 503.3-4 (1989), pp. 865–884.

[115] R. Timmermans, T. A. Rijken, and J. J. de Swart. “Antiproton-proton partial-wave analysis below 925 MeV/c”. In: *Phys. Rev. C* 50.1 (1994), p. 48.

[116] L. A. Kondratyuk and M. G. Sapozhnikov. “Interaction of antiprotons with neutrons and nuclei at LEAR energies”. In: *Sov. J. Nucl. Phys.* 46.1 (1987).

[117] J. Mahalanabis. “Determination of antiproton-neutron amplitude from elastic $\bar{\text{p}}$-deuteron scattering at 600 MeV/c”. In: *Z. Phys. A* 342 (1992), pp. 101–105.

[118] W. Brückner et al. “Search for a narrow resonance in antiproton-proton annihilation cross sections in the beam momentum range between 400 and 600 MeV/c”. In: *Phys. Lett. B* 197.3 (1987), pp. 463–468.

[119] D. Rohmann et al. “Measurement of the 4f strong interaction level width in light antiprotonic atoms”. In: *Z. Phys. A* 325 (1986), pp. 261–265.

[120] T. Köhler et al. “Precision measurement of strong interaction isotope effects in antiprotonic ^{16}O, ^{17}O, and ^{18}O atoms”. In: *Phys. Lett. B* 176.3-4 (1986), pp. 327–333.

[121] P. L. McGaughey et al. “Dynamics of low-energy antiproton annihilation in nuclei as inferred from inclusive proton and pion measurements”. In: *Phys. Rev. Lett.* 56.20 (1986), p. 2156.

[122] J. Jastrzebski et al. “Signature of a neutron halo in ^{232}Th from antiproton absorption”. In: *Nucl. Phys. A* 558 (1993), pp. 405–414.

[123] D. Polster et al. “Light particle emission induced by stopped antiprotons in nuclei: Energy dissipation and neutron-to-proton ratio”. In: *Phys. Rev. C* 51 (3 Mar. 1995), pp. 1167–1180.

[124] A. Trzcinska et al. “Information on the nuclear periphery deduced from the properties of heavy antiprotonic atoms”. In: *Nucl. Instrum. Methods Phys. Res. B* 214 (2004). Low Energy Antiproton Physics (LEAP’03), pp. 157–159.

[125] C. J. Batty, E. Friedman, and A. Gal. “Density-dependent $\bar{\text{p}}$-nucleus optical potentials from global fits to $\bar{\text{p}}$ atom data”. In: *Nucl. Phys. A* 592.4 (1995), pp. 487–512.

[126] J. W. Sunier et al. “Calliope—a large acceptance multiparticle magnetic spectrometer for intermediate energy physics”. In: *Nucl. Instrum. Methods A* 241.1 (1985), pp. 139–152.

[127] Y.S. Kim et al. “A double-arm fission fragment spectrometer with PIN diode arrays”. In: *Nucl. Instrum. Methods A* 329.3 (1993), pp. 403–417.

[128] M. Schlaich et al. “A multi-reflection time-of-flight mass spectrometer for the offline ion source of the PUMA experiment”. In: *Int. J. Mass Spectrom.* (2023), p. 117166.

[129] L. S. Brown and G. Gabrielse. “Geonium theory: Physics of a single electron or ion in a Penning trap”. In: *Rev. Mod. Phys.* 58 (1 Jan. 1986), pp. 233–311.

[130] F. Heiße et al. “High-precision mass spectrometer for light ions”. In: *Phys. Rev. A* 100.2 (2019), p. 022518.

[131] M. J. Borchert et al. “A 16-parts-per-trillion measurement of the antiproton-to-proton charge–mass ratio”. In: *Nature* 601.7891 (2022), pp. 53–57.

[132] G. Bollen et al. “Ramsey technique applied in a Penning trap mass spectrometer”. In: *Nucl. Instrum. Methods B* 70.1 (1992), pp. 490–493.

[133] S. Eliseev et al. “Phase-Imaging Ion-Cyclotron-Resonance Measurements for Short-Lived Nuclides”. In: *Phys. Rev. Lett.* 110 (8 Feb. 2013), p. 082501.

[134] L. Brillouin. “A theorem of Larmor and its importance for electrons in magnetic fields”. In: *Phys. Rev.* 67 (7-8 Apr. 1945), pp. 260–266.

[135] M. D. Tinkle, R. G. Greaves, and C. M. Surko. “Modes of spheroidal ion plasmas at the Brillouin limit”. In: *Phys. Plasmas* 3.3 (Mar. 1996), pp. 749–758.

[136] M. Hobein et al. “Evaporative Cooling and Coherent Axial Oscillations of Highly Charged Ions in a Penning Trap”. In: *Phys. Rev. Lett.* 106 (1 Jan. 2011), p. 013002.

[137] S. Bharadia et al. “Dynamics of laser-cooled Ca+ ions in a Penning trap with a rotating wall”. In: *Appl. Phys. B* 107.4 (June 2012), pp. 1105–1115.

[138] D. H. E. Dubin. “Theory of electrostatic fluid modes in a cold spheroidal non-neutral plasma”. In: *Phys. Rev. Lett.* 66 (16 Apr. 1991), pp. 2076–2079.

[139] G. Werth. “Non-neutral plasmas and collective phenomena in ion traps”. In: *Plasma Physics: Confinement, Transport and Collective Effects*. Ed. by A. Dinklage et al. Berlin, Heidelberg: Springer Berlin Heidelberg, 2005, pp. 269–295.

[140] X.-P. Huang et al. “Steady-state confinement of non-neutral plasmas by rotating electric fields”. In: *Phys. Rev. Lett.* 78 (5 Feb. 1997), pp. 875–878.

[141] E. M. Hollmann, F. Anderegg, and C. F. Driscoll. “Confinement and manipulation of non-neutral plasmas using rotating wall electric fields”. In: *Phys. Plasmas* 7.7 (July 2000), pp. 2776–2789.

[142] F. Anderegg. “Rotating wall technique and centrifugal separation”. In: *Trapped Charged Particles*. Chap. 11, pp. 221–238.

[143] V. Frankevich, R. Knochenmuss, and R. Zenobi. “The origin of electrons in MALDI and their use for sympathetic cooling of negative ions in FTICR”. In: *Int. J. Mass Spectrom.* 220.1 (2002), pp. 11–19.

[144] S. L. Rolston and G. Gabrielse. “Cooling antiprotons in an ion trap”. In: *Hyperfine Interact.* 44.1 (Mar. 1989), pp. 233–245.

[145] X. Fei and W. M. Snow. “Cylindrical Penning traps with dynamic orthogonalized anharmonicity compensation for precision experiments”. In: *Nucl. Instrum. Methods A* 425.3 (1999), pp. 431–440.

[146] D. S. Hall and G. Gabrielse. “Electron cooling of protons in a nested Penning trap”. In: *Phys. Rev. Lett.* 77.10 (1996), p. 1962.

[147] G. Gabrielse et al. “Antiproton confinement in a Penning-Ioffe trap for antihydrogen”. In: *Phys. Rev. Lett.* 98.11 (2007), p. 113002.

[148] S. Ulmer. “First observation of spin flips with a single proton stored in a cryogenic Penning trap”. PhD thesis. Ruprecht-Karls-Universität Heidelberg, Germany, 2011.

[149] M. Bohman et al. “Sympathetic cooling of protons and antiprotons with a common endcap Penning trap”. In: *J. Mod. Opt.* 65.5-6 (2018), pp. 568–576.

[150] G. H. Low, P. F. Herskind, and I. L. Chuang. “Finite-geometry models of electric field noise from patch potentials in ion traps”. In: *Phys. Rev. A* 84.5 (2011), p. 053425.

[151] M. Amoretti et al. “Complete nondestructive diagnostic of nonneutral plasmas based on the detection of electrostatic modes”. In: *Phys. Plasmas* 10 (Aug. 2003).

[152] J. Fischer. “Plasma diagnostics and electron source for PUMA”. Master’s Thesis. Technische Universität Darmstadt, Darmstadt, Germany, 2019.

[153] H.-J. Kluge et al. “HITRAP: a facility at GSI for highly charged ions”. In: *Adv. Quantum Chem.* 53 (2008), pp. 83–98.

[154] V. Benda et al. “Cryogenic infrastructure for superfluid helium testing of LHC prototype superconducting magnets”. In: *Adv. Cryog. Eng.* (1994), pp. 641–648.

[155] M. Marie-Jeanne et al. “Towards a magnetic field stabilization at ISOLTRAP for high-accuracy mass measurements on exotic nuclides”. In: *Nucl. Instrum. Methods A* 587.2 (2008), pp. 464–473.

[156] *Properties of solid materials from cryogenic- to room-temperatures*. Accessed: 2023-08-17.

[157] E. Marquardt, J. Le, and R. Radebaugh. “Cryogenic material properties database”. In: Jan. 2002, pp. 681–687.

[158] N. J. Simon, E. S. Drexler, and R. P. Reed. *Properties of copper and copper alloys at cryogenic temperatures. Final report*. Tech. rep. National Inst. of Standards and Technology (MSEL), 1992.

[159] *Keysight 33600A Series Trueform Waveform Generators - Data Sheet*. Accessed: 2023-10-30.

[160] J. R. Danielson, C. M. Surko, and T. M. O’Neil. “High-density fixed point for radially compressed single-component plasmas”. In: *Phys. Rev. Lett.* 99 (13 Sept. 2007), p. 135005.

[161] *Sapphire (Al2O3)*. Accessed: 2023-08-17.

[162] *Overview of materials for Polyetheretherketone, Unreinforced*. Accessed: 2023-08-17.

[163] *Oxygen-free high conductivity Copper, Hard, UNS C10200*. Accessed: 2023-08-17.

[164] C. Arvinte et al. "Technical requirements and materials used in firefighters gloves manufacturing". In: *IOP Conf. Ser.: Mater. Sci. Eng.* 572 (Aug. 2019), p. 012070.

[165] C. Amole et al. "The ALPHA antihydrogen trapping apparatus". In: *Nucl. Instrum. Methods. Phys. Res. A* 735 (2014), pp. 319–340.

[166] S. Sellner et al. "Improved limit on the directly measured antiproton lifetime". In: *New J. Phys.* 19.8 (2017), p. 083023.

[167] N. Marquardt. "Introduction to the principles of vacuum physics". In: (1999).

[168] W. Steckelmacher. "A review of the molecular flow conductance for systems of tubes and components and the measurement of pumping speed". In: *Vacuum* 16.11 (1966), pp. 561–584.

[169] C. Benvenuti. "Extreme vacua: achievements and expectations". In: *Phys. Scr.* 1988.T22 (1988), p. 48.

[170] M. M. Dubinin. "Modern state of the theory of volume filling of micropore adsorbents during adsorption of gases and steams on carbon adsorbents". In: *Zh. Fiz. Khim.* 39.19 (1965), pp. 1305–1317.

[171] M. M. Dubinin. "The equation of the characteristic curve of activated charcoal". In: *Dokl. Akad. Nauk. SSSR.* Vol. 55. 1947, pp. 327–329.

[172] M. G. Kaganer. "A method for determining the specific surface from the adsorption of gases in the monomolecular region". In: *Doklady Akademii Nauk*. Vol. 116. 2. Russian Academy of Sciences. 1957, pp. 251–254.

[173] R. Haefer. *Cryopumping. Theory and practice*. Oxford: Oxford Science Publications, 1989.

[174] E. Wallen. "Adsorption isotherms of He and H2 at liquid He temperatures". In: *J. Vac. Sci. Technol. A* 15.2 (Mar. 1997), pp. 265–274.

[175] F. Chill, S. Wilfert, and L. Bozyk. "Cryopumping of hydrogen on stainless steel in the temperature range between 7 and 18 K". In: *J. Vac. Sci. Technol. A* 37.3 (2019).

[176] V. Baglin. "Cryopumping and vacuum systems". In: *arXiv preprint arXiv:2006.01574* (2020).

[177] A. Stöltzel and B. Jenninger. "Comparison of ionization vacuum gauges close to their low pressure limit". In: *Vacuum* 207 (2023), p. 111573.

[178] P. Kumar and R. Balasubramaniam. "Determination of hydrogen diffusivity in austenitic stainless steels by subscale microhardness profiling". In: *J. Alloys Compd.* 255.1-2 (1997), pp. 130–134.

[179] G.A. Young and J.R. Scully. "The diffusion and trapping of hydrogen in high purity aluminum". In: *Acta Mater.* 46.18 (1998), pp. 6337–6349.

[180] H. Magnusson and K. Frisk. "Diffusion, permeation and solubility of hydrogen in copper". In: *J. Phase Equilibria Diffus.* 38 (2017), pp. 65–69.

[181] J. Fischer. "Design and characterisation of the low-energy antiproton beam of PUMA at ELENA". in preparation. Dissertation. Technische Universität Darmstadt, Darmstadt, Germany, 2024.

[182] Y. Ishikawa, Y. Koguchi, and K. Odaka. “Outgassing rate of some austenitic stainless steels”. In: *J. Vac. Sci. Technol. A* 9.2 (Mar. 1991), pp. 250–253.

[183] J. N. Chubb, L. Gowland, and I. E. Pollard. “Condensation pumping of hydrogen and deuterium on to liquid-helium-cooled surfaces”. In: *J. Phys. D: Appl. Phys.* 1.3 (1968), p. 361.

[184] R. Salemme et al. *Vacuum performance of amorphous carbon coating at cryogenic temperature with presence of proton beams*. Tech. rep. 2016.

[185] C. Carli and F. Caspers. *Stochastic cooling at the CERN Antiproton Decelerator*. Tech. rep. 2000.

[186] S. Maury. “The antiproton decelerator: AD”. In: *Hyperfine Interact.* 109.1-4 (1997), pp. 43–52.

[187] A. Sorensen. “Liouville’s theorem and emittance”. In: (1989).

[188] W. Bartmann et al. “The ELENA facility”. In: *Philos. Trans. R. Soc. A* 376.2116 (2018), p. 20170266.

[189] H. Kalinowsky. “Deceleration of antiprotons from MeV to keV energies”. In: *Hyperfine Interact.* 76.1 (1993), pp. 73–80.

[190] N. Kuroda et al. “Confinement of a large number of antiprotons and production of an ultraslow antiproton beam”. In: *Phys. Rev. Lett.* 94 (2 Jan. 2005), p. 023401.

[191] M. Hori and J. Walz. “Physics at CERN’s antiproton decelerator”. In: *Prog. Part. Nucl. Phys.* 72 (2013), pp. 206–253.

[192] S. Fabbri and W. Bertsche. *Optimization of antiproton capture and delivery for antihydrogen creation*. 2021.

[193] A. Husson and D. Lunney. “An antiproton deceleration device for the GBAR experiment at CERN”. In: *arXiv preprint arXiv:1909.07493* (2019).

[194] A. Husson et al. “A pulsed high-voltage decelerator system to deliver low-energy antiprotons”. In: *Nucl. Instrum. Methods A* 1002 (2021), p. 165245.

[195] S. Maury et al. “ELENA: the extra low energy anti-proton facility at CERN”. In: *Hyperfine Interact.* 229.1 (Oct. 2014), pp. 105–115.

[196] M. Fraser. *An additional beam line at ELENA: LNE51*. 2021.

[197] *simionx.SimplexOptimizer - Simplex optimizer*. Accessed: 2023-08-24.

[198] J. Fischer et al. “Design and characterisation of the low-energy antiproton beamline of PUMA at ELENA”. 2024.

[199] F. A. Berends and P. Singer. “On the lifetime of the η meson”. In: *Phys. Lett.* 19.CERN-TH-611 (1965), pp. 249–251.

[200] M. Kawaguchi and S. Matsuzaki. “Lifetime of ρ meson in correlation with magnetic-dimensional reduction”. In: *Eur. Phys. J. A* 53 (2017), pp. 1–9.

[201] N. Gelfand et al. “Lifetime of the ω Meson”. In: *Phys. Rev. Lett.* 11.9 (1963), p. 436.

[202] R. J. Ott and T. W. Pritchard. “Precise measurement of the K^+ lifetime”. In: *Phys. Rev. D* 3.1 (1971), p. 52.

[203] L. K. Gibbons et al. “New measurements of the neutral kaon parameters Δm, τ S, Φ00-Φ+-, and Φ+-”. In: *Phys. Rev. Lett.* 70.9 (1993), p. 1199.

[204] C. Boros, J. T. Londergan, and A. W. Thomas. “Structure and production of Lambda baryons”. In: *Phys. Rev. D* 61.1 (1999), p. 014007.

[205] B. Povh. “Hypernuclei”. In: *Annu. Rev. Nucl. Part. Sci.* 28.1 (1978), pp. 1–32.

[206] A. Schmidt et al. “Production of hypernuclei from antiproton capture within a relativistic transport model”. In: *Eur. Phys. J. A* (2023). submitted.

[207] R. Machleidt et al. “The Bonn meson-exchange model for the nucleon—nucleon interaction”. In: *Phys. Rep.* 149.1 (1987), pp. 1–89.

[208] R. Machleidt. “High-precision, charge-dependent Bonn nucleon-nucleon potential”. In: *Phys. Rev. C* 63 (2 2001), p. 024001.

[209] R. Machleidt et al. “Towards a consistent approach to nuclear structure: EFT of two- and many-body forces”. In: *J. Phys. G: Nucl. Part. Phys.* 31.8 (2005), S1235.

[210] K. Hebeler et al. “Nuclear forces and their impact on neutron-rich nuclei and neutron-rich matter”. In: *Annu. Rev. Nucl. Part. Sci.* 65.1 (2015), pp. 457–484.

[211] A. Deloff. “Phenomenological study of Lambda-nucleon interaction”. In: *Phys. Rev. C* 20.4 (1979), p. 1528.

[212] J. Haidenbauer et al. “Lambda-nuclear interactions and hyperon puzzle in neutron stars”. In: *Eur. Phys. J. A* 53.6 (2017), p. 121.

[213] K. S. Myint et al. “Neutron rich Lambda hypernuclei”. In: *Few-Body Problems in Physics’ 99: Proceedings of the 1st Asian-Pacific Conference, Tokyo, Japan, August 23–28, 1999*. Springer. 2000, pp. 383–386.

[214] A. Nogga. “Light hypernuclei based on chiral and phenomenological interactions”. In: *Nucl. Phys. A* 914 (2013), pp. 140–150.

[215] J. Haidenbauer and I. Vidaña. “Structure of single-Λ hypernuclei with chiral hyperon–nucleon potentials”. In: *Eur. Phys. J. A* 56.2 (2020), p. 55.

[216] H. Le. “Single-& double-strangeness hypernuclei up to $A = 8$ within chiral effective field theory”. In: *arXiv preprint arXiv:2210.02860* (2022).

[217] J. Haidenbauer et al. “Hyperon–nucleon interaction at next-to-leading order in chiral effective field theory”. In: *Nucl. Phys. A* 915 (2013), pp. 24–58.

[218] S. Petschauer et al. “Leading three-baryon forces from SU (3) chiral effective field theory”. In: *Phys. Rev. C* 93.1 (2016), p. 014001.

[219] D. Lonardoni et al. “Hyperon Puzzle: Hints from Quantum Monte Carlo Calculations”. In: *Phys. Rev. Lett.* 114 (9 Mar. 2015), p. 092301.

[220] R. Lastowiecki et al. “Strangeness in the cores of neutron stars”. In: *arXiv preprint arXiv:1112.6430* (2011).

[221] L. Tolos and L. Fabbietti. “Strangeness in nuclei and neutron stars”. In: *Prog. Part. Nucl. Phys.* 112 (2020), p. 103770.

[222] J. Antoniadis et al. “A massive pulsar in a compact relativistic binary”. In: *Science* 340.6131 (2013), p. 1233232.

[223] H. T. Cromartie et al. “Relativistic Shapiro delay measurements of an extremely massive millisecond pulsar”. In: *Nat. Astron.* 4.1 (2020), pp. 72–76.

[224] R. Wirth and R. Roth. “Induced hyperon-nucleon-nucleon interactions and the hyperon puzzle”. In: *Phys. Rev. Lett.* 117.18 (2016), p. 182501.

[225] D. Logoteta, I. Vidaña, and I. Bombaci. “Impact of chiral hyperonic three-body forces on neutron stars”. In: *Eur. Phys. J. A* 55.11 (2019), p. 207.

[226] G. Alexander et al. “Interactions of Lambdas with protons”. In: *Phys. Rev. Lett.* 7 (9 1961), pp. 348–351.

[227] T. H. Groves. “Elastic scattering of Lambda hyperons from protons”. In: *Phys. Rev.* 129.3 (1963), p. 1372.

[228] G. Alexander et al. “Study of the $\Lambda - N$ system in low-energy $\Lambda - p$ elastic scattering”. In: *Phys. Rev.* 173 (5 1968), pp. 1452–1460.

[229] J. Rowley et al. “Improved Λp Elastic Scattering Cross Sections between 0.9 and 2.0 GeV/c as a Main Ingredient of the Neutron Star Equation of State”. In: *Phys. Rev. Lett.* 127.27 (2021), p. 272303.

[230] K. Miwa et al. “Study of ΣN interaction from the Σp scattering experiment at J-PARC”. In: *J. Phys. Conf. Ser.* 1643.1 (2020), p. 012174.

[231] T. A. Rijken, V. G. J. Stoks, and Y. Yamamoto. “Soft-core hyperon-nucleon potentials”. In: *Phys. Rev. C* 59 (1 Jan. 1999), pp. 21–40.

[232] J. Haidenbauer and U.-G. Meißner. “Jülich hyperon-nucleon model revisited”. In: *Phys. Rev. C* 72 (4 Oct. 2005), p. 044005.

[233] Henk Polinder, Johann Haidenbauer, and Ulf-G. Meißner. “Hyperon–nucleon interactions—a chiral effective field theory approach”. In: *Nucl. Phys. A* 779 (2006), pp. 244–266.

[234] J. Haidenbauer, U.-G. Meißner, and A. Nogga. “Hyperon–nucleon interaction within chiral effective field theory revisited”. In: *Eur. Phys. J. A* 56.3 (Mar. 2020), p. 91.

[235] S. Acharya et al. “Study of the Λ–Λ interaction with femtoscopy correlations in p–p and p–Pb collisions at the LHC”. In: *Phys. Lett. B* 797 (2019), p. 134822.

[236] S. Acharya et al. “Constraining the $K^{-}N$ coupled channel dynamics using femtoscopic correlations at the LHC”. In: *Eur. Phys. J. C* 83.4 (2023), p. 340.

[237] S. Acharya et al. “Towards the understanding of the genuine three-body interaction for p–p–p and p–p–Λ”. In: *Eur. Phys. J. A* 59.7 (2023), p. 145.

[238] S. Acharya et al. “$p - p, p - \Lambda$, and $\Lambda - \Lambda$ correlations studied via femtoscopy in pp reactions at $\sqrt{s} = 7\,\mathrm{TeV}$”. In: *Phys. Rev. C* 99 (2 2019), p. 024001.

[239] R. A. Adelseck and L. E. Wright. “Lambda-neutron interaction in kaon photoproduction from the deuteron”. In: *Phys. Rev. C* 39.2 (1989), p. 580.

[240] X. Li and L. E. Wright. “Final-state Lambda-neutron interaction in kaon photoproduction from the deuteron”. In: *J. Phys. G: Nucl. Part. Phys.* 17.7 (1991), p. 1127.

[241] A. Gal et al. “A shell-model analysis of Λ binding energies for the p-shell hypernuclei. I. Basic formulas and matrix elements for ΛN and ΛNN forces”. In: *Ann. Phys.* 63.1 (1971), pp. 53–126.

[242] A. Gal et al. “A shell-model analysis of Λ binding energies for the p-shell hypernuclei II. Numerical Fitting, Interpretation, and Hypernuclear Predictions”. In: *Ann. Phys.* 72.2 (1972), pp. 445–488.

[243] A. Gal et al. “A shell-model analysis of Λ binding energies for the p-shell hypernuclei III. Further analysis and predictions”. In: *Ann. Phys.* 113.1 (1978), pp. 79–97.

[244] M. Rayet. “Skyrme parametrization of an effective Λ-nucleon interaction”. In: *Nucl. Phys. A* 367.3 (1981), pp. 381–397.

[245] T. Motoba et al. “Light p-Shell Λ-Hypernuclei by the Microscopic Three-Cluster Model”. In: *Prog. Theor. Phys.* 70.1 (July 1983), pp. 189–221.

[246] M. Rufa et al. “Single-particle spectra of Λ hypernuclei and the enhanced interaction radii of multi-strange objects”. In: *J. Phys. G: Nucl. Part. Phys.* 13.8 (Aug. 1987), p. L143.

[247] J. Mareš et al. “On Λ-hyperon(s) in the nuclear medium”. In: *Z. Phys. A* 333.2 (1989), pp. 209–212.

[248] T. Y. Tretyakova et al. “Structure of neutron-rich Λ hypernuclei”. In: *Eur. Phys. J. A* 5.4 (Aug. 1999), pp. 391–398.

[249] J. Cugnon et al. “Hypernuclei in the Skyrme-Hartree-Fock formalism with a microscopic hyperon-nucleon force”. In: *Phys. Rev. C* 62 (6 Nov. 2000), p. 064308.

[250] E. Hiyama et al. “Structure of light hypernuclei”. In: *Prog. Part. Nucl. Phys.* 63.2 (2009), pp. 339–395.

[251] D. J. Millener. “Shell-model interpretation of γ-ray transitions in p-shell hypernuclei”. In: *Nucl. Phys. A* 804.1 (2008). Special Issue on Recent Advances in Strangeness Nuclear Physics, pp. 84–98.

[252] D. J. Millener. “Shell-model structure of light hypernuclei”. In: *Nucl. Phys. A* 835.1 (2010). Proceedings of the 10th International Conference on Hypernuclear and Strange Particle Physics, pp. 11–18.

[253] D. J. Millener. “Shell-model calculations for p-shell hypernuclei”. In: *Nucl. Phys. A* 881 (2012). Progress in Strangeness Nuclear Physics, pp. 298–309.

[254] R. Wirth et al. “Ab Initio Description of p-Shell Hypernuclei”. In: *Phys. Rev. Lett.* 113 (19 Nov. 2014), p. 192502.

[255] R. Wirth et al. “Induced Hyperon-Nucleon-Nucleon Interactions and the Hyperon Puzzle”. In: *Phys. Rev. Lett.* 117 (18 Oct. 2016), p. 182501.

[256] R. Wirth et al. “Light neutron-rich hypernuclei from the importance-truncated no-core shell model”. In: *Phys. Lett. B* 779 (2018), pp. 336–341.

[257] R. Wirth et al. “Hypernuclear no-core shell model”. In: *Phys. Rev. C* 97 (6 June 2018), p. 064315.

[258] D. Lonardoni et al. “Effects of the two-body and three-body hyperon-nucleon interactions in Λ hypernuclei”. In: *Phys. Rev. C* 87 (4 Apr. 2013), p. 041303.

[259] D. Lonardoni et al. “Accurate determination of the interaction between Λ hyperons and nucleons from auxiliary field diffusion Monte Carlo calculations”. In: *Phys. Rev. C* 89 (1 Jan. 2014), p. 014314.

[260] *Chart of Hypernuclides - Hypernuclear Structure and Decay Data*. Accessed: 2023-08-15.

[261] M. A. Faessler et al. "Spectroscopy of the hypernucleus ${}^{12}_{\Lambda}\mathrm{C}$". In: *Phys. Lett. B* 46.3 (1973), pp. 468–470.

[262] W. Brückner et al. "Strangeness exchange reaction on nuclei". In: *Phys. Lett. B* 62.4 (1976), pp. 481–484.

[263] R. Bertini et al. "Neutron hole states in ${}^{6}_{\Lambda}\mathrm{Li}$, ${}^{7}_{\Lambda}\mathrm{Li}$, ${}^{9}_{\Lambda}\mathrm{Be}$ and ${}^{12}_{\Lambda}\mathrm{C}$ hypernuclei". In: *Nucl. Phys. A* 368.3 (1981), pp. 365–374.

[264] C. Milner et al. "Observation of Λ-hypernuclei in the reaction ${}^{12}\mathrm{C}$ (π^+, K^+) ${}^{12}_{\Lambda}\mathrm{C}$". In: *Phys. Rev. Lett.* 54.12 (1985), p. 1237.

[265] P. H. Pile et al. "Study of hypernuclei by associated production". In: *Phys. Rev. Lett.* 66.20 (1991), p. 2585.

[266] T. Hasegawa et al. "Spectroscopic study of ${}^{10}_{\Lambda}\mathrm{B}$, ${}^{12}_{\Lambda}\mathrm{C}$, ${}^{28}_{\Lambda}\mathrm{Si}$, ${}^{89}_{\Lambda}\mathrm{Y}$, ${}^{139}_{\Lambda}\mathrm{La}$, and ${}^{208}_{\Lambda}\mathrm{Pb}$ by the (π^+, K^+) reaction". In: *Phys. Rev. C* 53.3 (1996), p. 1210.

[267] T. Miyoshi et al. "High resolution spectroscopy of the ${}^{12}_{\Lambda}\mathrm{B}$ hypernucleus produced by the $(e, e'K^+)$ reaction". In: *Phys. Rev. Lett.* 90.23 (2003), p. 232502.

[268] F. Dohrmann et al. "Angular distributions for ${}^{3,4}_{\Lambda}\mathrm{H}$ bound states in the ${}^{3,4}\mathrm{He}$ $(e, e'K^+)$ reaction". In: *Phys. Rev. Lett.* 93.24 (2004), p. 242501.

[269] H. Tamura et al. "Gamma spectroscopy of hypernuclei: a decade of Hyperball project and future plans at J-PARC". In: *Nucl. Phys. A* 835.1-4 (2010), pp. 3–10.

[270] H. Akikawa et al. "Hypernuclear fine structure in ${}^{9}_{\Lambda}\mathrm{Be}$". In: *Phys. Rev. Lett.* 88.8 (2002), p. 082501.

[271] M. Ukai et al. "Hypernuclear fine structure in ${}^{16}_{\Lambda}\mathrm{O}$ and the ΛN tensor interaction". In: *Phys. Rev. Lett.* 93.23 (2004), p. 232501.

[272] H. Tamura et al. "Gamma-ray spectroscopy of hypernuclei — present and future". In: *Nucl. Phys. A* 914 (2013). XI International Conference on Hypernuclear and Strange Particle Physics (HYP2012), pp. 99–108.

[273] R. W. Hackenburg. "Observation of hypernuclear γ rays in ${}^{7}_{\Lambda}\mathrm{Li}$ and ${}^{9}_{\Lambda}\mathrm{Be}$". PhD thesis. Houston Univ., 1983.

[274] M. Ukai et al. "γ-ray spectroscopy of ${}^{16}_{\Lambda}\mathrm{O}$ and ${}^{15}_{\Lambda}\mathrm{N}$ hypernuclei via the ${}^{16}\mathrm{O}$ $(K^-, \pi^-\gamma)$ reaction". In: *Phys. Rev. C* 77.5 (2008).

[275] M. May et al. "First observation of the p $\Lambda\rightarrow$ s Λ γ-ray transition in ${}^{13}_{\Lambda}\mathrm{C}$". In: *Phys. Rev. Lett.* 78.23 (1997), p. 4343.

[276] A. Bouyssy and other. "Hypernuclei with A $\geq$ 12". In: *Phys. Lett. B* 64.3 (1976), pp. 276–278.

[277] W. M. Alberico and G. Garbarino. "Weak decay of Λ-hypernuclei". In: *Phys. Rep.* 369.1 (2002), pp. 1–109.

[278] A. K. Kerman et al. "Superstrange nuclei". In: *Phys. Rev. C* 8.1 (1973), p. 408.

[279] S. Acharya et al. "Hypertriton production in p-Pb collisions at $\sqrt{s_{NN}} = 5.02$ TeV". In: *Phys. Rev. Lett.* 128 (25 2022), p. 252003.

[280] R. Abou Yassine et al. “New results on light nuclei, hyperons and hypernuclei from HADES (HADES collaboration)”. In: *EPJ Web Conf.* Vol. 271. EDP Sciences. 2022, p. 08004.

[281] A. R. Timmins et al. “Overview of strangeness production at the STAR experiment”. In: *J. Phys. G: Nucl. Part. Phys.* 36.6 (2009), p. 064006.

[282] B. E. Aboona et al. “Observation of directed flow of hypernuclei ${}^{3}_{\Lambda}\mathrm{H}$ and ${}^{4}_{\Lambda}\mathrm{H}$ in $\sqrt{s_{\mathrm{NN}}} = 3\ \mathrm{GeV}\ \mathrm{Au}+\mathrm{Au}$ collisions at RHIC”. In: *Phys. Rev. Lett.* 130 (21 May 2023), p. 212301.

[283] B. Dönigus. “Hypernuclei at relativistic energies”. In: *EPJ Web Conf.* 276 (2023), p. 04002.

[284] Y. Ji. “Measurements on the production and properties of light hypernuclei at STAR”. In: *EPJ Web Conf.* Vol. 276. EDP Sciences. 2023, p. 04003.

[285] Saito T. R. et al. “Production of hypernuclei in peripheral HI collisions: The HypHI project at GSI”. In: *Nucl. Phys. A* 881 (2012). Progress in Strangeness Nuclear Physics, pp. 218–227.

[286] H. Ekawa. “ WASA-FRS HypHI experiment at GSI for studying light hypernuclei”. In: *EPJ Web Conf.* 271 (2022), p. 08012.

[287] Y. K. Tanaka et al. “WASA-FRS experiments in FAIR Phase-0 at GSI”. In: *Acta Phys. Pol. B* 16.4 (2023).

[288] Y. Sun et al. “Production of light hypernuclei with light-ion beams and targets”. In: *Phys. Rev. C* 98.2 (2018), p. 024903.

[289] The STAR Collaboration. *Observation of the Antimatter Hypernucleus* ${}^{4}_{\Lambda}\overline{H}$. 2023.

[290] K. Riisager. “Halos and related structures”. In: *Phys. Scr.* 2013.T152 (2013), p. 014001.

[291] S. Velardita et al. “Method to evidence hypernuclear halos from a two-target interaction cross section measurement”. In: *Eur. Phys. J. A* 59.6 (2023), p. 139.

[292] N. Buyukcizmeci et al. “Mechanisms for the production of hypernuclei beyond the neutron and proton drip lines”. In: *Phys. Rev. C* 88 (1 July 2013), p. 014611.

[293] T. R. Saito et al. “Novel method for producing very-neutron-rich hypernuclei via charge-exchange reactions with heavy ion projectiles”. In: *Eur. Phys. J. A* 57.5 (2021), p. 159.

[294] J. P. Bocquet et al. “Delayed fission from the antiproton annihilation in ${}^{209}\mathrm{Bi}$ — evidence for hypernuclear decay”. In: *Phys. Lett. B* 192.3-4 (1987), pp. 312–314.

[295] T. A. Armstrong et al. “Fission of heavy hypernuclei formed in antiproton annihilation”. In: *Phys. Rev. C* 47 (5 1993), pp. 1957–1969.

[296] A. Sanchez Lorente et al. “Double Λ-hypernuclei at the PANDA experiment”. In: *Hyperfine Interact.* 213.1-3 (2012), pp. 41–50.

[297] J. Pochodzalla. “Future hypernuclear physics at MAMI-C and PANDA-GSI”. In: *Nucl. Phys. A* 754 (2005). Proceedings of the Eighth International Conference on Hypernuclear and Strange Particle Physics, pp. 430–442.

[298] O. Buss et al. “Transport-theoretical description of nuclear reactions”. In: *Phys. Rep.* 512.1-2 (2012), pp. 1–124.

[299] P. Kaitaniemi et al. “INCL intra-nuclear cascade and ABLA de-excitation models in Geant4”. In: *Prog. Nucl. Sci. Techn.* 2 (2011).

[300] H. Mori et al. “The quantum-statistical theory of transport phenomena, I: On the Boltzmann-Uehling-Uhlenbeck equation”. In: *Prog. Theor. Phys.* 8.3 (1952), pp. 327–340.

[301] G. A. Lalazissis et al. “The effective force NL3 revisited”. In: *Phys. Lett. B* 671.1 (2009), pp. 36–41.

[302] W. D. Myers and W. J. Swiatecki. “Nuclear properties according to the Thomas-Fermi model”. In: *Nucl. Phys. A* 601.2 (1996), pp. 141–167.

[303] R. Schmidt et al. “Nucleon density in the nuclear periphery determined with antiprotonic x-rays: Cadmium and tin isotopes”. In: *Phys. Rev. C* 67.4 (2003), p. 044308.

[304] K. Tsushima et al. “Strangeness production from πN collisions in nuclear matter”. In: *Phys. Rev. C* 62.6 (2000), p. 064904.

[305] A. Baldini et al. “Total cross-sections for reactions of high energy particles”. In: Springer, 1988.

[306] T. Gaitanos et al. “Formation of double-Λ hypernuclei at PANDA”. In: *Nucl. Phys. A* 881 (2012), pp. 240–254.

[307] C. Samanta et al. “Generalized mass formula for non-strange and hypernuclei with SU (6) symmetry breaking”. In: *J. Phys. G: Nucl. Part. Phys.* 32.3 (2006), p. 363.

[308] V. F. Weisskopf and D. H. Ewing. “On the yield of nuclear reactions with heavy elements”. In: *Phys. Rev.* 57 (6 Mar. 1940), pp. 472–485.

[309] M. Wang et al. “The AME2016 atomic mass evaluation”. In: *Chin. Phys. C* 41.030003 (2017), pp. 1674–1137.

[310] Y. Ayyad et al. “Proton-induced fission of $^{181}\mathrm{Ta}$ at high excitation energies”. In: *Phys. Rev. C* 89.5 (2014), p. 054610.

[311] Y. Ayyad et al. “Dissipative effects in spallation-induced fission of $^{208}\mathrm{Pb}$ at high excitation energies”. In: *Phys. Rev. C* 91.3 (2015), p. 034601.

[312] J. L. Rodríguez-Sánchez et al. “Hypernuclei formation in spallation reactions by coupling the Liège intranuclear cascade model to the deexcitation code ABLA”. In: *Phys. Rev. C* 105.1 (2022), p. 014623.

[313] M. Rey-Campagnolle. *Production of heavy hypernuclei with antiprotons*. Tech. rep. CERN-EP-89-13. 1989.

[314] Z. Feng. “Strangeness production and hypernuclear formation in proton- and antiproton-induced reactions”. In: *Phys. Rev. C* 101 (6 2020), p. 064601.

[315] I. Vidaña. “Hyperons: the strange ingredients of the nuclear equation of state”. In: *Proc. Math. Phys. Eng. Sci.* 474.2217 (2018), p. 20180145.

[316] N. Grigoryan et al. *Study of light hypernuclei by pionic decay at JLab*. 2007.

[317] J. Iwanowska et al. “Performance of cerium-doped Gd3Al2Ga3O12 (GAGG:Ce) scintillator in gamma-ray spectrometry”. In: *Nucl. Instrum. Methods A* 712 (2013), pp. 34–40.

[318] J. F. Ziegler and J. P. Biersack. “The stopping and ranges of ions in solids, Vol. 1”. In: Springer, 1985. Chap. The Stopping and Ranges of Ions in Matter.

A. Thermal and mechanical properties of cryostat materials

Overview of the main thermal and mechanical properties of the materials included in the cryostat setup. The presented values indicate the properties at room temperature. The properties of most of the listed materials between cryogenic and room temperature are presented in [156].

material	dens. [g/cm^{-3}]	lin. th. exp. [10^{-6}/K]	th. cond. [W/m K]
stainl. steel (316LN)	8.00	15.9	15
aluminum (AW-6082)	2.70	23.4	200
aluminum (AW-6061)	2.70	23.0	190
copper (OFE)	8.94	17.7	391
Manganin (CuMnNi)	8.40	18.0	22
sapphire (Al_2O_3)	3.98	6.0	25
ruby (Al_2O_3)	3.98	6.0	40
zirkonia (ZrO_2)	5.45	12.2	2
PEEK	1.46	57.7	0.2
aramide	1.44	-2.4	0.05

B. Technical drawings of trap electrodes

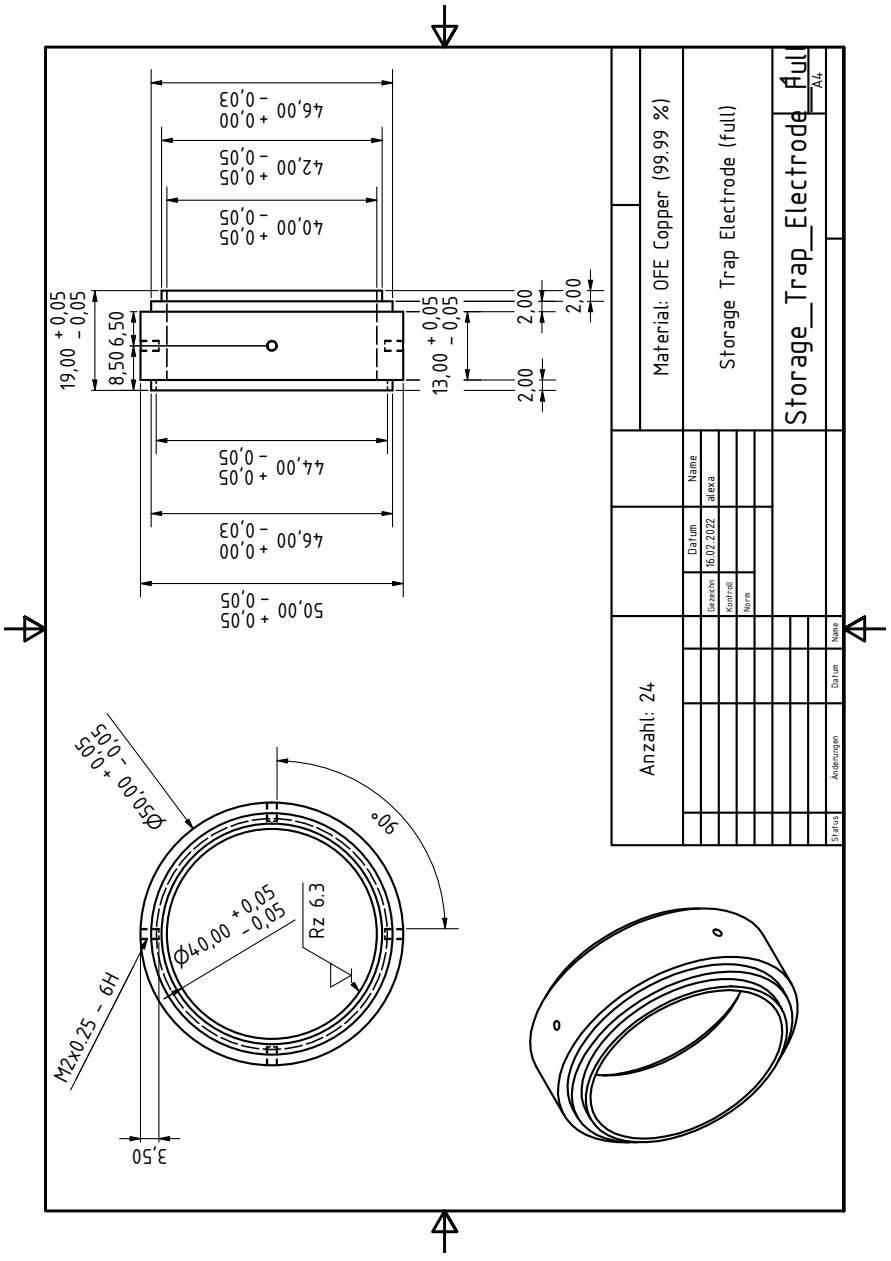

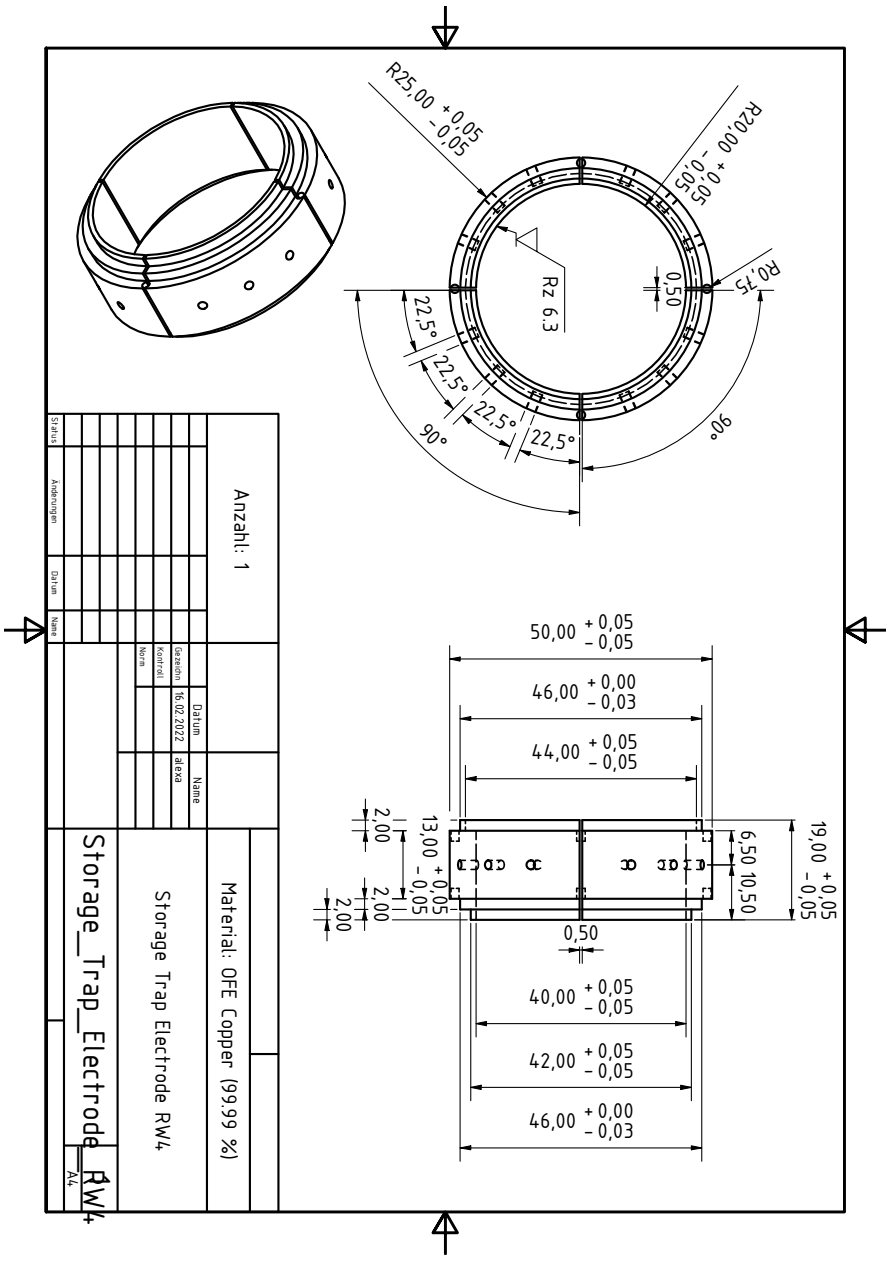
R25,00 + 0,05 - 0,05
R20,00 + 0,05 - 0,05
R0,75
Rz 6.3
0,50
22,5°
22,5°
22,5°
22,5°
90°
90°
50,00 + 0,05 - 0,05
46,00 + 0,00 - 0,03
44,00 + 0,05 - 0,05
2,00
13,00 + 0,05 - 0,05
2,00
2,00
6,50
10,50
19,00 + 0,05 - 0,05
0,50
40,00 + 0,05 - 0,05
42,00 + 0,05 - 0,05
46,00 + 0,00 - 0,03
Anzahl: 1
Material: OFE Copper (99,99 %)
Storage Trap Electrode RW4
Storage_Trap_Electrode_RW4
A4
Status
Änderungen
Datum
Name
Gezeichn
Kontrol
Norm
Datum
16.02.2022
Name
alexa

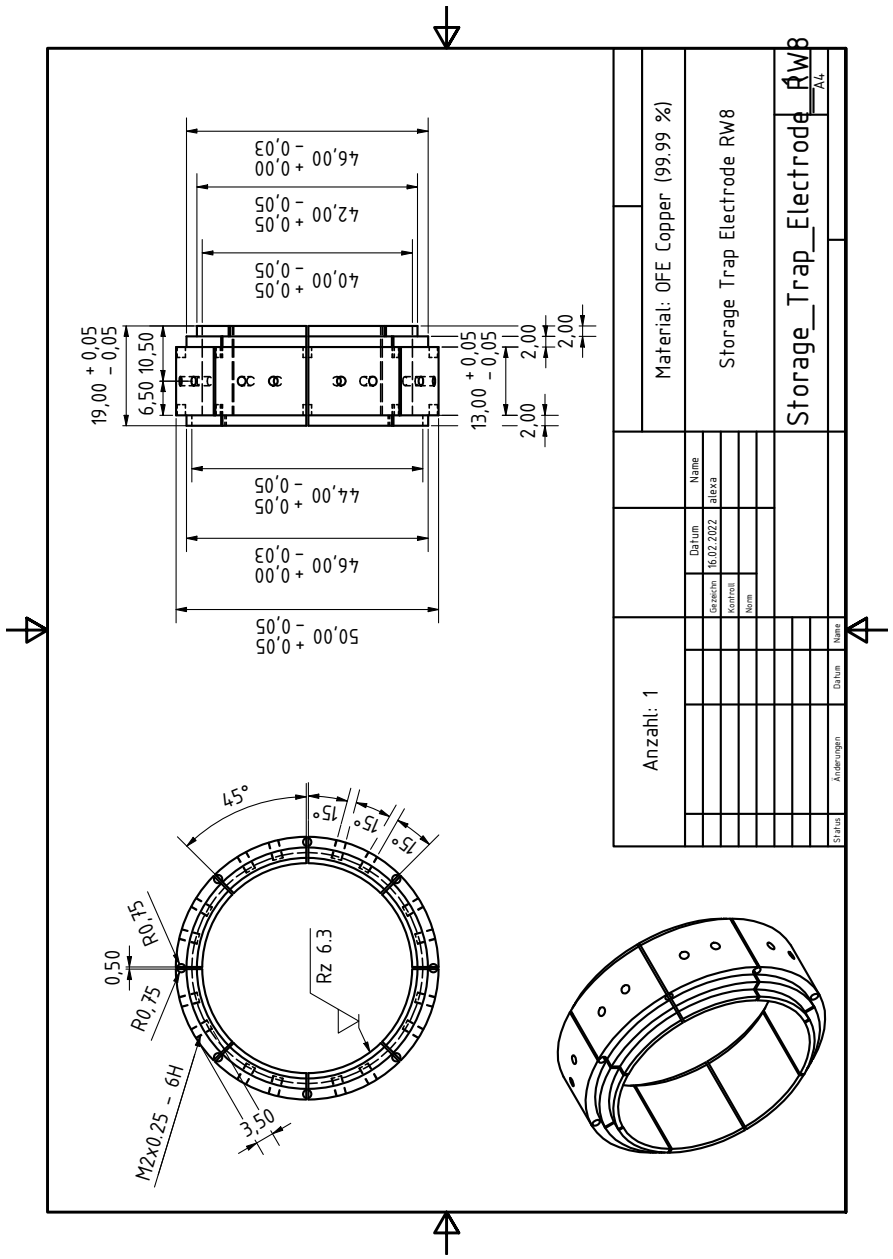
Storage_Trap_Electrode_RW8
A4
Material: OFE Copper (99.99 %)
Storage Trap Electrode RW8
Anzahl: 1
Name
Datum
16.02.2022
alexa
Gezeichn.
Kontrolli
Norm
Änderungen
Datum
Name
Status
46,00 + 0,00 - 0,03
42,00 + 0,05 - 0,05
40,00 + 0,05 - 0,05
44,00 + 0,05 - 0,05
46,00 + 0,00 - 0,03
50,00 + 0,05 - 0,05
19,00 + 0,05 - 0,05
6,50
10,50
13,00 + 0,05 - 0,05
2,00
2,00
2,00
45°
15°
15°
15°
R0,75
R0,75
0,50
Rz 6,3
M2x0,25 - 6H
3,50

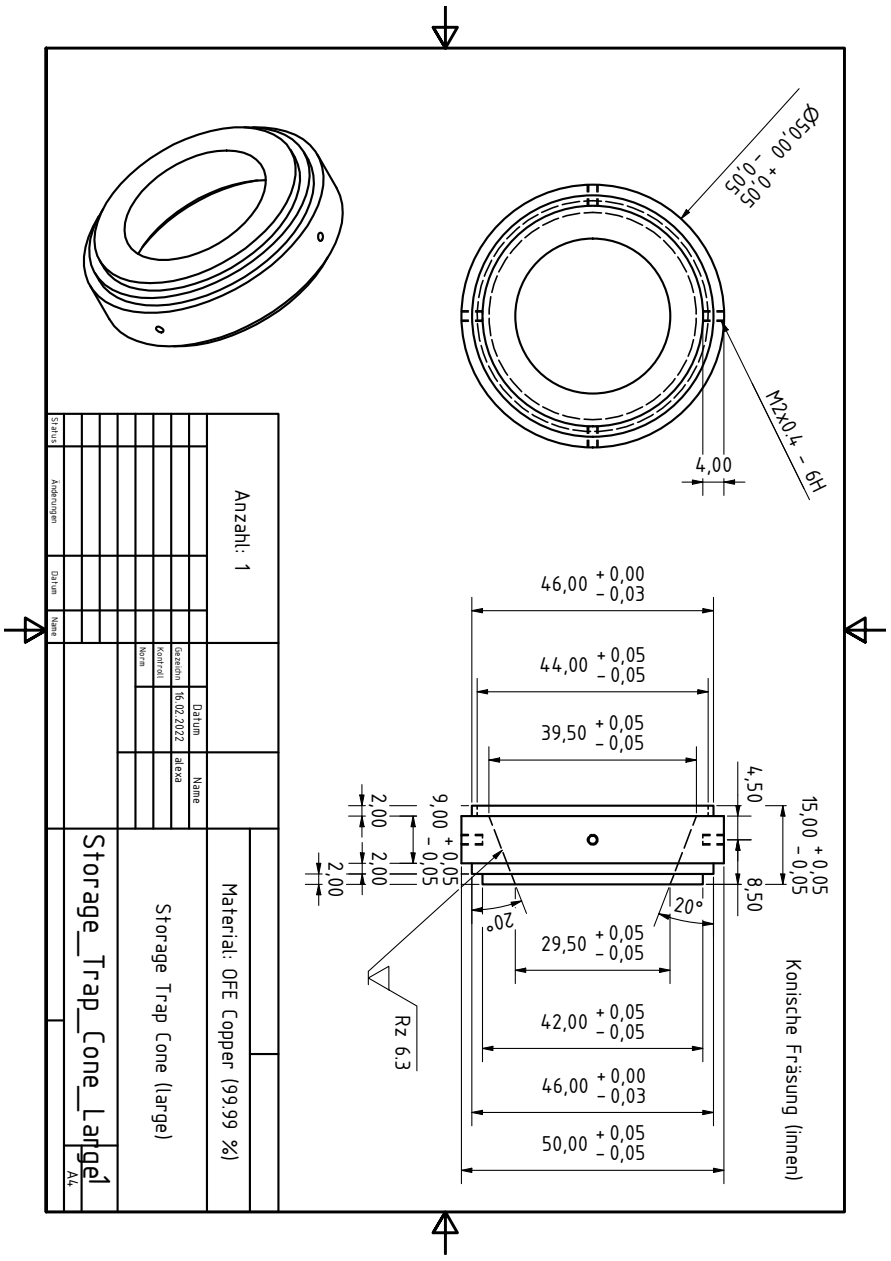
Ø50,00 +0,05 -0,05
M12x0,4 - 6H
4,00
46,00 +0,00 -0,03
44,00 +0,05 -0,05
39,50 +0,05 -0,05
4,50
15,00 +0,05 -0,05
8,50
9,00 +0,05 -0,05
2,00
2,00
2,00
20°
20°
29,50 +0,05 -0,05
42,00 +0,05 -0,05
46,00 +0,00 -0,03
50,00 +0,05 -0,05
Rz 6,3
Konische Fräsung (innen)
Anzahl: 1
Material: OFE Copper (99,99 %)
Storage Trap Cone (large)
Storage_Trap_Cone_Large1
A4
Status
Änderungen
Datum
Name
Gezeichn
Kontrolliert
Norm
Datum
16.02.2022
Name
alexa

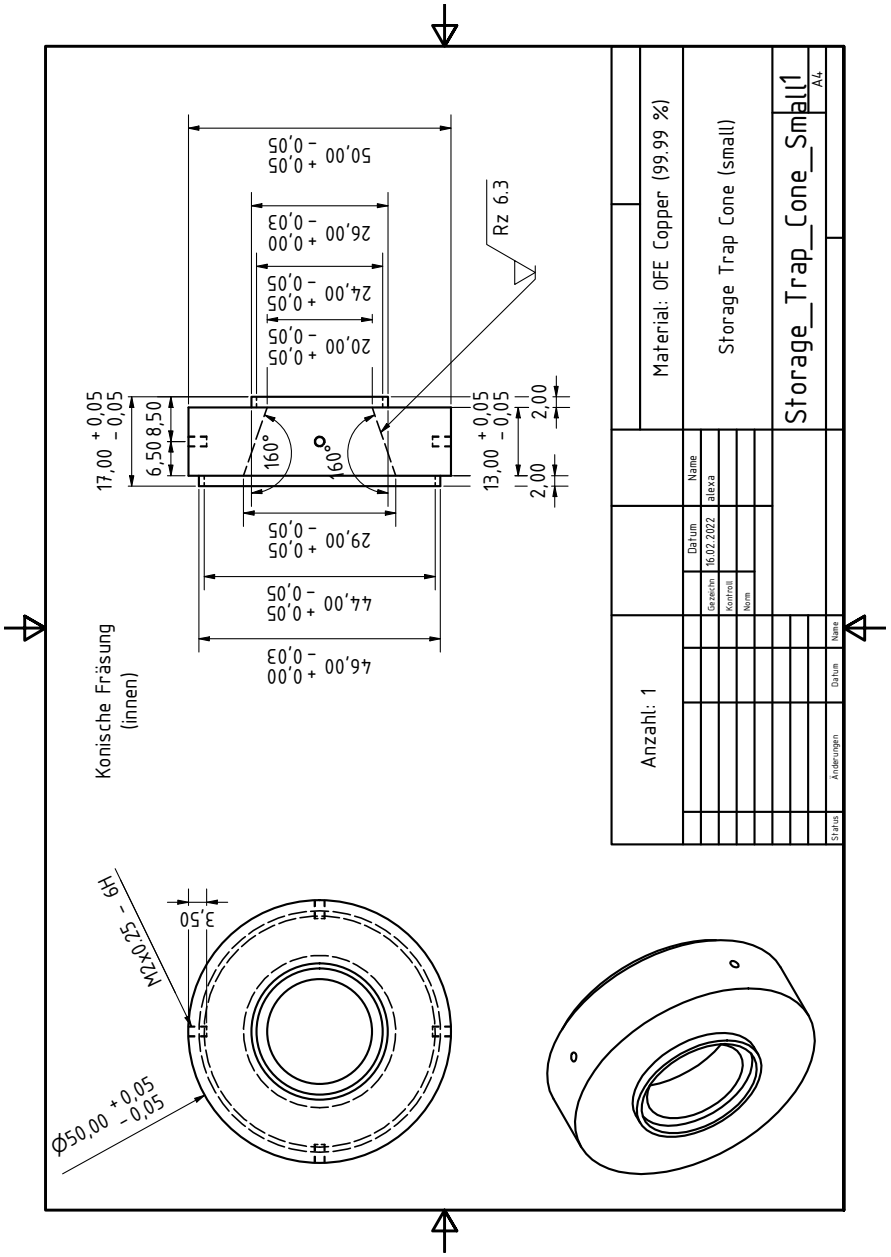
Storage_Trap_Cone_Small1
A4
Material: OFE Copper (99.99 %)
Storage Trap Cone (small)
Anzahl: 1
Name
alexa
Datum
16.02.2022
Gezeichn.
Kontrolli
Norm
Änderungen
Datum
Name
Status
Rz 6.3
50,00 +0,05 −0,05
26,00 +0,00 −0,03
24,00 +0,05 −0,05
20,00 +0,05 −0,05
29,00 +0,05 −0,05
44,00 +0,05 −0,05
46,00 +0,00 −0,03
17,00 +0,05 −0,05
6,50
8,50
13,00 +0,05 −0,05
2,00
2,00
160°
160°
Konische Fräsung
(innen)
3,50
M42x0,25 − 6H
Ø50,00 +0,05 −0,05

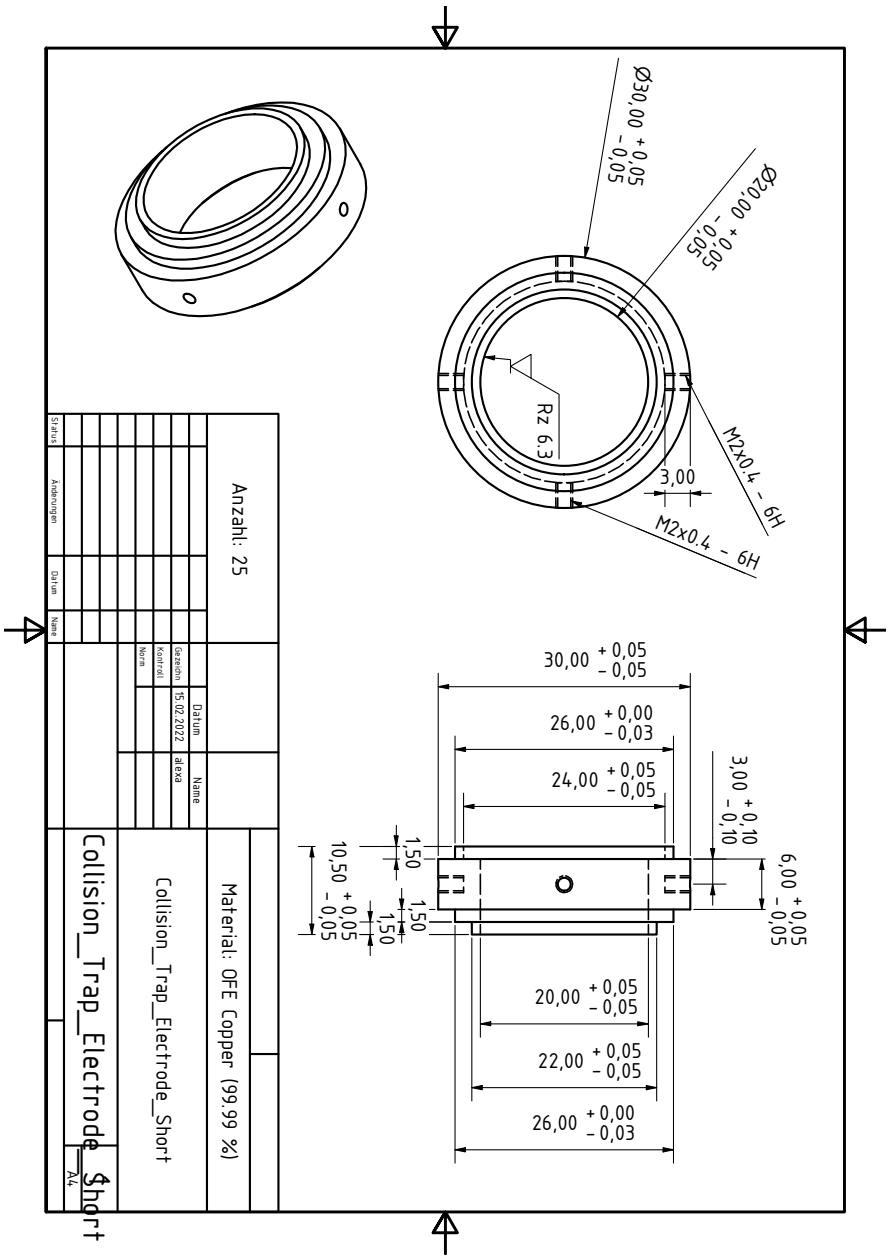
Ø30,00 + 0,05 - 0,05
Ø20,00 + 0,05 - 0,05
Rz 6,3
M2x0,4 - 6H
3,00
M2x0,4 - 6H
30,00 + 0,05 - 0,05
26,00 + 0,00 - 0,03
24,00 + 0,05 - 0,05
3,00 + 0,10 - 0,10
6,00 + 0,05 - 0,05
1,50
1,50
1,50
10,50 + 0,05 - 0,05
20,00 + 0,05 - 0,05
22,00 + 0,05 - 0,05
26,00 + 0,00 - 0,03
Anzahl: 25
Material: OFE Copper (99,99 %)
Collision_Trap_Electrode_Short
Collision_Trap_Electrode_Short
A4
Status
Änderungen
Datum
Name
Gezeichn
Kontrolliert
Norm
Datum
15.02.2022
Name
alexa

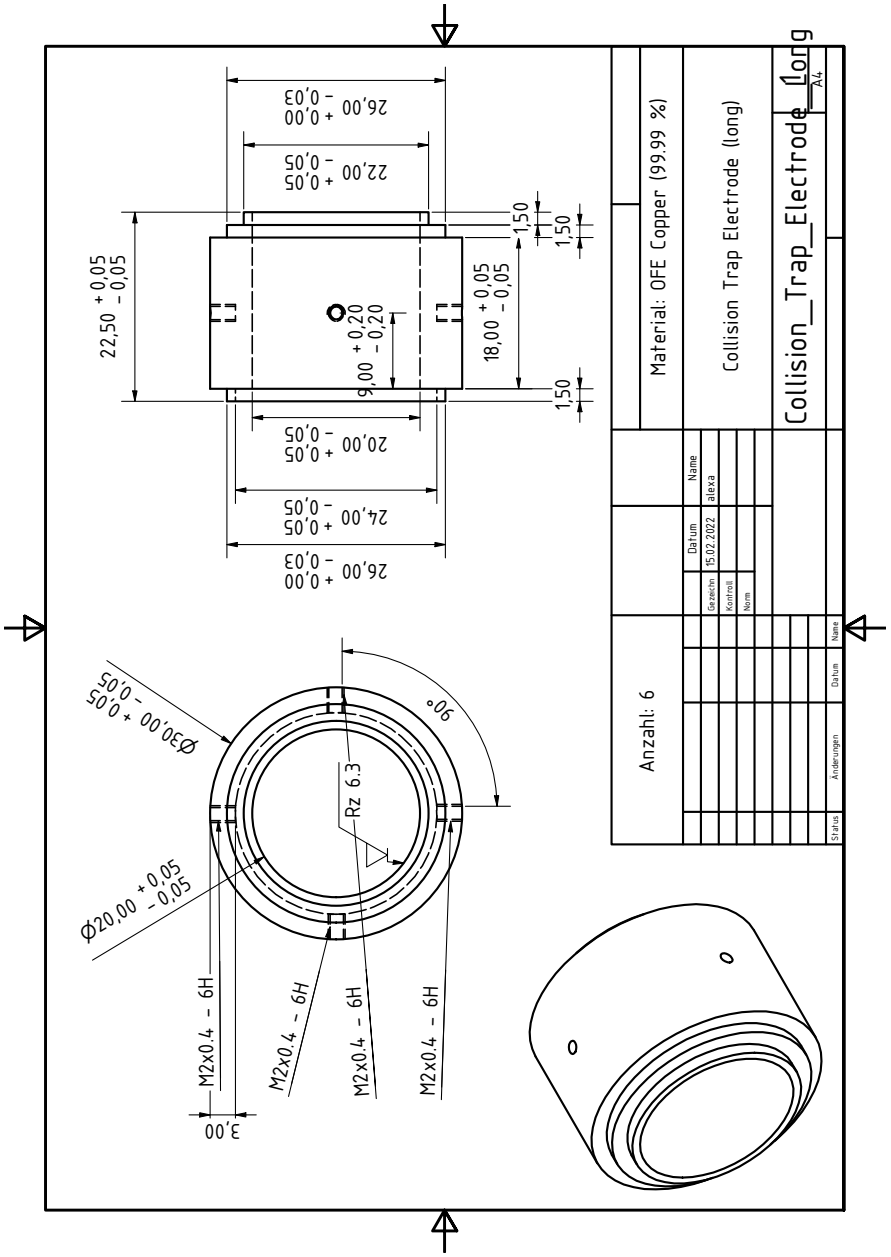
Collision_Trap_Electrode_Long
A4
Collision Trap Electrode (long)
Material: OFE Copper (99.99 %)
Anzahl: 6
Name
alexa
Datum
15.02.2022
Gezeichn.
Kontrolli
Norm
Änderungen
Datum
Name
Status
26,00 + 0,00 - 0,03
22,00 + 0,05 - 0,05
20,00 + 0,05 - 0,05
24,00 + 0,05 - 0,05
22,50 + 0,05 - 0,05
18,00 + 0,05 - 0,05
9,00 + 0,20 - 0,20
1,50
Ø30,00 + 0,05 - 0,05
Ø20,00 + 0,05 - 0,05
90°
Rz 6.3
M2x0.4 - 6H
3,00

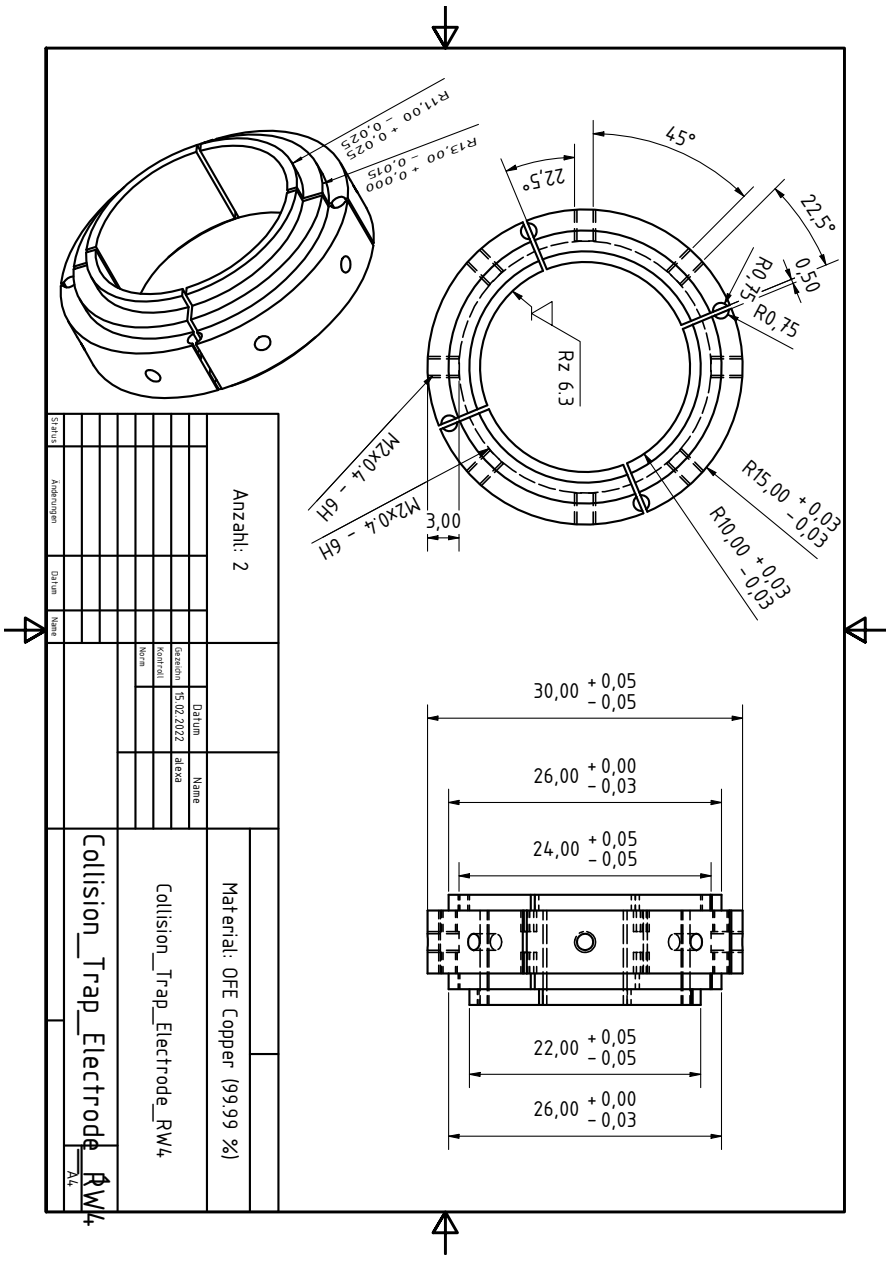
45°
22,5°
22,5°
R0,75
R0,75
0,50
Rz 6.3
M2X0,4 - 6H
M2X0,4 - 6H
3,00
R15,00 +0,03 -0,03
R10,00 +0,03 -0,03
30,00 +0,05 -0,05
26,00 +0,00 -0,03
24,00 +0,05 -0,05
22,00 +0,05 -0,05
26,00 +0,00 -0,03
Anzahl: 2
Material: OFE Copper (99,99 %)
Collision_Trap_Electrode_RW4
Collision_Trap_Electrode_RW4
A4
Name
Datum
alexa
15.02.2022

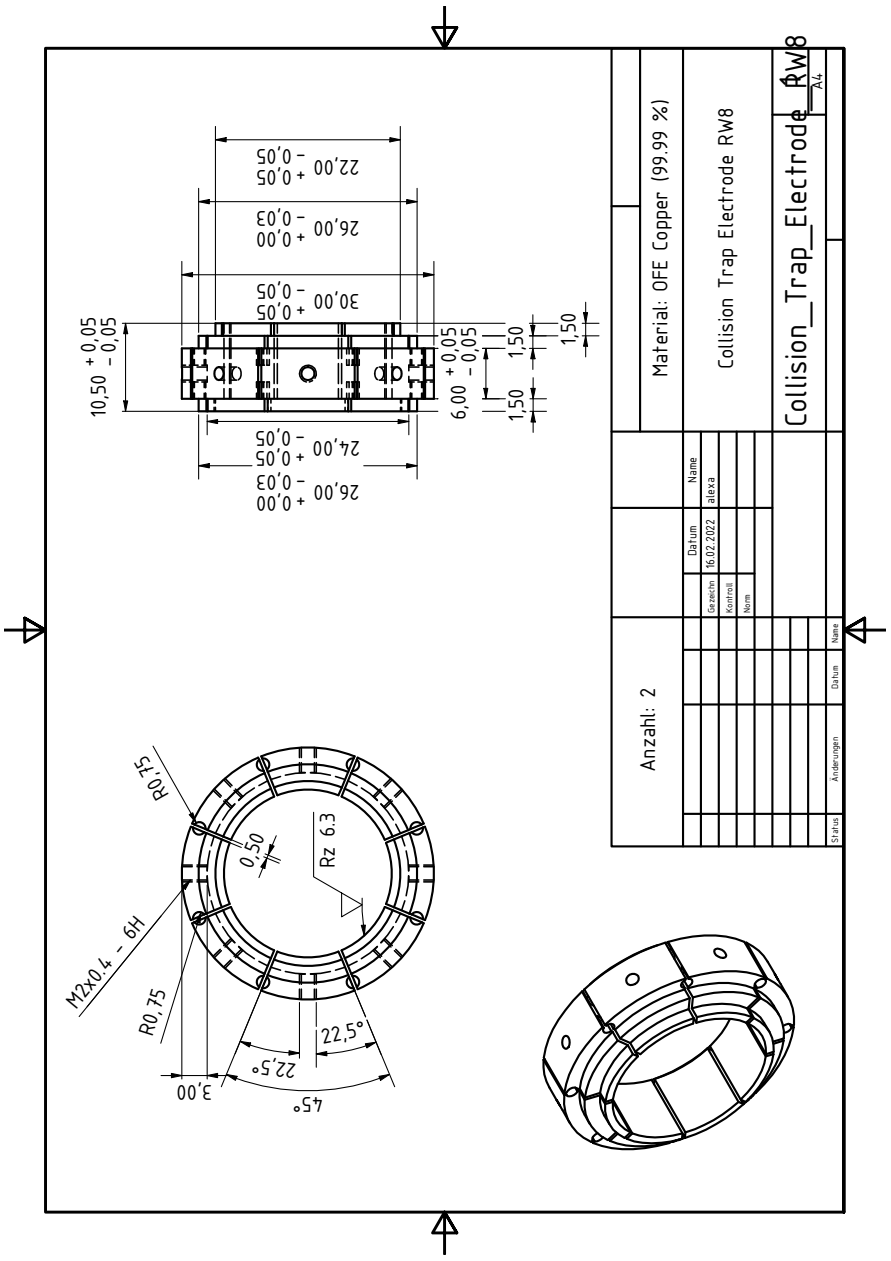
Collision_Trap_Electrode_RW8
A4
Material: OFE Copper (99.99 %)
Collision Trap Electrode RW8
Anzahl: 2
Name
Datum
alexa
16.02.2022
Gezeichn.
Kontrolli
Norm
Änderungen
Datum
Name
Status
22,00 + 0,05 - 0,05
26,00 + 0,00 - 0,03
30,00 + 0,05 - 0,05
24,00 + 0,05 - 0,05
26,00 + 0,00 - 0,03
10,50 + 0,05 - 0,05
6,00 + 0,05 - 0,05
1,50
1,50
1,50
R0,75
0,50
Rz 6.3
M2x0.4 - 6H
R0,75
22,5°
22,5°
45°
3,00

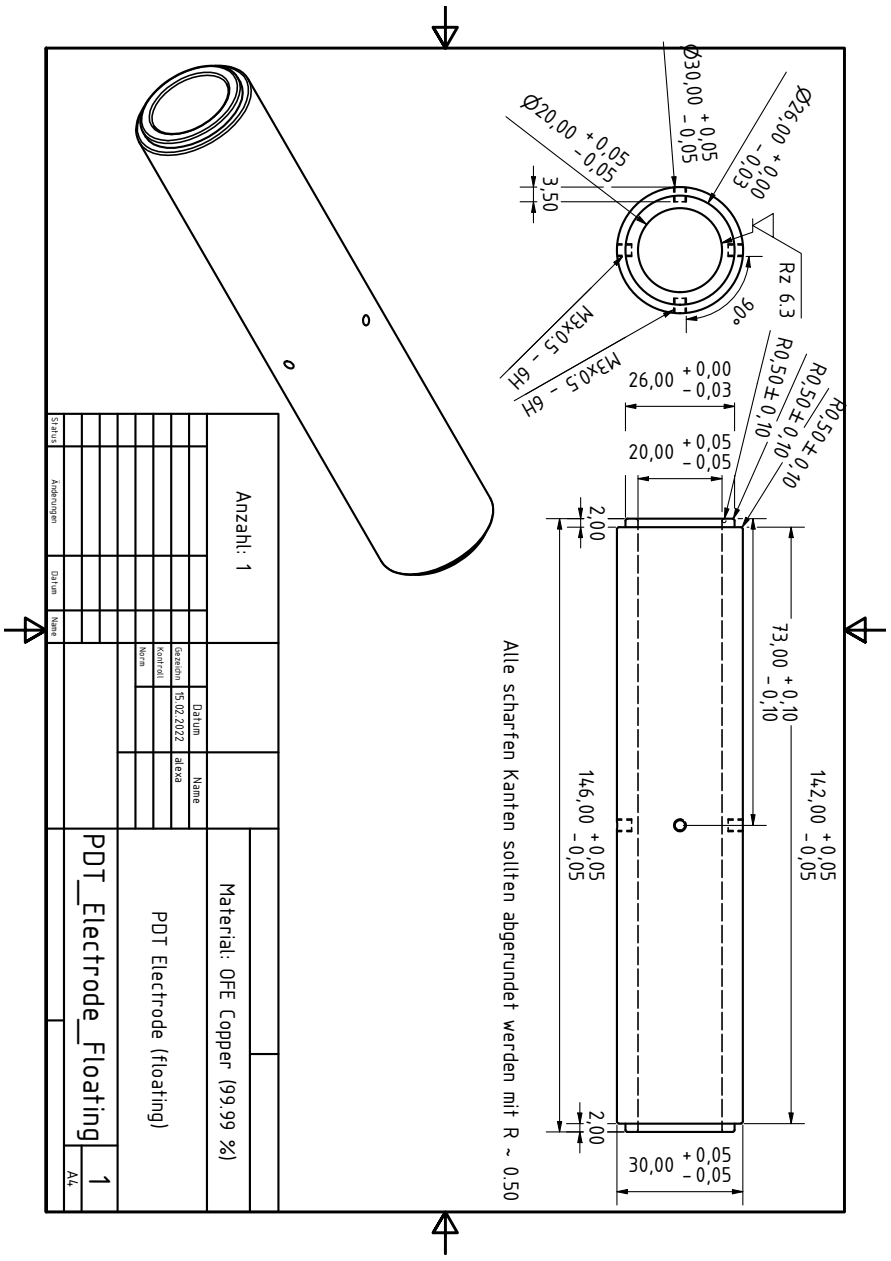
Ø30,00 + 0,05 - 0,05
Ø26,00 + 0,00 - 0,03
Ø20,00 + 0,05 - 0,05
3,50
Rz 6.3
90°
M3x0.5 - 6H
M3x0.5 - 6H
R0,50 ± 0,10
R0,50 ± 0,10
R0,50 ± 0,10
26,00 + 0,00 - 0,03
20,00 + 0,05 - 0,05
2,00
73,00 + 0,10 - 0,10
146,00 + 0,05 - 0,05
142,00 + 0,05 - 0,05
2,00
30,00 + 0,05 - 0,05
Alle scharfen Kanten sollten abgerundet werden mit R ~ 0.50
Anzahl: 1
Material: OFE Copper (99.99 %)
PDT Electrode (floating)
PDT_Electrode_Floating
1
A4
Status
Änderungen
Datum
Name
Gezeichn
Kontrol
Norm
Datum
15.02.2022
Name
alexa

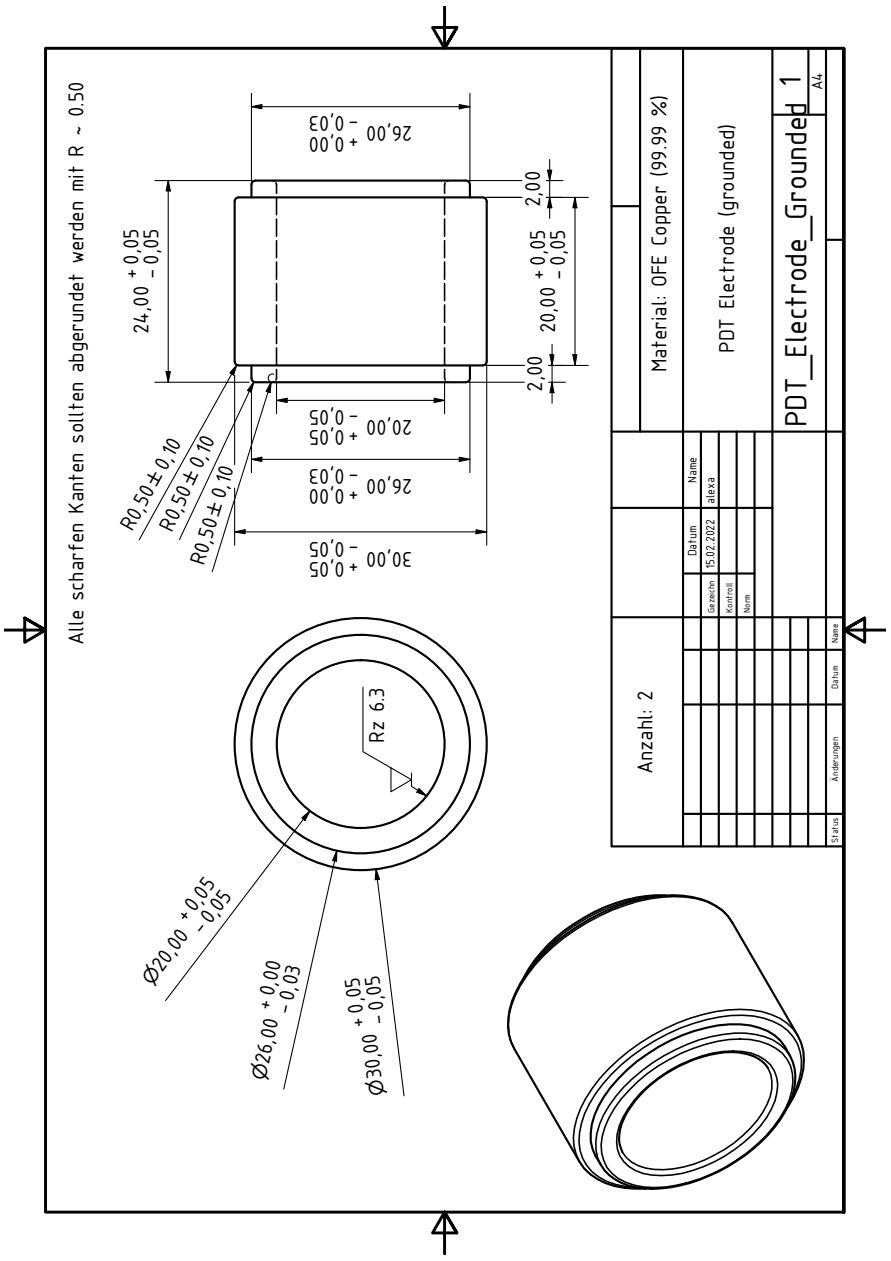
Alle scharfen Kanten sollten abgerundet werden mit R ~ 0.50
26,00 + 0,00 - 0,03
2,00
24,00 + 0,05 - 0,05
20,00 + 0,05 - 0,05
2,00
20,00 + 0,05 - 0,05
26,00 + 0,00 - 0,03
30,00 + 0,05 - 0,05
R0,50±0,10
R0,50±0,10
R0,50±0,10
Rz 6.3
Ø20,00 + 0,05 - 0,05
Ø26,00 + 0,00 - 0,03
Ø30,00 + 0,05 - 0,05
Material: OFE Copper (99,99 %)
PDT Electrode (grounded)
PDT_Electrode_Grounded_1
A4
Anzahl: 2
Name
Datum
alexa
15.02.2022
Gezeichn.
Kontrolli
Norm
Änderungen
Datum
Name
Status

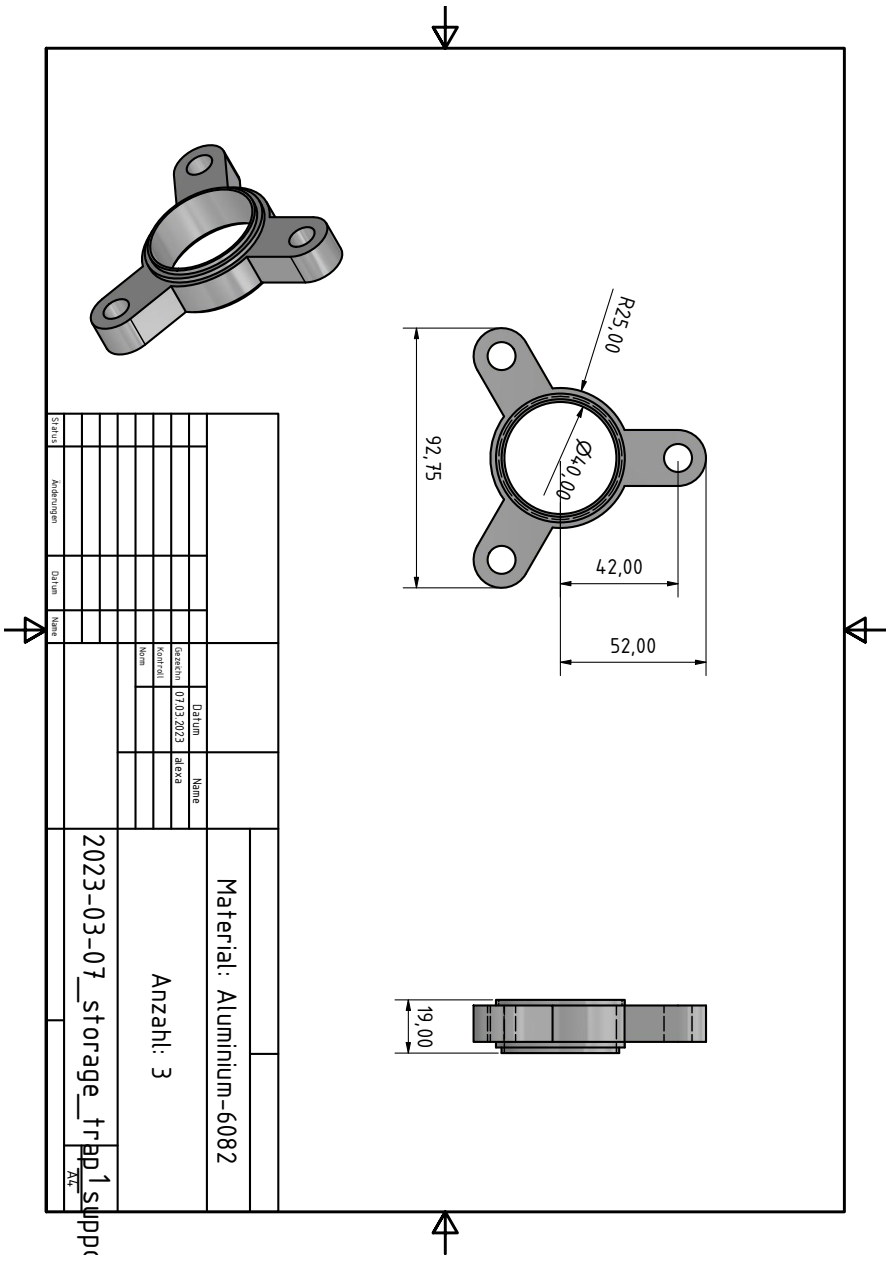
R25,00
92,75
Ø40,00
42,00
52,00
19,00
Material: Aluminium-6082
Anzahl: 3
2023-03-07_storage_tray_top_1_suppo
A4
Name
Datum
alexa
07.03.2023
Gezeichn
Kontrolliert
Norm
Status
Änderungen
Datum
Name

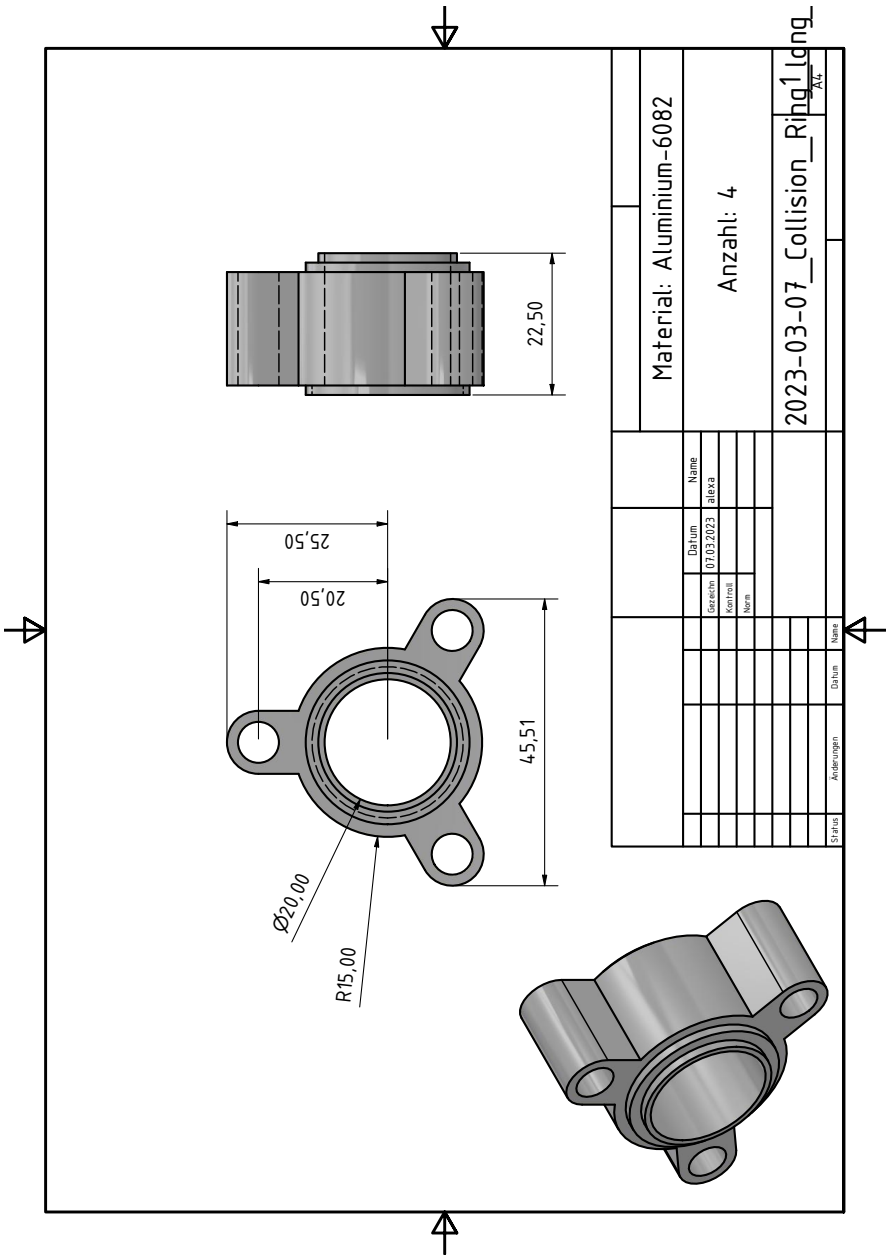
22,50
25,50
20,50
45,51
Ø20,00
R15,00
Material: Aluminium-6082
Anzahl: 4
2023-03-07_Collision_Ring1_long
A4
Name
aleka
Datum
07.03.2023
Gezeichn.
Kontrolli
Norm
Name
Datum
Änderungen
Status

C. Weight budget of the PUMA trap and cryostat setup

Weight budget of the 300 K stage of PUMA trap and cryostat assembly. The abbreviation US represents components on the upstream end of the assembly and DS on the downstream end, while CUST indicates the custom flange connection on the upstream end of the main vacuum chamber.

component	weight/piece [kg]	quantity	total weight [kg]
CF200 cube	26.52	2	53.04
CF200-4xCF40 align. chamber	10.54	2	21.08
CF200-CUST main vacuum chamber	27.97	1	27.97
CF200-CUST 0-L reducer	8.02	1	8.02
CF200 pipe (333 mm)	9.67	2	19.34
CF200-160 0-L reducer	5.36	3	16.09
CF160 coldhead (US)	18.00	1	18.00
CF160 coldhead (DS)	16.80	1	16.80
CF200-63 reducer nipple	9.67	1	9.67
CF200 einzel lens feedthrough	9.23	1	9.23
CF200 trap feedthrough	8.69	1	8.69
CF200-100 0-L reducer	7.63	1	7.63
CF100 pipe (150 mm)	3.62	1	3.62
CF100 NEG cartridge flange	3.22	1	3.22
CF200 blind flange	9.28	2	18.56
CF200-40 0-L reducer	9.04	1	9.04
CF40 XYZ precision table	4.69	1	4.69
CF40 rotary feedthrough	4.50	1	4.50
CF40 heavy-load lin. feedthrough	6.41	2	12.82
CF40 med.-load lin. feedthrough	1.20	6	7.20
CF40 pipe (150 mm)	0.67	9	6.03
CF40 angle valve	1.73	1	1.73
full 300 K stage	286.97	1	286.97

Weight budget of the 50 K stage of PUMA trap and cryostat assembly. The abbreviation US represents components on the upstream end of the assembly and DS on the downstream end.

component	weight/piece [kg]	quantity	total weight [kg]
main step-profile tube	4.58	1	4.58
removable flange	0.12	1	0.12
trap elec. feedthrough reducer	1.45	1	1.45
DS BTU nipple (90 mm)	0.33	1	0.33
Al cuboid	1.74	2	3.48
einzel lens feedthrough reducer	1.18	1	1.18
einzel lens assembly	0.33	1	0.33
US alignment chamber	1.67	1	1.67
US coldhead chicane (lower)	0.80	1	0.80
US coldhead chicane (upper)	0.91	1	0.91
US coldhead connector	0.98	1	0.98
US cold shutter flange	0.55	1	0.55
DS alignment chamber	0.83	1	0.83
DS coldhead chicane (lower)	0.48	1	0.48
DS coldhead chicane (upper)	0.53	1	0.53
DS coldhead connector	0.88	1	0.88
DS bottom flange	0.56	1	0.56
copper braid (200 mm)	0.27	4	1.08
cylinder shutter	0.27	1	0.27
full 50 K stage	21.01	1	21.01

Weight budget of the 4 K stage of PUMA trap and cryostat assembly. The abbreviation ST represents components on the storage trap, while CT represents the collision trap.

component	weight/piece [kg]	quantity	total weight [kg]
ST ring electrode	0.09	21	1.89
ST RW electrode (8 seg.)	0.09	1	0.09
ST RW electrode (4 seg.)	0.09	1	0.09
ST conical electrode (l)	0.11	1	0.11
ST conical electrode (s)	0.17	1	0.17
ST alignment piece	0.07	1	0.07
CT ring electrode long	0.07	4	0.28
CT ring electrode short	0.03	24	0.72
CT RW electrode (8 seg.)	0.03	2	0.06
CT RW electrode (4 seg.)	0.03	2	0.06
CT alignment piece	0.03	2	0.06
PDT grounded electrode	0.08	2	0.16
PDT floated electrode	0.51	1	0.51
CT support endcap	0.01	1	0.01
CT-ST support piece	0.15	1	0.15
ST base support piece	0.50	1	0.50
CT support rod	0.06	3	0.18
ST support rod	0.11	3	0.33
trap tower support bar	0.15	3	0.45
elec. feedthrough flange	4.35	1	4.35
trap chamber	13.99	1	13.99
cryostat entrance tube	3.87	1	3.87
conductance barrier	0.10	1	0.10
thermal conduct. bar	4.47	1	4.47
copper braid	0.26	1	0.26
entrance cube	1.00	1	1.00
copper blades	0.31	1	0.31
US coldhead adapter	0.83	1	0.83
full 4 K stage	35.07	1	35.07

D. Annihilation branching ratios

Branching ratios of final states for antiproton proton annihilations (*left*) and antiproton neutron annihilations (*right*). In case of non-strange final states, only channels with at least 2 % probability are depicted, and for kaonic final states with at least 0.2 %.

Antiproton - Proton

Final State	Probability in %
$\rho^+\rho^-$	3.37
$\pi^+\pi^-\pi^0$	2.34
$\pi^+\pi^-\rho^0$	2.02
$\pi^+\pi^0\rho^-$	2.02
$\pi^-\pi^0\rho^+$	2.02
$\pi^+\pi^-\omega$	3.03
$\pi^+\pi^-\pi^0\omega$	2.84
$\pi^+\pi^+\pi^-\pi^-$	2.74
$\pi^+\pi^-\pi^0\pi^0$	3.89
$\pi^+\pi^+\pi^-\rho^-$	2.58
$\pi^+\pi^-\pi^-\rho^+$	2.58
$\pi^+\pi^-\pi^0\rho^0$	6.29
$\pi^+\pi^0\pi^0\rho^-$	5.05
$\pi^-\pi^0\pi^0\rho^+$	5.05
$\pi^+\pi^+\pi^-\pi^-\pi^0$	2.61
$\pi^+\pi^-\pi^0\pi^0\omega$	2.58
$\pi^+\pi^+\pi^+\pi^-\pi^-\pi^-$	2.83
$\pi^+\pi^+\pi^-\pi^-\pi^0\pi^0$	9.76
$\pi^+\pi^-\pi^0\pi^0\pi^0\pi^0$	2.68
$K^{*+}K^{*-}$	0.225
$K^{*0}\bar{K}^{*0}$	0.225
$K^0\bar{K}^0\omega$	0.232
$K^+K^-\omega$	0.232
$K^0\bar{K}^0\rho^0$	0.202
$K^+K^-\rho^0$	0.202
$K^0K^-\rho^+$	0.234
$\bar{K}^0K^+\rho^-$	0.234
$K^{*+}\bar{K}^0\pi^-$	0.23
$K^{*-}K^0\pi^+$	0.23

Antiproton - Neutron

Final State	Probability in %
$\rho^-\rho^0$	3.51
$\rho^-\eta$	2.27
$\rho^-\omega$	3.51
$\pi^+\pi^-\pi^-$	2.86
$\pi^+\pi^-\rho^-$	3.62
$\pi^-\pi^0\rho^0$	5.61
$\pi^0\pi^0\rho^-$	3.51
$\pi^-\rho^+\rho^-$	2.09
$\pi^-\pi^0\omega$	5.05
$\pi^+\pi^-\pi^-\omega$	10.52
$\pi^+\pi^-\pi^-\pi^0$	5.51
$\pi^+\pi^-\pi^-\pi^0\pi^0$	2.72
$\pi^+\pi^+\pi^-\pi^-\pi^-\pi^0$	8.33
$\pi^+\pi^-\pi^-\pi^0\pi^0\pi^0$	6.67
$K^0K^-\pi^0$	0.316
$K^0\bar{K}^0\pi^-$	0.432
$K^+K^-\pi^-$	0.513
$K^0K^-\omega$	0.35
$K^0\bar{K}^0\rho^-$	0.77
$K^+K^-\rho^-$	0.77
$K^{*-}K^0\pi^0$	0.245
$K^{*0}K^-\pi^0$	0.245

E. Acknowledgements

At the end of this thesis, I would like to thank Prof. Dr. Alexandre Obertelli for the very special experience of being part of the PUMA team. Both Prof. Dr. Alexandre Obertelli and Dr. Frank Wienholtz have been fantastic and amicable mentors, who always supported me by sharing their great experience and extensive knowledge.
Also, I would like to thank all members of the research group, with whom I was able to work, in particular the PUMA team - Jonas Fischer, Moritz Schlaich, Clara Klink and Sabrina Zacarias - as well as Simone Velardita and Christina Xanthopoulou. I met you as colleagues and now I regard many of you as friends.
Special thanks go to Jose Antonio Ferreira Somoza, Paolo Chiggiato, Berthold Jenninger, Anke Stölzel and Cédric Garion from the CERN vacuum group for the regular discussions and the helpful input for the cryostat design, as well as to Yann Dutheil from the CERN ion optics group for the matching of the antiproton bunch properties at the optical handover point.
Additional special thanks go to Assoc. Prof. Dr. Theodoros Gaitanos and José-Luis Rodríguez-Sánchez for the provision and explanation of the GiBUU and ABLA++ simulation codes.
Finally, this work, like the rest of my education, would not have been possible without the support of my parents and my sister Tamara.

F. Academic CV

The academic CV has been removed in the published version.